Radiative transfer in hot gas of galaxy clusters: constraints on ICM turbulence

Irina Zhuravleva

München 2011

Radiative transfer in hot gas of galaxy clusters: constraints on ICM turbulence

Irina Zhuravleva

Dissertation
an der Fakultät für Physik
der Ludwig–Maximilians–Universität
München

vorgelegt von
Irina Zhuravleva
aus Pestovo, Russland

München, den 26. September 2011

Erstgutachter: Prof. Dr. Rashid Sunyaev

Zweitgutachter: Prof. Dr. Hans Böhringer

Tag der mündlichen Prüfung: 4. November 2011

Contents

List of Figures

List of Tables

Zusammenfassung

Die vorliegende Arbeit zielt darauf ab Folgendes bereitzustellen: (i) indirekte Methoden zur Bestimmung der Eigenschaften von Geschwindigkeitsfeldern im Intracluster-Medium (ICM) mittels des Resonanzstreuung (RS) Effekts in den hellen Röntgenlinien in Spektren von Galaxienhaufen; (ii) Bestimmung der Eigenschaften von Leistungsspektren von 3D Geschwindigkeiten mittels zukünftigen direkten Messungen. Es wird angenommen, dass wenn Galaxienhaufen sich vereinigen oder wenn Masse entlang von Filamenten akkretiert wird, werden turbulente Bewegungen angetrieben. Diese transferieren kinetische Energie eingespeist aus großen ($\sim$ Mpc) Skalen hinunter zu kleinen dissipativen Skalen durch eine Kaskadierung der kinetischen Energie. Um die komplexe Physik, die die Dynamik von Galaxienhaufen betrifft zu verstehen, wollen wir einige wichtige Fragen adressieren: Wie hoch ist der Beitrag vom turbulentem Druck am Gesamtdruck, und wie hoch ist die statistische Verzerrung in Bezug auf die Masse; Wie hoch ist die Heizrate des turbulenten ICM; Wie werden Turbulenzen transportiert, und magnetische Felder verstärkt; Welche Rolle spielt die kinetische Gasbewegung bei der Beschleunigung von Teilchen?

Die direkte Messung der Geschwindigkeiten der Gasbewegung durch Linienverschiebung und -verbreiterung benötigen eine Energieauflösung, die eine Größenordnung höher ist, als das Auflösungsvermögen von derzeitigen Röntgeninstrumenten. Indirekte Messungen von Turbulenzen durch den RS Effekt mittels Gitterspektrometern erlauben uns bereits die Bestimmung der charakteristischen Amplituden der Bewegungen. Wir wendeten diese Methode an der elliptischen Galaxie NGC 4636 an, und fanden dass die isotropen, turbulenten Geschwindigkeiten mit räumlichen Skalen kleiner als 1 kpc kleiner als 100 km/s sind, und dass die Unterstützung des turbulenten Drucks auf den Galaxienkern kleiner als 5 % des thermalen Drucks mit einer Konfidenzniveau von 90 % (Kapitel 2).

Neben den Geschwindigkeitsamplituden würden wir gerne die Ausrichtung und die räumlichen Skalen der Bewegungen (d.h. die Größe der Eddies, welche Energie beinhalten) verstehen. Wir zeigten auf dass (i) RS ist hauptsächlich empfindlich an kleinmaßstäbigen Bewegungen, (ii) es ist insbesondere sensibel an radialen Bewegungen (Kapitel 3). Dies erlaubt uns die Bestimmung der Anisotropie und der Skalen der räumlichen Bewegungen mit der Kombination von direkten Messungen von Bewegungen mit Messungen des RS Effekts.

Ein eindeutiger Weg zur Messung von Amplituden der Gasbewegung senkrecht zur Sichtlinie mittels der Polarisation von hellen Röntgenlinien, die durch RS verursacht werden, werden in Kapitel 4 vorgestellt. Wir zeigten, dass aufgrund der Quadrupolmo-

mente im Strahlungsfeld von Galaxienhaufen, welche aufgrund der spitzen Emissivität
natürlicherweise auftreten, der erwartete Polarisationsgrad im Perseushaufen bei der He-
lium ähnlichen Eisenlinie von 6.7 keV 7% beträgt, und im Virgohaufen ist es ungefähr ein
paar Prozent in den versprechendsten Linien. Mit Hilfe von hydrodynamischen Simulatio-
nen von Galaxienhaufen zeigten wir, dass die Polarisation empfindlich zu Transversalbewe-
gungen des Gases ist. Insbesondere zeigten wir, dass der Polarisationsgrad in der Helium
ähnlichen Eisenlinie ~ 25 % innerhalb der Distanz von 500 kpc vom Kern des Haufens
beträgt, wenn das Gas des Haufens ruht. Die Einbindung von Gasbewegungen verringert
die Polarisation herunter zu ~ 10 %, und verursacht eine Rotation der Polarisationsebene.

Im letzten Teil der Dissertation werden wir eine Methode zur Bestimmung des Leis-
tungsspektrum von 3D Geschwindigkeiten und der Strukturfunktion mittels beobachteter
Verschiebung der Linien und Linienverbreiterung. Analytische Lösungen wurden hergeleitet
und eine Analyse wurde anhand eines einfachen Model-Galaxienhaufens illustriert. Ins-
besondere zeigen wir, dass (i) die Linienbreite als Funktion von projizierten Abständen vom
Zentrum ist eng verbunden mit der Strukturfunktion des 3D Geschwindigkeitfeldes; (ii) das
Verhältnis von beobachteter Amplitudenveränderungen der mittleren Geschwindigkeit und
der Geschwindigkeitsdispersion kann genutzt werden, um die Einschuss-Skala der Turbulen-
zen zu finden; (iii) Abbildung des projizierten 2D Geschwindigkeitsfeldes bietet den direk-
testen Weg, um das Leistungsspektrum von 3D Geschwindigkeiten abzuschätzen (Kapitel
5).

Summary

The work presented here aims to (i) provide indirect ways to constrain the properties of the velocity field in the intracluster medium (ICM) using the resonant scattering (RS) effect in the bright X-ray lines in spectra of galaxy clusters; (ii) using future direct measurements, constrain properties of 3D velocity power spectra. It is believed that as clusters merge or as matter accretes along the filaments, turbulent motions, which transfer kinetic energy injected on large scales $\sim$ Mpc to small dissipative scales through the cascade of kinetic energy, are driven. Understanding the complex physics involved in cluster dynamics, we would be able to address a number of important questions: how much turbulent pressure contributes to the total pressure and what is the mass bias; what is the ICM turbulent heating rate; how turbulence transports and amplifies magnetic fields; what is the role of gas motions in particle acceleration.

Direct measurements of velocities of gas motions through the line shift and broadening require an energy resolution an order of magnitude higher than the resolution of current X-ray observatories. Indirect measurements of turbulence through the RS effect already allow us to constrain characteristic amplitudes of motions now using grating spectrometers. I applied this method to elliptical galaxy NGC4636 and found that the isotropic turbulent velocities on spatial scales smaller than ≈ 1 kpc are less than 100 km/s and that the turbulent pressure support in the galaxy core is smaller than 5 per cent of the thermal pressure at the 90 per cent confidence level (Chapter 2).

Besides velocity amplitudes, we would like to understand the anisotropy and spatial scales of motions (i.e. size of energy-containing eddies). I showed that (i) RS is sensitive mainly to small-scale motions, (ii) it is particularly sensitive to radial motions (Chapter 3). This allows us to constrain anisotropy and spatial scales of motions combining the direct measurements of motions with measurements of the RS effect.

A unique way to measure amplitudes of gas motions perpendicular to the line of sight using polarization in bright X-ray lines caused by RS is presented in Chapter 4. I showed that due to quadrupole moment in a radiation field in galaxy clusters, which arises naturally due to the peaked emissivity profile, the expected polarization degree in the Perseus cluster is ~ 7 per cent in the He-like iron line at 6.7 keV and in the Virgo cluster it is about a few cent in the most promising lines. Using hydrodynamical simulations of galaxy clusters I showed that polarization is sensitive to transverse motion of gas. In particular I showed that the polarization degree in the He-like iron line reaches ~ 25 per cent within the distance of 500 kpc from the cluster core if the cluster gas is at rest. The inclusion of gas

motions decreases the polarization down to ~ 10 per cent and causes a rotation of the polarization plane.

In the last part of thesis a method to constrain the 3D velocity power spectrum and structure function using the observed shift of lines and line broadening is presented. Analytical solutions were derived and the analysis was illustrated on a simple model of galaxy clusters. In particular, I show that (i) the width of the line as a function of projected distance from the center is closely linked to the structure function of the 3D velocity field; (ii) the ratio of observed amplitude variations of mean velocity and velocity dispersion can be used to find the injection scale of turbulence; (iii) mapping of the projected 2D velocity field provides the most direct way of estimating the 3D velocity power spectrum (Chapter 5).

Chapter 1

Introduction

1.1 Galaxy clusters as cosmological and astrophysical laboratories

Galaxy clusters are the largest objects in the Universe which have already undergone gravitational relaxation and are in virial equilibrium. Cluster masses range from $\sim 10^{14} M_\odot$ to more than $10^{15} M_\odot$, the majority of which are dark matter (80%) and hot X-ray gas (15%). The contribution of stars to the total mass is of the order of a few %. Clusters are formed from the rare high peaks in primordial Gaussian density perturbations during the hierarchical clustering scenario of the cosmic structure formation (e.g. Peebles, 1993; Peacock, 1999).

Galaxy clusters offer an important probe of the fundamental cosmological parameters. The matter content of clusters provides a fair sample of the matter content in the Universe. The observed ratio of baryon mass to total mass in galaxy clusters should closely match the ratio Ω_b/Ω_m of the mean baryon and total matter densities of the Universe (e.g. White et al., 1993).

The abundance of clusters and their distribution in redshift is determined by the geometry of the Universe and the power spectrum of initial density fluctuations since the formation of dark matter halos is independent of the gas dynamics. Therefore, the observed abundance of clusters at different redshifts allows us to constrain the amplitude of the power spectrum on cluster scales and test the models, which include a dark energy component, since the dark energy equation of the state parameter w directly affects the linear growth of fluctuations (e.g. Haiman, Mohr, & Holder, 2001; Allen et al., 2004; Vikhlinin et al., 2006).

Galaxy clusters are also very important astrophysical laboratories, which allow us to study the physics of intergalactic and intracluster medium. Optical and infrared observations help to study the distribution of galaxies and their properties through imaging and spectroscopy. The overall optical luminosity scales with the overall mass of a cluster, the velocity dispersion of individual galaxies responds to the potential well of clusters. Infrared observations are used to find high redshift clusters. Gravitational lensing measurements
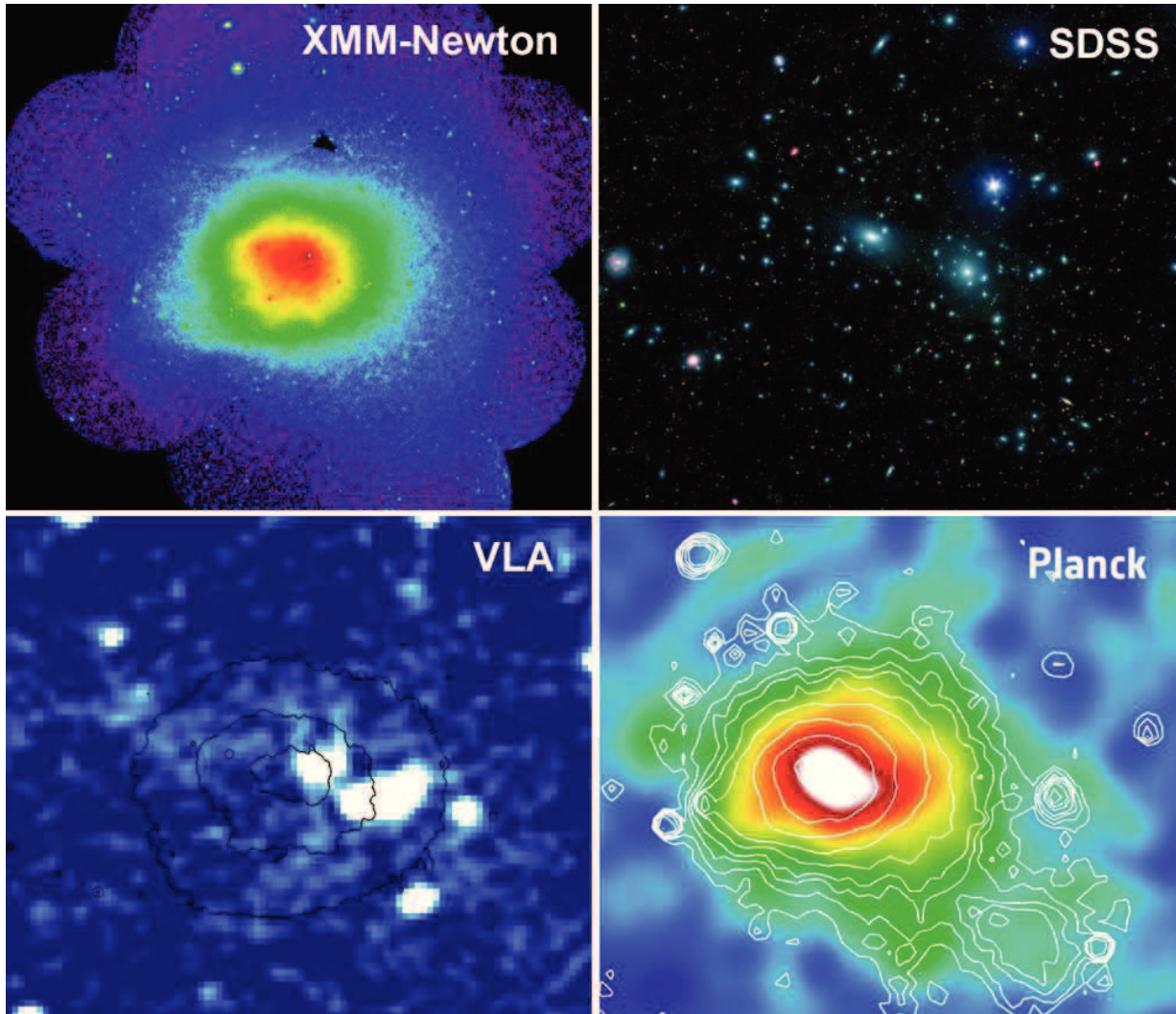
Figure 1.1: Coma cluster in X-ray (top left), optical (top right), radio (bottom left) and Sunyaev-Zeldovich (bottom right) observations.

give information about dark matter distribution and total mass. Radio observations show a number of diffuse structures, allowing us to study non-thermal phenomena. Most of the detailed knowledge about clusters of galaxies comes from X-ray observations of hot gas trapped in the cluster's gravitational potential. The state of gas is determined by the propagation of shock waves, gas sloshing, AGN activity, cluster mergers, radiative cooling and thermal feedback. Clusters are observed in microwave band as cold spots below 218 GHz due to the inverse Compton scattering of the photons of the cosmic microwave background radiation (Sunyaev-Zel'dovich effect) (see Fig. 1.1).

1.2 Hot X-ray gas: spectrum and radiation mechanisms

Hot ($10^6 - 10^7$ K) X-ray emitting gas in the dominant constituent of baryons in clusters, making 10–15 % of the total cluster mass of $10^{14} - 10^{15}$ M$_\odot$. The theoretical model of the typical X-ray spectrum of a galaxy cluster is shown in Fig. 1.2. Bremsstrahlung, recombination continuum and emission lines excited by electron collisions are the main emission components in this plasma.

In spite of a large gas mass, the optical depth of the hot plasma for free-free absorption is extremely low in the X-ray regime. This is immediately clear from a comparison of the observed X-ray luminosity of the brightest clusters, $L_X \sim 10^{45}$ erg s^{-1}, with the black body radiation of a Mpc size object with a temperature $T \sim 10^7 - 10^8$K:

$$\tau_{ff} \approx \frac{L_X}{4\pi R^2 \sigma T^4} = 1.5 \cdot 10^{-33} \left(\frac{L_X}{10^{45} \text{ erg s}^{-1}} \right) \left(\frac{R}{\text{Mpc}} \right)^{-2} \left(\frac{T}{10^8 \text{ K}} \right)^{-4}, \qquad (1.1)$$

where R is the characteristic cluster size. The depth for Thomson scattering is also low:

$$\tau_T = \sigma_T n_e R = 2 \cdot 10^{-3} \left(\frac{n_e}{10^{-3}\text{cm}^{-3}} \right) \left(\frac{R}{\text{Mpc}} \right), \qquad (1.2)$$

where n_e is the electron density. This means that effectively clusters are transparent for X-rays. However, this statement is not valid for the brightest X-ray resonant lines of the most abundant elements like iron. Gilfanov, Sunyaev & Churazov (1987) have shown that the optical depth in the 6.7 keV line of He-like iron in the brightest cluster A426 (Perseus) is larger than unity[1] and therefore the radiative transfer becomes important, in particular, the effects of resonant scattering should be visible in the surface brightness distribution, element abundance variations or in the spectral shape of the line. It was immediately clear that all these effects are sensitive to the turbulent broadening of the line, making resonant scattering a unique tool to probe the characteristic amplitude of the gas velocities using telescopes with limited energy resolution.

Using current observatories we can measure the radial distribution of plasma temperature and density in galaxy clusters. Indeed, the bremsstrahlung emissivity is $\propto n_i n_e e^{-\frac{E}{kT}}$,

---

[1]For pure thermal broadening of the line.
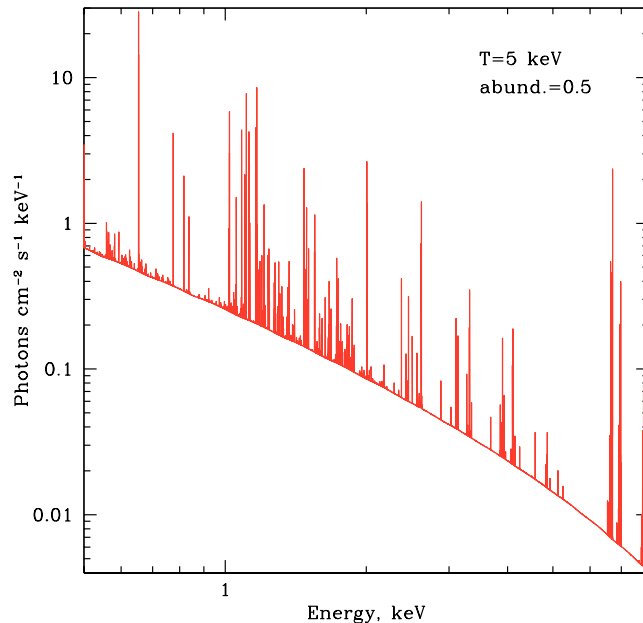
Figure 1.2: Theoretical model of typical X-ray spectrum from galaxy cluster with plasma temperature 5 keV and abundance of heavy elements 0.5 relative to the Solar abundances (Anders & Grevesse, 1989).

where $n_i n_e$ is the product of ion density and the electron density, T is the temperature of plasma, E is the energy and k is the Boltzmann constant. Therefore, the shape of continuum is used to find projected temperature of hot gas in clusters, while normalization of the spectrum determines the projected gas density. Using parametric models of temperature and number density distributions (e.g. Vikhlinin et al., 2006) or deprojection technique (e.g. Churazov et al., 2003) one can find deprojected spectrum and reconstruct profiles of 3D temperature and density. Line emissivity is proportional to the ion abundance, which one can obtain from the spectroscopic analysis.

To analyse spectra we need robust theoretical predictions of observed spectra, which has three main properties: (i) radiation is primarily due to the bremsstrahlung emission and collisionally excited lines,(ii) plasma is optically thin and (3) the number density of ions is consistent with collisional ionization equilibrium. Currently there are two most widely used in X-ray astrophysics models: APEC (Smith et al., 2001) and MEKAL/SPEX (Mewe, Gronenschild & van den Oord, 1985)

Fig. 1.2 shows theoretical spectrum of galaxy cluster with $T = 5$ keV. However, current X-ray observatories, such as *Chandra* and *XMM-Newton* suffer from low energy resolution and often we cannot resolve individual lines. Future X-ray observatories, such as *Astro-H* and *Athena* will reach energy resolution of the order of few eV, allowing us to measure broadening and shift of individual lines and additionally constrain the velocity field. Table 1.1 shows a list of main characteristics of current and future X-ray observatories. Fig. 1.3

Table 1.1: The main characteristics of current and future X-ray observatories.

Instrument	En.band(keV)	En.res.(eV)@6keV	Ang.res.(FWHM)	Eff.area(cm^2)@6keV
CHANDRA				
ASIS	0.1-10	150	1"	$\sim$220
HRC	0.1-10	$\sim$6000	<0.5"	45
LETG	0.1-6	5.4@1keV	-	20
HETG	0.6-10	29	-	25
XMM-Newton				
EPIC	0.2-12	130	6"	800
RGS	0.4-2.5	2.9@1keV	-	180@1keV
Astro-H(2014)				
SXI	0.5-12	150	1.7'	360
SXS	0.3-12	7	1.7'	210

shows spectrum of the Perseus cluster observed with *Chandra* and predicted for *Astro-H*. Spectra are extracted from the same region with 1 Ms observation.

In this thesis I present a follow up study of the resonant scattering effect and polarization caused by scattering via radiative transfer calculations, in particular focusing on studies of the velocity field. There have been numerous experimental studies aimed at detecting effects of resonant scattering in rich clusters and elliptical galaxies. For the Perseus cluster, an initial analysis suggested that resonant scattering effects were present (Molendi et al., 1998; Akimoto et al., 1999) , although subsequent studies (Churazov et al., 2004; Gastaldello & Molendi, 2004) did not support these results (see also Ezawa et al., 2001; Dupke & Arnaud, 2001; Sanders et al., 2004). Several other clusters, including M87, Centaurus and A2199 , were searched for resonant scattering effects (e.g. Kaastra, Bleeker & Mewe, 1999; Akimoto et al., 2000; Sanders & Fabian, 2006; Sakelliou et al., 2002), with mixed results. For M87 and Perseus, resonant scattering was mentioned as one of the possible explanations of the central abundance dip (Böhringer et al., 2001; Sanders et al., 2004). However a breakthrough in this field will be in the nearest future with the launch of *Astro-H* observatory with its excellent energy resolution of <7 eV. The question about which information on gas motions in clusters we can get from near future high resolution data is also addressed in this thesis.

1.3 Gas motions in the ICM

It is believed that cluster mergers, motions of galaxies and AGN feedback lead to turbulent motions in hot gas with eddy sizes ranging from Mpc near the virial radius down to few kpc near the cluster core (see e.g. Sunyaev, Norman, & Bryan, 2003). Kinetic energy injected on large scales $L \sim$ Mpc cascades over inertial range down to small dissipative scales. During cascade the kinetic energy does not dissipate, which means that the energy flux
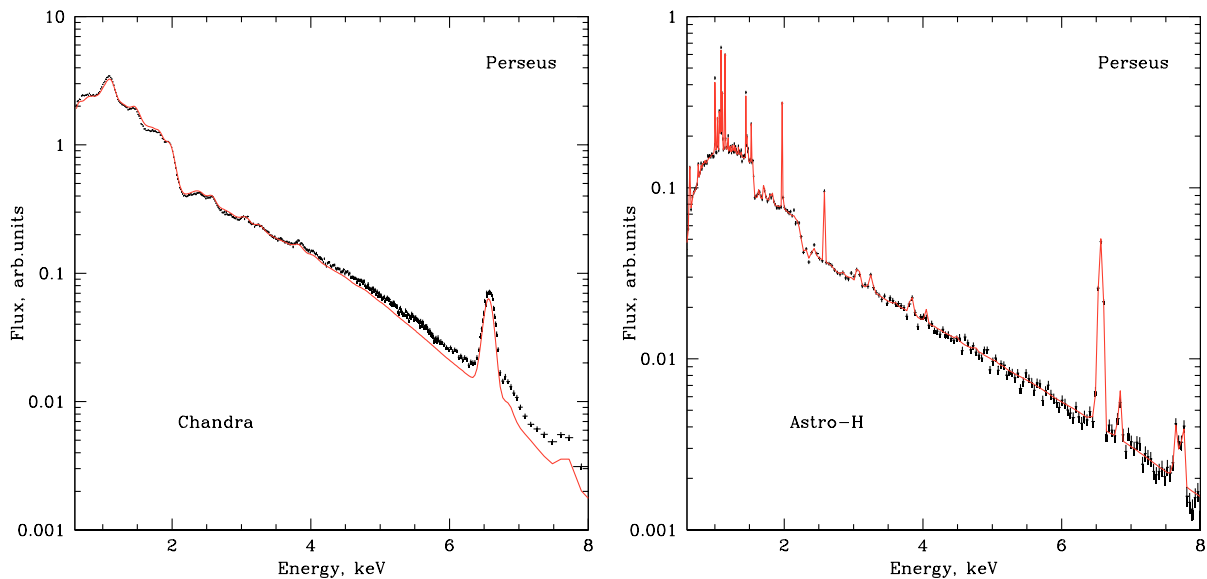
Figure 1.3: Spectrum of the Perseus cluster extracted from *Chandra* data (left) and predicted for *Astro-H* (right) observations of the same region close to the cluster center and one temperature plasma emission model.

$\propto \dfrac{V^2}{t}$ is constant. If $t = \dfrac{l}{V}$, where l is characteristic size of eddy then $\dfrac{V^2}{l}$ is constant or $V \propto k^{-1/3}$. Characteristic velocity amplitude and velocity power spectrum (P) in 3D are related as $V^2 = 4\pi P k^3$, therefore

$$P \propto k^{-11/3}. \tag{1.3}$$

This is Kolmogorov-like spectrum of turbulence (Kolmogorov, 1941; Landau & Lifshitz, 1966). Schematic model of Kolmogorov spectrum is illustrated in Fig. 1.4.

Knowledge of properties of gas motions in cluster can help us to understand better physics in the ICM and answer a number of important questions: what is the bias in the cluster mass measurements; what is the ICM turbulent heating rate in clusters; what is the role of gas motions in particle acceleration. There are two ways to study the physics of motions: through simulations and using measurements of X-ray spectroscopic missions.

Hydrodynamical simulations provide us information about full 3D velocity field in galaxy clusters (Dolag et al., 2005; Cassano & Brunetti, 2005; Norman & Bryan, 1999; Iapichino et al., 2011; Vazza et al., 2011). Example of velocity field in AMR simulations is shown on Fig. 1.6. Using results of SPH and AMR simulations we calculated velocity power spectrum using variance method described in Chapter 6, which avoids a problem of non-periodic boundaries in data boxes. Fig. 1.5 shows calculated power spectra for a sample of SPH (red) and AMR (blue) clusters. One can see that different simulations show power spectrum of gas motions similar to Kolmogorov-like spectrum (dotted line in Fig. 1.5), however, despite it, results are still controversial mainly due to insufficient resolution of simulations and, therefore, due to low Reynolds numbers in cosmological simulations.
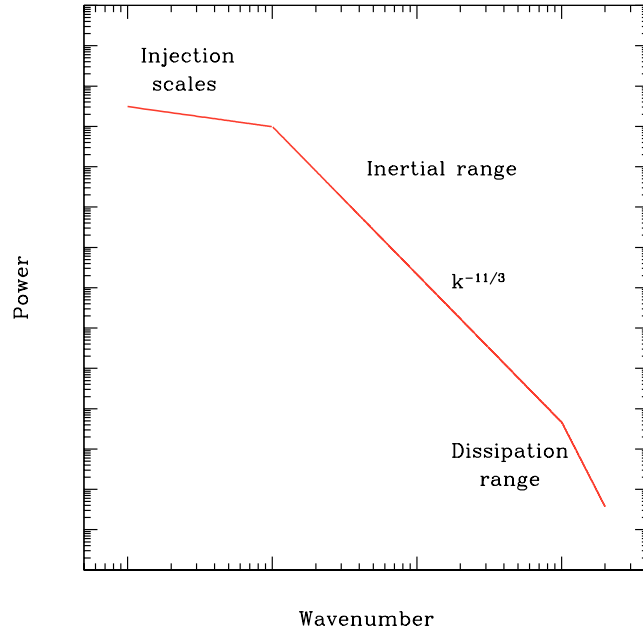
Figure 1.4: Schematic model of the Kolmogorov-like power spectrum of turbulence.
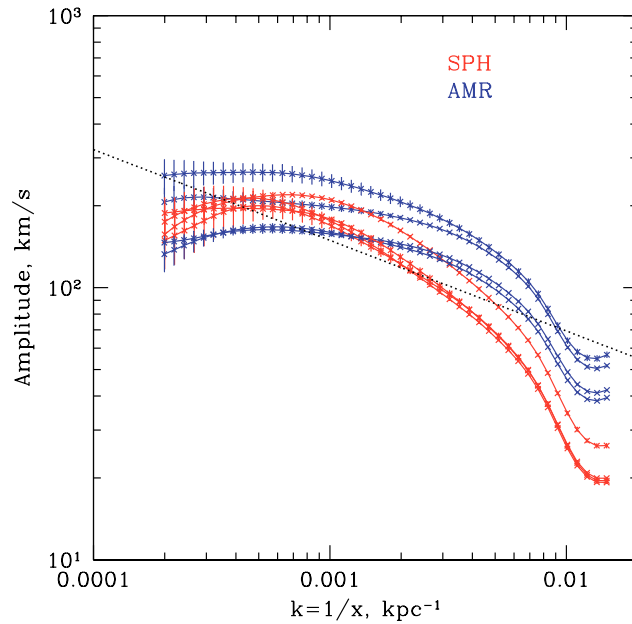
Figure 1.5: Power spectrum (amplitude $V = \sqrt{2\pi k^3 P}$) of velocity field for a sample of simulated SPH (red curves) and AMR (blue curves) galaxy clusters. The amplitude is in units of km/s. Kolmogorov-like power spectrum is shown with dotted line. SPH simulation were taken from Dolag et al. (2005) and AMR were done by Vazza et al. (2011).

Figure 1.6: One component of velocity field in simulated galaxy cluster (slice through the cluster center) in km/s. Size of the map is 12.5×12.5 Mpc. AMR simulations were done by F.Vazza (Vazza et al., 2011).

X-ray observations currently cannot provide direct measurements of the velocity field in clusters since the energy resolution is still low. Only *XMM RGS* grating can provide weak upper limits on velocity amplitude (Sanders, Fabian, & Smith, 2011). Moreover, in order to avoid smearing of the data, one should use grating only for compact and bright objects. Indirect indications of ICM turbulence come from measurements of resonant scattering effect (Churazov et al., 2004; Werner et al., 2009), from measurements of pressure (Schuecker et al., 2004) and surface brightness fluctuations (Churazov et al., 2011). Indirect ways to constrain velocity field, in particular resonant scattering and polarization in X-ray lines, are discussed in details later in this thesis.

Future observatories, such as *Astro-H* and *Athena* will allow us to measure directly centroid shift of lines and line broadening in spectra of galaxy clusters with high accuracy, since expected energy resolution is of order of few eV. In this thesis I also discuss ways to constrain properties of turbulence power spectra in cluster using future high resolution data.

1.4 Basics of resonant scattering

Based on the review paper Space Science Rev., 2010, 157, 193
E. Churazov, I. Zhuravleva, S. Sazonov & R. Sunyaev

1.4.1 Optical depth

The cross section for scattering at the center of a resonant line can be written as

$$\sigma_0 = \frac{\sqrt{\pi} h r_e c f}{\Delta E_D}, \tag{1.4}$$

where r_e is the classical electron radius and f is the absorption oscillator strength of a given atomic transition and ΔE_D is the Doppler width of the line. In a plasma with a temperature typical of galaxy clusters, the line width is determined by the velocities of thermal and turbulent motions, rather than by the radiative width. For example, for the 6.7 keV line of He-like iron the radiative width is ~ 0.3 eV, while thermal broadening is ~ 3 eV for a 5 keV gas. The Doppler width of the line is defined as

$$\Delta E_D = E_0 \left[\frac{2kT_e}{A m_p c^2} + \frac{V_{turb}^2}{c^2} \right]^{1/2}, \tag{1.5}$$

where A is the atomic mass of the corresponding element, m_p is the proton mass and V_{turb} is the characteristic turbulent velocity. V_{turb} is often parametrized as $V_{turb} = c_s M$, where M is the Mach number[2] and the sound speed in the plasma is $c_s = \sqrt{\gamma kT/\mu m_p}$, where

---

[2]This form of parametrization is rather arbitrary. For isotropic turbulence in a gas with $\gamma = 5/3$, the value of $M = 1$ corresponds to the energy in turbulent motions being equal to 0.83 times the thermal energy density $\frac{1}{\gamma - 1} \frac{\rho}{\mu m_p} kT$.

$\gamma = 5/3$ is the adiabatic index for an ideal mono-atomic gas and $\mu = 0.61$ is the particle mean atomic weight. We can rewrite the previous expression as

$$\Delta E_D = E_0 \left[\frac{2kT_e}{Am_p c^2}(1 + 1.4AM^2) \right]^{1/2}. \qquad (1.6)$$

The optical depth of the cluster at the center of the line is then $\tau = \int \sigma_0 n_i dl$, where l is the distance along the photon propagation direction and n_i is the number density of ions in the ground state of a given transition. For cluster conditions all ions are in the ground state (the frequency of collisions or any other excitation process are negligible compared to the radiative decay rate of the excited state) and $n_i = n_p Z \delta_i$, where n_p is the density of protons, Z the abundance of the element relative to hydrogen and δ_i is the fraction of the element in the appropriate ionization state. That is

$$\tau = \int \frac{\sqrt{\pi} h r_e c f}{E_0 \left[\frac{2kT_e}{Am_p c^2}(1 + 1.4AM^2) \right]^{1/2}} n_p Z \delta_i dl. \qquad (1.7)$$

Obviously, to have a large optical depth in the line one needs an astrophysically abundant element, a large oscillator strength of the transition, an appreciable ionization fraction of a given ion and a small line width. If the line width is dominated by thermal broadening then the lines of the heaviest elements have an advantage over lighter elements, since the thermal broadening scales as $1/\sqrt{A}$.

Gilfanov, Sunyaev & Churazov (1987) give a convenient expression for the optical depth (from the cluster center to the observer) at the midpoint of a Doppler-broadened resonance line when the isothermal gas density distribution can be approximated by a β-model $n = N_0 \left[1 + \left(\frac{r}{r_c} \right)^2 \right]^{-3/2\beta}$:

$$\tau_0 = \frac{\sqrt{\pi}}{2} \frac{\Gamma(3\beta/2 - 1/2)}{\Gamma(3\beta/2)} N_{z,0} r_c \sigma_0 \approx 2.7 \frac{\Gamma(3\beta/2 - 1/2)}{\Gamma(3\beta/2)} \frac{N_0}{10^{-3} \, \text{cm}^{-3}} \frac{Z}{Z_\odot} \delta_i(T)$$

$$\times \frac{r_c}{250 \, \text{kpc}} \frac{\sigma_0(10^7 \, \text{K}, \mathcal{M} = 0)}{10^{-16} \, \text{cm}^2} \left[\frac{T}{10^7 \, \text{K}}(1 + 1.4A\mathcal{M}^2) \right]^{-1/2}, \qquad (1.8)$$

where Γ is the gamma-function; parameters of the 6.7 keV line of FeXXV are used; and $Z/Z_\odot$ is the abundance of a given element relative to the solar abundance of iron. In Table 1.2 we quote the optical depths of several promising lines for 3 objects, representing different mass limits – from an elliptical galaxy (NGC4636) to a rich cluster (Perseus). The optical depths were calculated using the observed temperature and density radial profiles. Pure thermal broadening of the lines was assumed.

From Table 1.2 it is clear that different lines can be optically thick in objects having drastically different masses and temperatures. For objects with $T \geq 3$ keV (e.g. Perseus cluster) the He-like iron line at 6.7 keV is a likely winner; while for cool systems (e.g. NGC4636 with $T \sim 0.6$ keV) the Ne-like iron line at 0.83 keV has the largest optical depth.

Table 1.2: Oscillator strength, Rayleigh scattering weights and optical depth of the most promising X-ray lines for the elliptical galaxy NGC 4636 and the M87/Virgo and Perseus (A426) clusters. The optical depths were calculated using the observed temperature and density profiles and assuming the flat abundance profile $Z = 0.5Z_\odot$ (relative to the Solar abundances of Anders & Grevesse, 1989), collisional ionization equilibrium and pure thermal broadening of the lines.

Ion	E, keV	f	w_2	τ, NGC 4636	τ, Virgo/M87	τ, Perseus
O VIII	0.65	0.28	0.5	1.2	0.34	0.19
Fe XVIII	0.87	0.57	0.32	1.3	0.0007	$1.5 \cdot 10^{-7}$
Fe XVII	0.83	2.73	1	8.8	0.0005	$2.8 \cdot 10^{-8}$
Fe XXIII	1.129	0.43	1	0.016	1.03	0.16
Fe XXIV	1.168	0.245	0.5	0.002	1.12	0.73
Fe XXV	6.7	0.78	1	0.0002	1.44	2.77

1.4.2 Phase function

For any transition, the resonant scattering can be represented as a combination of two processes: isotropic scattering with a weight w_1 and Rayleigh scattering with a weight $w_2 = 1 - w_1$ (Hamilton, 1947; Chandrasekhar, 1950). The weights w_1 and w_2 depend on the total angular momentum j of the ground level and on the difference between the total angular momenta of the excited and ground levels Δj ($=\pm 1$ or 0). The expressions for the weights are given by Hamilton (1947). For a subset of the most promising lines the w_2 values are given in Table 1.2.

If the radiation is initially unpolarized, then the probability for a photon to scatter into a unit sold angle at an angle θ with respect to the incident direction is

$$P(\mu) = \frac{1}{4\pi} \left[w_1 + \frac{3}{4}(1 + \mu^2)w_2 \right], \tag{1.9}$$

where $\mu = \cos\theta$.

If polarization has to be accounted for (see Section 4), then the scattering matrix of resonant scattering can be written as

$$\begin{pmatrix} I'_l \\ I'_r \\ U' \end{pmatrix} = \frac{1}{4\pi} \left[\frac{1}{2}w_1 \begin{pmatrix} 1 & 1 & 0 \\ 1 & 1 & 0 \\ 0 & 0 & 0 \end{pmatrix} + \frac{3}{2}w_2 \begin{pmatrix} \mu^2 & 0 & 0 \\ 0 & 1 & 0 \\ 0 & 0 & \mu \end{pmatrix} \right] \begin{pmatrix} I_l \\ I_r \\ U \end{pmatrix}, \tag{1.10}$$

where I_l, I_r, U are the Stokes parameters as defined by Hamilton (1947); Chandrasekhar (1950).

For the changes in the surface brightness (see Section 1.4), the difference between the isotropic and Rayleigh phase functions is not very important, while it is crucial if one needs to evaluate the degree of polarization (see Section 4). Isotropic scattering does not produce

polarization. Instead it "erases" information on the initial direction and orientation of the electric vector in the "memory" of the scattered photon. On the contrary, Rayleigh scattering changes the polarization state of the radiation field.

1.5 Resonant scattering: surface brightness and line shape

1.5.1 Impact on surface brightness profile and abundance

Since the density of the gas declines faster than $\sim r^{-1}$ in the outer regions of all clusters, the optical depth of the outer regions in any line is small (see Fig. 1.7, left). We therefore do not expect strong modifications of the line surface brightness profile at large projected distances from the cluster center (see Fig. 1.7, right). The central part on the contrary is dense and in the region where the optical depth is of order unity one can expect that resonant scattering will erase all features in the surface brightness, leading to a flattened (see Fig. 1.7, right) surface brightness distribution (Gilfanov, Sunyaev & Churazov, 1987). Due to the conservative nature of resonant scattering, the photons removed from the line of sight going through the cluster center are re-distributed to larger projected distances. This effect causes a slight increase of the surface brightness at $R > r_1$ (see Fig. 1.7, right). Since the surface brightness in the continuum is not modified, the resonant scattering causes a decrease of the equivalent width of the line in the cluster center and a slight increase of the equivalent width in the outer regions. This could cause an apparent decrease in the abundance of heavy elements in the central part of the cluster if resonant lines are used to measure it (Gilfanov, Sunyaev & Churazov, 1987).

This effect was suggested to play a role in the spurious "abundance holes" in cluster centers (e.g. Böhringer et al., 2001; Sanders et al., 2004), although other effects such as the presence of multi-temperature plasma may be more important in these environments (e.g. Buote, 2000).

Note that optically thin lines are not modified by resonant scattering and therefore the observed spectrum might have line ratios different from the expected values for an optically thin thermal plasma. This implies that one can use the line ratios (the flux in an optically thick line divided by the flux in an optically thin line) rather than the line equivalent width (i.e. the ratio of the flux in the optically thick line to the spectral intensity of the continuum). The ideal situation is when two lines from the same ion are used, since in this case many issues related to the modeling of the ionization state can be avoided.

A set of simple expressions was derived by Gilfanov, Sunyaev & Churazov (1987); Sazonov, Churazov & Sunyaev (2002) for model gas density distributions and in the limit of $\tau \ll 1$ for the isotropic and Rayleigh phase functions. These expressions can be used for making order of magnitude estimates, while for real systems it is necessary to solve a radiative transfer problem to predict the shape of distortions, especially when substantial temperature gradients are present, which affect the ionization state and therefore the radial distribution of ions.
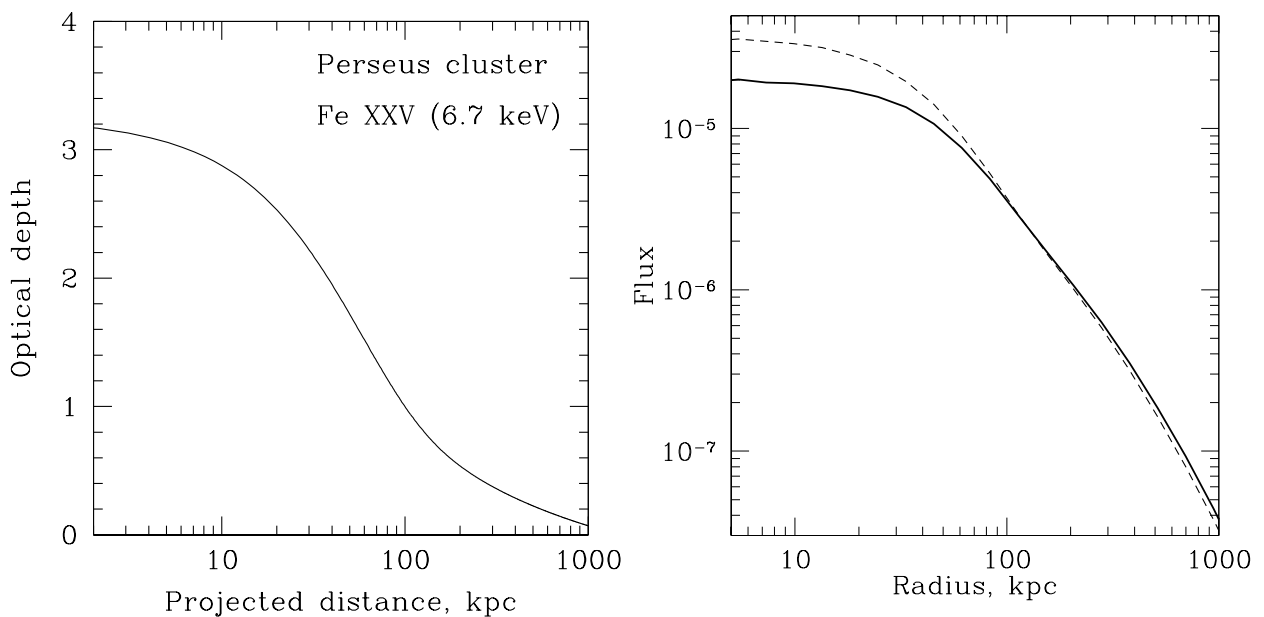
Figure 1.7: **Left:** Optical depth of the Perseus cluster in the 6.7 keV FeXXV line over the range of radii from r to ∞. For $r_1 \approx 70$ kpc the optical depth is of order 1. To a first approximation the surface brightness is expected to be only weakly disturbed by resonant scattering for projected radii $R \gg r_1$. For smaller projected radii the surface brightness profile is expected to be flat. **Right:** Radial profiles of the He-like iron K_α line with (thick solid line) and without (dashed line) resonant scattering in the Perseus cluster. Resonant scattering suppresses the line intensity in the core and redistributes line photons to larger radii. Pure thermal broadening and a flat radial abundance profile were assumed in this calculation. Adapted from Churazov et al. (2004).

Overall the resonant scattering has been searched for in a number of objects, although clear evidence for the effect was found only in few systems – for the Ne-like iron (Fe XVII) line at 15.01 Å in NGC4636 (Xu et al., 2002; Kahn et al., 2003; Werner et al., 2009; Hayashi et al., 2009) and for NGC1404, NGC5813 and NGC4472 (Werner et al., 2009). Nevertheless, the magnitude of the effect (modification of the surface brightness distribution in the line) is well within the capabilities of modern X-ray telescopes. In fact, one can use the absence of resonant scattering effects to infer the properties of the gas velocity field, as discussed in the next section.

1.5.2   Impact on the line shape

The optical depth given by eq. 1.8 corresponds to the center of the line, i.e. to a photon energy equal to the line energy E_0. If a photon is born in the wing of the line, then the optical depth will be lower,

$$\tau(E) = \tau_0 e^{-\left(\frac{E-E_0}{\Delta E_D}\right)^2}. \tag{1.11}$$

If $\tau(E) \ll 1$, then such photons will leave the cluster without scattering, while photons with $E \sim E_0$ will be scattered from the line of sight going through the cluster center. It is therefore clear that resonant scattering should affect the shape of optically thick lines. The spectral profiles of the He-like iron line at 6.7 keV calculated in the core of the Perseus cluster and at a projected distance of ~ 800 kpc are shown in Fig. 1.8. The calculations were done with (black curves) and without (blue curves) allowance for scattering. The lines are broadened only due to thermal motions of ions. One can notice the suppression of the emission in the line center (left panel) caused by resonant scattering: photons with the energy close to the line central energy are scattered from the line of sight because of the large optical depth, while photons born in the wings escape freely. At the edge of the cluster the optical depth is small and the line profiles almost match each other.

1.6   Resonant scattering: sensitivity to the velocity field of hot gas

If one accurately measures the temperature of the intracluster medium (ICM), then the line ratios of (optically thick) resonant and (optically thin) non-resonant lines can be used as a powerful tool to measure the line widths and therefore to get information on the velocity field, which is difficult to obtain by other means. Given that the optical depth sensitively depends on the turbulent broadening of resonant lines, especially for heavy elements like iron, the comparison of the fluxes of e.g. iron and nickel lines could be used to place constraints on the level of turbulence in clusters (Churazov et al., 2004). For the Perseus cluster, the XMM-Newton spectra of the central region do not show a suppression of the resonant 6.7 keV line of iron relative to a much more optically thin nickel line when the APEC (Smith et al., 2001) plasma emission model is used, although one should expect the 6.7 keV line of He-like iron to be suppressed in the core if the iron line were only thermally
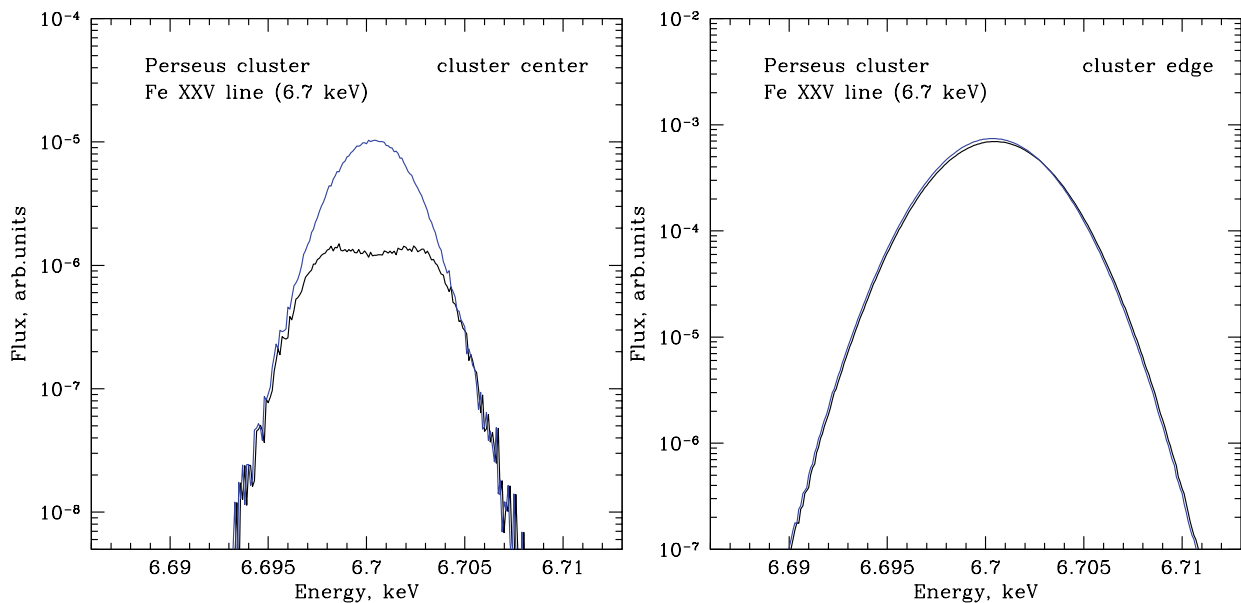
Figure 1.8: Simulated spectra of the 6.7 keV line emerging from the core of the Perseus cluster (left) and at a projected distance of 800 kpc (right). Lines are broadened only due to thermal motions of ions. The calculations were done with (black curves) and without (blue curves) accounting for resonant scattering. The line in the cluster outskirts (right panel) is broader due to the higher temperature in the outer regions of the Perseus cluster.

broadened. Indeed, without additional line broadening the optical depth of the 6.7 keV line is ~ 3 (see Table 1.2). Therefore, the line in the central $\sim 1'$ region must be suppressed by a factor of about 1.7 (see Fig. 1.9), in contrast with observations.

Even more robust constraints are expected if optically thick and optically thin lines of the same element or even better of the same ion are used. Werner et al. (2009) obtained high resolution spectra of the giant elliptical galaxy NGC 4636 using the grating spectrometers on the XMM-Newton satellite. Comparing the model to the data, it was found that the isotropic turbulent velocities on spatial scales smaller than ≈ 1 kpc are less than 100 km/s and the turbulent pressure support in the galaxy core is smaller than 5 per cent of the thermal pressure at the 90 per cent confidence level (see Section 2).

While there is still a bit of a controversy in the results, which definitely suffer from the limited energy resolution of the present-day CCDs or from the finite size of the emitting region for RGS data, it is clear that the magnitude of the effect is within the reach of the current generation of telescopes and the situation will improve in future.

The relation between the resonant scattering effects and the velocity field can be used to test even more subtle effects, such as e.g. anisotropy of gas motions. It is showed in Section 3 that radial motions strongly affect the optical depth for the photons coming from the cluster center and decrease the efficiency of the resonant scattering. On the contrary, pure tangential motions do not affect much the magnitude of the resonant scattering effect.

Polarization caused by resonant scattering of emission lines owing to a quadruple com-
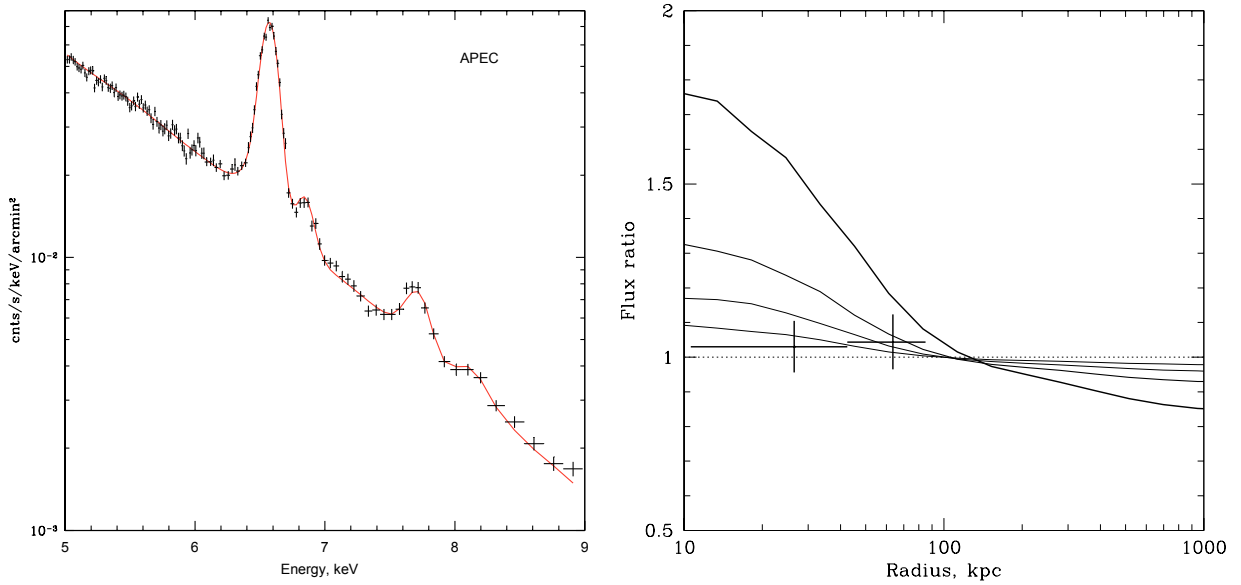
Figure 1.9: **Left:** 5-9 keV spectrum of the $30''$ to $2'$ annulus centered on NGC 1275 and fitted with APEC (Smith et al., 2001) models. **Right:** Influence of turbulence on the strength of the resonant scattering effect. The curves show the expected ratio of the optically thick and optically thin lines calculated for effective Mach numbers of 0, 0.25, 0.5 and 1 (from top to bottom). For comparison, crosses show the observed ratio of heavy element abundances obtained ignoring parts of the spectrum containing the 6.7 keV and 7.9 keV complexes, respectively. Given that the resonant K_α line of He-like iron contributes about 50% to the 6.6-6.8 keV complex of lines, the measured abundance ratio is consistent with the curves for Mach number $\geq$0.5. Adapted from Churazov et al. (2004).

ponent in the radiation field in clusters is particular sensitive to the gas motions perpendicular to the line-of-sight. Polarization degree as a proxy of transverse gas motions and requirements for observations are discussed in details in Section 4.

1.7 Structure of the thesis

This thesis aims to show various studies of physics and dynamical state of hot gas motions in galaxy clusters, proposes several indirect ways to constrain the amplitude, anisotropy and spatial scales of full 3D velocity field and discusses feasibility by current and future X-ray observatories. Thesis is based on three published papers, one review paper and two submitted papers.

Chapter 2 gives indirect constraints on turbulence in elliptical galaxy NGC4636 using *XMM-Newton RGS* observations and radiative transfer simulations of resonant scattering in this galaxy.

Chapter 3 shows how resonant scattering can be used to constrain not only velocity amplitudes, but also the anisotropy and spatial scales of motions.

A unique way to measure velocities of gas motions perpendicular to the line of sight in galaxy clusters through the X-ray polarization in bright lines caused by resonant scattering is discussed in Chapter 4.

Chapter 5 proposes a way to constrain structure function and power spectrum of gas motions via high spectral resolution measurements of the mean velocity (shift of line centroid) and mean velocity dispersion (broadening of the line), which will be provided by the near future X-ray missions.

Chapter 6 presents a simple method for calculating a power spectrum from non-periodic data with gaps, which was used in analysis presented in previous chapters.

The main conclusions and finding are summarized in conclusions.

Bibliography

Akimoto F., Furuzawa A., Tawara Y., Yamashita K., 1999, AN, 320, 283

Akimoto F., Furuzawa A., Tawara Y., Yamashita K., 2000, AdSpR, 25, 603

Allen S. W., Schmidt R. W., Ebeling H., Fabian A. C., van Speybroeck L., 2004, MNRAS, 353, 457

Anders E., Grevesse N., 1989, GeCoA, 53, 197

Böhringer H., et al., 2001, A&A, 365, L181

Buote D.A. 2000, ApJ, 539, 172

Cassano R., Brunetti G., 2005, MNRAS, 357, 1313

Chandrasekhar S., 1950, Radiative Transfer, Oxford, Clarendon Press, 1950

Churazov E., Forman W., Jones C., Böhringer H., 2003, ApJ, 590, 225

Churazov E., Forman W., Jones C., Sunyaev R., Böhringer H., 2004, MNRAS, 347, 29

Churazov E., Vikhlinin A., Zhuravleva I. et al., 2011, MNRAS, in prep.

Dolag K., Vazza F., Brunetti G., Tormen G., 2005, MNRAS, 364, 753

Dupke R. A., Arnaud K. A., 2001, ApJ, 548, 141

Ezawa H., et al., 2001, PASJ, 53, 595

Gastaldello F., Molendi S., 2004, ApJ, 600, 670

Gilfanov M. R., Sunyaev R. A., Churazov E. M., 1987, SvAL, 13, 3

Haiman Z., Mohr J. J., Holder G. P., 2001, ApJ, 553, 545

Hamilton D. R., 1947, ApJ, 106, 457

Hayashi K., Fukazawa Y., Tozuka M., Nishino S., Matsushita K., Takei Y., Arnaud K. A., 2009, PASJ, 61, 1185

Iapichino L., Schmidt W., Niemeyer J. C., Merklein J., 2011, MNRAS, 483

Kaastra J. S., Bleeker J. A. M., Mewe R., 1999, NuPhS, 69, 567

Kahn S. M., et al., 2003, ASPC, 301, 23

Kolmogorov A., 1941, DoSSR, 30, 301

Landau L. D., Lifshitz E. M., 1966, hydr.book,

Mathews W. G., Buote D. A., Brighenti F., 2001, ApJ, 550, L31

Mewe R., Gronenschild E. H. B. M., van den Oord G. H. J., 1985, A&AS, 62, 197

Molendi S., Matt G., Antonelli L. A., Fiore F., Fusco-Femiano R., Kaastra J., Maccarone M. C., Perola C., 1998, ApJ, 499, 608

Norman M. L., Bryan G. L., 1999, LNP, 530, 106

Peacock J.A., 1999, Cosmological Physics, UK: Cambridge Univ. Press

Peebles P. J. E., 1993, Physical cosmology, Princeton, NJ: Princeton Univ. Press

Sakelliou I., et al., 2002, A&A, 391, 903

Sanders J. S., Fabian A. C., 2006, MNRAS, 370, 63

Sanders J. S., Fabian A. C., Allen S. W., Schmidt R. W., 2004, MNRAS, 349, 952

Sanders J. S., Fabian A. C., Smith R. K., 2011, MNRAS, 410, 1797

Sazonov S. Y., Churazov E. M., Sunyaev R. A., 2002, MNRAS, 333, 191

Smith R. K., Brickhouse N. S., Liedahl D. A., Raymond J. C., 2001, ApJ, 556, L91

Sunyaev R. A., Norman M. L., Bryan G. L., 2003, AstL, 29, 783

Vazza F., Brunetti G., Gheller C., Brunino R., Brüggen M., 2011, A&A, 529, A17

Vikhlinin A., Kravtsov A., Forman W., Jones C., Markevitch M., Murray S. S., Van Speybroeck L., 2006, ApJ, 640, 691

Werner N., Zhuravleva I., Churazov E., Simionescu A., Allen S. W., Forman W., Jones C., Kaastra J. S., 2009, MNRAS, 398, 23

White S. D. M., Navarro J. F., Evrard A. E., Frenk C. S., 1993, Natur, 366, 429

Xu H., et al., 2002, ApJ, 579, 600

Chapter 2

Constraints on turbulent pressure in the X-ray halos of giant elliptical galaxies from resonant scattering

N.Werner, I.Zhuravleva, E.Churazov, A. Simionescu, S. W. Allen, W. Forman, C. Jones, J.S. Kaastra

Abstract. The dense cores of X-ray emitting gaseous halos of large elliptical galaxies with temperatures $kT \lesssim 0.8$ keV show two prominent Fe XVII emission features, which provide a sensitive diagnostic tool to measure the effects of resonant scattering. We present here high-resolution spectra of five bright nearby elliptical galaxies, obtained with the Reflection Grating Spectrometers (RGS) on the *XMM-Newton* satellite. The spectra for the cores of four of the galaxies show the Fe XVII line at 15.01 Å being suppressed by resonant scattering. The data for NGC 4636 in particular allow the effects of resonant scattering to be studied in detail and to prove that the 15.01 Å line is suppressed only in the dense core and not in the surrounding regions. Using deprojected density and temperature profiles for this galaxy obtained with the *Chandra* satellite, we model the radial intensity profiles of the strongest resonance lines, accounting for the effects of resonant scattering, for different values of the characteristic turbulent velocity. Comparing the model to the data, we find that the isotropic turbulent velocities on spatial scales smaller than ≈ 1 kpc are less than 100 km s^{-1} and the turbulent pressure support in the galaxy core is smaller than 5% of the thermal pressure at the 90% confidence level, and less than 20% at 95% confidence. Neglecting the effects of resonant scattering in spectral fitting of the inner 2 kpc core of NGC 4636 will lead to underestimates of the chemical abundances of Fe and O by $\sim$10–20%.

2.1   Introduction

The hot intra-cluster medium and the hot halos around giant elliptical galaxies are usually assumed to be optically thin. Although this assumption is valid for most of the emitted X-ray photons, at the energies of the strongest resonant transitions, the hot plasma can be optically thick (Gilfanov et al., 1987). The transition probabilities of strong resonance lines are large and, if the column density of the ion along a line of sight is sufficiently high, photons with the energies of these resonance lines will get absorbed and, within a short time interval, reemited in a different direction. Because of the short time between absorption and emission, this process can be regarded as scattering. Since resonant scattering in clusters and elliptical galaxies will cause the radial intensity profile of an emission line to become weaker in the centre and stronger outside, it can also lead to an underestimate of metal abundances in the dense cores and a corresponding overestimate in the surrounding region. This effect is, however, not expected to be large. Sanders & Fabian (2006) found that metallicities in cluster cores could be underestimated by at most 10% due to resonant scattering.

Gilfanov et al. (1987) pointed out that since the optical depth τ in the core of a resonance line depends on the characteristic velocity of small-scale motion, measurements of τ give important information about the turbulent velocities in the hot plasma. Measuring the level of resonant scattering in clusters and giant elliptical galaxies is thus a good way to constrain the energy in turbulence and the turbulent pressure support. The first constraints on turbulent velocities using resonant scattering were obtained for the Perseus cluster by Churazov et al. (2004). Using *XMM-Newton* EPIC data, they compared the relative fluxes of the 1s–2p and 1s–3p He-like Fe lines in the core and in an annulus surrounding the core of the Perseus cluster. The expected optical depth of the 6.7 keV 1s–2p Fe XXV resonance line is much larger than that of the 1s–3p line, therefore the ratio provides information about the level of resonant scattering. Churazov et al. (2004) found no evidence for resonant scattering in Perseus, indicating that differential gas motions on scales smaller than ~100 kpc in the core of the cluster must have a range of velocities of at least half of the sound speed. Independently, using the same data, Gastaldello & Molendi (2004) reached similar conclusions.

The most sensitive spectral lines to determine the level of resonant scattering are the Fe XVII lines at 15.01 Å (2p–3d) and the unresolved blend of the same ion at 17.05 and 17.10 Å (2p–3s). The optical depth is directly proportional to the column density of the ion and the oscillator strength of the given transition. While the oscillator strength of the 15.01 Å line is $f = 2.73$, and thus the line is expected to have a relatively large optical depth, the oscillator strength of the 17.05 Å line is $f = 0.12$ and the optical depth of this line blend is negligible (the oscillator strength of the 17.10 Å line is of the order of 10^{-8})[1]. Because of this dramatic difference in expected optical depths, and the fact that both lines originate from the same ion of the same element, the Fe XVII lines provide, in principle, an excellent diagnostic tool to measure the magnitude of resonant scattering. At the relatively low

---

[1]http://cxc.harvard.edu/atomdb/WebGUIDE/index.html
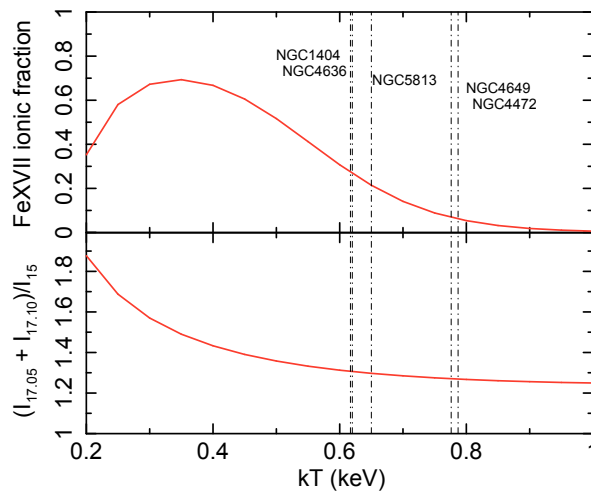
Figure 2.1: Fraction of Fe in the form of Fe XVII and the theoretical line ratio $(I_{\lambda 17.05} + I_{\lambda 17.10})/I_{\lambda 15.01}$ for an optically thin plasma as a function of the plasma temperature. The vertical lines mark the RGS measured temperatures of the five galaxies in our sample.

temperatures of hot halos around giant elliptical galaxies, $\sim$0.6–0.8 keV, both lines are very strong and, in this temperature range, their expected intensity ratios have only a very weak dependence on temperature (see Fig. 2.1, Doron & Behar, 2002). Therefore, any observed spatial dependence of the intensity ratios is unlikely to be due to gradients in temperature or Fe abundance in the hot plasma, making these lines especially clean diagnostic tools. The Fe XVII line ratios in extended objects can be measured with the *XMM-Newton* Reflection Grating Spectrometers (RGS, den Herder et al., 2001). Xu et al. (2002) reported the first and so far only radial profile of the $(I_{\lambda 17.05} + I_{\lambda 17.10})/I_{\lambda 15.01}$ ratio for the X-ray luminous elliptical galaxy NGC 4636, which indicates the presence of resonant scattering. Attempts to measure resonant scattering in NGC 5044 and M 87, which are hotter and more massive systems with weaker Fe XVII lines, were not successful (Tamura et al., 2003; Werner et al., 2006).

Here we follow up on the work by Xu et al. (2002), by reporting the Fe XVII $(I_{\lambda 17.05} + I_{\lambda 17.10})/I_{\lambda 15.01}$ line ratios measured in the cores of five nearby bright elliptical galaxies observed with *XMM-Newton* RGS: NGC 4636, NGC 5813, NGC 1404, NGC 4649, and NGC 4472. In Sect. 2 we describe the sample and observations; in Sect. 3 we discuss the details of the data analysis; and in Sect. 4 we present the results of the observations. We focus our attention on NGC 4636, for which data are of very high quality. Because NGC 4636 is X-ray bright, has a relatively long exposure and a favorable temperature, for this system we can measure and compare the observed line ratios in the core and surrounding regions. In Sect. 5 we present a model for the radial profile of the 15.01 Å line in NGC 4636 for different values of turbulent velocities, derived using deprojected density and temperature profiles from *Chandra* data. Comparing this model to the data, we place constraints on the characteristic velocity of isotropic turbulence in the core of the galaxy.

Table 2.1: List of the galaxies in the sample, with their distance (luminosity distances, obtained from the NASA/IPAC Extragalactic Database, http://nedwww.ipac.caltech.edu/), corresponding linear scale per arcminute, Galactic N_{H} value (Kalberla et al., 2005), average temperature measured by *ROSAT*. The last three columns give the *XMM-Newton* revolution of the observation, and the total and filtered RGS exposure times, respectively.

galaxy	distance	scale	N_{H}	kT	rev.	Exp. time	Clean time
	Mpc	kpc/arcmin	10^{20} cm^{-2}	keV		ks	ks
NGC 4636	17.5	5.1	1.90	0.55[*]	197	64406	58205
NGC 5813	29.9	8.7	4.37	0.52[†]	1029	36708	29899
NGC 1404	25.5	7.4	1.51	0.60[*]	1033	55032	17231
NGC 4649	19.8	5.8	2.1	0.78[*]	196	54210	46096
NGC 4472	18.4	5.4	1.53	0.88[*]	744	111033	81850

[*] O'Sullivan et al. (2003)
[†] Reiprich & Böhringer (2002)

Implications of the results are discussed in Sect. 6.

Throughout the paper, abundances are given with respect to the "proto-solar values" by Lodders (2003). All errors are quoted at the 68% confidence level for one interesting parameter ($\Delta C = 1$; for C statistics).

2.2   Sample and *XMM-Newton* observations

We have analyzed a sample of five nearby, giant elliptical galaxies observed with *XMM-Newton* RGS. The sample is listed in Table 2.1. The galaxies were selected based on their relatively low core temperatures, at which a significant fraction of Fe is expected to be in the form of Fe XVII (see Fig. 2.1), their large X-ray fluxes, and strongly peaked surface brightness distributions, which are necessary to obtain RGS spectra with sufficient statistics. The sample contains both relatively relaxed galaxies and systems showing very clear signs of interaction between the hot halo gas and central Active Galactic Nucleus (AGN). In Figs. 2.2 and 2.3 we show 0.5–2.0 keV *Chandra* images of the galaxies in our sample with the RGS extraction regions overplotted. The images show that the cores of NGC 4649, NGC 4472, and NGC 1404 are *relatively* relaxed (although on larger scales NGC 1404 shows a prominent cold front to the Northwest, and NGC 4649 and NGC 4472 harbor central radio sources, which exhibit interaction with the hot gas, Shurkin et al., 2008; Biller et al., 2004). NGC 4636 and NGC 5813, on the other hand, look much more disturbed, with obvious signs of recent episodes of interaction between the hot plasma and the AGN. NGC 4636 has a very dense core and X-ray bright arm-like structures which might have been produced by shocks (Jones et al., 2002). The core of NGC 5813 is highly disturbed with most of the hot gas being pushed into dense sheets by the rising bubbles of
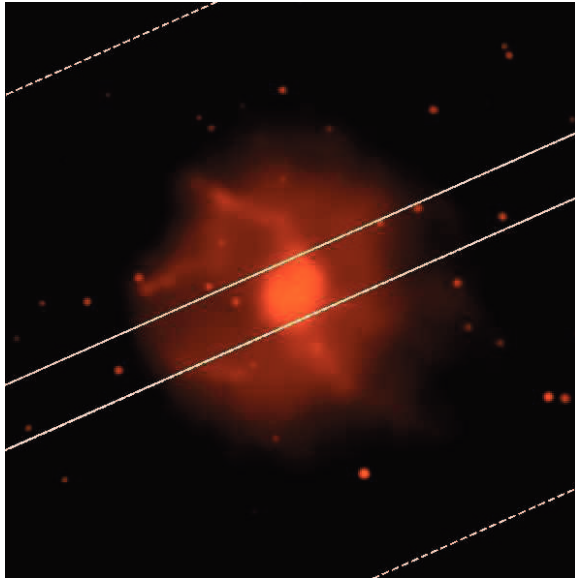
Figure 2.2: *Chandra* image of NGC 4636 with the RGS extraction regions over-plotted. The central extraction region is 0.5′ wide (indicated by full lines), the two extraction regions next to the core (between the full and dashed lines) are 2.25′ wide. The image was extracted in the 0.5–2.0 keV band, cleaned and adaptively smoothed.

relativistic plasma.

Currently the best data set for the study of resonant scattering is that for NGC 4636. The X-ray halo of this galaxy has a conveniently low temperature, at which ∼26% of Fe is in the form of Fe XVII, a very dense core and a deep *XMM-Newton* observation, which also allows us to extract spectra from outside the core region with reasonably good statistics in the Fe XVII lines. Using a deep *Chandra* observation of this galaxy we derive deprojected density and temperature profiles which we use to model radial intensity profiles for the strongest resonance lines, taking into account the effects of resonant scattering for different assumed values of turbulent velocities.

2.3   Data analysis

2.3.1   *XMM-Newton* RGS data analysis

We processed the RGS data using version 8.0.0 of the *XMM-Newton* Science Analysis System (SAS), and extracted spectra using the method described by Tamura et al. (2001). To minimize the contamination by soft-protons from Solar flares, we extracted a light curve for each dataset using events on CCD 9 of the RGS, outside the central region, with a distance larger than 30 arcsec from the dispersion axis, and excluded time intervals with elevated count rates. The original exposure time and the total time after cleaning are listed
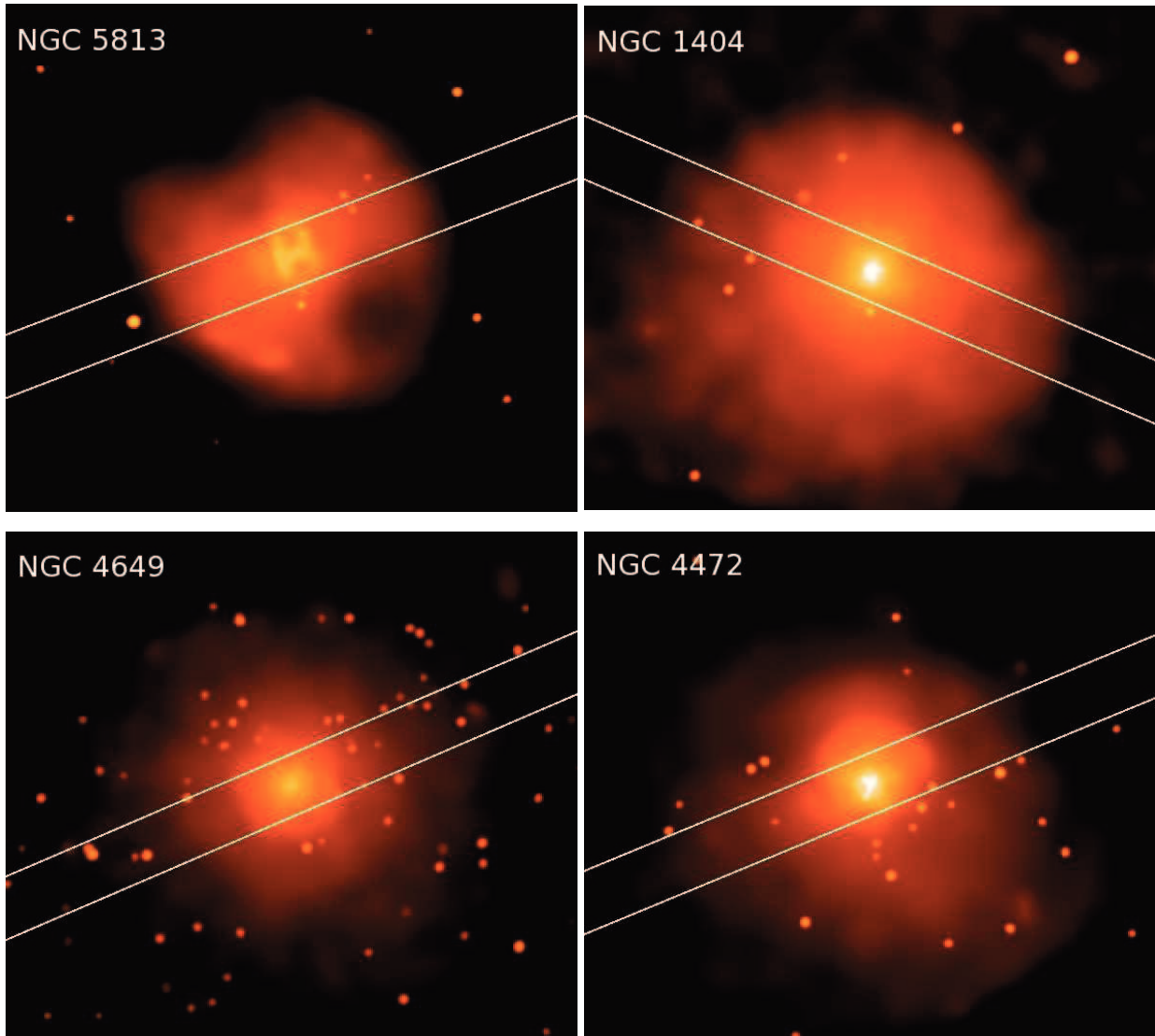
Figure 2.3: *Chandra* images of the giant elliptical galaxies in our sample with over-plotted RGS extraction regions (see also Fig. 2.2). The extraction regions are 0.5′ wide. While the core of NGC 5813 is strongly disturbed, the cores of the other three galaxies are relatively relaxed. The images were extracted in the 0.5–2.0 keV band, cleaned and adaptively smoothed.

Table 2.2: The best fit parameters for a single-temperature, optically thin plasma model fitted to the *XMM-Newton* RGS spectra extracted from $0.5'$ wide regions centred on the cores of the galaxies. For NGC 4636 we also show the results from fits to spectra extracted from two $2.25'$ wide regions surrounding the core (see Fig. 2.2). The 13.8–15.5 Å part of the spectrum, where the strongest Fe XVII and Fe XVIII resonance lines are present was initially excluded from the fits. Fluxes (in 10^{-12} erg cm^{-2}) are given in the 0.3–2.0 keV band. The emission measure is defined as $Y = \int n_\mathrm{e} n_\mathrm{H} dV$ (in 10^{64} cm^{-3}). The scale factor s is the ratio of the observed LSF width to the expected LSF for a flat abundance distribution. Abundances are quoted with respect to the proto-solar values of Lodders (2003). The last three rows list the best fit line ratios (predicted and observed ratio $(I_{\lambda 17.05} + I_{\lambda 17.10})/I_{\lambda 15.01})$) in the full spectral band (after the Fe XVII ion was set to zero in the modl and replaced by gaussian lines), the theoretical line ratios predicted for an optically thin plasma, and the derived level of suppression of the 15.01 Å line, $(I/I_0)_{15.01\text{Å}}$.

	NGC4636 core	NGC4636 out	NGC5813	NGC1404	NGC4649	NGC4472
flux	1.75 ± 0.08	2.57 ± 0.17	1.47 ± 0.12	1.08 ± 0.11	1.63 ± 0.10	1.44 ± 0.08
Y	0.47 ± 0.02	0.46 ± 0.03	1.01 ± 0.10	0.50 ± 0.05	0.31 ± 0.03	0.34 ± 0.02
kT (keV)	0.606 ± 0.006	0.695 ± 0.004	0.645 ± 0.008	0.608 ± 0.009	0.774 ± 0.007	0.781 ± 0.006
s	0.40 ± 0.04	1.02 ± 0.04	0.87 ± 0.11	0.97 ± 0.22	0.69 ± 0.21	0.79 ± 0.12
N	1.3 ± 0.3	1.5 ± 0.4	2.0 ± 0.8	2.3 ± 0.8	1.3 ± 0.7	1.3 ± 0.5
O	0.44 ± 0.05	0.61 ± 0.06	0.53 ± 0.09	0.58 ± 0.10	0.61 ± 0.15	0.53 ± 0.07
Ne	0.31 ± 0.08	0.39 ± 0.18	0.33 ± 0.19	0.81 ± 0.22	1.31 ± 0.35	1.18 ± 0.22
Fe	0.52 ± 0.03	0.92 ± 0.06	0.75 ± 0.09	0.67 ± 0.08	0.87 ± 0.18	0.83 ± 0.08
$[I_{\lambda 17}/I_{\lambda 15}]_\mathrm{o}$	2.04 ± 0.21	1.28 ± 0.13	1.99 ± 0.34	1.98 ± 0.29	1.25 ± 0.28	2.24 ± 0.34
$[I_{\lambda 17}/I_{\lambda 15}]_\mathrm{p}$	1.31	1.31	1.30	1.31	1.27	1.27
$I_{15.01}/I_{0\ 15.01}$	0.64 ± 0.07	1.02 ± 0.10	0.65 ± 0.11	0.66 ± 0.10	1.02 ± 0.23	0.57 ± 0.09
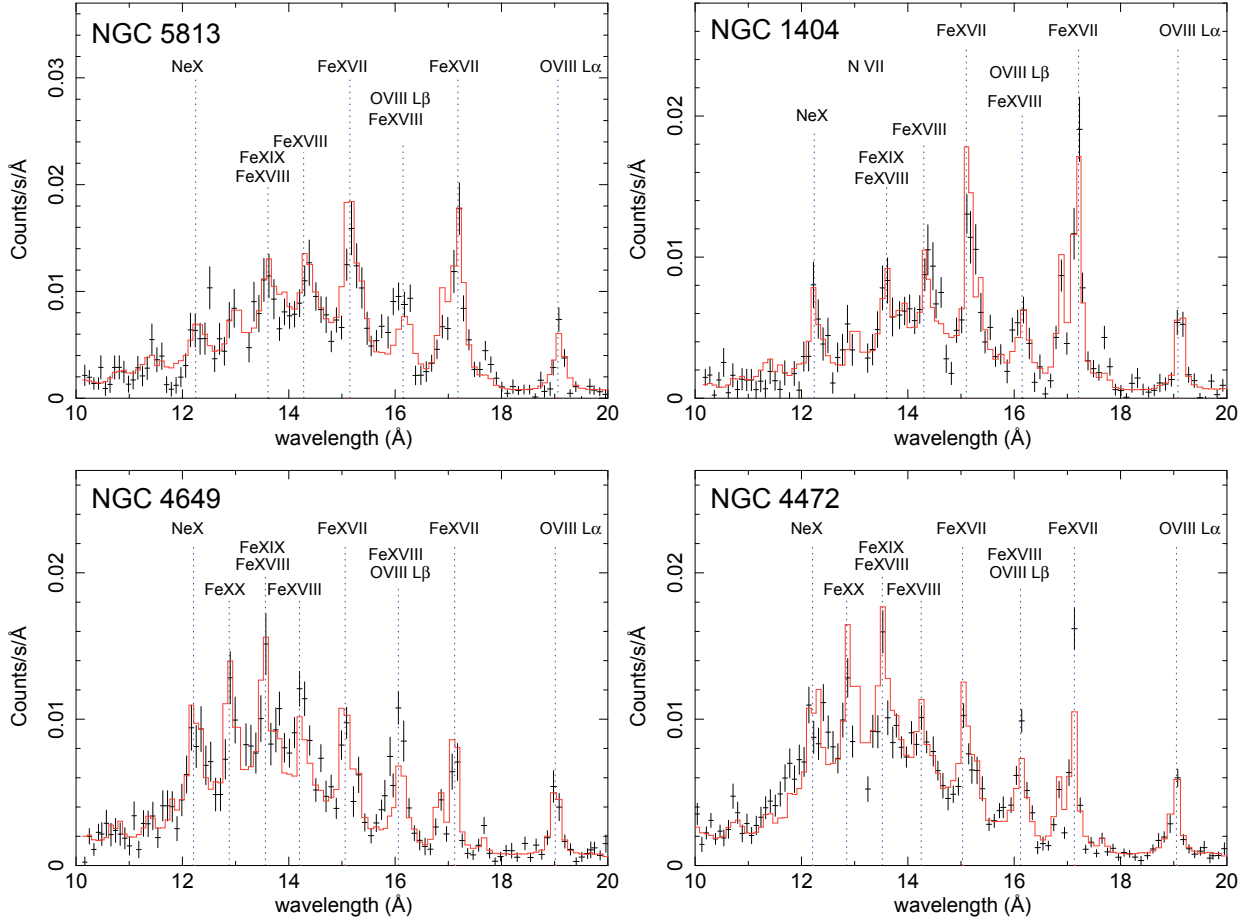
Figure 2.4: RGS spectra for NGC 5813, NGC 1404, NGC 4649, and NGC 4472. The spectra were extracted from 0.5′ wide extraction regions centred on the cores of the galaxies. The full line indicates the best-fit optically-thin single-temperature plasma model. The 13.8–15.5Å part of the spectrum, where the strongest Fe XVII and Fe XVIII resonance lines are present, was excluded from these spectral fits.

in Table 2.1. The flares in the observation of NGC 1404 were weak and we obtain the same best fit spectral parameters for both the filtered and unfiltered data set. Therefore, for this galaxy we used the full observation. Because emission from the galaxies fills the entire field of view of the RGS, the background cannot be estimated from a region on the detector away from the source. Therefore, we modeled the background using the standard RGS background model for extended sources available in SAS (Gonzaléz-Riestra, 2004).

The effects of resonant scattering are most significant in the centermost parts of the galaxies, where the density is highest. Therefore, we extract spectra from narrow 30 arcsec wide bands centred on the cores of the galaxies, probing regions within radii of 1.3–2.2 kpc (depending on distance) in the cross dispersion direction of the RGS. We extract and fit both first and second order spectra. Because the RGS operates without a slit, it collects all photons from within the $0.5' \times \sim 12'$ field of view. Line photons originating at angle $\Delta\theta$ (in arcminutes) along the dispersion direction, will be shifted in wavelength by

$$\Delta\lambda = 0.138 \, \Delta\theta \text{\AA}. \tag{2.1}$$

Therefore, every line will be broadened by the spatial extent of the source. To account for this broadening in our spectral model, for each RGS spectrum, we produce a predicted line spread function (LSF) by convolving the RGS response with the surface brightness profile of the galaxy derived from the EPIC/MOS1 image in the 0.8–1.4 keV band along the dispersion direction. Because the radial profile of a particular spectral line can be different from the overall radial surface brightness profile (e.g. in the presence of metallicity gradients), the line profile is multiplied by a scale factor s, which is the ratio of the observed LSF width to the expected LSF for a flat abundance distribution. This scale factor is a free parameter in the spectral fit.

For the spectral modeling of the RGS data we use the SPEX package (Kaastra et al., 1996). Spectral fitting of the RGS data is done in the 10 Å to 28 Å band. We model the emission of the observed galaxies as optically thin plasmas in collisional ionization equilibrium, absorbed by neutral Galactic gas with Solar abundances. For each object we fix the Galactic column density to the value determined by the Leiden/Argenitine/Bonn (LAB) Survey of Galactic H I (Kalberla et al., 2005). For the emission of the elliptical galaxies we assume a single-temperature plasma. Using more complicated multi-temperature models does not improve the fits and differential emission measure models always converge to a simple single-temperature approximation. The spectral normalization, plasma temperature, and the abundances of N, O, Ne, and Fe are free parameters in the fit. For the spectral fitting we use C-statistics.

2.3.2 *Chandra* analysis of NGC 4636

We reprocessed the *Chandra* observations of NGC 4636 (OBSID 3926 and 4415) applying the latest CTI and time-dependent gain calibrations using standard methods (see Vikhlinin et al., 2005, for more details). In brief, we performed the usual filtering by grade, excluded bad/hot pixels and columns, removed cosmic ray 'afterglows', and applied

the VF mode filtering. We excluded data with anomalously high background. The remaining exposure time for NGC 4636 is 150.4 ks. The background files were processed in the same manner as the observations. An additional background component is produced during the 41 ms of the 3.2 s nominal exposure readout of the ACIS CCDs, while the chips are exposed to the sky. This small contribution of the source flux, 1.3%, is uniformly re-distributed along the readout direction and is subtracted using the technique described by Markevitch et al. (2000). The blank-field background is also renormalized by reducing its integration time by 1.3% to account for this additional subtraction.

As the final step in data preparation (see Churazov et al., 2008, for more details), we computed, for each X-ray event, the ratio of the effective area (a function of photon energy and position) to that at a predefined energy and position:

$$\eta = A(E, x_d, y_d)/A_0(E), \tag{2.2}$$

where $A(E, x_d, y_d)$ includes mirror and detector efficiencies (including non-uniformity of the detector quantum efficiency and the time and spatially dependent contamination on the optical blocking filter). Finally, for each event list, we make an exposure map that accounts for all position dependent, but energy independent, efficiency variations across the focal plane (e.g., overall chip geometry, dead pixels or rows, and variation of telescope pointing direction). We use these data in Sect. 2.5 to derive deprojected gas density and temperature profiles.

2.4 Observations of resonant scattering

The results from the spectral fitting of the *XMM-Newton* RGS data with an optically thin single-temperature plasma model are shown in Table 2.2 and Figures 2.4 and 2.5. The 13.8–15.5Å part of the spectrum, where the strongest Fe XVII and Fe XVIII resonance lines are present, was initially excluded from this fit. These lines are expected to be suppressed by resonant scattering and this suppression, which is not accounted for in the plasma model, could slightly bias the best fit spectral parameters. After obtaining the best fit, we freeze the temperature and Fe abundance of the thermal component, set the abundance of the Fe XVII ion to zero in the model, add narrow Gaussians at the wavelength of the strongest Fe XVII lines (restframe wavelengths of 15.01 Å, 17.077 Å, 15.30 Å, and 16.80 Å) and re-fit the full 10–28 Å spectral band. Freezing the temperature and the Fe abundance is necessary because by setting the Fe XVII ion to zero and replacing it with Gaussians in the model we lose important constraints on these parameters. The line normalisations, the continuum level (normalisation of the thermal component), the abundances of the other elements and the broadening factor s are free parameters. In the error calculation, we also marginalise over the uncertainties of the temperature and Fe abundance as determined in the initial fit. We determine the best fitting normalisations for these Gaussians and the value of $(I_{\lambda 17.05} + I_{\lambda 17.10})/I_{\lambda 15.01}$ (the 17.05 and 17.10 Å lines are blended and we fit them with a single Gaussian at 17.077 Å). We divide the theoretical ratio $(I_{\lambda 17.05} + I_{\lambda 17.10})/I_{\lambda 15.01}$ by the measured value, which, assuming the lines at $\sim$17 Å are optically thin, gives us the level
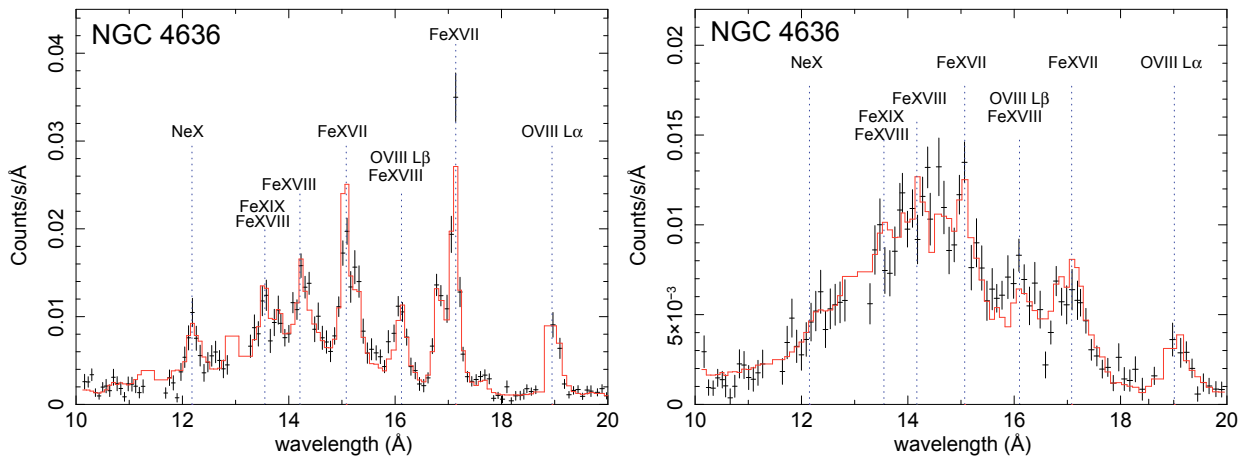
Figure 2.5: *XMM-Newton* RGS spectra extracted from a 0.5′ wide extraction region centered on the core of NGC 4636 (left panel) and from two 2.25′ wide extraction regions surrounding the core (right panel). The ratios of the Fe XVII lines at 15.01 and ∼17 Å change. The full line indicates the best fit optically thin single-temperature plasma model. The 13.8–15.5 Å part of the spectrum, where the strongest Fe XVII and Fe XVIII resonance lines are present, was excluded from these spectral fits.

at which the 15.01 Å line is suppressed, $(I/I_0)_{15.01\text{Å}}$. These values are listed in Table 2.2. In four out of five galaxies the line ratios are significantly higher (observed values ∼ 2.0) than the expected theoretical value for an optically thin plasma of 1.27–1.31, indicating that the 15.01 Å line is optically thick. In NGC 4649, the line ratios are consistent with the 15.01 Å line being optically thin.

A number of factors argue that the observed high $(I_{\lambda17.05}+I_{\lambda17.10})/I_{\lambda15.01}$ line ratio is due to resonant scattering. The $(I_{\lambda17.05}+I_{\lambda17.10})/I_{\lambda15.01}$ line ratio in an optically thin plasma can reach values ∼ 1.9 only for temperatures as low as 0.2 keV (see Fig. 2.1, Doron & Behar, 2002), which is much lower than the observed temperatures of the galaxies. Moreover, if the plasma in the cores of the galaxies were multiphase with an additional 0.2 keV component, which would alter the Fe XVII line ratios, then we would also observe other strong lines (e.g. O VII), which we do not. Another possibility to obtain such high line ratios in an optically thin plasma is non-equilibrium ionization (NEI). However, NEI effects are unlikely in the dense plasma in cores of giant elliptical galaxies because, due to the high density, the equilibration time is short. If the higher-than-expected line ratios were due to incomplete atomic physics in the current spectral models, then they should not change as a function of radius. This can be directly verified in NGC 4636, which has the best combination of X-ray flux, temperature, and exposure. The data for this galaxy allow us to extract spectra and determine the $(I_{\lambda17.05} + I_{\lambda17.10})/I_{\lambda15.01}$ line ratios in the combined spectrum from two regions surrounding the core at 15–150 arcsec from the centre of the galaxy, in the crossdispersion direction of the RGS (see Fig. 2.2). We follow here the same fitting procedure as for the cores of the galaxies. The best fitting results are shown in the third column of Table 2.2. The off-centre line ratios are consistent with the 15.01 Å line being

optically thin in this region. The difference in the spectra of the core and surrounding regions of NGC 4636 can be seen clearly in Fig. 2.5. While the 15 Å line is suppressed in the centre, it may be slightly enhanced outside the dense core.

The best fit line broadening scale factor s indicates that in NGC 4636 the distribution of the line producing ions is more peaked than the surface brightness, suggesting that the distribution of metals is centrally peaked. In the other systems this effect is smaller and less significant.

2.5   Modelling of resonant scattering in NGC 4636

To gain a better understanding of the observed line ratios, we simulate the effects of resonant scattering on the radial intensity profiles of the strongest X-ray emission lines in NGC 4636. For this we use the deprojected temperature and density profiles measured with *Chandra*.

In our deprojection analysis, we follow the approach described by Churazov et al. (2008). We assume spherical symmetry, but make no specific assumption about the form of the underlying gravitational potential. For a given surface brightness profile in n_a annuli, we choose a set of n_s ($n_\mathrm{s} \le n_\mathrm{a}$) spherical shells with the inner radii $r(\mathrm{i})$, $\mathrm{i} = 1, \ldots, n_\mathrm{s}$. The gas emissivity $\mathcal{E}$ is assumed to be uniform inside each shell, except for the outermost shell, where the gas emissivity is assumed to decline as a power law of radius: $\mathcal{E} = \mathcal{E}_\mathrm{out} r^{-6\beta_\mathrm{out}}$, where β_out is a parameter. The deprojection process is a simple least square solution to determine the set of emissivities in the set of shells (along with the emissivity normalization $\mathcal{E}_\mathrm{out}$ of the outer layers) that provides the best description of the observed surface brightness. The emissivity of each shell can then be evaluated as an explicit linear combination of the observed quantities. Since the whole procedure is linear, the errors in the observed quantities can be propagated straightforwardly. With our definition of η (see subsection 2.3.2), the projection matrix does not depend on energy. Therefore, the deprojection in *any energy band* is precisely that used to deproject the surface brightness. Thus, we can accumulate a set of spectra (corrected for background and readout) for each of the n_a annuli, and apply the deprojection to determine the emissivities of each shell in each of the ACIS energy channels.

The *Chandra* data were modeled using XSPEC V12 (Arnaud, 1996) and the APEC model (Smith et al., 2001). The gas temperature and normalization were free parameters in the model. The heavy element abundance was either a free parameter in the fit or fixed to 0.68 Solar (as determined from a spectral fit to *Chandra* data extracted within the radius of $1'$ from the centre of NGC 4636). The metallicity profile in NGC 4636 has large uncertainties, because the metal abundance distribution in the deprojected *Chandra* spectra has a large scatter as a result of noise enhancement during deprojection coupled with the limited spectral resolution of the CCDs.

The electron density profile was derived from the spectral normalization, fixing the proton to electron ratio to 0.83. Fig. 2.6 shows the deprojected electron density (lower panel) and the temperature (upper panel) as a function of distance from the centre of

Table 2.3: Oscillator strengths and optical depths for the strongest X-ray lines in the spectrum of NGC 4636 for Mach numbers 0.0, 0.25, 0.5, 0.75. The expected suppression due to resonant scattering $(I/I_0)_{\mathrm{circ}}$ gives the value integrated within a radius of 2 kpc from the centre of the galaxy. The approximate values $(I/I_0)_{\mathrm{RGS}}$ were obtained by integrating within an "effective extraction region" which is $0.5'$ wide and $3'$ long. The metallicity is assumed to be constant with the radius.

Ion	λ (Å)	f	$M = 0.0$			$M = 0.25$			$M = 0.5$			$M = 0.75$		
			τ	$(I/I_0)_{\mathrm{circ}}$	$(I/I_0)_{\mathrm{RGS}}$	τ	$(I/I_0)_{\mathrm{circ}}$	$(I/I_0)_{\mathrm{RGS}}$	τ	$(I/I_0)_{\mathrm{circ}}$	$(I/I_0)_{\mathrm{RGS}}$	τ	$(I/I_0)_{\mathrm{circ}}$	$(I/I_0)_{\mathrm{RGS}}$
Fe XVII	15.01	2.73	8.8	0.47	0.69	3.6	0.59	0.79	1.9	0.68	0.85	1.3	0.76	0.89
Fe XVII	17.05	0.12	0.5	0.89	0.95	0.2	0.95	0.98	0.1	0.97	0.99	0.07	0.98	0.99
Fe XVIII	14.20	0.57	1.3	0.72	0.87	0.5	0.86	0.94	0.3	0.91	0.96	0.2	0.95	0.98
Fe XVIII	16.08	0.005	0.01	0.99	1.00	0.005	0.99	1.00	0.003	1.00	1.00	0.002	1.00	1.00
O VIII Lα	18.96	0.28	1.2	0.74	0.87	0.8	0.81	0.91	0.5	0.88	0.94	0.3	0.91	0.96
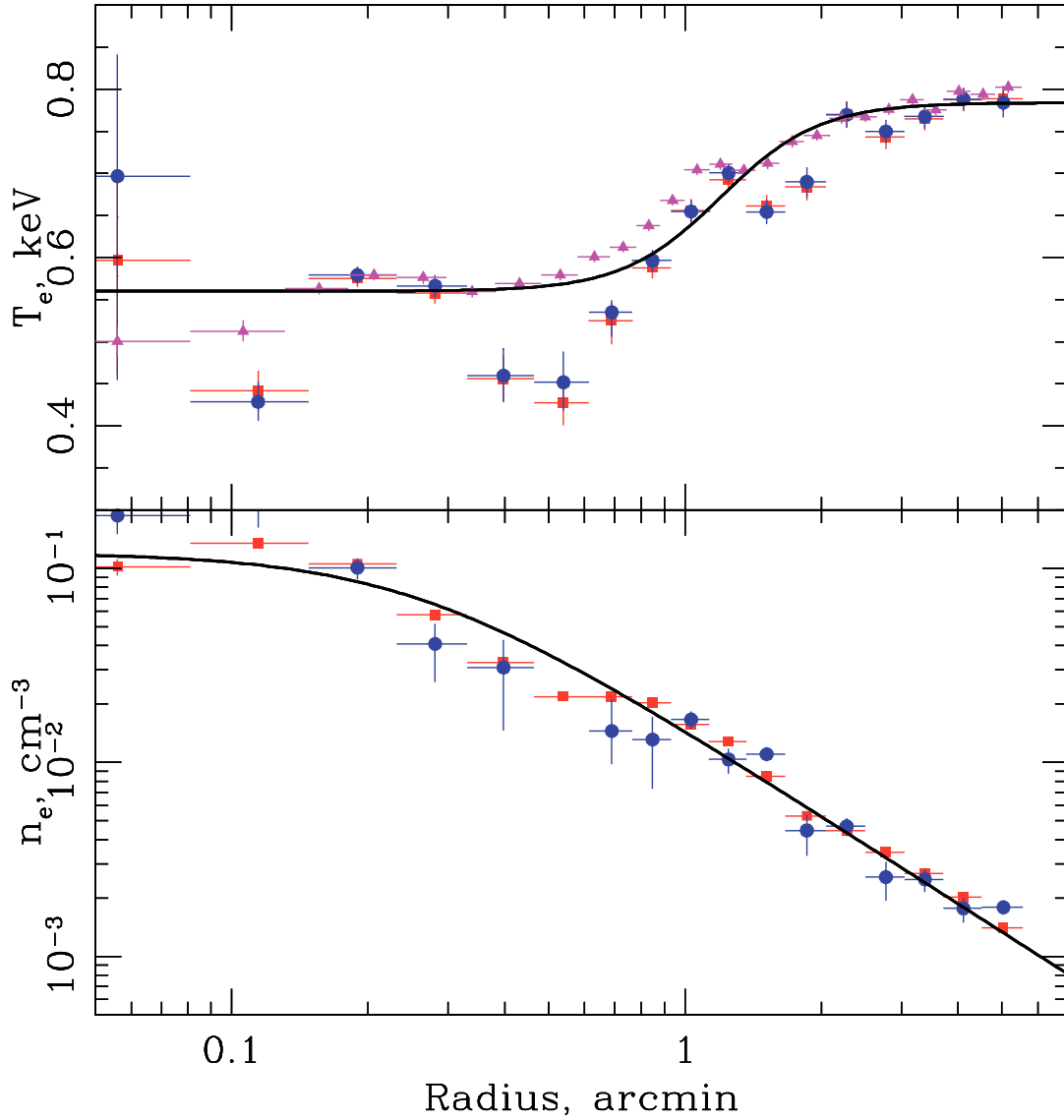
Figure 2.6: Observed radial profiles of the electron density and temperature used to model resonant scattering in NGC 4636. The blue circles and red squares indicate the deprojected profiles determined from *Chandra* data with metallicity as a free parameter in the fit and with metallicity fixed to 0.68 Solar, respectively. The magenta triangles show the projected radial temperature profile with the metallicity as a free parameter in the fit. The solid lines show the parametrization of the gas density and gas temperature profiles given in eqs. 2.3 and 2.4.

the galaxy. The circles and squares show the deprojected profiles for metallicity as a free parameter and for metallicity fixed to 0.68 Solar, respectively. The triangles show the projected temperature profile with the metallicity as a free parameter.

Based on the observed radial distributions of electron density n_e and temperature kT_e in NGC 4636, we adopt the following approximate forms for the deprojected density and temperature profiles:

$$n_e = 1.2 \times 10^{-1} \left[1 + \left(\frac{r}{0.25'} \right)^2 \right]^{-0.75} \text{ cm}^{-3}, \tag{2.3}$$

and

$$kT = 0.56 \frac{1 + 1.4(r/1.2')^4}{1 + (r/1.2')^4} \text{ keV}. \tag{2.4}$$

We consider two possible radial behaviors for metallicity: a simple constant abundance of 0.68 Solar; and a centrally peaked abundance distribution, which is more consistent with the best fit *XMM-Newton* RGS line profile ($s = 0.40 \pm 0.04$). In the latter case we approximate the metallicity profile with the following function:

$$Z = 0.95 \frac{2 + (r/0.8')^3}{1 + (r/0.8')^3} - 0.4. \tag{2.5}$$

We calculate the optical depth of the 15 Å line from the centre of the galaxy to infinity, $\tau = \int n_i \sigma_0 dr$, where n_i is the ion concentration and σ_0 is the cross section at the line centre, which for a given ion is

$$\sigma_0 = \frac{\sqrt{\pi} h r_e c f}{\Delta E_D}, \tag{2.6}$$

where the Doppler width is given by

$$\Delta E_D = E_0 \left(\frac{2kT_e}{A m_p c^2} + \frac{V_{turb}^2}{c^2} \right)^{1/2}. \tag{2.7}$$

In these equations r_e is the classical electron radius, f is the oscillator strength of a given atomic transition, E_0 is the rest energy of a given line, A is the atomic mass of the corresponding element, m_p is the proton mass, c is the speed of light, and V_{turb} is the characteristic velocity of isotropic turbulence. $V_{turb} \equiv \sqrt{2} V_{1D,turb}$, where $V_{1D,turb}$ is the velocity dispersion in the line of sight due to turbulence. Using the adiabatic sound speed, $c_s = \sqrt{\gamma k T / \mu m_p}$, the expression for the broadening can be rewritten as

$$\Delta E_D = E_0 \left[\frac{2kT_e}{A m_p c^2} (1 + \frac{\gamma}{2\mu} A M^2) \right]^{1/2}, \tag{2.8}$$
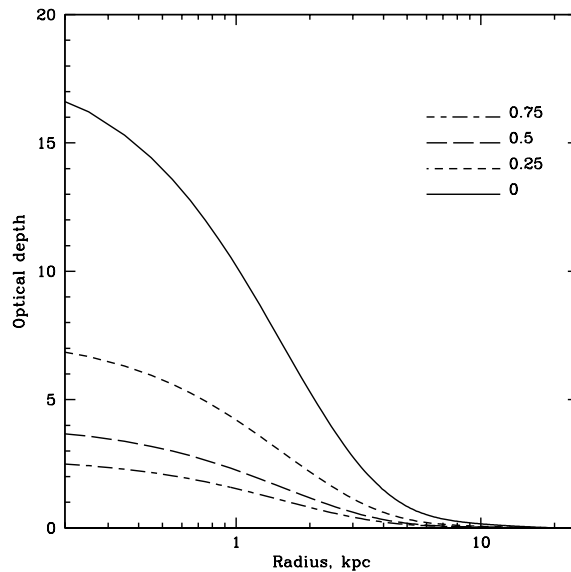
Figure 2.7: Optical depth of the 15.01 Å line calculated from the given radius to infinity, for isotropic turbulent velocities corresponding to Mach numbers 0.0, 0.25, 0.5, and 0.75. A centrally peaked Fe abundance distribution is assumed.

where $\mu = 0.6$ is the mean particle mass, γ is the adiabatic index, which for ideal monatomic gas is 5/3, and $M = V_{\mathrm{turb}}/c_{\mathrm{s}}$ is the corresponding Mach number. The line energies and oscillator strengths were taken from ATOMDB[2] and the NIST Atomic Spectra Database[3].

The resonant scattering effect has been calculated using Monte-Carlo simulations, as described by Churazov et al. (2004). We model the hot halo as a set of spherical shells and obtain line emissivities for each shell using the APEC plasma model (Smith et al., 2001). We account for scattering by assuming a complete energy redistribution and dipole scattering phase matrix. The line of Fe XVII has a pure dipole scattering phase matrix. In Fig. 2.7 we show the optical depth of the 15.01 Å Fe XVII line as a function of radius, for various turbulent velocities, assuming the peaked Fe abundance distribution. For higher turbulent velocities, the optical depth becomes smaller. In Fig. 2.8 we show the ratio of the 15.01 Å line intensity calculated including the effect of resonant scattering to the line intensity without accounting for resonant scattering for various turbulent velocities, both for constant and peaked iron abundance distributions. The figure clearly shows the effect of the resonant scattering: in the core of the galaxy the intensity of the line is suppressed, whereas in the surrounding regions the intensity of the line rises. The effect is more prominent in the case of the centrally peaked Fe abundance distribution, where the central suppression is larger and the enhancement in the outer part is stronger.

[2]http://cxc.harvard.edu/atomdb/WebGUIDE/index.html
[3]www.physics.nist.gov/PhysRefData/ASD/index.html
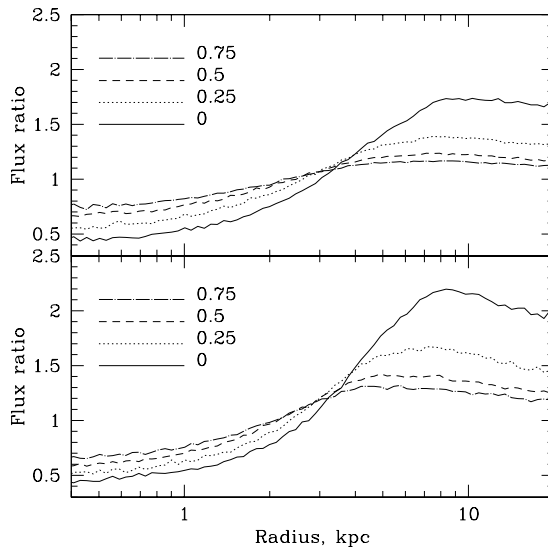
Figure 2.8: Radial profiles of the ratio of the 15.01 Å line intensity with and without the effect of resonant scattering, for isotropic turbulent velocities corresponding to Mach numbers 0.0, 0.25, 0.5, and 0.75. The upper panel shows the profiles for a constant metallicity, and the lower panel for a centrally peaked Fe abundance distribution.

We compare the models of resonant scattering with the observations and determine the systematic uncertainties involved by simulating spectra corresponding to each of these models, which are then fit in the same way as the observed data. To this end, we multiply the surface brightness profile of NGC 4636 with the theoretical suppression profiles for the 15.01 Å line (Fig. 2.8) to determine the predicted RGS line profile for the four considered characteristic turbulent velocities, for both assumed abundance distributions. We simulate spectra with photon statistics comparable to that of the actual observation, using the best fit values for the core of NGC 4636 from Table 2.2 as input parameters, and convolving the 15.01 Å line through these predicted line profiles. By fitting the data simulated with no turbulence, we obtain $(I/I_0)_{15.01Å} = 0.69$ and 0.71 for peaked and flat abundance profiles, respectively. The ratios of $(I/I_0)_{15.01Å}$ for isotropic turbulent velocity of $M = 0.25$ are 0.76 and 0.78, and for $M = 0.50$ they are 0.80 and 0.82, for peaked and flat abundance profiles, respectively. The systematic uncertainty on these values due to our lack of knowledge about the actual Fe abundance distribution is ±0.02. We add this uncertainty in quadrature to the uncertainties associated with our modeling of the line broadening, which is at most 0.03, resulting in a total uncertainty of 0.04. Thus we conclude that the turbulent velocities in NGC 4636 are relatively small and that isotropic turbulence with a characteristic velocity of $M > 0.25$ can be ruled out at the 90% confidence level; turbulent gas motions at $M > 0.5$ can be ruled out at the 95% confidence level. (The sound speed in NGC 4636 is $c_s \sim 400$ km s^{-1}.)

In Table 2.3, we list the strongest lines observed in the spectrum of NGC 4636, their

oscillator strengths and optical depths for different Mach numbers. Clearly, Fe XVII at 15.01 Å is the most optically thick line in the spectrum, but O VIII Lα and Fe XVIII at 14.2 Å also have relatively large optical depths. For $M = 0$, the depth of the Fe XVII line at 17.05 Å line is $\tau = 0.5$, meaning that our assumption that the 17.05 Å and 17.10 Å line blend is optically thin is not completely correct, and our *observed* values of $(I/I_0)_{15.01\text{Å}}$ are biased slightly high, which further increases the significance of our upper limits on the turbulent velocities. In Table 2.3, we also list the predicted suppression for the strongest emission lines, $(I/I_0)_{\text{circ}} = \int I \mathrm{d}A / \int I_0 \mathrm{d}A$, integrated within a circular region of radius 2 kpc, and within the RGS extraction region $(I/I_0)_{\text{RGS}}$. The suppression for the RGS is determined in a simplified way, integrating within our $0.5'$ wide, and for line emission effectively about $3'$ long, RGS extraction region. These predicted ratios in Table 2.3 were determined assuming a flat abundance distribution. By adopting an optically thin plasma in the analysis, the best fitting O abundance within the 2 kpc radius can be underestimated by ∼10–25%, and the Fe abundance by ∼10–20%.

2.6   Discussion and conclusions

High-resolution spectra obtained with *XMM-Newton* RGS reveal that the Fe XVII line at 15.01 Å in the cores of the elliptical galaxies NGC 4636, NGC 1404, NGC 5813, and NGC 4472 is suppressed by resonant scattering. The effects of resonant scattering can be investigated in detail for NGC 4636. The comparison of the measured suppression of the 15.01 Å Fe XVII line in the spectrum of NGC 4636 with the simulated effects of resonant scattering reveals that the characteristic velocity of isotropic turbulence in the core of the galaxy is smaller than 0.25 and 0.5 of the sound speed at the ∼90% and 95% confidence levels, respectively. The energy density in turbulence is:

$$\epsilon_{\text{turb}} = \frac{3}{2} \rho \, V_{\text{1D,turb}}^2 = \frac{3}{4} \rho \, c_{\text{s}}^2 \, M^2 \tag{2.9}$$

where ρ is the density of the plasma. The thermal energy of the plasma is given as:

$$\epsilon_{\text{therm}} = \frac{3}{2} \frac{\rho}{\mu m_{\text{p}}} kT. \tag{2.10}$$

By combining these equations we obtain the ratio of turbulent to thermal energy:

$$\frac{\epsilon_{\text{turb}}}{\epsilon_{\text{therm}}} = \frac{\gamma}{2} \, M^2. \tag{2.11}$$

For the 90% and 95% confidence level upper limits of $M \lesssim 0.25$ and 0.5 on the characteristic velocity of isotropic turbulence in NGC 4636, the upper limit on the fraction of energy in turbulent motions is 5% and 20%, respectively. This is in agreement with the upper limits on the non-thermal pressure component in elliptical galaxies obtained on larger spatial scales by Churazov et al. (2008) and with the properties of AGN induced turbulence in
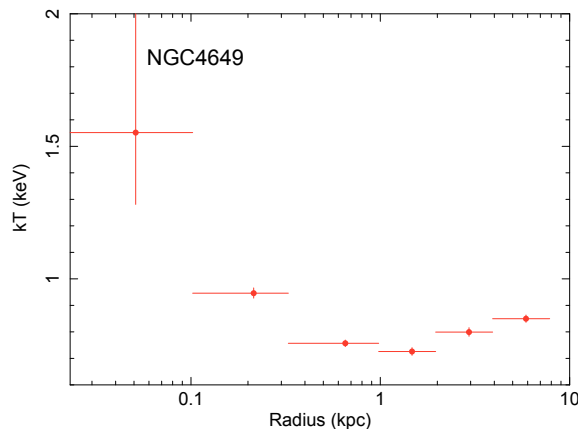
Figure 2.9: The deprojected temperature profile of NGC 4649 determined using *Chandra* data. It shows an unusual central peak.

three-dimensional simulations, that use adaptive mesh hydrodynamic code with a subgrid model of turbulence and mixing (Scannapieco & Brüggen, 2008).

A small value for the average turbulent velocity dispersion was also inferred in the initial analysis of the RGS spectra for NGC 4636 by Xu et al. (2002). They estimated that the turbulent velocities in the galaxy do not strongly exceed 1/10 of the sound speed. Caon et al. (2000) studied the kinematics of line emission nebulae in NGC 4636 and found an irregular radial velocity curve which indicates turbulent motions in the core. The measured radial velocities of the emission line nebulae are mostly within about $\sim$100 km s^{-1}. The kinematics of emission line nebulae in the sample of elliptical galaxies studied by Caon et al. (2000) indicates chaotic gas motions with velocities of about $M = 0.2$–0.4. In cooling cores, optical emission line nebulae often spatially coincide with soft X-ray emission (e.g. Sparks et al., 2004; Fabian et al., 2006), which indicates a coupling, suggesting that the two gas phases should share the same turbulent velocities.

The dense cores of NGC 4636 and NGC 5813 show strong evidence of recent violent interaction between the hot plasma and the AGN. This interaction is expected to induce turbulence through the mechanical activity of the outflows (Churazov et al., 2001). Our results indicate that the typical velocities of the AGN induced turbulent motions in the hot plasma on sub-kpc spatial scales are less than 100–200 km s^{-1}. Gas motions on larger spatial scales likely have larger velocities. Observations of the Perseus cluster suggest both turbulent and laminar gas motions with velocities as high as 700 km s^{-1} (Fabian et al., 2003a,b). The observed lack of resonant scattering in the 6.7 keV Fe-K line within the inner $\sim$100 kpc (Churazov et al., 2004) of Perseus confirms the presence of such strong gas motions. AGN induced gas motions with large range of velocities along our line of sight, perhaps even on spatial scales smaller than $\approx$1 kpc, could explain the observed lack of resonant scattering in the 15.01 Å Fe XVII line in M 87 (the analysis of a 0.5′ wide extraction region centred on the core of M 87 gives $(I_{\lambda17.05} + I_{\lambda17.10})/I_{\lambda15.01} = 1.3 \pm 0.3$,

Werner et al., 2006). We note that the central AGN in Perseus and in M 87 are more active in X-rays than the AGN in the target galaxies of this study.

The dense cores of galaxies showing smaller disturbance by AGN might be expected to exhibit less turbulence than the heavily disturbed systems. Therefore, we might expect the 15.01 Å line to be more suppressed in the most relaxed galaxies in our sample. While there is a weak indication of the suppression increasing from the least to the most relaxed systems: from NGC 5813 and NGC 4636, to NGC 4472, the large errorbars on the line ratios and the small number of galaxies in the sample do not allow us to draw firm conclusions.

The best fit line ratio in the apparently relaxed galaxy NGC 4649 shows no indication for resonant scattering in its core. The lack of observable optical depth effects in this galaxy can be explained by the unusual temperature profile of its gaseous halo, which exhibits a sharp temperature peak in its centre (see Fig. 2.9, Allen et al. in prep.). Within the central 0.1 kpc of the galaxy, the temperature increases by about a factor of 2 to $\sim$1.5 keV, at which no Fe XVII is present in the gas, implying that all the observed Fe XVII emission is from lower density regions surrounding the hot core. The high temperature might be due to shock heating by the central AGN (e.g. Shurkin et al., 2008). None of the other galaxies in our sample shows such an unusual temperature profile (Allen et al., 2006, Allen et al. in prep.).

Unfortunately, the high temperatures of cluster cores do not allow us to use Fe XVII lines as a diagnostic tool to measure the effects of resonant scattering and thus place firm constraints on turbulent velocities in the intra-cluster medium. No other lines have a comparable sensitivity to the turbulent velocities. However, the dense cores of elliptical galaxies, are in terms of the dominant physical processes like cooling and AGN feedback, sufficiently similar to cooling cores of clusters of galaxies to argue that the turbulent velocities on small spatial scales, and thus the turbulent pressure support in these systems, are also likely to be low. This is encouraging for cosmological studies based on X-ray observations of galaxy clusters (e.g. Allen et al., 2008; Mantz et al., 2008; Henry et al., 2008; Vikhlinin et al., 2008). Simulations predict that turbulent gas motions in the intra-cluster medium can provide 5%–25% of the total pressure support through the virial region of clusters, potentially biasing low hydrostatic mass estimates, even in relaxed systems (e.g. Nagai et al., 2007). However, these predictions depend sensitively on the gas physics assumed. Our results argue that such turbulence may be suppressed in nature, at least within the inner regions of such systems. For the merging unrelaxed Coma cluster, a $\sim$10% lower limit on turbulent pressure support was obtained by Schuecker et al. (2004) from a Fourier analysis of pressure maps. In the range 40–90 kpc, the turbulent spectrum was found to be well described by a projected Kolmogorov/Oboukhov-type model.

Future, deeper (of the order of $\sim$500 ks) observations of large nearby elliptical galaxies with the *XMM-Newton* RGS should provide even tighter constraints on turbulent velocities from resonant scattering. X-ray calorimeters on future missions such as *Astro-H* and *International X-ray Observatory (IXO)* will enable direct measurements of the velocity-broadening of emission lines in the hot gas in galaxies, groups, and clusters of galaxies (Sunyaev et al., 2003; Inogamov & Sunyaev, 2003; Rebusco et al., 2008), thereby allowing an independent check on our results as well as a critical extension to higher mass systems.

However, we note that even the excellent (2–5 eV) spectral resolution of these instruments will not allow measurements of turbulent motions with velocities significantly smaller than 100–200 km s^{-1}. Even though, the broad point spread function of the *Astro-H* mirrors will prohibit investigations of the effects of resonant scattering on spatial scales smaller than presented in this paper, it will for the first time allow us to directly measure the gas motions and spatially map them out to larger radii. The next planned X-ray observatory able to produce a real breakthrough by mapping the gas motions in groups and clusters of galaxies at high spatial resolution, will be *IXO*.

An important consequence of resonant scattering is the bias it can introduce in measurements of radial profiles of abundances of chemical elements. As we show in Table 2.3, the integrated emission of several strong resonance lines is significantly suppressed within the inner 2 kpc of NGC 4636. By ignoring the effects of resonant scattering, the Fe and O abundance will be underestimated by 10–20% within this region. This conclusion is in line with the results of Sanders & Fabian (2006). However, while resonant scattering makes abundances appear to be 10–20% lower than the real value, it cannot explain the much stronger abundance dips seen in the cores of several clusters of galaxies (e.g. Sanders & Fabian, 2002).

Acknowledgements

Bibliography

Allen, S. W., Dunn, R. J. H., Fabian, A. C., Taylor, G. B., Reynolds, C. S. 2006, MNRAS, 372, 21

Allen, S. W., Rapetti, D. A., Schmidt, R. W., et al. 2008, MNRAS, 383, 879

Arnaud, K. A. 1996, in Astronomical Society of the Pacific Conference Series, Vol. 101, Astronomical Data Analysis Software and Systems V, ed. G. H. Jacoby & J. Barnes, 17

Biller, B. A., Jones, C., Forman, W. R., Kraft, R., & Ensslin, T. 2004, ApJ, 613, 238

Caon, N., Macchetto, D., & Pastoriza, M. 2000, ApJ, 127, 39

Churazov, E., Brüggen, M., Kaiser, C. R., Böhringer, H., & Forman, W. 2001, ApJ, 554, 261

Churazov, E., Forman, W., Jones, C., Sunyaev, R., & Böhringer, H. 2004, MNRAS, 347, 29

Churazov, E., Forman, W., Vikhlinin, A., et al. 2008, MNRAS, 388, 1062

den Herder, J. W., Brinkman, A. C., Kahn, S. M., et al. 2001, A& A, 365, L7

Doron, R. & Behar, E. 2002, ApJ, 574, 518

Fabian, A. C., Sanders, J. S., Allen, S. W., et al. 2003a, MNRAS, 344, L43

Fabian, A. C., Sanders, J. S., Crawford, C. S., et al. 2003b, MNRAS, 344, L48

Fabian, A. C., Sanders, J. S., Taylor, G. B., et al. 2006, MNRAS, 366, 417

Gastaldello, F. & Molendi, S. 2004, ApJ, 600, 670

Gilfanov, M. R., Sunyaev, R. A., & Churazov, E. M. 1987, Soviet Astronomy Letters, 13, 3

Gonzaléz-Riestra, R. 2004, http://xmm.vilspa.esa.es/docs/documents/CAL-TN-0058-1-0.ps.gz

Henry, J. P., Evrard, A. E., Hoekstra, H., Babul, A., & Mahdavi, A. 2008, ArXiv e-prints

Inogamov, N. A. & Sunyaev, R. A. 2003, Astronomy Letters, 29, 791

Jones, C., Forman, W., Vikhlinin, A., et al. 2002, ApJL, 567, L115

Kaastra, J. S., Mewe, R., & Nieuwenhuijzen, H. 1996, in UV and X-ray Spectroscopy of Astrophysical and Laboratory Plasmas p.411, K. Yamashita and T. Watanabe. Tokyo : Universal Academy Press

Kalberla, P. M. W., Burton, W. B., Hartmann, D., et al. 2005, A& A, 440, 775

Lodders, K. 2003, ApJ, 591, 1220

Mantz, A., Allen, S. W., Ebeling, H., & Rapetti, D. 2008, MNRAS, 387, 1179

Markevitch, M., Ponman, T. J., Nulsen, P. E. J., et al. 2000, ApJ, 541, 542

Nagai, D., Vikhlinin, A., & Kravtsov, A. V. 2007, ApJ, 655, 98

O'Sullivan, E., Ponman, T. J., & Collins, R. S. 2003, MNRAS, 340, 1375

Rebusco, P., Churazov, E., Sunyaev, R., Böhringer, H., & Forman, W. 2008, MNRAS, 384, 1511

Reiprich, T. H. & Böhringer, H. 2002, ApJ, 567, 716

Sanders, J. S. & Fabian, A. C. 2002, MNRAS, 331, 273

Sanders, J. S. & Fabian, A. C. 2006, MNRAS, 371, 1483

Scannapieco, E. & Brüggen, M. 2008, ApJ, 686, 927

Schuecker, P., Finoguenov, A., Miniati, F., Böhringer, H., & Briel, U. G. 2004, A& A, 426, 387

Shurkin, K., Dunn, R. J. H., Gentile, G., Taylor, G. B., & Allen, S. W. 2008, MNRAS, 383, 923

Smith, R. K., Brickhouse, N. S., Liedahl, D. A., & Raymond, J. C. 2001, ApJL, 556, L91

Sparks, W. B., Donahue, M., Jordán, A., Ferrarese, L., & Côté, P. 2004, ApJ, 607, 294

Sunyaev, R. A., Norman, M. L., & Bryan, G. L. 2003, Astronomy Letters, 29, 783

Tamura, T., Bleeker, J. A. M., Kaastra, J. S., Ferrigno, C., & Molendi, S. 2001, A& A, 379, 107

Tamura, T., Kaastra, J. S., Makishima, K., & Takahashi, I. 2003, A& A, 399, 497

Vikhlinin, A., Kravtsov, A. V., Burenin, R. A., et al. 2008, ArXiv e-prints

Vikhlinin, A., Markevitch, M., Murray, S. S., et al. 2005, ApJ, 628, 655

Werner, N., Böhringer, H., Kaastra, J. S., et al. 2006, A& A, 459, 353

Xu, H., Kahn, S. M., Peterson, J. R., et al. 2002, ApJ, 579, 600

Chapter 3

Resonant scattering in galaxy clusters for anisotropic gas motions on various spatial scales

I.Zhuravleva, E.Churazov, S.Sazonov, R.Sunyaev, K.Dolag

Abstract. The determination of characteristic amplitudes and anisotropy of hot gas motions in galaxy clusters from observations of the brightest resonance lines is discussed. Gas motions affect (i) the spectral line shape through the Doppler effect and (ii) the radial surface brightness profiles in lines during resonant scattering. Radiative transfer calculations have been performed by the Monte Carlo method in the FeXXV resonance line at 6.7 keV for the Perseus cluster (Abell426). It was shown that (a) radial motions reduce the scattering efficiency much more dramatically than purely tangential motions; (b) large-scale gas motions weakly affect the scattering efficiency. The uncertainty in measuring the characteristics of gas motions using resonant scattering has been estimated from existing and future observations of clusters.

3.1   Introduction

The intergalactic gas in galaxy clusters is the dominant (in mass) baryonic component and accounts for about 15% of the virial cluster mass. Falling into the potential well of a cluster, the gas heats up to a temperature of 2–10 keV. The presence of gas motions with velocities of hundreds and thousands km s^{-1} in galaxy clusters is indirectly confirmed both by high-angular-resolution X-ray data, namely the observations of substructure in surface brightness and temperature distributions (e.g. see the review by Markevitch and Vikhlinin 2007), and by numerical simulations, which show gas motions on various spatial scales, both far from the center and in the central regions of clusters (Norman and Bryan 1999; Inogamov and Sunyaev 2003; Dolag et al. 2005; Vazza et al. 2009).

The anisotropy, velocity amplitudes and scales of the motions along the line-of-sight can be determined from the shift and broadening of spectral lines (e.g. see Inogamov and Sunyaev 2003). However, measurements with a sufficient energy resolution will become possible only after the launch of an X-ray microcalorimeter on-board of the *ASTRO-H* mission with an energy resolution of $\sim$ 4 eV at 6 keV (Mitsuda 2009). For example, for the FeXXV line at 6.7 keV, a shift of $\sim$ 10 eV emerges during gas motions with a velocity of 500 km s^{-1}. The tangential component of gas motions is even more difficult to determine[1]. Another method for diagnostics of gas motions is based on analysis of the scattering in bright lines in the spectra of galaxy clusters (e.g. see the review by Churazov et al. 2010). The characteristic amplitudes of gas motions in galaxy clusters (Churazov et al. 2004; Sanders et al. 2010) and elliptical galaxies (e.g. see Xu et al. 2002; Werner et al. 2009) have been estimated by comparing the surface brightness profiles in optically thin and thick lines of the same ion. Finally, information about the power spectrum of the velocities of gasmotions can be obtained by considering the surface brightness or pressure fluctuations. For example, using a Fourier analysis of the surface brightness and gas temperature fluctuations in the Coma cluster (A1656), Schuecker et al. (2004) claimed the power spectrum of gas motions to be a Kolmogorov one. A Kolmogorov turbulence power spectrum was also obtained by Vogt and Enßlin (2003) using measurements of the spatial Faraday rotation fluctuations.

In this paper, we are interested in what information about the gas motions we can obtain by considering the distortions of the surface brightness profiles in resonance lines. We are interested in the reliability of determining the directions, amplitudes and spatial scales of gasmotions in real clusters from resonant scattering observations.

The velocity of ion motions can be represented as $\mathbf{V} = \mathbf{V_{bulk}} + \mathbf{V_{turb}} + \mathbf{V_{therm}}$. Here, $\mathbf{V_{bulk}}$ are the large-scale (bulk) gas motions that affect both the line broadening and the energy shift at the line center; $\mathbf{V_{turb}}$ are the gas motions on scales smaller than any characteristic sizes, in particular, the size of the region inside which the optical depth in lines > 1 (microturbulent motions), that cause only line broadening; and $\mathbf{V_{therm}}$ are the thermal ion motions leading to the line broadening. Under conditions of galaxy clusters,

---

[1]Zhuravleva et al. (2010) proposed a method for determination of tangential gas velocities based on analysis of the polarization in resonance X-ray lines.

the thermal broadening of heavy-element lines can be much smaller than that for other types of motions.

In this paper, we separately consider the influence of large- and small-scale gas motions on the line profiles and resonant scattering. The cluster model used and details of our calculations are described. The main results and conclusions are discussed.

3.2 Line profiles

3.2.1 The influence of microturbulent gas motions on the line profiles

As has been mentioned above, we will use the term "microturbulence" to describe motions with spatial scales of velocity variations much smaller than any characteristic size present in the problem. Such motions lead to line broadening.

Microturbulence can arise, for example, from the mergers of clusters, from buoyant bubbles of relativistic plasma or convection caused by the mixing of thermal plasma and cosmic rays. Talking about turbulence, one usually refers to gas motions with the same velocity dispersion in all directions. However, the cases when anisotropic turbulence, radial and tangential, appears are possible. For example, purely radial motions naturally arise if the energy from the central active galactic nucleus (AGN) powers shocks and sound waves that propagate through the intergalactic medium mainly in the radial direction away from the central source (e.g. see Forman et al. 2005, 2007; Fabian et al. 2003, 2006). In contrast, tangential motions can naturally emerge in stratified atmospheres, where internal waves carry the energy of vertical motions away from the region of space under consideration. This can give rise to two dimensional (tangential) motions (Churazov et al. 2001, 2002; Rebusco et al. 2008).

Let consider how the anisotropy of turbulent gas motions changes the spectral line profiles. Let us assume that the gas as a whole is at rest at each point of the cluster and there is a Gaussian ion velocity distribution,

$$P(V_r, V_\theta, V_\phi) = \frac{1}{(2\pi)^{3/2}\sigma_r\sigma_\theta\sigma_\phi} \exp\left[-\frac{1}{2}\left(\frac{V_r}{\sigma_r}\right)^2 - \frac{1}{2}\left(\frac{V_\theta}{\sigma_\theta}\right)^2 - \frac{1}{2}\left(\frac{V_\phi}{\sigma_\phi}\right)^2\right], \qquad (3.1)$$

where r, θ, ϕ are three spatial coordinates at a given point (in the radial and tangential directions) and the set of three quantities $\Sigma^2 = \left(\sigma_r^2, \sigma_\theta^2, \sigma_\phi^2\right)$ characterizes the velocity dispersion in these directions. Writing the ion velocity vector in some direction $\mathbf{m} = (m_r, m_\theta, m_\phi)$ as $\mathbf{V} = V\mathbf{m}$, the probability that the projection of the ion velocity vector onto the direction $\mathbf{m}$ at a given point of space will be V is

$$P(V) = \frac{1}{\sqrt{2\pi}\sigma_{\text{eff}}} \exp\left[-\frac{1}{2}\left(\frac{V}{\sigma_{\text{eff}}}\right)^2\right], \qquad (3.2)$$

where σ_{eff} can be represented as (given only the broadening due to turbulence)

$$\sigma_{\text{eff}}^2 = (\sigma_{\text{turb,r}} m_{\text{r}})^2 + (\sigma_{\text{turb,}\theta} m_\theta)^2 + (\sigma_{\text{turb,}\phi} m_\phi)^2. \tag{3.3}$$

Clearly, for isotropic turbulence, the velocity dispersion in all directions is the same, i.e. $\sigma_{\text{turb,r}} = \sigma_{\text{turb,}\theta} = \sigma_{\text{turb,}\phi}$. For radial turbulence, only the radial component remains and, accordingly, for tangential turbulence, the radial component of the velocity dispersion is zero. Thus, these three cases can be described as follows:

$$\Sigma^2 = \begin{cases} (\sigma_{\text{turb,r}}^2, \sigma_{\text{turb,}\theta}^2, \sigma_{\text{turb,}\phi}^2), \text{isotropic} \\[2mm] (\sigma_{\text{turb,r}}^2, 0, 0), \text{radial} \\[2mm] (0, \sigma_{\text{turb,}\theta}^2, \sigma_{\text{turb,}\phi}^2), \text{tangential} \end{cases} . \tag{3.4}$$

The kinetic energy is related to the velocity dispersion as $\varepsilon_{\text{kin}} = \frac{1}{2}\rho(\sigma_{\text{turb,r}}^2 + \sigma_{\text{turb,}\theta}^2 + \sigma_{\text{turb,}\phi}^2)$. Fixing the kinetic energy in all velocity components, we obtain

$$\Sigma^2 = \begin{cases} (\frac{2}{3\rho}\varepsilon_{\text{kin}}, \frac{2}{3\rho}\varepsilon_{\text{kin}}, \frac{2}{3\rho}\varepsilon_{\text{kin}}), \text{isotropic} \\[2mm] (\frac{2}{\rho}\varepsilon_{\text{kin}}, 0, 0), \text{radial} \\[2mm] (0, \frac{1}{\rho}\varepsilon_{\text{kin}}, \frac{1}{\rho}\varepsilon_{\text{kin}}), \text{tangential} \end{cases} . \tag{3.5}$$

Substituting (3.5) into (3.3), we find σ_{eff}^2 at fixed total kinetic energy of turbulent motions:

$$\sigma_{\text{eff}}^2 = \begin{cases} \frac{2}{3\rho}\varepsilon_{\text{kin}}, \text{isotropic} \\[2mm] \frac{2}{\rho}\varepsilon_{\text{kin}} \cos^2(\alpha), \text{radial} \\[2mm] \frac{1}{\rho}\varepsilon_{\text{kin}} \sin^2(\alpha), \text{tangential} \end{cases} , \tag{3.6}$$

where α is the angle between the direction of photon motion $\mathbf{m}$ and the radius vector.

Analogously we can derive expressions for σ_{eff} by fixing not the total energy but the velocity dispersion ξ in a given direction. Assuming that $\sigma_{\text{turb,r}} = \sigma_{\text{turb,}\theta} = \sigma_{\text{turb,}\phi} = \xi$ for isotropic turbulence, $\sigma_{\text{turb,r}} = \xi$, $\sigma_{\text{turb,}\theta} = \sigma_{\text{turb,}\phi} = 0$ for radial turbulence, and $\sigma_{\text{turb,r}} = 0$, $\sigma_{\text{turb,}\theta} = \sigma_{\text{turb,}\phi} = \xi$ for tangential turbulence, we obtain

$$\sigma_{\text{eff}}^2 = \begin{cases} \xi^2, \text{isotropic} \\[2mm] \xi^2 \cos^2(\alpha), \text{radial} \\[2mm] \xi^2 \sin^2(\alpha), \text{tangential} \end{cases} . \tag{3.7}$$

To calculate the spectral line profile from the entire cluster, let consider a spherically symmetric cluster and an infinitely thin, homogeneous spherical shell at distance $r = 1$ from the cluster center. The shell thickness along the line-of-sight is approximately equal to $\dfrac{\Delta r r}{\sqrt{r^2 - R^2}} = \dfrac{\Delta r}{\sqrt{1 - R^2}}$, where Δr is the shell thickness in the radial direction and R is the projected radius in the plane of the sky. Let V be the velocity along the line-of-sight and the Gaussian ion velocity distribution (3.2) be valid. We will take into account only the turbulent line broadening, i.e., $\sigma_{\mathrm{eff}}^2 = (\sigma_{\mathrm{turb,r}} m_{\mathrm{r}})^2 + (\sigma_{\mathrm{turb},\theta} m_\theta)^2 + (\sigma_{\mathrm{turb},\phi} m_\phi)^2$. At fixed velocity dispersion in a given direction Eq. (3.7) will then be rewritten as

$$\sigma_{\mathrm{eff}}^2 = \begin{cases} \xi^2, \text{isotropic} \\[2ex] \xi^2(1 - R^2), \text{radial} \\[2ex] \xi^2 R^2, \text{tangential} \end{cases} \tag{3.8}$$

Substituting (3.8) into (3.2) and integrating (3.2) over the area $R dR$, we obtain the following line profiles for isotropic, radial and tangential turbulence:

$$\int_0^1 \frac{\Delta r}{\sqrt{2\pi} s} \frac{R}{\sqrt{1 - R^2}} \exp\left(-\frac{1}{2} \frac{V^2}{s^2}\right) dR, \text{isotropic} \tag{3.9}$$

$$\int_0^1 \frac{\Delta r}{\sqrt{2\pi}\sqrt{1 - R^2} s} \frac{R}{\sqrt{1 - R^2}} \exp\left(-\frac{1}{2} \frac{V^2}{s^2(1 - R^2)}\right) dR, \text{radial} \tag{3.10}$$

$$\int_0^1 \frac{\Delta r}{\sqrt{2\pi} R s} \frac{R}{\sqrt{1 - R^2}} \exp\left(-\frac{1}{2} \frac{V^2}{s^2 R^2}\right) dR, \text{tangential}, \tag{3.11}$$

where $s = \xi$. The expressions for the line profiles at fixed total kinetic energy are similar but with the substitution $s = 2\varepsilon_{\mathrm{kin}}/3\rho, 2\varepsilon_{\mathrm{kin}}/\rho, \varepsilon_{\mathrm{kin}}/\rho$ for isotropic, radial and tangential turbulence, respectively. Figure 3.1 shows the derived averaged profiles that agree well with those from our numerical simulations in the limit of a low temperature and a large amplitude of gas motions. Note that the root-mean-square (rms) line widths at fixed kinetic energy of turbulent motions are identical for any anisotropy, although the line shapes do not coincide.

The change in line width with distance from the cluster center for various types of turbulence was considered by Rebusco et al. (2008). It was shown that the linewidth is constant along the radius for isotropic turbulence, the lines are considerably broader at the cluster center than at the edges for radial turbulence, and, on the contrary, the broadest lines are at the cluster edges for tangential turbulence.
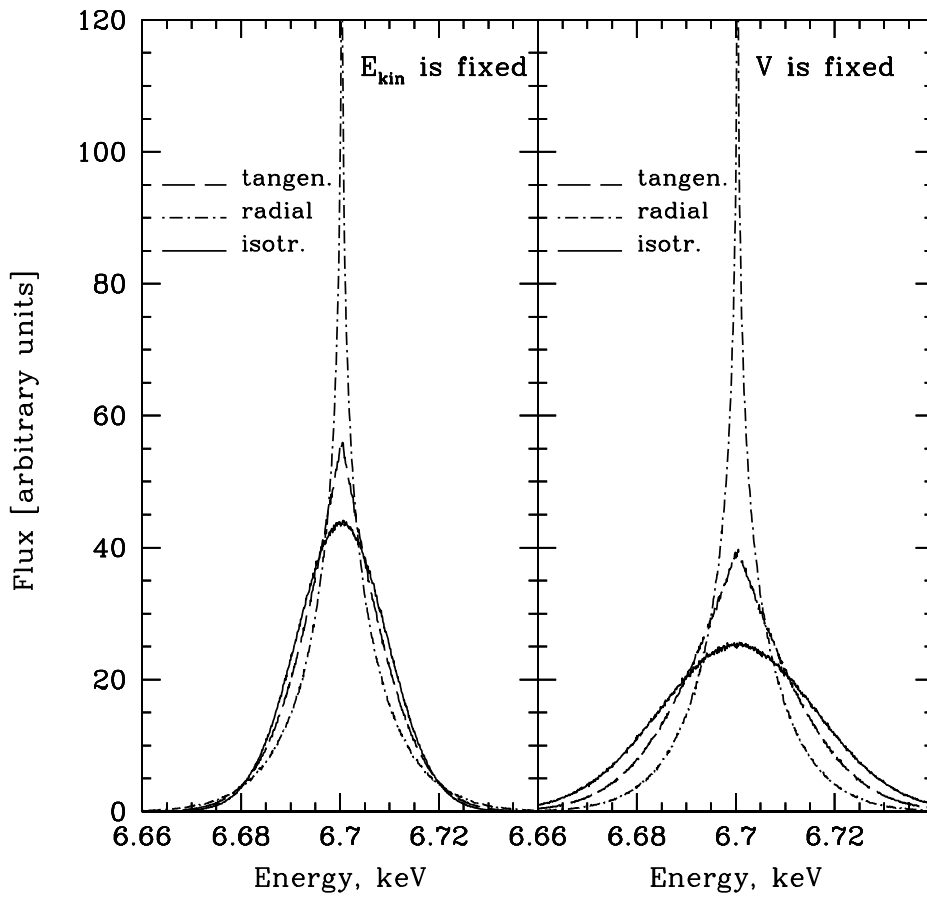
Figure 3.1: Analytical spectral profiles of the helium-like iron line at 6.7 keV for isotropic microturbulent (solid curves), radial (dash-dotted curves) and tangential (dashed curves) gas motions. The line broadening only due to turbulence is taken into account. The profiles were calculated at fixed total kinetic energy and fixed velocity amplitude of gas motions (3.9, 3.10, 3.11).

3.2.2 The Influence of Large-Scale Gas Motions on the Line Profiles

As was said in the Introduction, large-scale gas motions cause the lines to be shifted and broadened. This is easy to see using the results of numerical simulations of galaxy clusters. Figure 3.2 shows the spectral profiles of the helium-like iron line at 6.7 calculated for the model cluster g676, which is an example of a low-mass, dynamically quiet cold cluster (see the "Velocity Field" Section and Table 3.1) by taking into account the large-scale motions and thermal line broadening. The profiles were calculated for nine lines-of-sight. For the central panel, the line-of-sight passes through the cluster center. The thin solid curves indicate the spectra that emerge in the case of purely thermal broadening; the profiles in the presence of gas motions are indicated by the thick solid curves. The dashed curves indicate the Gaussian line profile fits. The profiles averaged over the entire cluster are shown in Fig. 3.3. We see that the profiles are broadened and shifted in the presence of gas motions. Strong deviations from the Gaussian profile are clearly seen at the cluster periphery, suggesting the presence of large-scale gas motions.

Depending on which cluster region we observe (the cluster center or edge), the line profiles will be more sensitive to radial or tangential gas motions. This is demonstrated in Fig. 3.4, where the spectral profiles of the helium-like iron line at 6.7 keV are shown for the model, dynamically quiet cluster g6212 (see the "Velocity Field" Section and Table 3.1) calculated in three cluster regions: the central region ($\sim$70 kpc in diameter) and two regions at a projected distance of $\sim$160 kpc from the center ($\sim$145 kpc in diameter each). We separately consider the influence of radial (dots) and tangential (dashes) gas motions and compare with the profiles in the case when the gas is at rest (solid curves). For this purpose, we set the radial, tangential, or both velocity components equal to zero in each cell of the computational volume and repeated the radiative transfer computation procedure. We exclude the motion of the cluster as a whole by subtracting the weighted mean (within a sphere at the cluster center 50 kpc in radius) velocity.

In the cluster center the scale of gas motions is small compared to the size of the central region. Therefore, we see an almost symmetric and slightly broadened line. At the cluster edges, the spatial scale of gas motions is comparable to the characteristic size of the region that makes a dominant contribution to the emission. Therefore, we see an asymmetric line with a shift of the central energy. Since the surface brightness and (gas density) rapidly falls toward the cluster edges, the regions along the line-of-sight located near the plane of the sky passing through the cluster center make a major contribution to the emission. Obviously, the observed energy shift for these regions is produced mainly by tangential motions.
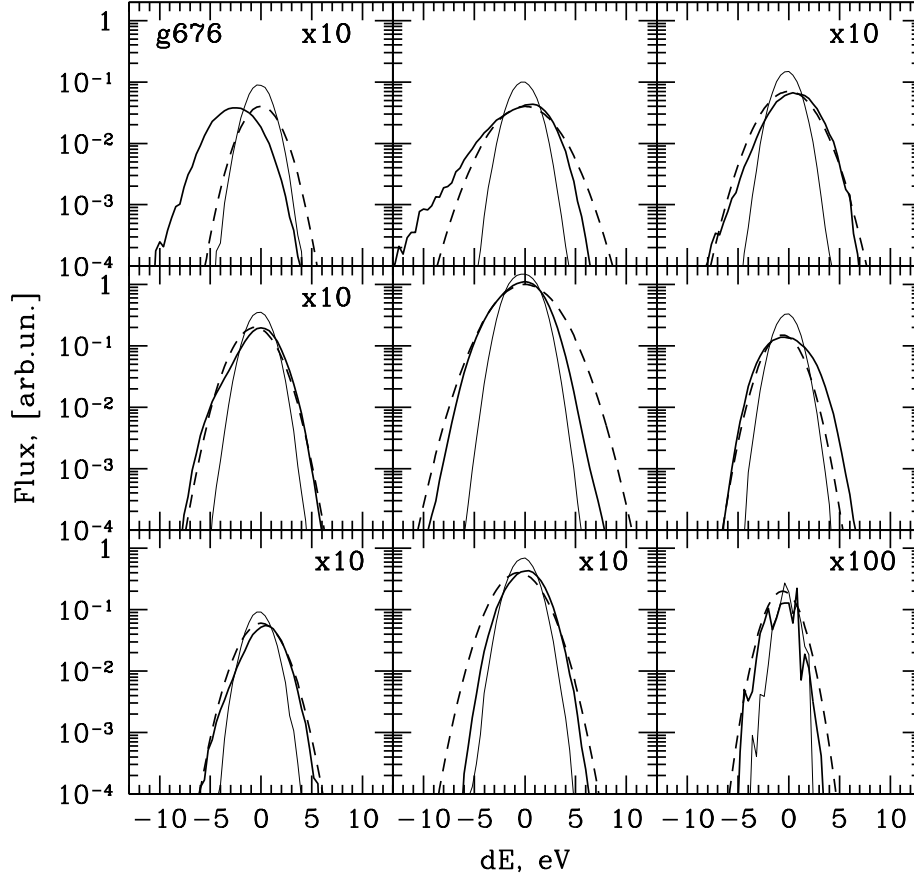
Figure 3.2: Profiles of the helium-like iron FeXXV line at 6.7 keV for nine lines-of-sight in the model cluster g676 (see the table). The cluster was divided into nine identical parts; the size of the entire cube is $1 \times 1 \times 1$ Mpc. For the central panel, the line of sight passes through the cluster center. The thick, thin and dashed curves indicate, respectively, the line profiles shifted and broadened through gas motions, the profiles emerging only in the case of thermal line broadening, and the Gaussian line profiles broadened through the mean temperature and V_{rms} in each region.
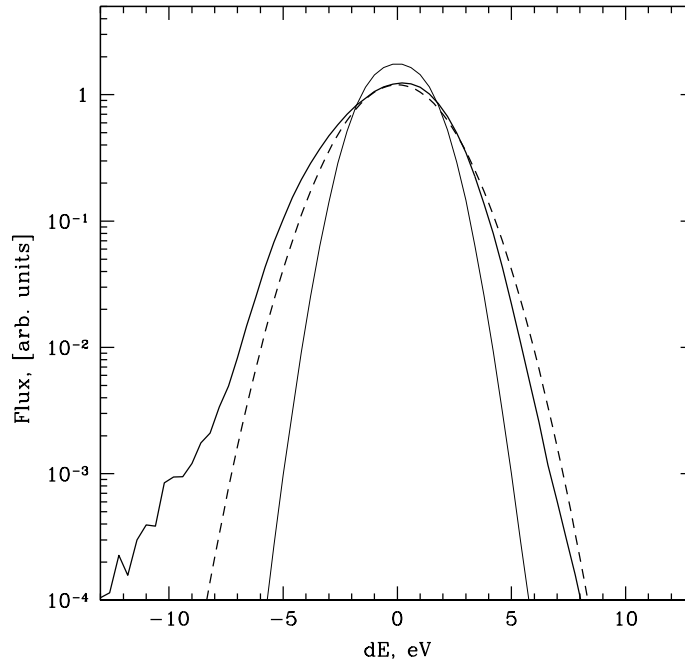
Figure 3.3: Profiles of the helium-like iron FeXXV line at 6.7 keV averaged over the entire model cluster g676. The notation is the same as that in Fig. 2.
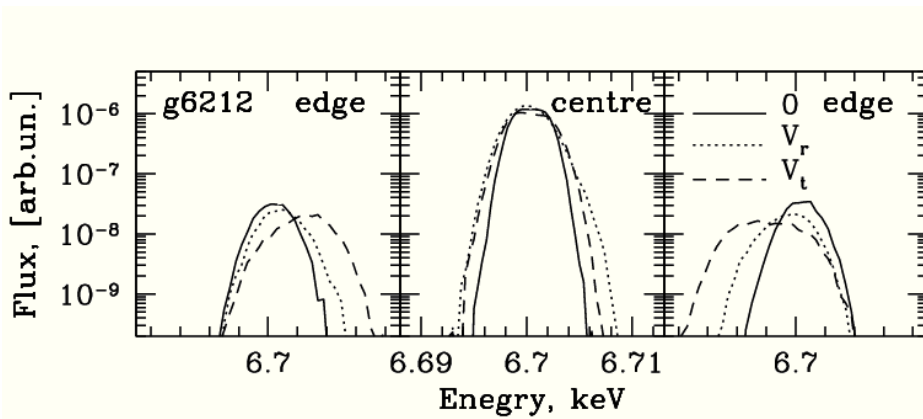
Figure 3.4: Spectral profile of the helium-like iron FeXXV line at 6.7 keV calculated for the model cluster g6212 (see the table) at the cluster center (the size is $\sim$70 kpc) and in two regions at a distance of 160 kpc from the center (the size is $\sim$145 kpc). The solid, dotted, and dashed curves indicate, respectively, the profiles when the gas is at rest, in the case of radial gas motions, and in the case of tangential gas motions.

Table 3.1: Basic parameters of the galaxy clusters from numerical simulations.

Cluster	$M_{\mathrm{vir}}, 10^{14} M_\odot$	R_{vir}, Mpc	T_{mean}, keV
g6212	1.61	1.43	1.5
g8	32.70	3.90	13
g51	19.21	3.26	8.6
g676	1.60	1.43	1.25

3.3 The Influence of the Velocity Field on Resonant Scattering

The photon scattering probability in a given line is determined by (a) the optical depth at the line center, (b) the deviation of the photon energy from the line energy, and (c) the line width.

Turbulent gas motions in the direction of photon propagation will broaden the line, reducing the optical depth and the resonant scattering effect (see, e.g., Gilfanov et al. 1987). Indeed, the optical depth at the line center can be found as $\tau = \int_0^\infty n_{\mathrm{i}} s_0 dl$, where n_i is the ion number density and s_0 is the scattering cross section at the line center:

$$s_0 = \frac{\sqrt{\pi} h r_{\mathrm{e}} c f}{\Delta E_{\mathrm{D}}}, \tag{3.12}$$

Here, r_{e} is the classical electron radius, f is the oscillator strength of a given transition, and ΔE_{D} is the Doppler line width. The line broadening ΔE_{D} can be divided into two components: the purely thermal broadening and the broadening due to turbulent motions, i.e.,

$$\Delta E_{\mathrm{D}} = \frac{E_0}{c} \sqrt{2(\sigma_{\mathrm{therm}}^2 + \sigma_{\mathrm{turb}}^2)}. \tag{3.13}$$

Here, σ_{turb} is the velocity dispersion due to turbulent motions and σ_{therm} is the thermal dispersion of ion velocities:

$$\sigma_{\mathrm{therm}}^2 = \frac{kT}{A m_{\mathrm{p}}}, \tag{3.14}$$

E_0 is the energy at the line center, k is the Boltzmann constant, m_{p} is the proton mass, A is the atomic weight of the element, and c is the speed of light. For heavy elements A is large (e.g., $A = 56$ for iron), therefore the thermal broadening of heavy-element lines is noticeably suppressed, while the broadening through gas motions is the same for all lines.

The presence of large-scale gas motions leads to a change in the resonant scattering cross section. In the reference frame of the gas, the cross section is proportional to

$\exp\left\{-\frac{\left(E\left[1 - \frac{(\mathbf{Vm})}{c}\right] - E_0\right)^2}{2\sigma^2}\right\}$, where E is the photon energy in the reference frame of

the cluster, E_0 is the transition energy, $\mathbf{V}$ is the velocity of large-scale gas motions, $\mathbf{m}$ is the photon propagation direction, and σ is the Gaussian line width determined by the thermal broadening and the broadening through turbulent gas motions.

3.4 Cluster Model and Scattering Calculation

At present, the gas density and temperature distributions in nearby X–ray bright galaxy clusters, such as Perseus cluster, are well known. At the same time, there is almost no information about the properties of the gas velocity field. It seems natural to supplement the density and temperature measurements with the results of numerical hydrodynamic velocity calculations and to use such a combined model to model the resonant scattering.

3.4.1 Gas Temperature and Density Distributions

The resonant scattering calculations were performed for the Perseus galaxy cluster A426, whose electron temperature and density profiles were taken from Churazov et al. (2003). Correcting the profile for the Hubble constant $H_0 = 72$ km s^{-1} Mpc^1, we find the electron density in cm^{-3} as

$$n_{\mathrm{e}} = \frac{4.68 \cdot 10^{-2}}{\left(1 + \left(\frac{r}{56}\right)^2\right)^{3/2 \cdot 1.2}} + \frac{4.86 \cdot 10^{-3}}{\left(1 + \left(\frac{r}{194}\right)^2\right)^{3/2 \cdot 0.58}}. \tag{3.15}$$

The temperature distribution in keV is

$$T_{\mathrm{e}} = 7 \frac{1 + \left(\frac{r}{100}\right)^3}{2.3 + \left(\frac{r}{100}\right)^3}, \tag{3.16}$$

where r is in kpc. The iron abundance is assumed to be constant in the cluster and equal to 0.5 of the solar one from the tables by Anders and Grevesse (1989) and 0.74 of the solar if one uses the newer tables by Asplund et al. (2009).

The mean temperature in the Perseus cluster is about 5-6 keV. At such temperatures, the strongest line in the spectrum is the K_α line of helium-like iron at 6.7 keV that corresponds to the $1s^2(^1S_0) - 1s2p(^1P_1)$ transition with an oscillator strength ~ 0.7. The optical depth in this line from the cluster center to infinity is ~ 3.

3.4.2 Velocity Field

The energy resolution of modern X-ray telescopes does not allow the gas velocity field in galaxy clusters to be measured directly. To make the assumption about the velocity field, we will use the results of numerical cluster simulations taken from the cosmological calculations of the large-scale structure (Dolag et al. 2005; Springel et al. 2001). The numerical simulations give the three-dimensional structure of the gas density and temperature and

three velocity components determined in a cube with a size of several Mpc. We considered nine clusters differing in mass. The rms velocity amplitudes in the coldest and hottest clusters are ~ 200 and ~ 1000 km s^{-1}, respectively.

To make the conclusion about the directions of motions, let us compare the rms amplitude of the radial velocity $V_{\rm r}$ with that of the tangential one $\sqrt{(V_\theta^2 + V_\phi^2)/2}$. We exclude the motion of the cluster as a whole by subtracting the weighted mean (within a sphere at the cluster center 50 kpc in radius) velocity. The rms amplitude $V_{\rm rms}$ was calculated in spherical shells with radius r and thickness $\Delta r = 0.1r$ separately for the velocity components along and perpendicular to the radius. The results for the available nine clusters show that the gas motions are almost isotropic. Figure 3.5 presents the results for three clusters. The rms amplitudes of the velocities of radial gas motions are indicated by the dashed curves; the solid curves indicate the amplitudes for each velocity component in the tangential direction. We see that the curves differ insignificantly at radii $< 300 - 400$ kpc and, hence, the amplitudes of the gas motions are identical in all directions.

Although the assumption that the gas motions are isotropic is justified by our numerical simulations, it should be remembered that in reality the gas motions are not necessarily isotropic. For example, considering the velocities of gas filaments in H$_\alpha$ in the Perseus cluster, Hatch et al. (2006) showed that the gas at distances larger than 30 kpc from the central galaxy (i.e., where the resonant scattering is significant) entrained by AGN-inflated plasma bubbles is involved predominantly into radial motions.

To make reasonable assumptions about the properties of the velocity field in our radiative transfer calculations, we analyzed the power spectra found in hydrodynamic simulations of cluster formation. An example for one cluster is shown in Fig. 3.6. Details of the method for calculating the power spectrum are given in Arevalo et al. (2011). Most of the numerical simulations suffer from an insufficient dynamic range of wave numbers needed to reliably determine the shape of the power spectrum. In particular, adaptive smoothing, which is especially significant for the SPH method (the solid curve in Fig. 3.6), leads to a cutoff in the power spectrum at large k. At the same time, non-adaptive smoothing leads to a sharp rise of the power spectrum at large wave numbers, which is related to Poissonian noise on these scales, in particular, when there are no particles at all within the cell. The true power spectrum at large k must lie between the dashed and solid curves shown in Fig. 3.6. The cutoff in the power spectrum at small wave numbers is related, in particular, to the choice of the size of the computational volume centered on the cluster. We discuss this effect in a separate publication (Zhuravleva et al. 2011). In Fig. 6, the dash-dotted curve indicates the Kolmogorov power spectrum[2] $\sim k^{-2/3}$. One can see that the assumption about a Kolmogorv spectrum appears as a reasonable compromise, although the Kolmogorov slope in the simulated clusters is observed in a fairly narrow range of wave numbers.

Yet another problem can be associated with an insufficient resolution of SPH simulations on small scales. The scales that are resolved in simulations range from tens of kpc at

---

[2]The Kolmogorov spectrum has such a slope when the total energy associated with the motions with a given scale of wave numbers k is considered.
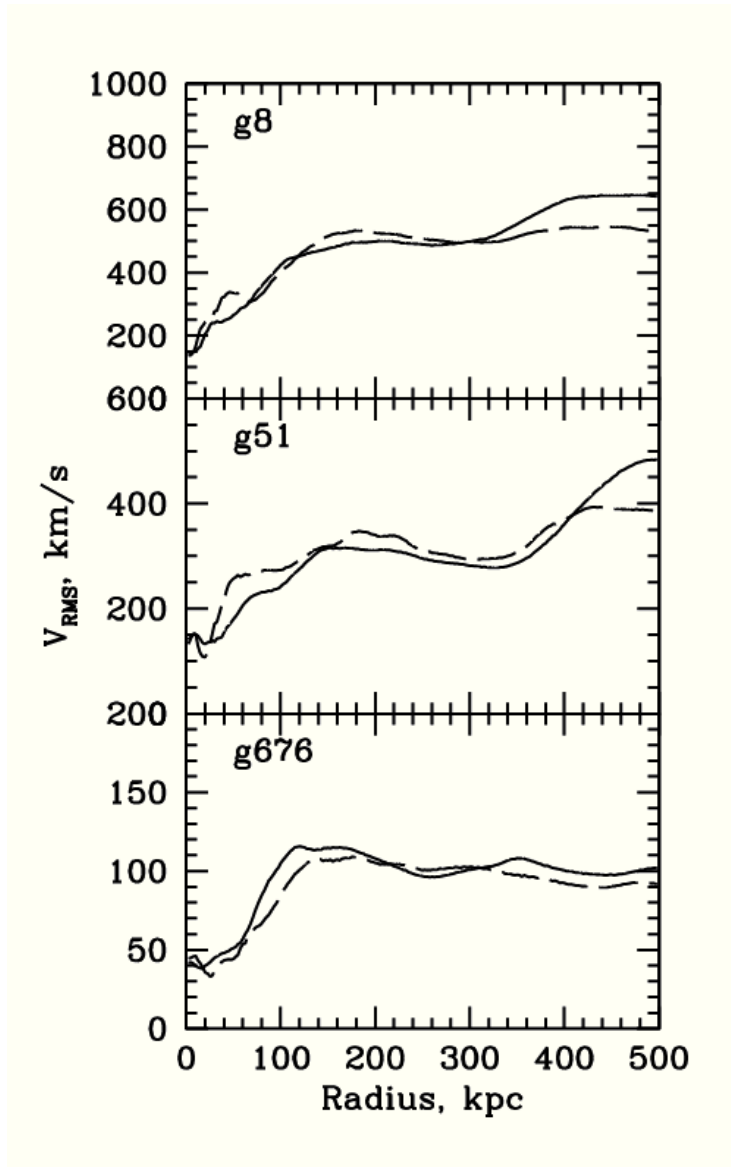
Figure 3.5: Rms amplitudes of the radial velocity of gas motions (dashed curves) and rms amplitudes of the tangential velocity $\sqrt{(V_\theta^2 + V_\phi^2)/2}$ (solid curves) versus distance from the cluster center for three model clusters taken from numerical simulations.
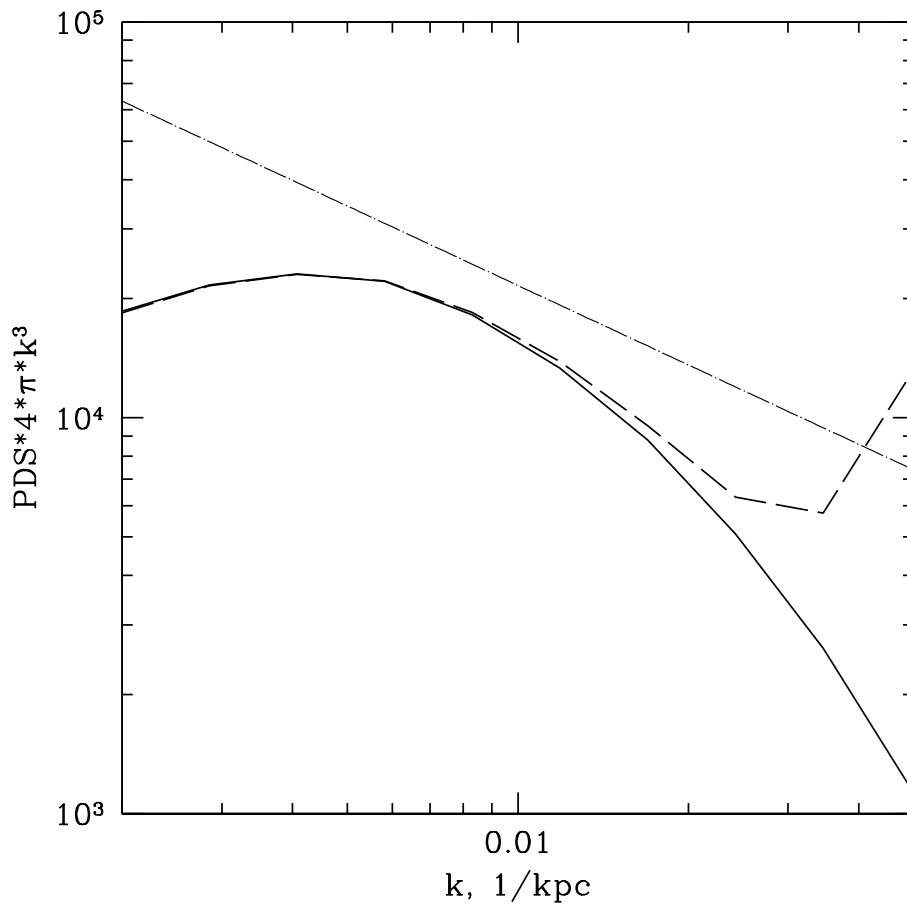
Figure 3.6: Power spectrum of the velocities of gas motions in the cluster g676 (see the table) from numerical simulations. To construct the spectra, we used the results of SPH simulations smoothed adaptively (solid curve) and non-adaptively (dashed curve). The Kolmogorov power spectrum $\sim k^{-2/3}$ is indicated by the dash-dotted curve.

the cluster center to several hundred kpc at the edges. An additional spatial scale arises in the scattering problem - the characteristic photon mean free path in scattering, i.e., the size at which an optical depth of the order of unity is accumulated. It is useful to compare this scale with the resolution of SPH simulations. For the cluster g676, the power spectrum is shown in Fig. 3.6; we see that on $k \leq 0.02$ kpc^{-1} the simulations are resolved. On shorter scales (large wave numbers), the calculations of the velocity field with an adaptive window (solid curve) and a non-adaptive window (dashed curve) give large difference in results. This discrepancy means that the simulation resolution limit was reached. The corresponding spatial scale[3] is ~ 50 kpc. In this case, an optical depth of the order of unity near the cluster center is accumulated at a size $1/(n_i s_0) \sim 150$ kpc. Thus, the resolution of our simulations is sufficient for our purposes.

In the subsequent simulations, we assumed the power spectrum of the velocity fluctuations to be $k^3 P(k) \sim k^{-2/3}$.

3.4.3 Monte Carlo Simulations of Scattering

To simulate multiple scattering, we used the Monte Carlo method (Pozdnyakov et al. 1983). Details of the simulations of scattering in lines are discussed in Sazonov et al. (2002), Churazov et al. (2004) and Zhuravleva et al. (2010). The line energies and oscillator strengths were taken from the ATOMDB[4] and NIST Atomic Spectra Database[5] databases.

During the scattering, the photon direction $\mathbf{m}$ is selected by taking into account the scattering phase function, which is a combination of Rayleigh and isotropic scattering phase functions (Hamilton 1947; Chandrasekhar 1950). For isotropic scattering, the new photon direction $\mathbf{m}'$ is drawn randomly. For Rayleigh scattering, the probability that the photon after its scattering will propagate in the direction $\mathbf{m}'$ is $P(\mathbf{m}', \mathbf{e}') \propto (\mathbf{e}' \cdot \mathbf{e})^2$, where the direction of the electric field is $\mathbf{e}' = (\mathbf{e} - \mathbf{m}' \cos(\alpha))/(\sqrt{1 - \cos^2(\alpha)})$ and α is the angle between the electric vector $\mathbf{e}$ before the scattering and the new photon direction $\mathbf{m}'$, i.e. $\cos(\alpha) = (\mathbf{e} \cdot \mathbf{m}')$.

The initial photon position (or initial weight) is chosen in accordance with the volume emissivity of various cluster regions. To calculate the line emissivity, we used the APEC code (Smith et al. 2001). The ionization balance was taken from Mazzotta et al. (1998). For a randomly chosen initial direction of photon propagation $\mathbf{m}$, we find the photon energy E with a Gaussian distribution with mean E_0 and standard deviation $\Delta E_D / \sqrt{2}$, where ΔE_D was found from eq. (3.13). Since the gas density is low, the pressure effects on the line broadening are neglected. We also neglect the contribution from the radiative decay of levels to the broadening by assuming the levels to be infinitely thin. When simulating the scattering process, we find the velocity of the scattering ion in such a way that the photon energy in the reference frame of the ion is exactly equal E_0 and the scattering occurs. Thus, the ion velocity in the direction of photon motion is $V_{\text{ion}} = \left(1 - \frac{E_0}{E}\right) c$. We

---

[3]We use the relation $k = 1/l$ between the spatial scales and wave numbers without the factor 2π.
[4]http://cxc.harvard.edu/atomdb/WebGUIDE/index.html.
[5]http://physics.nist.gov/PhysRefData/ASD/index.html.

find the other two ion velocity components V_{ion1} and V_{ion2} in the directions $\mathbf{m_1}$ and $\mathbf{m_2}$ orthogonal to $\mathbf{m}$ as $(\mathbf{V}_{\text{gas}}, \mathbf{m_1}) + V_{\text{gauss}}$ and $(\mathbf{V}_{\text{gas}}, \mathbf{m_2}) + V_{\text{gauss}}$, where V_{gauss} is the velocity with a Gaussian distribution. We take into account the velocity dispersion in the directions $\mathbf{m_1}$ and $\mathbf{m_2}$ according to eqs. (3.6) or (3.8). As a result, the velocity of the scattering ion is $\mathbf{V}_{\text{tot}} = V_{\text{ion}}\mathbf{m} + V_{\text{ion1}}\mathbf{m_1} + V_{\text{ion2}}\mathbf{m_2}$. Accordingly, after the selection of a new photon direction by taking into account the scattering phase matrix, we find the photon energy after the scattering as $E = E_0\left(1 + (\mathbf{V}_{\text{tot}} \cdot \mathbf{m'})/c\right)$. In this case, we neglect the change in photon direction when going from the laboratory reference frame to the reference frame of the ion and vice versa, because $V/c \ll 1$. This approximation also assumes the velocity field and the gas distribution to be constant on the time scales of the photon propagation through the cluster.

3.5   Results

To calculate the influence of the velocity field on the scattering, we generate a random realization of the power spectrum with a given shape and normalization for each velocity component and make the inverse Fourier transform to obtain the velocity field with given properties.

We performed our calculations for three velocity fields.

A. **The regime of microturbulence:** there are no large-scale motions, microturbulence leads to line broadening through isotropic, radial, and tangential turbulence with $V_{rms} = 500$ km s^{-1}.

B. **The sensitivity to large-scale gas motions:** the power spectrum is flat at small k up to k_{s} and then falls off as the Kolmogorov one (see Fig. 3.7c). In this case, the flat power spectrum at small k implies the absence of large-scale motions with sizes $> 1/k_{\text{s}}$. The bulk of the power is related to wave numbers of the order of k_{s}. Our calculations were performed for several values of k_{s} (l_{s}): 0.005 kpc^{-1} (200 kpc), 0.05 kpc^{-1} (20 kpc), and 0.2 kpc^{-1} (5 kpc). The rms amplitude of the velocity V_{rms} is 500 km s^{-1} in all cases.

C. **The sensitivity to small-scale motions:** the power spectrum is cut off at $k > k_{\text{s}}$ (see Fig. 3.7d); in this case, the decrease in the characteristic amplitude of the velocity is compensated by the line broadening, i.e., the power is transferred to microturbulence (the shortest scales).

In all three cases, the total energy in large- and small-scale motions is the same. The results are presented in Figs. 7 and 8 (corresponding to cases A, B, and C).

Figure 3.8 shows the ratio of the fluxes in the helium-like iron line at 6.7 keV with and without scattering in the case when there are no gas motions and in the case of different microturbulence designated in the figure (case A). The case of fixed velocity amplitude is indicated by the thick curves. The corresponding results of our calculations at fixed total energy are indicated by the thin curves. We see that when the gas is at rest, the optical depth is maximal, the line flux at the cluster center is strongly suppressed and the flux at the edges increases due to the scattering. When the gas motions are tangential, it is clear that the optical depth in the line calculated in the radial direction will not change.

Figure 3.7: The upper panels: the ratio of the fluxes in the helium-like iron FeXXV line at 6.7 keV with and without scattering in the cluster A426 for gas motions on various scales. The left upper panel: the sensitivity to large-scale motions (case B, see the "Results" Section). The curves correspond to different values of k_s (see the lower left panel). The curve for microturbulence is presented for comparison. The right upper panel: the sensitivity to small-scale motions when the power spectrum (see the lower right panel) of the velocities of gas motions is cut off at various k (case C, see the "Results" Section). The lower panels: the power spectra of the velocities of gas motions in galaxy clusters assumed in the calculations. The left lower panel: the power spectrum is flat at small k_s (=0.005, 0.05, and 0.2) and then falls off as the Kolmogorov one (see the "Results" Section). The right lower panel: the power spectrum for $k_s = 0.05$ (see the left panel) is cut off at $k >$ 0.005, 0.05, 0.1 and 0.2 (see the "Results" Section).

Since the photons produced in the cluster center moving in the radial direction make a major contribution to the scattering, the changes in brightness profiles are insignificant. The radial gas motions that directly affect the optical depth for the photons emerging from the cluster center and that reduce considerably the scattering efficiency have the strongest effect on the resonant scattering. Note that the optical depth in this case decreases by almost a factor of 3. Clearly, the case of isotropic turbulence is intermediate.

Considering large-scale gas motions (case B), note that when the bulk of the power of the motions is on large scales, the scattering is almost as efficient as that in the case when the gas is at rest (Fig. 3.7a, the curve with long dashes). In this case, a bulk motion of large gas volumes (the scales of the motions are larger than r_c) inside which the scattering actually takes place. An increase in k_s, i.e. assuming the power spectrum to be flat at small k (with the total energy of the motions conserved), leads to suppression of the role of large-scale motions and to an increase in the velocity dispersion on small scales. This immediately leads to a decrease in the optical depth in the line and resonance scattering effect is less strong (the curve with short dashes and the dash-dotted curve; the dotted curve is drawn for comparison with the case of isotropic microturbulence).

We also see from Fig. 3.7b that the earlier we "cut off" the power spectrum (case C), i.e. the larger the power is in the small-scale motions affecting the line broadening, the weaker is the resonant scattering.

3.6   Conclusions

We considered the influence of large- and small-scale anisotropic gas motions on the resonant scattering in the FeXXV line at 6.7 keV for the Perseus cluster as an example. The model velocity field is taken from the results of hydrodynamic simulations of galaxy cluster formation (Dolag et al. 2005).

We showed that (1) the resonant scattering is sensitive mainly to small-scale gas motions, (2) it is particularly sensitive to radial motions, (3) large-scale gas motions affect mainly the shift of the line center and (4) the directions of small-scale motions can be estimated by considering the broadening of spectral lines and the resonant scattering in lines simultaneously.

The sensitivity to anisotropy of microturbulent motions is illustrated by the following example: at fixed total kinetic energy corresponding to $V_{rms} = 500$ km s^{-1}, the expected decrease in FeXXV line flux at the center ($R < 10$ kpc) of the cluster A426 is a factor of 0.77, 0.9 and 0.61 for isotropic, radial, and tangential turbulence, respectively. At fixed velocity dispersion in one direction (eq. 3.8), the corresponding decreases are a factor of 0.84, 0.9, and 0.63, respectively. In other words, if a significant anisotropy of small-scale gas motions is allowed, then the same ratio of the line fluxes corresponds to different characteristic velocity amplitudes. For example, for the case considered above (Fig. 3.8), approximately the same ratio of the line fluxes from a region 10 kpc in radius arises at $V_{rms} = 500$ km s^{-1} for isotropic motions, $V_{rms} \approx 200$ km s^{-1} for radial motions, and $V_{rms} \approx 1700$ km s^{-1} for tangential motions. Note that such a large difference is related, in
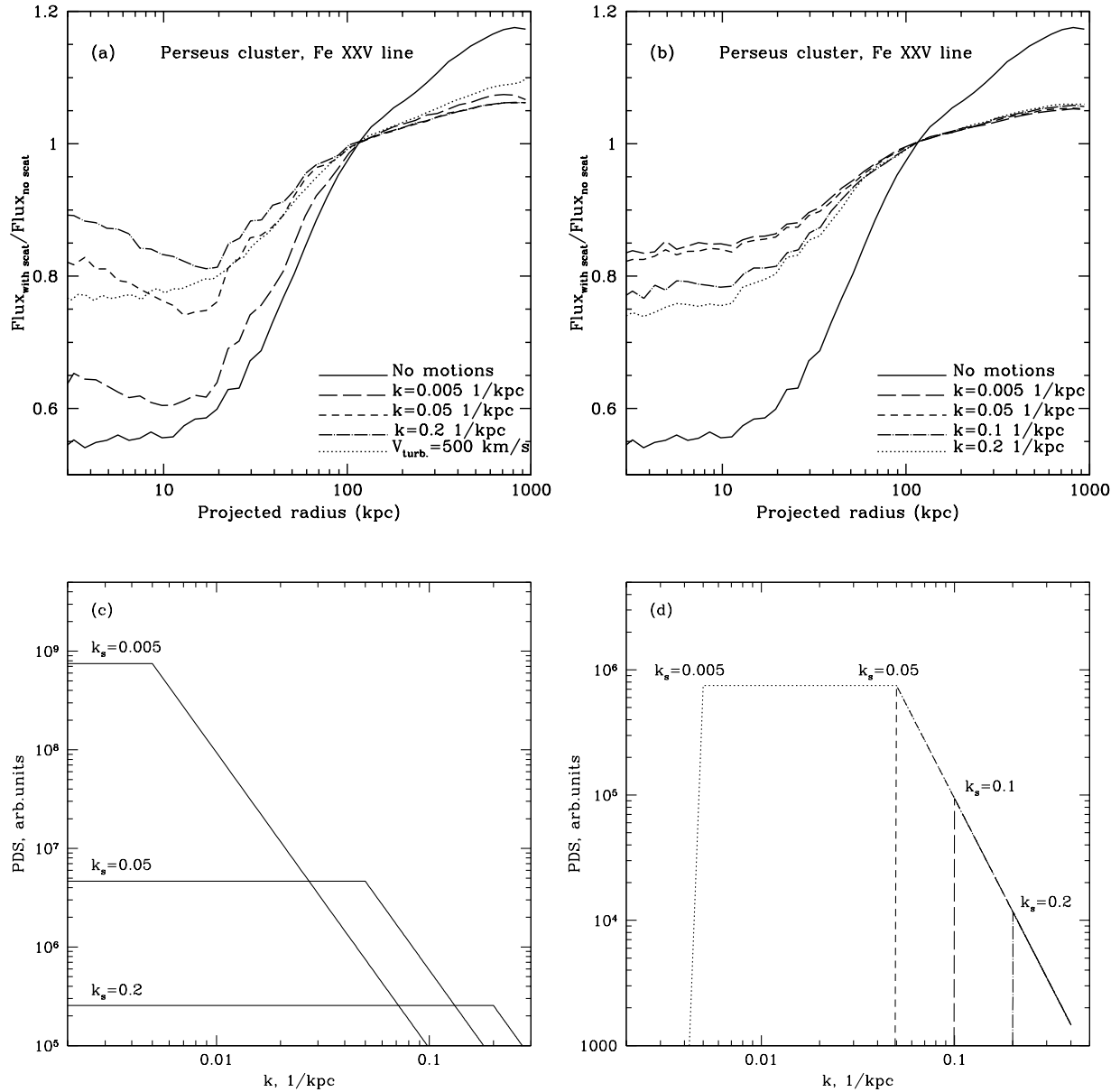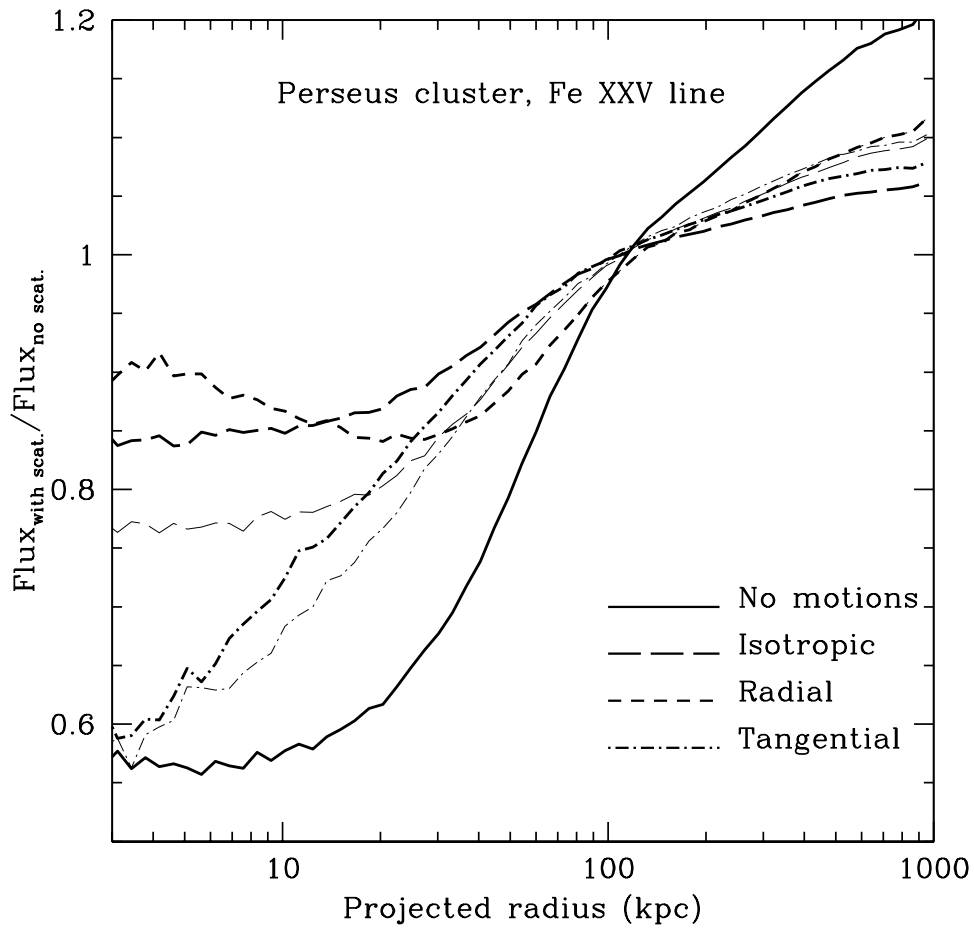
Figure 3.8: Ratio of the fluxes in the helium-like iron FeXXV line at 6.7 keV with and without scattering in the cluster A426 for isotropic, radial, and tangential microturbulent gas motions (case A). The thick and thin curves correspond to the cases of fixed velocity amplitude and fixed total kinetic energy, respectively.
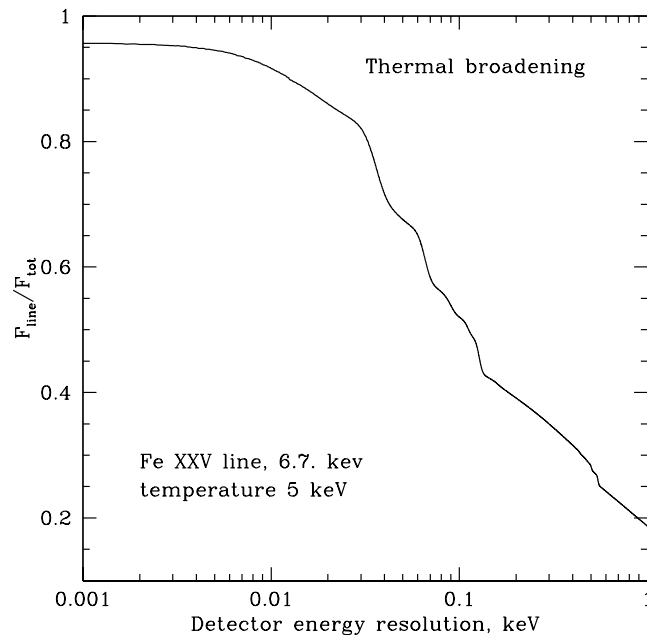
Figure 3.9: Ratio of the FeXXV line flux to the total flux, including the continuum and neighboring lines, versus detector energy resolution for a cluster with a mean temperature of 5 keV. Only the thermal line broadening is taken into account.

particular, to a nonlinear dependence of the line flux ratio on the velocity of gas motions. For a larger region ($r < 30$ kpc), a comparable line flux ratio arises at $V_{\rm rms} = 500$ km s^{-1} (isotropic motions), $V_{\rm rms} \approx 300$ km s^{-1} (radial motions), and $V_{\rm rms} \approx 1200$ km s^{-1} (tangential motions). In this case, the difference between the velocity amplitudes is about a factor of 4. Of course, the presence of purely radial or purely tangential motions in clusters is unlikely and the typical uncertainty is not so great. Note also that the results of our calculations, obtained under the assumption of isotropic gas motions, can be used to set conservative upper limits on the amplitude of purely radial motions, while robust constraints on the amplitude of tangential motions are difficult to obtain from resonant scattering observations.

Large-scale gas motions affect weakly the scattering efficiency. For example, we see from Fig. 3.7a that if the whole power of the motions is on scales of 200 kpc, then the scattering efficiency at the cluster center is a factor of 1.13 lower than that in the case when the gas is at rest. In contrast, if the bulk of the power is concentrated on small scales, for example, on scales of ~ 5 kpc, then the scattering efficiency decreases by a factor of 1.56 (see Figs. 3.7a and 3.7b).

Note that the considered line of helium-like iron at 6.7 keV has bright forbidden and intercombination lines as well as satellites. The optical depths of the forbidden and inter-combination ($1s^2 - 1s2p(^3P_0)$) lines are almost zero, while the oscillator strength of the intercombination ($1s^2 - 1s2p(^3P_1)$) line is a factor of 10 smaller than that of the resonance

line and its optical depth is ~ 0.26. The satellites correspond to the transitions from excited states and have a negligible optical depth at a low matter density. Thus, only the resonance transition is essentially involved in the scattering itself. Clearly, the lower the detector energy resolution, the more difficult to measure the suppression of the flux in the resonance line through scattering. In Fig. 3.9, the ratio of the 6.7 keV line flux to the total flux, including the continuum and neighboring lines, $F_{\text{line}}/F_{\text{tot}}$ is plotted against the detector energy resolution. We see that the 6.7 keV line flux for a cluster with a mean temperature of ~ 5 keV accounts for 50% of the total incoming flux in the energy range $E_0 \pm \Delta/2$ even at an energy resolution $\Delta \sim 100$ eV.

Apart from their influence on the surface brightness profile, gas motions change the degree of polarization in X-ray lines, which results from resonant scattering in the presence of a quadrupole moment in the radiation field. Zhuravleva et al. (2010) showed that in the presence of isotropic microturbulent or large-scale gas motions, the degree of polarization in galaxy clusters can decrease by several times. Clearly, depending on the directions of microturbulent motions, the degree of polarization will also change.

3.7 Acknowledgements

Bibliography

E. Anders and N. Grevesse, 1989, Geochim. Cosmochim. Acta 53, 197

P. Arévalo, E. Churazov, I. Zhuravleva, C. Hernández-Monteagudo, M. Revnivtsev, 2011, ApJ, submitted

M. Asplund, N.Grevesse,A. J. Sauval and P. Scott, Ann. Rev. Astron. Astrophys. , 2009, 47, 481

S. Chandrasekhar, 1950, Radiative Transfer, Clarendon, Oxford

E. Churazov, M. Brueggen, C. R. Kaiser et al., 2001, ApJ, 554, 261

E. Churazov,W. Forman, C. Jones and H. Boehringer, 2003, ApJ, 590, 225

E. Churazov, W. Forman, C. Jones et al., 2004, MNRAS, 346, 29

E. Churazov, R. Sunyaev, W. Forman and H. Boehringer, 2002, MNRAS, 332, 792

E. Churazov, I. Zhuravleva, S. Sazonov and R. Sunyaev, 2010, Space Sci. Rev., 157, 193

K. Dolag, F. Vazza, G. Brunetti and G. Tormen, 2005, MNRAS, 364, 753

A. C. Fabian, J. S. Sanders, S. W. Allen et al., 2003, MNRAS, 344, L43

A. C. Fabian, J. S. Sanders, G. B. Taylor et al., 2006, MNRAS, 366, 417

W. Forman, C. Jones, E. Churazov et al., 2007, ApJ, 665, 1057

W. Forman, P. Nulsen, S. Heinz et al., 2005, ApJ, 635, 894

M. R. Gilfanov, R. A. Sunyaev and E.M. Churazov, 1987, Sov. Astron. Lett. 13, 3

D. R. Hamilton, 1947, ApJ, 106, 457

N. A. Hatch, C. S. Crawford, R. M. Johnstone, A. C. Fabian, 2006, MNRAS, 367, 433

N. A. Inogamov and R. A. Sunyaev, 2003, Astron. Lett. 29, 791

M. Markevitch and A. Vikhlinin, 2007, Phys. Rev., 443, 1

P. Mazzotta, G. Mazzitelli, S. Colafrancesco and N. Vittorio, 1998, A& A, 133, 403

K. Mitsuda, 2009, High Resolution X-ray Spectroscopy: Towards IXO, proceedings of the international workshop held at the Mullard Space Science Laboratory of University College London, ed. G. Branduardi-Raymont and A. Blustin

M. L. Norman and G. L. Bryan, 1999, Numerical Astrophysics : Proceedings of the International Conference on Numerical Astrophysics held at the National Olympic Memorial Youth Center, ed. Shoken M. Miyama, Kohji Tomisaka and Tomoyuki Hanawa, Astrophysics and space science library, v. 240, p.19

L. A. Pozdnyakov, I. M. Sobol and R. A. Syunyaev, 1983, Astrophys. Sp. Phys. Rev. 2, 189

P. Rebusco, E. Churazov, R. Sunyaev et al., 2008, MNRAS, 384, 1511

J. S. Sanders, A. C. Fabian, R. K. Smith and J. R. Peterson, 2010, MNRAS, 402, L11

S. Y. Sazonov, E. M. Churazov and R. S. Sunyaev, 2002, MNRAS, 333, 191

P. Schuecker, A. Finoguenov, F. Miniati et al., 2004, A& A, 426, 387

R. K. Smith, N. S. Brickhouse, D. A. Liedahl and J. C. Raymond, 2001, ApJ, 556, L91

V. Springel, N. Yoshida and S. D. M. White, 2001, New Astron., 6, 79

F. Vazza, G. Brunetti, A. Kritsuk et al., 2009, A& A, 504, 33

S.Vogt and T. A. Enßlin, 2003, A& A, 412, 373

N. Werner, I. Zhuravleva, E. Churazov et al., 2009, MNRAS, 398, 23

H. Xu, S. M. Kahn, J. R. Peterson et al., 2002, ApJ, 579, 600

I.Zhuravleva, E. Churazov, S. Sazonov et al., 2010, MNRAS, 403, 129

I. Zhuravleva et al., 2011, in preparation

Chapter 4

Polarization of X-ray lines from galaxy clusters and elliptical galaxies – a way to measure tangential component of gas velocity

I.Zhuravleva, E.Churazov, S.Sazonov, R.Sunyaev, W.Forman, K.Dolag

Abstract. We study the impact of gas motions on the polarization of bright X-ray emission lines from the hot intercluster medium (ICM). The polarization naturally arises from resonant scattering of emission lines owing to a quadrupole component in the radiation field produced by a centrally peaked gas density distribution. If differential gas motions are present then a photon emitted in one region of the cluster will be scattered in another region only if their relative velocities are small enough and the Doppler shift of the photon energy does not exceed the line width. This affects both the degree and the direction of polarization. The changes in the polarization signal are in particular sensitive to the gas motions *perpendicular* to the line of sight.

We calculate the expected degree of polarization for several patterns of gas motions, including a slow inflow expected in a simple cooling flow model and a fast outflow in an expanding spherical shock wave. In both cases, the effect of non-zero gas velocities is found to be minor. We also calculate the polarization signal for a set of clusters, taken from large-scale structure simulations and evaluate the impact of the gas bulk motions on the polarization signal.

We argue that the expected degree of polarization is within reach of the next generation of space X-ray polarimeters.

4.1   Introduction

Galaxy clusters are the largest gravitationally bound structures in the Universe with cluster masses of $10^{14} - 10^{15} M_\odot$. About 80% of this mass is due to dark matter, 15% due to hot gas and only a few % of the mass corresponds to stars. Hot gas is therefore the dominant baryonic component of clusters and the largest mass constituent which can be observed directly.

In relaxed clusters, during periods of time without strong mergers, the hot gas is in approximate hydrostatic equilibrium, when characteristic gas velocities are small compared to the sound speed. However, during rich cluster mergers, the gas velocities can be as high as ~ 4000 km/s as expected from numerical simulations and suggested by recent *Chandra* and *XMM-Newton* measurements (Markevitch et al., 2004). But even in seemingly relaxed clusters, bulk motions with velocities of hundreds of km/s should exist. The existence of gas bulk motions in clusters of galaxies is supported by several independent theoretical and numerical studies (e.g. Sunyaev, Norman, & Bryan, 2003; Dolag et al., 2005; Vazza et al., 2009). Recent grid-based, adaptive mesh refinement (AMR) simulations have reached unprecedented spatial resolution and are now providing very detailed information on the velocity of the ICM on small scales (Iapichino & Niemeyer, 2008; Vazza et al., 2009). In these simulations velocities as large as few hundred km/s are found all the way to the cluster center.

The most direct way to detect gas bulk velocities along the line of sight is through the measurement of the Doppler shifts of X-ray spectral lines (Inogamov & Sunyaev, 2003). However, robust detection of intracluster gas velocities has to await a new generation of X-ray spectrometers with high spectral resolution, given that the expected shift, of e.g. 6.7 keV line of He-like iron, is ~ 20 eV for a line-of-sight velocity of 1000 km/s. Measuring the line broadening by microturbulence or bulk motions also requires high spectral resolution, which will become possible after the launch of the *NEXT* mission with X-Ray microcalorimeter on-board. This microcalorimeter will have an energy resolution of 4 eV at the 6.7 keV line (Mitsuda et al., 2008; Mitsuda, 2009).

Even more difficult is to measure the gas motion perpendicular to the line of sight through the usual spectroscopic techniques. Indeed, the shift of the line centroid due to this velocity component is proportional to the $\frac{1}{2}\left(\frac{v_\perp}{c}\right)^2 \ll 1$ (transverse Doppler effect) and amounts to ~ 0.3 eV for 6.7 keV line if $v_\perp = 3000$ km s^{-1}. We discuss below a unique possibility to determine such velocities using the polarization, due to resonant scattering, of X-ray lines from galaxy clusters.

The continuum emission from hot gas in galaxy clusters is optically thin. However at the energies of strong resonant transitions, the gas can be optically thick (Gilfanov, Sunyaev & Churazov, 1987). Oscillator strengths of resonant lines are large and if ion concentrations along the line of sight are sufficient, photons with energies of the resonant lines will be scattered. The geometry of the problem is sketched in Fig.4.1 (right panel) - from any gas lump we observe both direct (thick dashed line) and scattered (thick solid black line) emission.
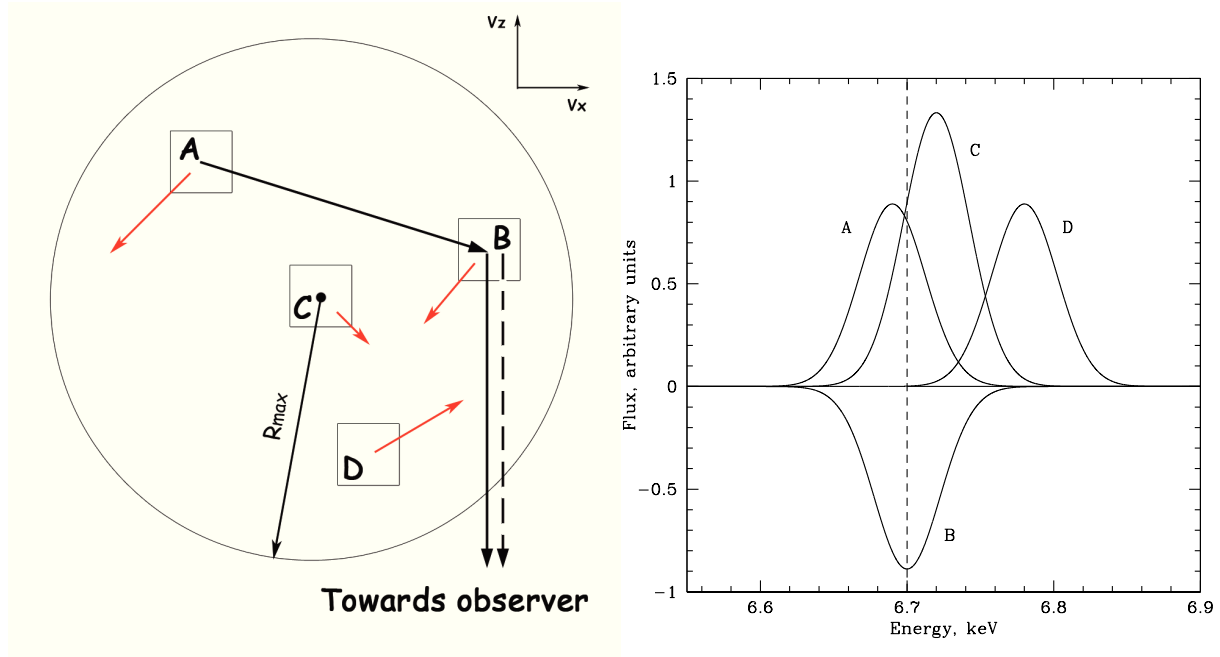
Figure 4.1: Geometry of the problem. **Left panel:** squares show different gas lumps located in one (X,Z) plane. Line of sight is along Z axis. Y axis is perpendicular to the paper. Red arrows show the projection of gas lump velocities onto this plane. The dashed arrow shows a photon emitted towards the observed from a gas lump B. Solid arrows show a photon which was emitted in lump A and subsequently scattered towards the observer in lump B. The efficiency of photon scattering depends on the gas density and temperature, on the line broadening and on the relative velocities of the lumps along the direction between the lumps. The motion of a given gas lump along the line of sight (v_Z) affects the observed energy of the lines , while the motion perpendicular to the line of sight (i.e. v_X and/or v_Y) affects both direction and degree of polarization (see also Fig. 4.2). The v_Z component also affects the poalrization degree by means of transverse Doppler effect, but much less than the other two components, therefore, we neglect this. **Right panel:** Line profiles in the reference system of lump B. The rest energy of the line is 6.7 keV. The energy dependent scattering cross section is schematically shown as a negative Gaussian and is marked with "B". Emission spectra coming from lumps A, C and D are marked as "A", "C", and "D" respectively. The quadrupole asymmetry needed for polarization arises both due to variations of the total line flux coming to lump B from different directions and due to the Doppler shift of the lines caused by the differential bulk motions of the lumps.

If there is an asymmetry in the radiation field (in particular, a quadrupole moment) then the scattering emission will be polarized. This asymmetry can be i) due to the centrally concentrated gas distribution and ii) owing to differential gas motions (see Fig. 4.1 and §4.2).

In clusters, polarization arises rather naturally. It is well known (Sunyaev, 1982) that the scattering of radiation from a bright central source leads to a very high (up to 66%) degree of linear polarization of the scattered radiation (for a King density distribution).

X-ray line emission is strongly concentrated toward the cluster center due to the collisional nature of the emission process and the decrease of the plasma density with distance from the cluster center. Gilfanov, Sunyaev & Churazov (1987) have shown that resonance scattering will decrease the line surface brightness in cluster cores and increase the line brightness in the periphery of clusters. Sazonov, Churazov & Sunyaev (2002) have shown that this process should lead to a high degree of polarization in the resonance lines in high spectral resolution maps of galaxy clusters. For the richest regular clusters and clusters whose X-ray emission is dominated by a central cooling flow, the expected polarization degree is about 15% (Sazonov, Churazov & Sunyaev, 2002).

In this paper we are interested primarily in the second possibility, i.e. in the modification of the polarization signal due to large scale gas motions. Of particular interest is the sensitivity of the polarization signal to $v_\perp$, the component of the velocity perpendicular to the line of sight.

Linear polarization $\propto (v_\perp/c)^2$ naturally appears as a result of scattering of unpolarized isotropic **continuum** radiation with a Rayleigh phase function. That is, for scattering of isotropic CMB radiation in the Rayleigh-Jeans limit the net polarization is given by $P \sim 0.1(v_\perp/c)^2\tau$ (Sunyaev & Zeldovich, 1980), where τ is the optical depth of the scattering medium. In the same paper Sunyaev and Zeldovich presented an approximate formula for the case of double scattering $P \sim 0.02 - 0.05(v/c)\tau^2$, where the coefficient depends on the gas distribution inside the cluster (it is ~ 0.01 for the King distribution, Sazonov & Sunyaev (1999)). Both these effects are very small. If there is an asymmetry in the initial angular distribution of radiation with the dimensionless amplitude a, then additional terms of order $a \times (v/c)$ can appear. But even these terms are expected to be small since the value of v/c itself is of order 10^{-2} or less.

A much larger impact of the gas bulk motions is expected if **line** rather than **continuum** emission is considered. If gas is moving and along the direction of motion the Doppler shift of the photon energy exceeds the line width (i.e. line leaves the resonance) then no scattering occurs. This is illustrated in Fig.4.1. We consider several gas lumps marked as A, B, C and D having different bulk velocities. Region C correspond to the center of the cluster. Photons emitted in regions A, C and D are scattered towards the observer in the region B. Shown in the right panel of Fig.4.1 are the line profiles in the reference system of the lump B. The rest energy of the line is 6.7 keV. The energy dependent scattering cross section is schematically shown as a negative Gaussian and is marked with "B". Emission spectra coming from lumps A, C and D are marked as "A", "C", and "D" respectively. It will be observed (§4.2) that a quadrupole asymmetry in the scattered radiation is needed to produce net polarization. This asymmetry arises both due to variations of the line flux
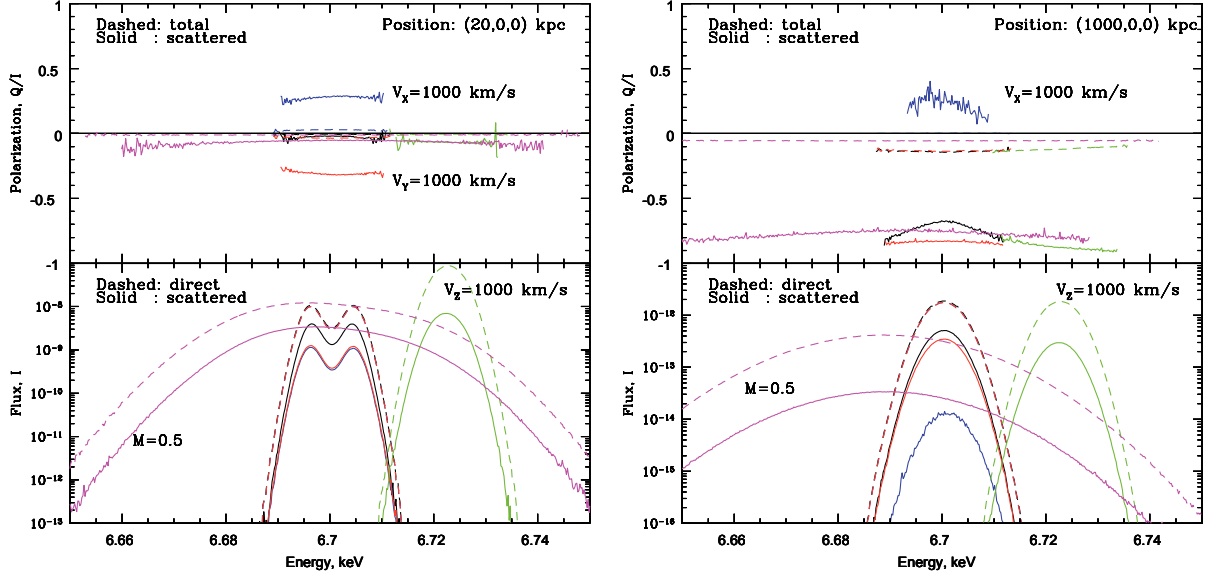
Figure 4.2: Line profile and polarization calculated assuming a single scattering for two small regions of a simulated galaxy cluster. **Left:** A region close to the cluster center with coordinates (20,0,0) kpc. X and Y are the coordinates in the picture plane along horizontal and vertical directions respectively, Z is along the line of sight. In the bottom panel dashed lines show the line photons which are emitted within a given region and directly reached an observer without scatterings I_{dir} (see dashed line in Fig.4.1). Solid lines show the emission scattered in a given region I_{scat} (see solid thick black line in Fig.4.1). In the top panel the solid line is the polarization of the scattered flux only (i.e. Q_{scat}/I_{scat}), while the dashed line shows the polarization of the total emission, coming from a given region (i.e. $Q_{scat}/(I_{scat} + I_{dir})$). **Right:** the same as in the left panel for a gas lump located at (1000,0,0) kpc relative to the cluster center. An appreciable polarization signal is present even in the case of the gas with zero velocities. **Color coding:** *Black* – lines are broadened by thermal ion velocities only, all bulk velocities are set to zero. The characteristic depression at the line center is caused by the large depth at the center of the line. The degree of polarization is small since this region is exposed to essentially isotropic radiation. *Blue* - the same as the black curves, but X component of the gas velocity v_X in a given region is set to 1000 km/s. Scattered flux decreases since along the direction of motion the line emission left the resonance. Polarization of the scattered flux is strong ($\sim$30%) in the direction perpendicular to the direction of motion. *Red* - the same as the black curves, but Y component of the gas velocity v_Y in the region is set to 1000 km/s. Polarization of scattered flux is strong ($\sim$30%) with the polarization plane rotated by 90° compared to blue curves. *Green* - the same as the black curves, but Z component (along the line of sight) of the gas velocity v_Z is set to 1000 km/s. The line energy is strongly shifted, while the polarization characteristics are similar to the case without gas motions (black curves). The larger flux of the line (compared to the case without gas motions) is due to a smaller optical depth towards the observer. *Magenta* - the same as the black curves, but the gas bulk velocities are not set to zero, but are taken from simulations. The lines are broadened by micro-turbulence with the parameter $M = 0.5$.

coming to lump B from different directions and due to Doppler shift of the photon ener-
gies caused by the differential bulk motions of the lumps. Indeed total (integrated over
energies) line flux coming from region C is the largest because of the high gas emissivity in
the cluster center. At the same time, gas lump A is moving away from lump B. Therefore,
in the frame of lump B, the line profile is shifted towards lower energies. The line coming
from lump D is, on the contrary, shifted towards higher energies. A comparison with the
energy dependent scattering cross section clearly shows that asymmetry in the scattered
emission coming from different directions (and therefore the polarization) is affected by
the gas velocities. What matters is the relative velocity of the gas lumps projected onto
the line connecting the lumps. For example, if lump B and C are only slowly moving to-
wards (or away) from each other then line photons coming from region C will be effectively
scattered in lump B and these photons will dominate in the scattered flux seen by the ob-
server. If on the contrary lumps B and C are approaching each other (or receding) with the
velocity larger than the width of the line profile then the lump B will not scatter photons
coming from C and photons coming from other direction will dominate in the scattered
flux. Therefore the intensity and polarization of the scattered flux will be different for
these two cases. The mutual position of lumps B and C sketched in Fig.4.1 shows that the
polarization signal is in particular sensitive to the velocity component of lumps B and C
along the X-axis, i.e. *perpendicular* to the line of sight.

In general relative velocities of any two gas lumps affect the polarization. However,
the central region of the cluster is very bright and therefore the motion of any gas lump
relative to the center is the most important, since a large fraction of scattered photons
were originally born near the cluster center. If the gas density rapidly drops off with
radius then the largest contribution to the scattered flux (and hence to polarization) is
provided by the regions along the line-of-sight which are most close to cluster center – not
far from the picture plane going though the center. Thus the scattering by $\sim 90°$ is the
most important: cluster center - gas lump in the picture plane - observer. In this case
the velocities perpendicular to the line-of-sight affect the scattering and polarization most
strongly. Of course, in real systems different scattering angles make contributions to the
scattered flux and therefore gas motions in different directions play a role. Below (Section
5) we make a full account for 3D velocity field using numerical simulations of galaxy cluster
and account for relative motions of the gas lumps in all directions.

At the same time, the presence of gas motions along the line of sight leads to strong fluc-
tuations of the centroid energy and the shape of the resonant lines (see Inogamov & Sunyaev,
2003)[1] and can be measured with high resolution spectrometers.

One can also consider the impact of small-scale random (turbulent) gas motions on
the line   profiles   and   the   polarization   signal .   As   has   been   shown   by
Gilfanov, Sunyaev & Churazov (1987), micro-turbulence makes the lines broader, decreas-
ing the optical depth and therefore reducing the effects of resonant scattering and polar-
ization. They pointed out that in galaxy clusters the effect is especially strong for heavy

---

[1]The change of the plasma density due to turbulent pulsations has orders of magnitude smaller ampli-
tudes

elements, which have thermal velocities much smaller than the sound velocity of the gas. For example, for the 6.7 keV iron line in the spectrum of the Perseus cluster, the inclusion of turbulent motions would reduce the optical depth from ~ 2.8 to ~ 0.3 for a Mach number of 1 (Churazov et al., 2004). Turbulent motions were also considered in the dense cores of X-ray halos of giant elliptical galaxies. Werner et al. (2009) placed tight constraints on turbulent velocities from the effect of resonant scattering on the ratio of optically thin and thick lines. They have shown that characteristic turbulent velocities in the center of the giant elliptical galaxy NGC4636 are less than 100 km/s.

These points are illustrated in Fig.4.2 where the spectra and the polarization signal coming from two gas clumps in a simulated galaxy cluster are shown. Here we are using a model cluster as described in section 4.5. All calculations for this plot were done assuming a single-scattering by 90°. The left panel shows the radiation emerging from a region close to the cluster center. Due to it's central location, the incident radiation field is almost isotropic and the resulting polarization signal is week. Adding bulk motions in the picture plane (v_x, v_y - blue and red lines, respectively) immediately produces polarization in the perpendicular direction, but does not affect the line shape. On the contrary, adding a line-of-sight velocity component (v_z - green line) shifts the line energy, but does not affect the polarization signal. Finally, adding micro-turbulence makes the line broader. The right panel of Fig.4.2 shows the same effects for a small region located in the cluster outskirts. For this region, the asymmetry in the incident radiation is already present and non-zero polarization is expected even without gas motions. Adding velocity in the "horizontal" direction changes the sign of the polarization signal.

Thus combining the data from high resolution X-ray spectrometers and X-ray polarimeters, one can constrain both line-of-sight and perpendicular components of the velocity field - an exercise hardly possible to do by any other means.

The structure of the paper is as follows. In Section 4.2 we discuss main criteria for selection of X-ray emission lines, most promising for polarization studies. In Section 4.3 we describe a Monte Carlo code used to simulate resonant scattering. Two characteristic flow patterns (a canonical cooling flow and an expanding spherical shock) in the approximation of a spherical symmetry are considered in Section 4.4. In Section 4.5 we present the results of resonant scattering simulations in full 3D geometry, using several clusters taken from cosmological simulations. The calculations described in Sections 4.4 and 4.5 take into account only line photons. In Section 4.6 we summarize our results, discuss additional effects which reduce the polarization degree in galaxy clusters – the most most important one is the contamination of the polarized line flux with unpolarized continuum and line emission from the thermal plasma. Finally in Section 4.7 we outline requirements for future X-ray polarimeters.

4.2   Resonant scattering and promising lines

For the most prominent lines (e.g. 6.7 keV line of He-like iron) the scattering is characterized by the Rayleigh phase function similar to the scattering phase function by free

electrons.

If E is the photon energy, E_0 is the energy of the transition (line), $\mathbf{v}$ is the gas bulk velocity, $\mathbf{m}$ is the photon propagation direction, σ is the Gaussian width of the line set by thermal broadening and micro-turbulent gas motions. The cross section for resonant scattering in the lines in the rest frame of a given gas lump is a strong function of energy

$$s \propto e^{-\frac{(E[1-(\mathbf{vm})/c]-E_0)^2}{2\sigma^2}}. \tag{4.1}$$

If $\mu = \cos\theta$, where θ and ϕ are the polar angles in the frame set by the photon direction of propagation after scattering, $I(E, \mu, \phi)$ is the initial unpolarized radiation, σ_0 is the scattering cross section by one ion and n_i is the number density of corresponding ions, then according to Chandrasekhar (1950), one can write a simple expression for the integrated energy flux scattered in a small volume of gas dV and for the Stokes parameter Q:

$$I_{scat} = \sigma_0 n_i dV \int e^{-\frac{(E[1-(\mathbf{vm})/c]-E_0)^2}{2\sigma^2}} \frac{3}{16\pi}(1+\mu^2)\ I(E, \mu, \phi)\mathrm{d}\mu\mathrm{d}\phi\mathrm{d}E$$

$$Q = \sigma_0 n_i dV \int e^{-\frac{(E[1-(\mathbf{vm})/c]-E_0)^2}{2\sigma^2}} \frac{3}{16\pi}(\mu^2-1)\cos2\phi\ I(E, \mu, \phi)\mathrm{d}\mu\mathrm{d}\phi\mathrm{d}E. \tag{4.2}$$

The presence of the term $(\mu^2-1)\cos2\phi$ in the expression for Q shows that net polarization arises when an angular function

$$F(\mu, \phi) \equiv \int e^{-\frac{(E[1-(\mathbf{vm})/c]-E_0)^2}{2\sigma^2}} I(E, \mu, \phi)\mathrm{d}E \tag{4.3}$$

has non-zero quadrupole moment. As discussed in §4.1 this quadrupole moment can arise due to the asymmetry in $\int I(E, \mu, \phi)dE$ and/or by angular dependence in the cross section $s(E, \mu, \phi)$ caused by the factor $(\mathbf{vm})/c$. Note that in the bottom panel of Fig. 4.1 all profiles are plotted in the rest frame of a given gas lump, while the above expressions are written in the laboratory frame.

The optical depth of a line is defined as

$$\tau = \int\limits_0^\infty n_\mathrm{i}\sigma_0\mathrm{d}r, \tag{4.4}$$

where n_i is the ion concentration and σ_0 is the cross section at the center of the line

$$\sigma_0 = \frac{\sqrt{\pi}hr_\mathrm{e}cf}{\Delta E_\mathrm{D}}, \tag{4.5}$$

where r_e is the classical electron radius and f is the oscillator strength of a given atomic transition. In plasma with a temperature characteristic of galaxy clusters, the line width is determined by the velocities of thermal and turbulent motions, rather than by the radiative width. The Doppler width of the line is defined as

$$\Delta E_{\mathrm{D}} = E_0 \left[\frac{2kT_{\mathrm{e}}}{Am_{\mathrm{p}}c^2} + \frac{V_{\mathrm{turb}}^2}{c^2} \right]^{1/2}, \qquad (4.6)$$

where A is the atomic mass of the corresponding element, m_{p} is the proton mass and V_{turb} is the characteristic turbulent velocity. V_{turb} is parametrized as $V_{\mathrm{turb}} = c_{\mathrm{s}}M$, where M is the Mach number and the sound speed in the plasma is $c_{\mathrm{s}} = \sqrt{\gamma kT/\mu m_{\mathrm{p}}}$, where $\gamma = 5/3$ is the adiabatic index for an ideal monoatomic gas and $\mu = 0.62$ is the mean atomic weight. We can rewrite the previous expression as

$$\Delta E_{\mathrm{D}} = E_0 \left[\frac{2kT_{\mathrm{e}}}{Am_{\mathrm{p}}c^2}(1 + 1.4AM^2) \right]^{1/2}. \qquad (4.7)$$

It is clear from the above expressions that to have large optical depth in the line, the oscillator strength has to be large. If the line width is dominated by thermal broadening then the lines of the heaviest elements will be narrower than for the lighter elements, and the optical depth for lines of heavy elements will be larger as well.

Resonant scattering can be represented as a combination of two processes: isotropic scattering with a weight w_1 and dipole (Rayleigh) scattering with weight $w_2 = 1 - w_1$ (Hamilton, 1947; Chandrasekhar, 1950). Weights w_1 and w_2 depend on the total angular momentum j of the ground level and on the difference between the total angular momentums of excited and ground levels Δj ($=\pm 1$ or 0). The expressions for the weights were calculated by Hamilton (1947). Isotropic scattering introduces no polarization, while Rayleigh scattering changes the polarization state of the radiation field. Therefore, to have noticeable polarization, we have to select lines with a large optical depth and with large Rayleigh scattering weight w_2.

In the spectrum of a typical rich cluster of galaxies, often the strongest line is the He-like K_α line of iron with rest energy 6.7 keV. Ions of He-like iron are present in plasma with temperature in the range from $\sim$1.5 to $\sim$10 keV. The transition $1s^2(^1S_0) - 1s2p(^1P_1)$ of He-like iron has an absorption oscillator strength ~ 0.7 and we can expect this line to be optically thick, leading to a significant role of resonant scattering. Also this transition corresponds to the change of the total angular momentum from 0 to 1 and according to Hamilton (1947) the scattering has a pure dipole phase function. So, we can expect a high degree of polarization in this line. In the vicinity of this resonant line there are intercombination ($1s^2(^1S_0) - 1s2p(^3P_{1,2})$), forbidden ($1s^2(^1S_0) - 1s2s(^3S_1)$) lines of He-like iron and many satellite lines. Forbidden and intercombination lines have an absorption oscillator strength at least a factor 10 smaller than the resonant line (Porquet et al., 2001) and a small optical depth accordingly. Satellite lines correspond to the transitions from excited states and in the low density environment have negligible optical depth.

In cooler clusters with temperatures below 4 keV, the Li-like iron is present in sufficient amounts and the Fe XXIV line $1s^2 2s(^2S_{1/2}) - 1s^2 3p(^2P_{3/2})$ at 1.168 keV is especially strong. The dipole phase function has a weight of 0.5 for this line.

At even cooler temperatures ~ 1 keV the most promising line for polarization studies is the Be-like line ($1s^2 2s(^1S_0) - 1s^2 2s3p(^1P_1)$) of iron with rest energy 1.129 keV, which has

an oscillator strength 0.43 and a unit weight of dipole scattering. Other lines are discussed in detail by Sazonov, Churazov & Sunyaev (2002).

4.3   Monte-Carlo simulations

We performed two types of numerical simulations for two different initial conditions:

- spherically symmetric clusters;

- full three-dimensional galaxy cluster models, taken from cosmological large-scale structure simulations.

4.3.1   Spherically symmetric clusters

In the spherically symmetric simulations, we describe a cluster as a set of spherical shells with given densities, temperatures and radial velocities. To calculate plasma line emissivities we use the Astrophysical Plasma Emission Code (APEC, Smith et al. (2001)). Line energies and oscillator strengths are taken from ATOMDB[2] and the NIST Atomic Spectra Database[3]. The ionization balance (collisional equilibrium) is that of Mazzotta et al. (1998) - the same as used in APEC.

Multiple resonant scattering is calculated using a Monte-Carlo approach (e.g. see Pozdnyakov et al., 1983; Sazonov, Churazov & Sunyaev, 2002; Churazov et al., 2004). We start by drawing a random position of a photon within the cluster, random direction of the photon propagation $\mathbf{m}$ and the polarization direction $\mathbf{e}$, perpendicular to $\mathbf{m}$. The photon is initially assigned a unit weight w. Finding an optical depth τ in the direction of photon propagation up to the cluster edge and an escape probability $p_{\mathrm{esc}} = e^{-\tau}$, we draw the optical depth of the next scattering as $\tau_{\mathrm{next}} = -\ln(1 - \xi(1 - p_{\mathrm{esc}}))$, where ξ is a random number distributed uniformly on the interval $[0, 1]$. Using the value of τ_{next} the position of the next scattering is identified. The code allows one to treat an individual act of resonant scattering in full detail. The phase function is represented as a combination of dipole and isotropic scattering phase matrixes with weights w_1 and w_2. In the scattering process the direction $\mathbf{m}'$ of the emerging photon is drawn in accordance with the relevant scattering phase matrix. For an isotropic phase function, the new direction $\mathbf{m}'$ is chosen randomly. For a dipole phase function, the probability of the emerging photon to have new direction $\mathbf{m}'$ is $P(\mathbf{m}', \mathbf{e}') \propto (\mathbf{e}', \mathbf{e})^2$, where the electric vector $\mathbf{e}' = \dfrac{\mathbf{e} - \mathbf{m}' \cos\alpha}{\sqrt{1 - \cos^2\alpha}}$ and α is an angle between the electric vector $\mathbf{e}$ before scattering and the new direction of propagation $\mathbf{m}'$, i.e. $\cos\alpha = (\mathbf{e}, \mathbf{m}')$. For the energy of the photon, we assume a complete energy redistribution. After every scattering, the photon weight w is reduced by the factor $(1 - e^{-\tau})$. The process repeats until the weight drops below the minimal value w_{min}. Thus,

---

[2]http://cxc.harvard.edu/atomdb/WebGUIDE/index.html
[3]http://physics.nist.gov/PhysRefData/ASD/index.html

Table 4.1: Oscillator strength and optical depth of the most promising X-ray lines in Virgo/M87 and Perseus clusters.

Ion	E, keV	f	w_2	τ, Virgo/M87	τ, Perseus
Fe XXII	1.053	0.675	0.5	0.65	0.02
Fe XXIII	1.129	0.43	1	1.03	0.16
Fe XXIV	1.168	0.245	0.5	1.12	0.73
Si XIV	2.006	0.27	0.5	0.6	0.24
S XV	2.461	0.78	1	0.68	0.03
Fe XXV	6.7	0.78	1	1.44	2.77
Fe XXV	7.881	0.15	1	0.24	0.45

specifying the minimum photon weight, we can control the number of multiple scatterings. A typical value of the minimum weight used in the simulations is $w_{min} = 10^{-9}$.

After every scattering for a photon propagating in the direction **m**, a reference plane perpendicular to **m** is set up for Stokes parameter calculations. One of the reference axes is set by projecting a vector connecting the cluster center and the position of the last scattering on the reference plane. The Stokes parameter Q is defined in such a way that it is non-zero when the polarization is perpendicular to the radius. From the symmetry of the problem, it is obvious that the expectation value of the U parameter in our reference system is $\equiv 0$. Then the projected distance R from the center of the cluster is calculated and the Stokes parameters I and Q are accumulated (as a function of R) with the weight $\propto \epsilon \times w \times e^{-\tau}$, where ϵ is the volume emissivity at the position where the initial photon was born. Finally the degree of polarization is calculated as $P(R) = Q(R)/I(R)$.

4.3.2 Full 3D clusters

In the full 3D simulations, cluster parameters (gas density and temperature) are computed on a 3D Cartesian grid and the velocity field is represented as a 3D vector field. In contrast to a symmetric code, the 3D code precisely takes into account the changes of photon energy due to scattering, assuming Gaussian distributions of thermal and turbulent ion velocities.

For every simulation we choose the viewing direction and setup a reference system in the plane, perpendicular to the viewing direction. The Stokes parameters I, Q and U are calculated with respect to this reference system and are accumulated in a form of 2D images. Finally the degree of polarization is calculated as $P = \sqrt{Q^2 + U^2}/I$.

4.4 Spherically symmetric problems

We have performed spherically symmetric calculations to simulate resonant scattering polarization effects in two galaxy clusters: Perseus and Virgo/M87, as examples of cooling flow clusters.

4.4.1   Perseus cluster

The electron density distribution for the Perseus cluster was adopted from Churazov et al. (2003). They describe the density profile as a sum of two $\beta-$models and they assume a Hubble constant of 50 km/s/Mpc. Correcting the density distribution to the value of the Hubble constant $H_0 = 72$ km/s/Mpc we find

$$n_e = \frac{4.68 \times 10^{-2}}{\left[1 + \left(\frac{r}{56}\right)^2\right]^{\frac{3}{2} \times 1.2}} + \frac{4.86 \times 10^{-3}}{\left[1 + \left(\frac{r}{194}\right)^2\right]^{\frac{3}{2} \times 0.58}} \quad \text{cm}^{-3} \tag{4.8}$$

The temperature distribution is described as

$$T_e = 7\frac{\left[1 + \left(\frac{r}{100}\right)^3\right]}{\left[2.3 + \left(\frac{r}{100}\right)^3\right]} \quad \text{keV}, \tag{4.9}$$

where r is measured in kpc.

The iron abundance is assumed to be constant over the whole cluster and equal to 0.5 solar using the Anders and Grevesse abundance table (Anders & Grevesse, 1989). This value is equivalent to 0.79 solar if the newer solar photospheric abundance table of Lodders (2003); Asplund, Grevesse, & Jacques Sauval (2006) is used.

Sazonov, Churazov & Sunyaev (2002) produced a list of the strongest X-ray lines in the Perseus cluster with optical depth $\tau > 0.5$. Only three lines have dipole scattering weight larger than the weight of isotropic scattering: the He-like K_α line with energy 6.7 keV, the He-like K_β line ($1s^2 - 1s3p(^1P_1)$) at 7.88 keV and the L-shell line of Li-like iron with energy 1.168 keV. The optical depths of these lines are ~ 3, ~ 0.45 and ~ 0.73 respectively (see Table 4.1). Therefore, for the Perseus cluster we performed calculations for the permitted line at 6.7 keV as the optical depth in this line is the largest, weight $w_2 = 1$, and hence the polarization of scattered radiation in this line is expected to be the most significant.

4.4.2   M87/Virgo cluster

Another example of a cooling flow cluster is the M87/Virgo cluster. In this cluster the temperature in the center is lower than in Perseus. The temperature and number electron density profiles in the inner region were taken from Churazov et al. (2008). The electron density is described by β-law distribution with

$$n_e = \frac{0.22}{\left[1 + \left(\frac{r}{0.93}\right)^2\right]^{\frac{3}{2} \times 0.33}} \quad \text{cm}^{-3}, \tag{4.10}$$

where r is in kpc. Temperature variations can be approximated as

$$T = T_0 \left[1 + \left(\frac{r}{r_c}\right)^2\right]^{0.18}, \tag{4.11}$$

where the central temperature is parameterized by $T_0 = 1.55$ keV and $r_c = 10.23$ kpc. In clusters with such low central temperatures the lines of Li-like and Be-like iron become very strong. In Table 4.1 we list potentially interesting lines in M87, which have weight $w_2 \geq 0.5$. The most interesting lines are those at 1.129 keV and at 6.7 keV as the optical depth is large and the scattering phase function is pure dipole. Also notable are the lines of Li-like iron at 1.168 keV and line of S XV at 2.461 keV, which have weights $w_2 = 0.5$ and $w_2 = 1$ respectively. The line at 1.168 keV has two components. The first component has zero weight of dipole scattering, while the second at 1.168 keV has equal weights of dipole and isotropic scattering. Therefore, we consider only the second component in our simulations.

The Fe and S abundances are assumed to be constant at $r < 10$ kpc, being Z(Fe)=1.1 and Z(S)=1 (relative to the solar values of Lodders (2003)), then gradually falling with radius to reach the values Z(Fe)=0.56 and Z(S)=0.63 at $r = 40$ kpc, and remain constant from there on. These approximations are in a good agreement with observations (e.g. Werner et al., 2006).

One can notice, that optical depths, presented in Table 4.1, are systematically lower than in Sazonov, Churazov & Sunyaev (2002). This is caused by differences in number density and temperature profiles. We are using newer profiles and, for example, in case of Virgo cluster number density is systematically lower and temperature in center is higher, leading to the changes in ion fractions. All this factors together reduce the optical depths of lines.

4.4.3   Degree of polarization without bulk motions

In Fig.4.3 the results for the Perseus cluster are shown. As already discussed the calculations were done for the He-like K_α line at 6.7 keV. The polarization is zero at the center of the cluster (as expected from the symmetry of the problem) and increases rapidly with increasing distance from the center. At large distances from the center the degree of polarization depends strongly on the maximum radius r_{max} used in the simulations. This is an expected result. Indeed for steep density profiles at the periphery of a cluster the largest contribution to the scattered signal is due to small region along the line-of-sight (near the closest approach to the cluster center). Since most of the photons are coming from the central bright part of the cluster, the role of 90°scatterings increases. Recall that for the Rayleigh phase function, 90°scattering produces 100% polarized radiation. Therefore near the edges of the simulated volume the degree of polarization is expected to increase, even although the polarized scattered radiation will always be diluted by locally generated line photons. Obviously the final value of polarization degree at a given projected radius depends also on the cluster properties at larger radii. The virial radius of the Perseus cluster is $r_{200} \approx 2.1$ Mpc. Our simple approximations for the gas density and temperature certainly break there (perhaps at a fraction of the virial radius). Nevertheless, the gas beyond virial radius has a very low density and it is likely not hot enough to produce strong emission in the 6.7 keV line. From this point of view an effective cut-off radius r_{max} in the gas distribution may suffice as an illustration of the polarization signal sensitivity

to the structure of the cluster outskirts. In Perseus simulations as $r_{\max}$ varies from 1 Mpc to 4 Mpc (Fig.4.3, the top panel), i.e. the boundary of the simulated volume extends to larger distances, the degree of polarization at the projected distance of 500 kpc decreases from $\sim$8 to 7%. At the very edge of the cluster one can expect the maximum degree of polarization in the Perseus cluster of order 10% . Also shown in Fig.4.3 are the surface brightness profiles in the 6.7 keV line with and without account for resonant scatterings (the bottom panel).

As already mentioned above, a flat abundance profile ($Z = 0.79$) was assumed in these calculations. We also tried a peaked abundance profile based on the XMM-Newton observations of the Perseus cluster (Churazov et al., 2003): the iron abundance is ~ 1.1 in the center ($r < 60$ kpc), gradually decreases to ~ 0.7 at $r \sim 200$ kpc and is flat at larger radii. The polarization degree, corresponding to the peaked abundance profile is shown in Fig.4.3 with the thick long dashed curve. In general the agreement with the calculations for a flat abundance profile is good. The maximum polarization does not change, while at distances $r < 200$ kpc a small bump in polarization degree appears. At $r = 100$ kpc the polarization degree increases from 5% to 6%, staying constant till 200 kpc. We further discuss the effect of the peaked abundance profile in Section 5.

Fig.4.4 (top panel) shows the simulated radial profiles of the degree of polarization for Virgo in several prominent lines. The highest polarization is achieved in the Fe XXIII 1.129 keV line, reaching a maximum of 3.5% at the distance $\sim$15 kpc from the center and falling off from this maximum with increasing distance from the center. A similar behaviour pertains for the lines at 1.168 keV and 2.461 keV. In spite of higher optical depth of line at 1.168 keV, the polarization is lower due to the smaller weight of dipole scattering. It is also important to note that close to the 1.168 keV line there is a second component at 1.163 keV, which produce unpolarized emission and contaminate polarized signal from 1.168 keV line unless the energy resolution is better that 5 keV. Polarization in the line of He-like (at 6.7 keV) iron increases slowly with projected radius and is of order 1%. Surface brightness profiles are also shown on the Fig.4.4 (bottom panel) for all lines shown on the upper panel. We see that lines of Fe XXIII and S XV have not only the largest polarization degree, but also the largest intensity in Virgo cluster.

Comparing profiles of the polarization degree in Perseus and M87 one can notice a different behavior of the curves: in Perseus cluster the polarization is an increasing function of radius, while in M87/Virgo cluster the degree of polarization decreases with radius. This is caused by different radial behavior of the density profiles, since the polarization degree strongly depends on the β-parameter. It is clear, that the polarization degree is smaller for smaller β, since for small β the cluster emission becomes less centrally peaked, leading to a more isotropic radiation field. According to the analytical solution given by Sazonov, Churazov & Sunyaev (2002), at large distances from the cluster center $P = Q/I \propto \dfrac{r^{-3\beta-1}}{r^{-6\beta+1}} = r^{3\beta-2}$. It is clear that if $\beta > 2/3$ (case of the Perseus cluster) the polarization degree will increase with distance, while if $\beta < 2/3$ (case of the M87/Virgo cluster) emission is less peaked and the polarization degree diminishes far from the cluster core.

Figure 4.3: Top panel: polarization degree as a function of projected distance from the center of the Perseus cluster in the most prominent resonant line of Fe XXV with energy 6.7 keV, assuming flat iron abundance (the thick solid curve). Other thin curves show results of calculations done for different sizes of the cluster (maximal radius r_{max}) assumed in the simulations: the upper dot-dashed curve for $r_{max} = 1000$ kpc, the dashed curve is for $r_{max} = 1400$ kpc, the dotted line is for $r_{max} = 3000$ kpc and the lower dot-dashed line for the cluster size $r_{max} = 4000$ kpc. Clearly the polarization degree in the cluster outskirts strongly depends on the assumed extent of the cluster. For reference, the virial radius of the Perseus cluster is $r_{200} \approx 2100$ kpc. Depending on r_{max} the degree of polarization at a distance of 1 Mpc can vary from 8 to 12%. At smaller distances the degree of polarization is less sensitive to the cluster properties at large radii. Thick long dashed curve shows polarization degree in the case of peaked abundance.

Bottom panel: simulated surface brightness of the Perseus in the 6.7 keV line with and without account for resonant scattering - dashed and solid lines respectively. Resonant scattering diminishes the flux in the cluster center and increases the flux at larger radii.
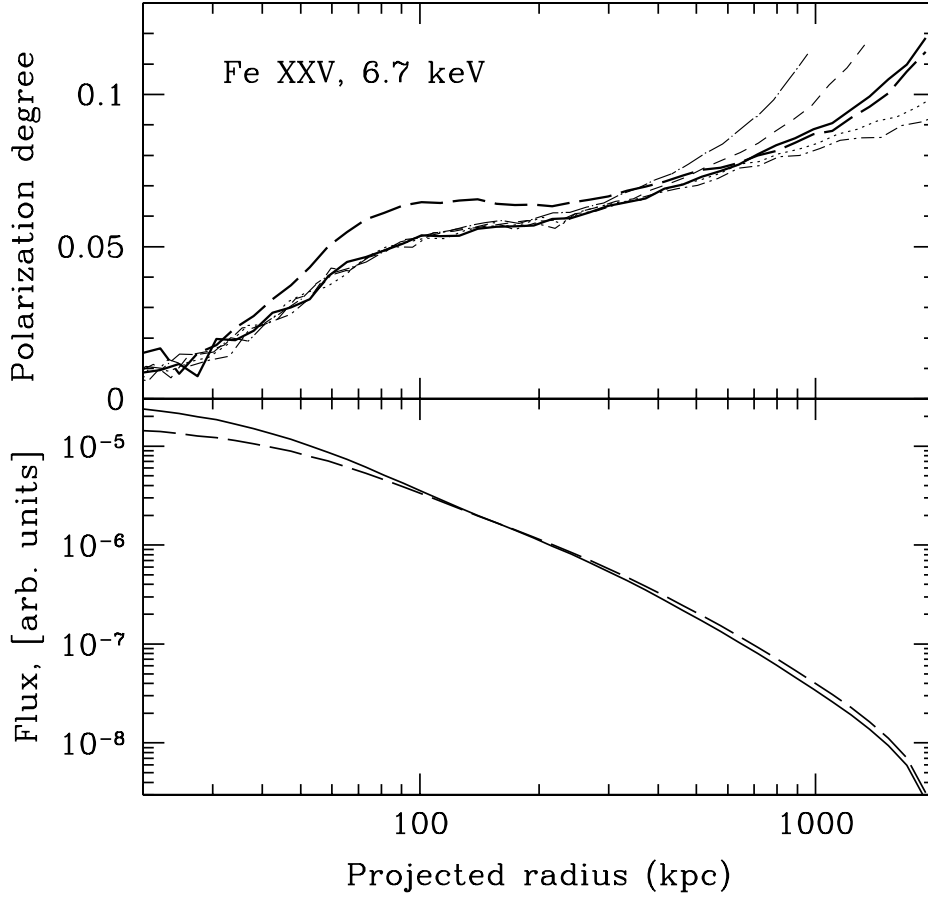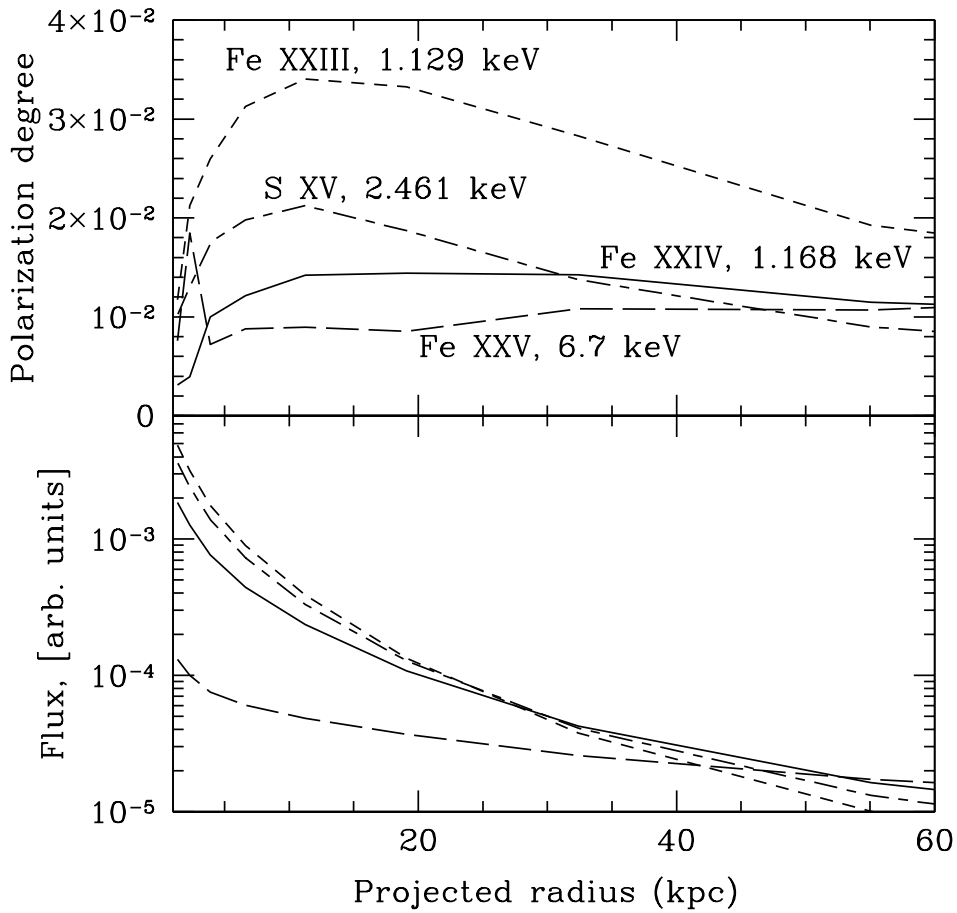
Figure 4.4: Top panel: polarization degree as a function of projected distance from the center of the Virgo/M87 cluster in the most prominent resonant lines, presented in Table 4.1. Bottom panel: simulated surface brightness on the Virgo/M87 cluster in the lines presented on the top panel. Scattering is included.
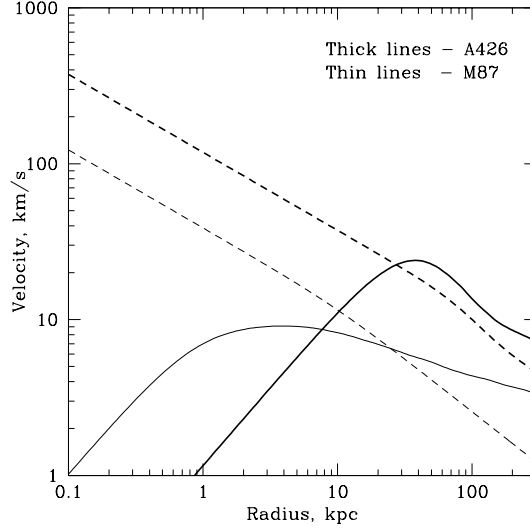
Figure 4.5: Inflow velocity v_r in homogeneous cooling flow models for Perseus (thick lines) and Virgo (thin lines). The solid lines show the radial velocities estimated from eq.(4.12) and the dashed lines show velocities calculated from eq.(4.13). The cooling rates for Perseus and Virgo are assumed to be constant and are $183 M_\odot$/yr and $10 M_\odot$/yr correspondingly.

4.4.4 Canonical cooling flow model

The polarization degree was calculated for several patterns of gas motions. First we consider a canonical cooling flow model (a slow flow of cooling gas toward the center of the cluster). While we understand the canonical cooling flow model has now been transformed into a picture of feedback from central supermassive black holes, the model provides a baseline for exploring symmetric gas flows. The velocity of the flow can be estimated, assuming that the flow time is approximately equal to the cooling time:

$$r/v \approx t_{\text{cool}}, \tag{4.12}$$

where $t_{\text{cool}} = \dfrac{5/2 nkT}{n^2 \Lambda(T)}$, n is the gas density, and $\Lambda(T)$ is the gas cooling function. The radial velocities estimated from eq. (4.12) using the observed temperature and density profiles in Perseus and M87 are shown in Fig.4.5 with solid lines. In both clusters the velocities are very small and do not exceed 30 km s^{-1}.

Larger velocities are anticipated in a **homogeneous** cooling flow model which assumes that the mass flow rate is constant at all radii: $\dot{M}_{\text{cool}}(r) = 4\pi r^2 \rho v_r = \text{const}$. Sarazin (1996) provides the following estimate of the inflow velocity for such a model:

$$v_r = 9 \left(\frac{r}{100 kpc} \right)^{-1/2} \left[\frac{\dot{M}_{\text{cool}}(r)}{300 M_\odot yr^{-1}} \right]^{1/2} \left[\frac{T(r)}{10^8 K} \right]^{-1/2} \quad \text{km s}^{-1}. \tag{4.13}$$
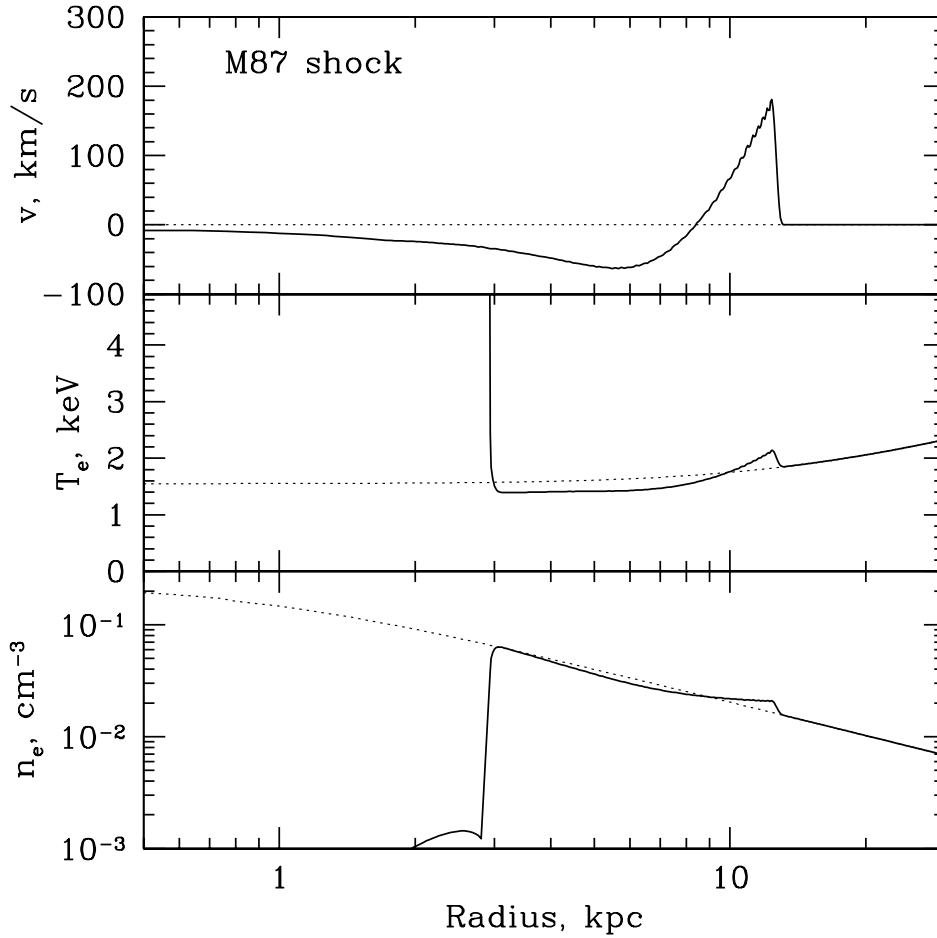
Figure 4.6: Density, temperature and gas velocity profiles in 1D simulations of an expanding shock wave produced by an AGN outburst in the giant elliptical galaxy M87 with the total energy release of $E_0 \sim 5 \times 10^{57}$ ergs and the duration of the outburst $\Delta t \sim 2 \times 10^6$ yr (Forman et al., 2009). Dotted lines show the assumed initial density and temperature distributions. Solid lines in each panel show the density, temperature and velocity distributions about 12 Myr after the beginning of the outburst.

According to Fabian (1994) the cooling rates in M87 and Perseus are $10M_\odot$/yr and $183M_\odot$/yr respectively. The radial velocities in Perseus and M87, estimated from eq.(4.13) using the observed temperature profiles[4], are shown in Fig.4.5 with the dashed lines. Even if velocities are calculated using eq.(4.13) they are not large: at a distance of 1 kpc from the center they are about 30 km/s for M87 and about 100 km/s for the Perseus cluster.

Inclusion of velocities of cooling flows does not change the degree of polarization in either M87 or Perseus since the flow velocities are small. The only appreciable effect is in the very central parts of the clusters (Fig.4.5) where the degree of polarization is very small anyway, with or without the flow.

4.4.5 Spherical shock model

As another possible pattern of gas motions, we consider an expanding spherical shock, using M87 as an example (Forman et al., 2005, 2007). This can be considered as a prototypical case of a cool core cluster, albeit less luminous than the Perseus cluster. All cool core clusters contain a supermassive black hole (an AGN) in a giant elliptical galaxy at the cluster center which is believed to be the source of energy for the cooling gas. AGN activity is also a natural candidate for generation of gas motions: it can either cause turbulent motions by stirring the gas or produce larger scale gas motions in a form of an expanding shock wave. Following Forman et al. (2007, 2009), we used 1D simulations of an expanding shock in M87, which is produced by the AGN outburst with the total energy release $E_0 \sim 5 \times 10^{57}$ ergs and the duration of the outburst $\Delta t \sim 2 \times 10^6$ yr. These parameters were derived based on the comparison of the shock simulations with the data of a 0.5 Ms long Chandra observations of M87 by Forman et al. (2007, 2009). Observed position of the shock is at $\sim 2.8'$ (13 kpc) from the center of M87 and the Mach number of the shock is ~ 1.2. Shown in Fig.4.6 are results of 1D simulations of shock propagation through the M87 atmosphere about 12 Myr after the beginning of the outburst: solid lines in each panel show the density, temperature and velocity distributions. Dotted lines show the assumed initial density and temperature distributions. The energy in the simulations was released in a small volume near the center which by the end of the simulations has expanded into a ~ 3 kpc sphere filled with a very high entropy gas. This is of course the result of our adopted 1D geometry. In reality, the structure of the inner 3 kpc is much more complicated (see Forman et al., 2007). We expect however that our modelling of the outer part is sufficiently accurate and can be used as an illustrative example of the impact of a weak shock on the polarization signal. The gas properties (Fig.4.6) show all the features of a weak spherical shock, in particular a "sine-wave" structure of the velocity distribution. The maximum positive velocity (expansion) is ~ 180 km s^{-1}, while maximal negative velocity (contraction) is ~ 60 km s^{-1}.

For the Virgo cluster we then carried out three radiative transfer simulations: **A**) using initial undisturbed profiles (dotted lines in Fig.4.6), **B**) using density and temperature

---

[4]We note here that the observed density and temperature profiles are not consistent with the homogeneous cooling flow model.
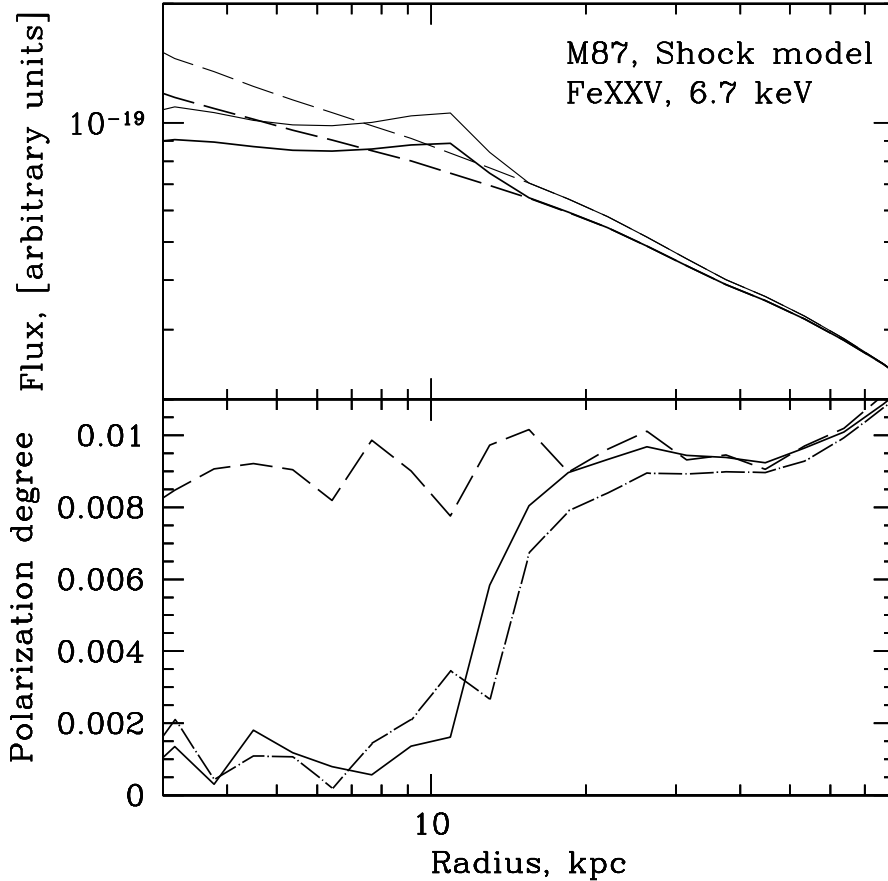
Figure 4.7: Top panel: surface brightness profile in the resonant K_α line of He-like iron at 6.7 keV for Virgo/M87. The dashed curves correspond to the initial temperature and electron number density distributions and the solid curves are for the case of a propagating shock wave. Here, the upper curves (dashed and solid) show profiles without scattering while the other two curves show surface brightness taking into account scattering.

Bottom panel: expected degree of polarization in the 6.7 kev line. The dashed curve corresponds to the initial gas density and temperature distributions without the shock. The solid curve corresponds to the density, temperature and velocity profile expected in the case of a Mach 1.2 shock at r=13 kpc propagating through the ICM. The dashed-dotted line correspond to the same case, but with the gas velocity set to zero. The differences between the last two profiles is not large. Therefore, changes in polarization degree are most sensitive to changes in number density and temperature profiles, rather than to the gas velocity.

distributions as in the shock, but setting the gas velocity to zero and **C**) using density, temperature and velocity distributions as in the shock (solid lines in Fig.4.6). The reason for doing simulations **B** is that we want to see the impact of the nonzero velocity separately from other effects. We preformed calculations for the line with energy 6.7 keV (see Table 4.1) as the influence of the shock wave at such energy is more noticeable.

The results of radiative transfer calculations are shown in Fig.4.7. Shown in the top panel are the surface brightness profiles for cases A (the dashed curves) and B (the solid curves). Profiles in the simulation C are the same as in case B. Here, the upper lines correspond to the profiles without scattering and the lower lines show surface brightness, taking into account scattering. Due to resonant scattering the surface brightness becomes weaker in the center and stronger outside. Because of shock wave propagation the number density in the center becomes smaller leading to the lower surface brightness in the cluster center. Also, due to the shock wave, we see a characteristic peak $\sim$10 kpc from the center. Bottom panel in Fig.4.7 shows the polarization degree for cases A, B, C. We see that after the shock wave propagates, the gas is less dense, therefore the line has smaller optical depth and the polarization decreases. The velocities of gas are larger than in the case of cooling flows and lead again to the decrease of the polarization degree.

4.5 Three-dimensional problem

We now consider full three-dimensional models of galaxy clusters, taken from large-scale structure formation. The density, temperature distributions and the velocity field are taken from a set of high-resolution simulations of galaxy clusters (see e.g. Dolag et al., 2005, 2008) which are based on Gadget-2 SPH simulations (Springel, Yoshida, & White, 2001) and include various combinations of physical effects. We use the output of non radiative simulations. All data are adaptively smoothed and placed in a cube with half size 1000 kpc and cell size 3 kpc. The resonant scattering is calculated using a Monte-Carlo approach, which is described above in section 3.

We discuss here results of calculations for three simulated galaxy clusters: g6212, g72 and g8. Table 4.2 shows the basic parameters of the chosen clusters. The slices of the density and temperature distributions for all clusters and their projected images in X-ray lines are shown in Fig.4.8.

From Fig.4.8, we see that the g6212 cluster is relatively cool with a maximum temperature $\sim$ 2 keV. In such clusters the lines of B-like and C-like iron and lines of lighter elements become strong. But only few of these lines have optical depth large enough for a signficant resonant scattering effect. In Table 4.3 we show the list of lines, which are the strongest in a typical cluster with mean temperature less then 2 keV and have a weight of dipole scattering $\geq$ 0.5. The optical depth presented in Table 4.3 was calculated in the line center as

$$\tau = \int\limits_{r_0}^{\infty} n_i \sigma_0 \mathrm{d}r \tag{4.14}$$
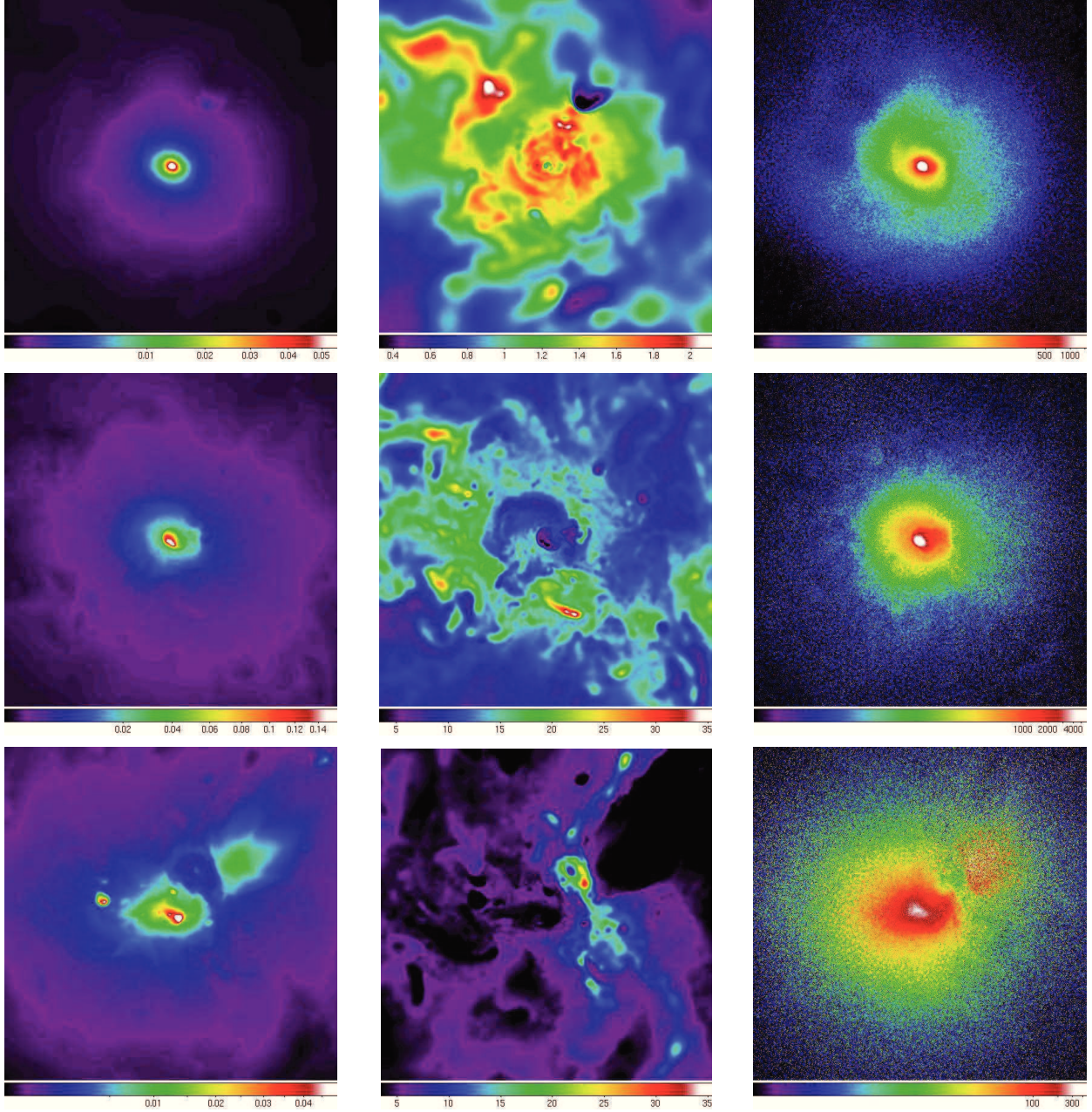
Figure 4.8: Simulated clusters g6212 (the top panels), g8 (the middle panels) and g72 (the bottom panels). Slices of the electron density in cm^{-3} are in the left column and the gas temperature in keV are in the middle column. The slices go through the center of the clusters and have an effective thickness of 3 kpc, corresponding to the size of one cell. The right panels show the projections of surface brightness (photons/s/cm^2/$arcmin^2$) on the plane perpedicular to the line of sight. For g8 and g72 clusters we consider the He-like iron line at 6.7 keV and for g6212 cluster the line of Fe XXI at 1.009 keV. The image size is 2×2 Mpc, resolution is 3.6 kpc.
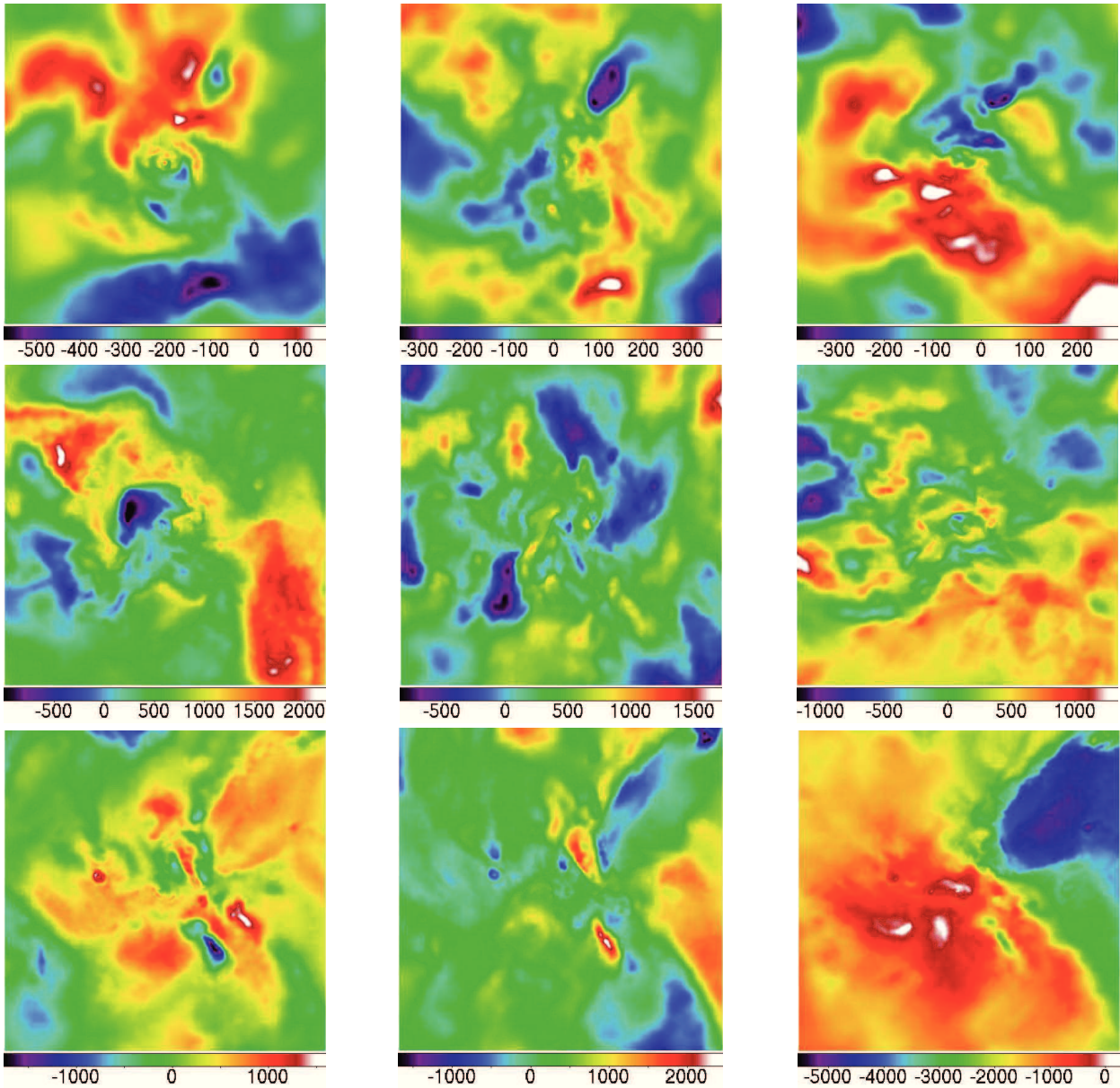
Figure 4.9: Slices of the velocity field (in km/s) in simulated clusters g6212 (the top panels), g8 (the middle panels) and g72 (the bottom panels). The right column shows x component of velocity, the middle column y component and the left column z component. The slices go through the center of the clusters and have an effective thickness of 3 kpc, corresponding to the size of one cell. The image size is 2×2 Mpc.
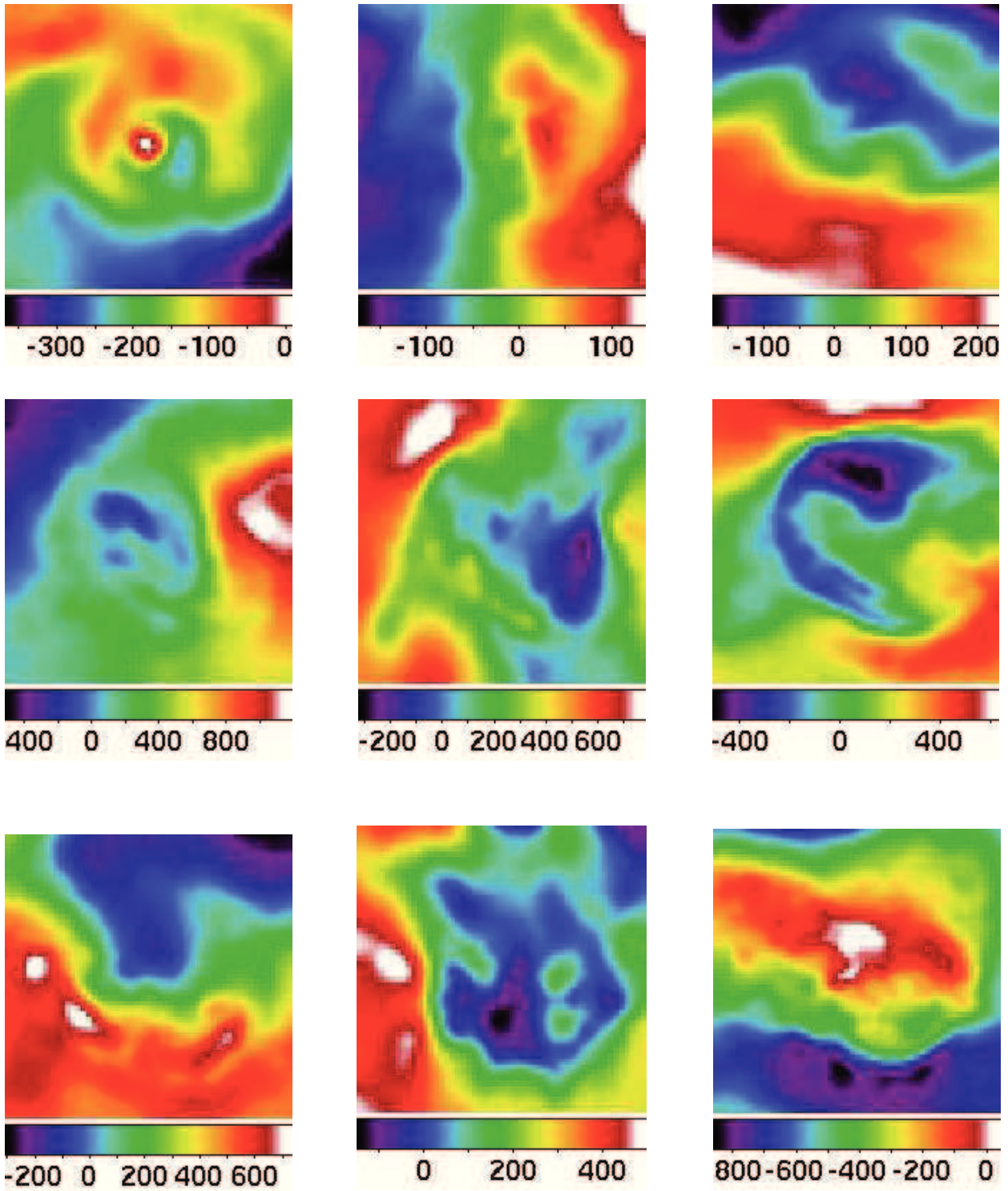
Figure 4.10: The same as in Fig.4.9, but for the central part of each cluster. The image size is 100×100 kpc.

Table 4.2: Basic properties of simulated clusters g6212, g72 and g8 at $z = 0$.

Cluster	M_{vir}, $10^{14} M_\odot$	R_{vir}, Mpc	$T_{\min}$, keV	$T_{\max}$, keV	$n_{\min}$, cm^{-3}	$n_{\max}$, cm^{-3}
g6212	1.61	1.43	0.2	2.2	$1\cdot10^{-5}$	0.1
g72	19.63	3.29	0.3	32	$7\cdot10^{-5}$	0.1
g8	32.70	3.90	3	35	$7\cdot10^{-5}$	0.2

along an arbitrary chosen radial direction, where the distance from the center $r_0 \sim 10$ kpc. We avoided integration in the very center of the cluster since the number density in few central cells and their contribution to the optical depth are very high in some of the simulated clusters. We see that for the cluster g6212 the most interesting line is the one at 1.009 keV, which corresponds to the $2s^2 2p^2(^3P_0) - 2s^2 2p 3d(^3D_1)$ transition in C-like iron and has a large optical depth and a pure dipole scattering phase function.

In the g8 cluster, the mean temperature is ~ 15 keV and the most promising lines for significant resonant scattering are: the K_α line of He-like iron at 6.7 keV and the K_α line of H-like iron at 6.96 keV. The H-like line has two components, $1s(^2S_{1/2}) - 2p(^1P_{1/2})$ at 6.95 keV and $1s(^2S_{1/2}) - 2p(^1P_{3/2})$ at 6.97 keV. The first component has an oscillator strength 0.135; the total angular momentum is equal to 1/2 both for the ground and excited states, and therefore (Hamilton, 1947) the scattering phase function is isotropic and scattered emission is unpolarized. The second component has an oscillator strength 0.265 and equal weights of dipole and isotropic scattering. The optical depth is ~ 3.56 for the line at 6.7 keV and ~ 1.14 for the line at 6.97. Therefore the highest polarization degree in the g8 cluster is expected in the 6.7 keV line of Fe XXV.

The g72 cluster is an example of a merging cluster, as is clearly seen from Fig.4.8. The mean temperature is similar to the temperature in Perseus, i.e. about 5-6 keV. Therefore the polarization degree was calculated in the 6.7 keV line of He-like iron.

The velocity field was taken directly from simulations. The slices of velocity components in all three clusters are shown in Fig.4.9. The slices go through the centers of the clusters and have a thickness of 3 kpc. The motion of a cluster as a whole was compensated for by subtracting the velocity vector corresponding to the central cell. This choice is convenient since it shows the gas velocities relative to the densest (and therefore brightest) part of the cluster, which is responsible for much of the line flux to be scattered in outer regions. To characterize the spread of velocities within the cluster we calculated mass-weighted value of the RMS of the velocity (relative to the velocity of the central cell) over entire volume of a $2 \times 2 \times 2$ Mpc cube. The RMS values are ~ 230 km/s in g6212 cluster, ~ 1000 km/s in g8 cluster and ~ 2400 km/s in g72. If instead we calculate the RMS relative to the mass-weighted mean velocity the value of RMS decreases to ~ 800 km/s for g8 cluster, ~ 200 km/s for g6212 cluster and to ~ 1400 km/s for g72 cluster. We note here that for radiative transfer calculation the value of the subtracted velocity vector is not important since the polarization signal is only sensitive to the relative velocities of different gas lumps and does not depend on the motion of the cluster as a whole. In Fig.4.10 velocities of gas

Table 4.3: Oscillator strengths and optical depths of the strongest X-ray lines with the weight of dipole scattering ≥ 0.5 in the simulated clusters g6212, g72 and g8.

Cluster	Ion	E, keV	f	w_2	τ $f=0$ $M=0$	τ $f=1$ $M=0$	τ $f=0$ $M=0.25$	τ $f=1$ $M=0.25$
g6212	Fe XXV	6.7	0.78	1	2.45	2.02	1.01	0.96
	Si XIII	1.86	0.75	1	1.78	1.47	0.96	0.88
	Fe XXII	1.0534	0.675	0.5	2.86	2.27	1.17	1.1
	Fe XXI	1.009	1.4	1	2.8	2.1	1.16	1.04
g72	Fe XXV	6.7	0.78	1	3.19	0.73	1.32	0.51
g8	Fe XXV	6.7	0.78	1	3.56	1.83	1.47	1.11
	Fe XXVI	6.97	0.265	0.5	1.14	0.52	0.47	0.34

motions in the cluster centers are shown. The size of the central region was chosen to be 100×100 kpc. Notations are the same as in Fig.4.9. The spread of velocities in the centers is lower than at the edges.

In order to see the influence of different gas motions on polarization degree, we made a number of radiative transfer simulations keeping the same density and temperature distributions, but varying the characteristic amplitude of the gas velocities. This was done by introducing a multiplicative factor f_v which is used to scale all velocities obtained from the hydrodynamical simulations. In particular $f_v = 0$ means no motions, $f_v = 1$ means the velocity field as computed in the simulations, $f_v = 2$ means doubled velocities compared to hydro simulations, etc. The second parameter characterizing the radiative transfer simulation is the level of micro-turbulence, parametrized via the effective Mach number M (see equations 4.5 and 4.6). As discussed above, increasing M causes the optical depth to decrease, leading to the decrease of the polarization signal. Thus the pair of parameters (f_v, M) completely specifies the scaling of the velocity field in a given radiative transfer run, compared to the original hydrodynamical simulations. In our simulations the values of f_v and M are treated as independent parameters, since our goal is to examine separately the impact of the large scale motions and the micro-turbulence on scattering and polarization. Strictly speaking, a more self-consistent approach would be to relate M and the spread of velocities on larger scales, resolved by the simulation, by assuming e.g. Kolmogorov scaling in a turbulent cascade.
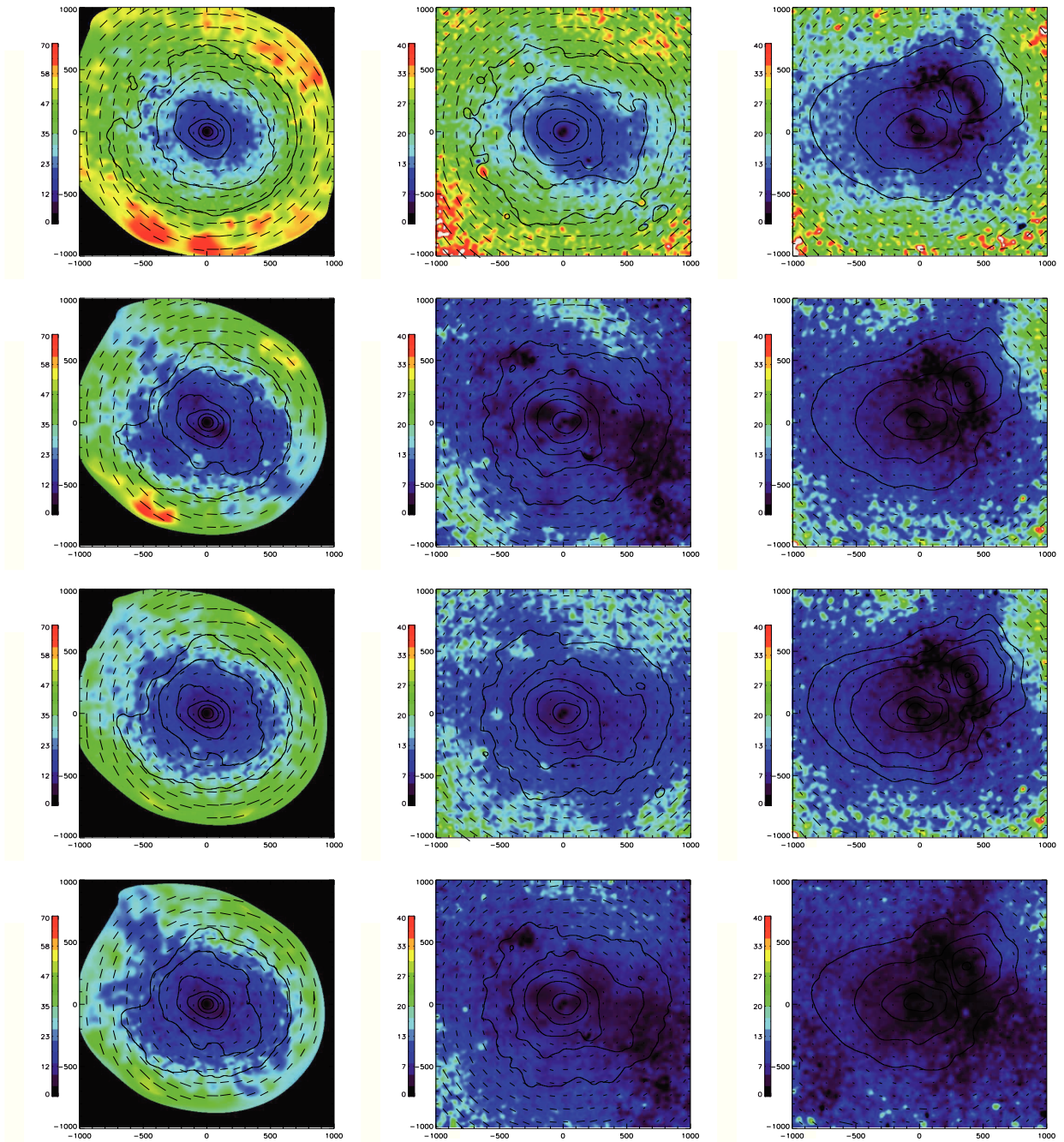
Figure 4.11: Polarization degree in simulated clusters g6212 (the left panels), g8 (the middle panels) and g72 (the right panels). For the g8 and g72 clusters, the polarization degree was calculated in the K_α line of Fe XXV at 6.7 keV and for the g6212 cluster calculations were done in Fe XXI line at 1.009 keV. The polarization degree was evaluated as $P = \sqrt{Q^2 + U^2}/I$, the value of which is shown in colorbar in percent. I is the total intensity, including scattered and direct emission. The colors in the images show polarization degree, the short dashed lines show the orientation of the electric vector. The contours (factor of 4 steps in intensity) of the X-ray surface brightness in the chosen line are superposed. The size of each picture is 2×2 Mpc. The top three pictures correspond to the case of no motion ($f_v = 0$, $M = 0$). The second raw of pictures shows the case of simulated gas motions ($f_v = 1$, $M = 0$). The third raw shows the polarization when there are only turbulent motions with Mach number $M = 0.25$ and the bottom three pictures demonstrate the case of simulated gas motions and turbulent motions ($f_v = 1$, $M = 0.25$). All results were adaptively smoothed.

The resolution of the SPH simulations used here is not fully sufficient to resolve small scale motions of the ICM. Typical resolved scales vary from few tens kpc in the center to few hundred kpc at the outskirts of simulated clusters. Our approach of "hiding" unresolved ICM motions as a micro-turbulence (i.e. as line broadening) is valid if the mean free path of the photons is larger than the resolved spatial scales. We tested this approximation for radial distances $\sim$300 kpc from the center and found that this criterion is safely satisfied. We further address this issue elsewhere (Zhuravleva et al., in preparation).

In Fig.4.11 and Fig.4.12 we show the results of radiative transfer calculations for the three clusters discussed above. Calculations are done for various combinations of the parameters f_v and M, namely ($f_v = 0, M = 0$), ($f_v = 1, M = 0$), ($f_v = 0, M = 0.25$) and ($f_v = 1, M = 0.25$). For the g6212 cluster, calculations are done for the L-shell line of C-like iron at 1.009 keV as discussed above. For the g8 and g72 clusters we analyze the Fe XXV line at 6.7 with optical depth $\sim$3.6 and $\sim$3.2 respectively. For g8 and g6212 clusters we consider multiple scattering by setting the minimum photon weight to 10^{-8} (see section 4.3). For g72 cluster (merger of two subclusters) we take into account only the first scattering. In the conditions characteristic for galaxy clusters account for multiple scattering does not have strong impact on the degree of polarization.

As expected in the very center of each cluster the radiation field is almost isotropic and the polarization degree is accordingly very low, increasing to the cluster edges.

We note here that apart from the real increase of the polarization signal towards the cluster outskirts, there are two spurious effects which lead to the increase of the polarization degree close to the edges of the simulated cube. i) The first effect is similar to the effect of finite r_{max} considered in the previous section (see Fig. 4.3): near the edges of the simulated volume, the radiation field is strongly anisotropic and the role of 90°scattering is enhanced where the line of sight is tangential to the boundary of the simulated volume. From the experiments with spherically symmetric models and the cubes of different sizes we concluded that it is safe to use the data at the projected distance approximately half of

R_{max}. For our cubes which are ~ 2 Mpc on a side, this means that the results within a 500 kpc circle (radius) are robust. ii) The second effect is caused by limited photon statistics in the regions close to the image edges, generated by our Monte-Carlo code.

The code is optimized to produce the smallest statistical uncertainties in the more central regions of simulated clusters. With only few simulated photons in the outskirts of a cluster, the derived degree of polarization can be spuriously very high - e.g. it is $\equiv 1$ if there is only one photon in a pixel. We suppress this effect by making sufficiently large smoothing windows: I, Q and U images are first smoothed and the polarization degree is calculated using smoothed images. The net result of these two effects is that outside the central 0.5 Mpc (radius) circle the estimated degree of polarization is less robust than in the inner region. As discussed below the outskirts of clusters are not a very promising target for measurements of the polarization.

In the g6212 cluster, the degree of polarization reaches 30-35% within a projected distance of ~ 500 kpc from the cluster center for the case ($f_v = 0$, $M = 0$). Adding bulk velocity from simulations and no microturbulence ($f_v = 1$, $M = 0$) causes a decrease of the optical depth from almost 3 to ~ 2, while the degree of polarization decreases to ~ 20-25%. If only turbulent motions are included ($f_v = 0$, $M = 0.25$), then the optical depth drops to ~ 1.16. The maximum polarization degree in this case is about 25% as shown in Fig.4.11. The combination of bulk velocities and micro-turbulence ($f_v = 1$, $M = 0.25$) further decreases the polarization signal and, according to our simulations, the maximum is about 15% (Fig.4.11, the bottom left panel).

In the g8 cluster, the polarization degree does not exceed 27% for the case ($f_v = 0$, $M = 0$) within 500 kpc from the cluster center. As in the previous example the gas motions affect the optical depth, diminishing it and leading to the decrease of the degree of polarization: for $f_v = 1$ the degree of polarization p is less then 10% (Fig.4.11).

For the g72 cluster the situation is similar: when there are no motions, polarization reaches $\sim 20\%$ at a distance $r = 500$ kpc from the cluster center and gas motions reduce the polarization to 7%.

The simulations discussed above are also illustrated in Fig.4.12, where radial slices of the surface brigtness and the polarization degree are shown for the same set of simulations as in Fig.4.11.

Results for various other combinations of f_v and M for the g6212 cluster are shown on Fig.4.13. Here, we show the projected polarization degree as we did in the spherically-symmetric case. The left panel shows profiles of polarization for velocity factors $f_v = 0$, 1, 2 and 5 and the right panel for Mach numbers $M = 0$, 0.25, 0.35 and 0.45. This results are in a good agreement with our predictions discussed above.

In our 3D simulations we assume a flat iron abundance profile of 0.79 solar. Any changes in the abundance profile will have an impact on the optical depth in lines and hence can affect the strength of the line scattering and the degree of polarization. Obviously, an overall decrease of the abundance will cause the decrease of the polarization signal.

An impact of a peaked abundance profile on the polarization signal is less obvious. Peaked abundance profiles are often observed in cool core clusters. The abundances vary from ~ 0.3 in the outer regions to ~ 1.2 at the center (e.g. Pratt et al., 2007). To test
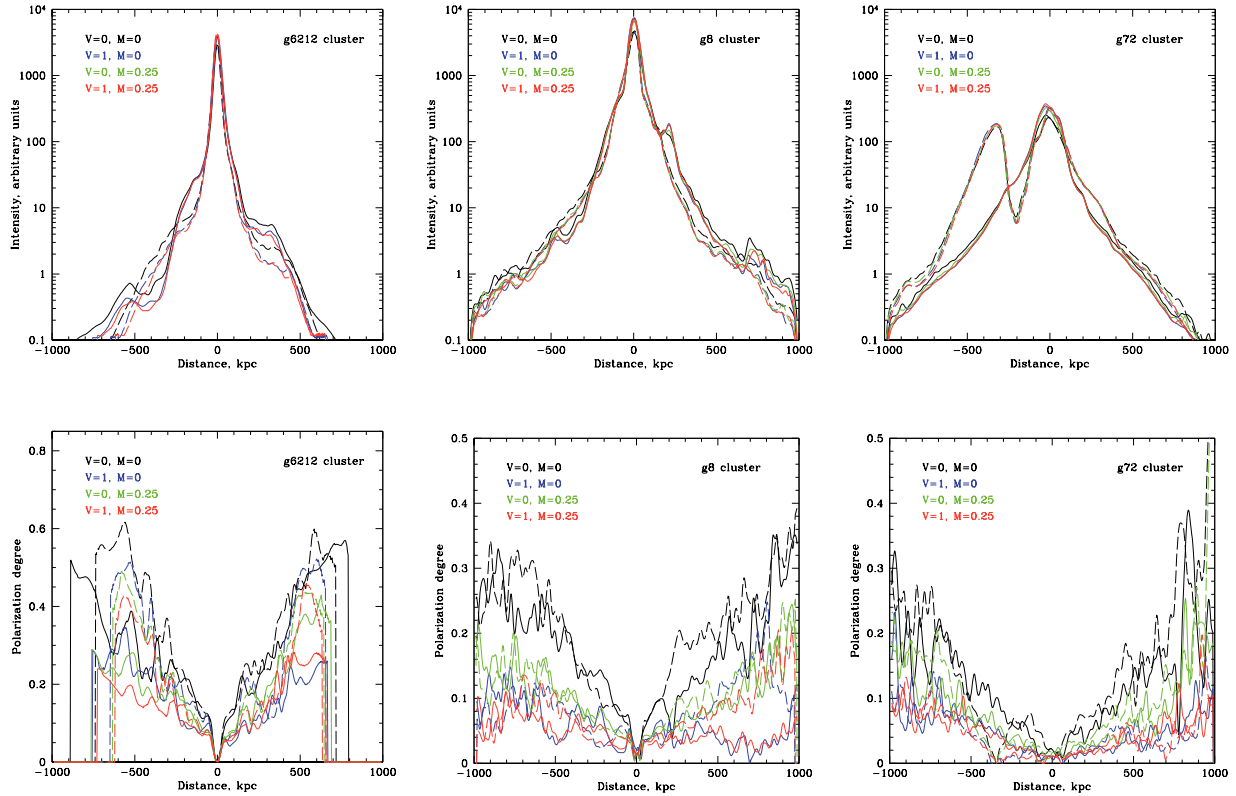
Figure 4.12: Radial slices of the surface brightness and the polarization degree for the g6212 cluster (right column), g8 cluster (middle column) and g72 cluster (left column), illustrating radial variations of these parameters for two position angles. Colors correspond to different combinations of the velocity factor f_v and the Mach number M, labels are shown in the top left corner. Solid curves show slices going from the top left conner to the bottom right conner of images shown in Fig. 4.11. The dashed curves show slices going from the top right conner to the left bottom.
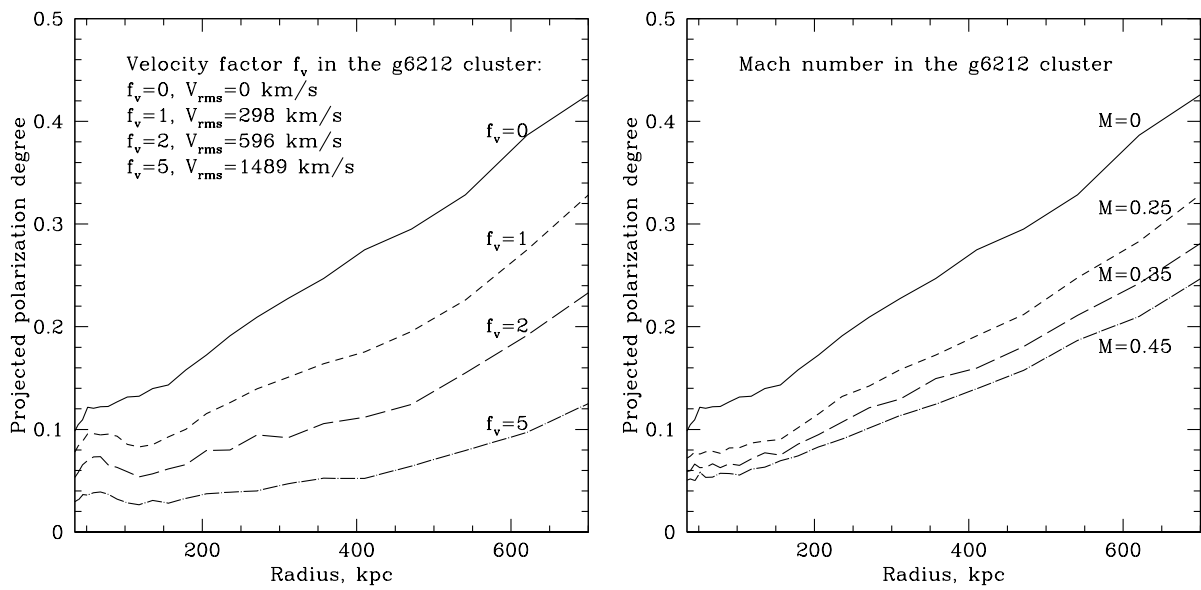
Figure 4.13: Radial profiles of polarization degree in the Fe XXI iron line at 1.009 keV for the simulated cluster g6212 for different values of velocity factors and Mach numbers. The left panel: the solid line is for (f_v=0, M=0), the short dashed line for (f_v=1, M=0), the long dashed line is for (f_v=2, M=0) and the dot-dashed line is for (f_v=5, M=0). The corresponding RMS values of the gas velocities V_{rms} in km/s are shown in the upper left corner. The right panel: the solid line is for ($f_v = 0$, $M = 0$), the short dashed line for ($f_v = 0$, $M = 0.25$), the long dashed line for ($f_v = 0$, $M = 0.35$) and the dot-dashed line for ($f_v = 0$, $M = 0.45$).

this case we consider an averaged metallicity profile for cool core clusters parametrized by De Grandi et al. (2004) as a function of r/r_{200}, where r_{200} is the radius corresponding to the mean overdensity of $200\times$ the critical density of the Universe. We used the mean temperature of simulated clusters to evaluate r_{200} and assumed that the metallicity is linearly decreasing with radius for $r < 0.15 r_{200}$ and is constant at larger radii. Rescaling the results of De Grandi et al. (2004) to the iron abundance scale of Lodders (2003) ,the final iron abundance changes from 0.85 at the center to 0.44 at large radii. Repeating the radiative transfer calculations we found only a very a slight ($\sim 10\%$) decrease of polarization degree (compared to the flat profile case) in the outer regions where the abundance has changed by almost a factor of 2: from 0.79 (flat profile) to 0.44 (peaked profile). The reason for this stability is as follows: polarized flux from outer parts of a cluster is largely due to the scattered line photons coming from the central bright region. This flux is obviously proportional to the product of the flux from the central region F_{central} and the optical depth of the outer region τ_{outer}. The optical depth in turn is proportional to the abundance Z_{outer}. The polarization signal is diluted by the flux of "locally" generated unpolarized line photons F_{outer}, which is also proportional to the abundance in the outer regions and to the product of the flux from the central region and the optical depth of the outer region, i.e. $P \approx \dfrac{a\tau_{\mathrm{outer}} F_{\mathrm{central}}}{b\tau_{\mathrm{outer}} F_{\mathrm{central}} + F_{\mathrm{outer}}}$, where a and b are some constants, which depend on the density distribution. Since both numerator and denominator scales linearly with the abundance Z_{outer} this dependence partly cancels out. In other words in the outer regions of clusters in the limit of low abundances the degree of the polarization is approximately proportional to the expression $\dfrac{\tau_{\mathrm{outer}} F_{\mathrm{central}}}{F_{\mathrm{outer}}} \propto \dfrac{Z_{\mathrm{outer}} F_{\mathrm{central}}}{Z_{\mathrm{outer}}} \approx F_{\mathrm{central}}$. Thus these two effects partly cancel each other leading to a relatively weak dependence of the degree of polarization on the abundance. In other words, the increase of the flux coming from the central region has larger impact on the polarization degree than the changes in abundance in outer regions (see also Sazonov, Churazov & Sunyaev, 2002, for the limiting case of a strong central source, when a dilution by locally produced line photons is not important).

Note, that these calculations assume that the line photons can be separated from the continuum, i.e. the energy resolution of the polarimeter is very high (see Section 4.6 for the discussion of the impact of limited energy resolution on the polarization signal).

4.5.1   Major merger

A particularly interesting case is when the polarization degree increases due to the anisotropy caused by gas motions. This can happen, for example, when gas blobs are moving in the cluster center or when two galaxy clusters are merging. The well-known example of merging clusters is the Bullet cluster in which gas motions reach velocities up to 4500 km/s. Even if the radiation field is originaly isotropic (e.g. in the very center of the galaxy cluster) the dependence of the scattering cross section on energy (see section 4.1) will produce anisotropy and polarization in the scattered radiation.
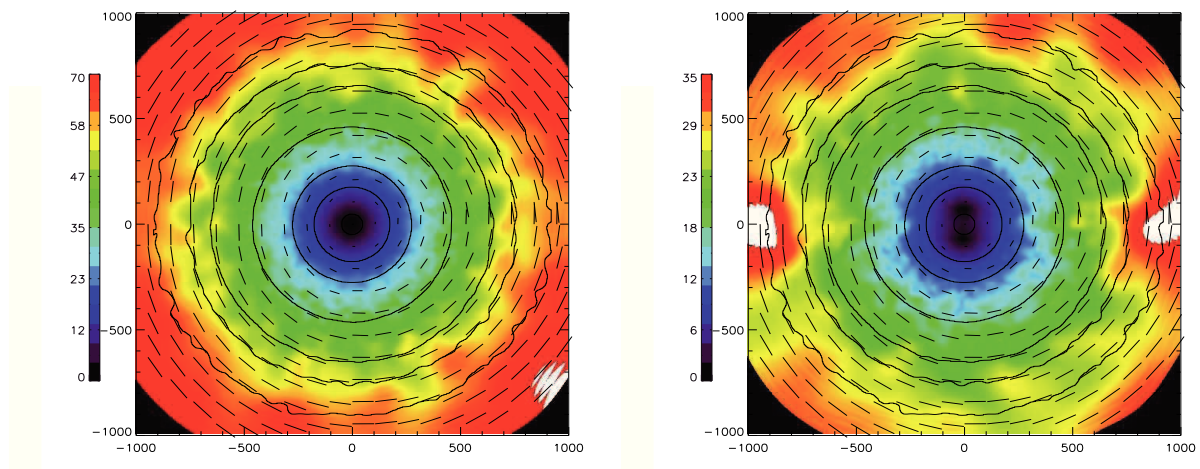
Figure 4.14: Polarization degree in a spherically-symmetric $\beta-$model galaxy cluster with $n_0 = 10^{-2}$ cm^{-3}, $r_{\rm c} = 100$ kpc, $\beta = 1$. Temperature is constant $T = 5$ keV and iron abundance is 0.79 solar. Calculations were done for the He-like iron line at 6.7 keV. The polarization degree was evaluated as $P = \sqrt{Q^2 + U^2}/I$, the value of which is shown in the colorbar in percent. I is intensity of both direct and scattered emission.The colors in the images show the polarization degree, the short dashed lines show the orientation of the electric vector. The contours of the X-ray surface brightness in the chosen line are superposed. The size of each picture is 2×2 Mpc. On the left panel are shown results when the gas is motionless. On the right panel is shown the case when two parts of the cluster are moving towards each other with velocities 500 km/s and -500 km/s respectively. In this case the asymmetry in the radiation field appears in the very center of the galaxy cluster and the polarization degree reaches about 2%.

To model the polarization from a major merger, we consider an illustrative example: two halves of galaxy cluster are moving towards each other with velocities ± 500 km/s. In such a situation, an anisotropy in the scattering cross section (see eq. 4.1) can produce polarized radiation even in the cluster center. We used a simple spherically-symmetric $\beta-$model for the density distribution $n_0 = 10^{-2}$ cm^{-3} with $r_{\rm c} = 100$ kpc, $\beta = 1$. The temperature of cluster is constant $T = 5$ keV and the iron abundance is 0.79 solar. Calculations were done for the He-like iron line at 6.7 keV. To show the sensitivity of polarization to the tangential component of gas motions, we assume that only the y-component of velocity is non-zero, while the viewing vector is along the z-axis (see, e.g. Fig.6.1). Fig.4.14 shows the results of our calculations. We see that in the case of such motions, the polarization in the center increases from 0% to 2%.

4.6   Discussion

Our results show that, owing to the asymmetry in the radiation field, the polarization for the brightest X-ray lines from galaxy clusters can reach values as high as 30%. In addition, we have shown that the polarization degree is sensitive to gas motions. Therefore, polarization measurements provide a method to estimate velocities of gas motions in the direction perpendicular to the line of sight.

One of the limiting factors which affects the expected degree of polarization is the contamination of the polarized emission in the resonant line by the unpolarized emission of the continuum emission of the ICM and neighboring lines. This factor critically depends on the energy resolution ΔE of the polarimeter. If we assume that only the emission in a given line is polarized, the measurable polarization will differ from the idealized case by a factor $f = F_{\rm line}/F_{\rm tot}$, where $F_{\rm line}$ is the flux in the resonant line and $F_{\rm tot}$ is the total flux measured by the detector in an energy band ΔE centered on the resonant line energy. In Fig.4.15 we plot this factor as a function of the width of the energy window (detector energy resolution) for different theoretical spectra for the model clusters discussed above assuming only thermal line broadening and both thermal and turbulent broadening. One can see that the contamination of the 6.7 keV line flux by the unpolarized flux is very minor for an energy resolution better than ≤ 10 eV. For the energy resolution of 100 eV the fraction of contaminating unpolarized flux is of order 30-60% depending on the plasma temperature. This line is most prominent in clusters with temperatures $\sim$ 3-6 keV as the line flux at such temperatures is the largest and neighbouring lines are not as strong as in a case of $\sim$2 keV plasmas (see the bottom left panel on Fig.4.15). For lines with energies $\sim$1 keV even better energy resolution is needed since in the spectrum there is a forest of low energy lines and the contamination from these lines dramatically decreases the flux of polarized emission (see the bottom right panel on Fig.4.15).
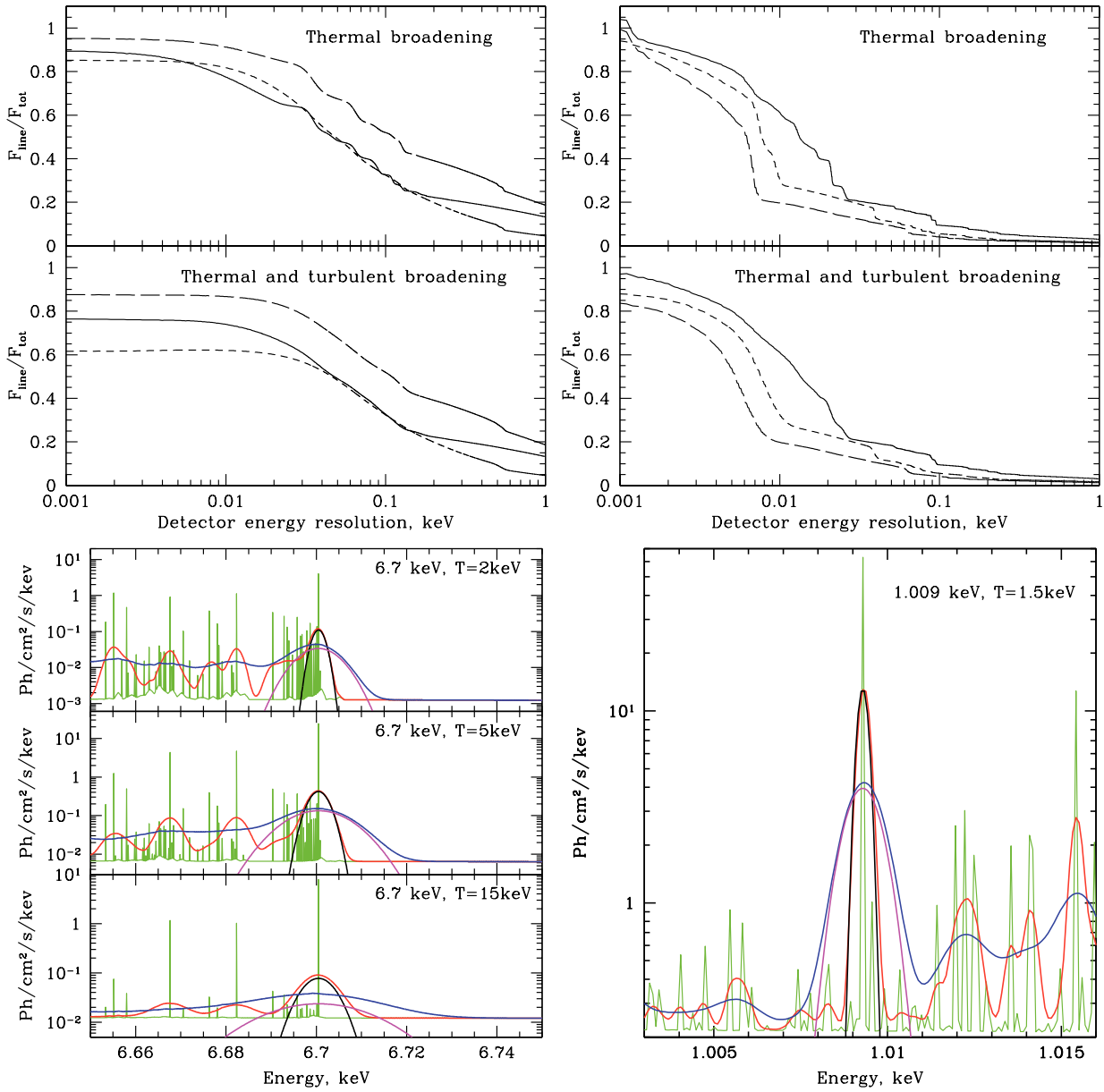
Figure 4.15: Top panel: changes of the polarization degree as a function of the instrument energy resolution. On the upper panels results are shown when only thermal broadening of lines is considered. The cases when turbulent broadening is included are shown on the lower panels. The lines in the left panel show the ratio of the resonant line flux (6.7 keV permitted line) to the total (continuum plus all lines) flux within an energy interval of a given width centered at the line energy. The solid, long dashed and short dashed lines correspond to plasma with the temperature of 2, 5 and 15 keV respectively. In the right panel similar curves are shown for the bright low energy lines: Fe XXI line at 1.009 keV (solid line), Fe XXIII line at 1.129 keV (short dashed line) and Fe XXII line at 1.053 keV (long dashed line) for the plasma with the the temperature 1.5 keV. The iron abundance is assumed to be 0.79 solar. Only the flux in the line is assumed to be polarized. Bottom panel: model spectra of the hot optically thin plasma with different temperatures.
Color coding: *Green* - spectrum with no line broadening (apec model in XSPEC). *Red* - spectrum with pure thermal line broadening (bapec model of XSPEC). *Black* - the Gaussian profile of the main line for pure thermal broadening. *Blue* - spectrum with thermal and turbulent line broadening (bapec model of XSPEC). Turbulent velocities are set to $V_{\text{turb}} = 0.25c_{\text{s}}$. *Magenta* - the Gaussian profile of the main line, accounting for the thermal and turbulent broadening. The left panel: model spectrum of cluster with temperature 2, 5 and 15 keV (the top, middle and bottom panels respectively). The main line is the Fe XXV line of He-like iron at 6.7 keV. The right panel: model spectrum for temperature 1.5 keV. The main line is the Fe XXI line at 1.009 keV.

   Another effect which also depends on the energy resolution of the polarimeter is the contamination of line flux by the contribution of the cosmic X-ray background (CXB) which starts to dominate at some distance from the galaxy cluster center. Assuming that the CXB is not resolved into individual sources by the polarimeter the contribution of the CXB starts to be the dominant source of contamination at a distance from the cluster center where the surface brightness of the cluster continuum emission matches the CXB surface brightness (at the line energy). As an illustrative example we use the results of simulations for the g6212 cluster in the Fe XXI line at 1.0092 keV, setting $f_v = 0$ and $M = 0$, and similarly for the g8 cluster in the Fe XXV line at 6.7 keV and for the g72 cluster in the same line. All clusters are placed at a distance of 100 Mpc and the energy resolution of the instrument is set to 10 eV. Using the CXB intensity from Gruber et al. (1999) (see also Churazov et al., 2007) we calculated the expected degree of polarization (Fig.4.16) including a CXB "contamination" flux $I_{CXB} \times \Delta E$. Accounting for the finite energy resolution and contamination by the ICM emission affects the polarization signal from any region of a cluster, while the CXB contribution (for an instrument with a modest energy resolution) effectively overwhelms the polarization signal in the cluster outskirts. In Fig.4.16 we show results for the g6212, g8 and g72 clusters, where the limiting factors discussed above are taken into account. According to Fig.4.15 the limiting factors due to the ICM are 0.6, 0.85 and 0.95 for g6212, g8 and g72 clusters if we assume an energy resolution of 10 eV. First we see that inclusion of the CXB reduces the very high polarization degree

in the outer parts of clusters. Second, the polarization degree is reduced everywhere by "contamination" from unpolarized radiation. Within the central region ($r \approx 500$ kpc), the polarization degree decreases from 30-35% to 20% in the g6212 cluster, from 27% to 20% in the g8 cluster. For the g72 cluster, the degree of polarization does not change significantly, since the contamination by the unpolarized radiation is small in this case.

It is also interesting to note, that when gas motions with velocities up to a few 1000 km/s exhibit, the Doppler shifts corresponding to such velocities are comparable or larger than some doublet separations (see e.g. 4.15). And flux from one line can be scattered in another neighbouring line. This can easily happen, for example, in doublet with the components at 6.97 keV and 6.93 keV.

4.7 Requirements for future X-ray polarimeters

Galaxy clusters are promising, but challenging targets for future polarimetric observations which pose requirements to essentially all basic characteristics of the telescopes, such as angular and energy resolutions, effective area and the size of the field of view. (i) First of all, in order to detect polarization in lines polarimeters should have good energy resolution to avoid contamination of the polarized line flux by the unpolarized continuum and nearby lines (Fig.4.15). (ii) An angular resolution has to be better than an arcminute even for nearby clusters. Indeed, the polarization largely vanishes when integrated over the whole cluster. For instance, the polarization of the 6.7 keV line flux, integrated over the whole cluster, is 1.2%, 0.55% and 1.2% for the g6212, g8 and g72 clusters respectively. As is clear from e.g. Fig.4.11 the polarization direction is predominantly perpendicular to the radius and the polarization degree varies with radius (see Fig.4.3). Therefore, to get most significant detection it is necessary to resolve individual wedges and to combine the polarization signal by aligning the reference frame, used for the calculations of Stokes parameters, with the radial direction. For nearby clusters (e.g. Perseus) this requires an arcminute angular resolution. (iii) Since the polarization is small in the central bright part of the cluster (e.g. Fig.4.3) the instrument should have sufficiently large effective area to collect enough photons from the cluster outskirts. (iv) For the same reason a large Field-of-View is important for collecting a large number of photons from the brightest nearby clusters like Perseus.

Currently, several polarimeters based on the photoelectric effect are actively discussed (see e.g. Muleri et al. (2008, 2007); Bellazzini et al. (2007); Jahoda et al. (2007); Soffitta et al. (2001)). These are basically gas detectors with fine 2-D position resolution to exploit the photoelectric effect. When a photon is absorbed in the gas, a photoelectron is emitted preferentially along the direction of polarization. As the photoelectron propagates its path is traced by the generated electron-ion pairs, which are amplified by a Gas Electron Multiplier (GEM) and are collected by a pixelized detector. Hence the detector sees the projection of the track of the photoelectron.

One of the polarimeters based on photoelectric effect is GEMS (Gravity and Extreme
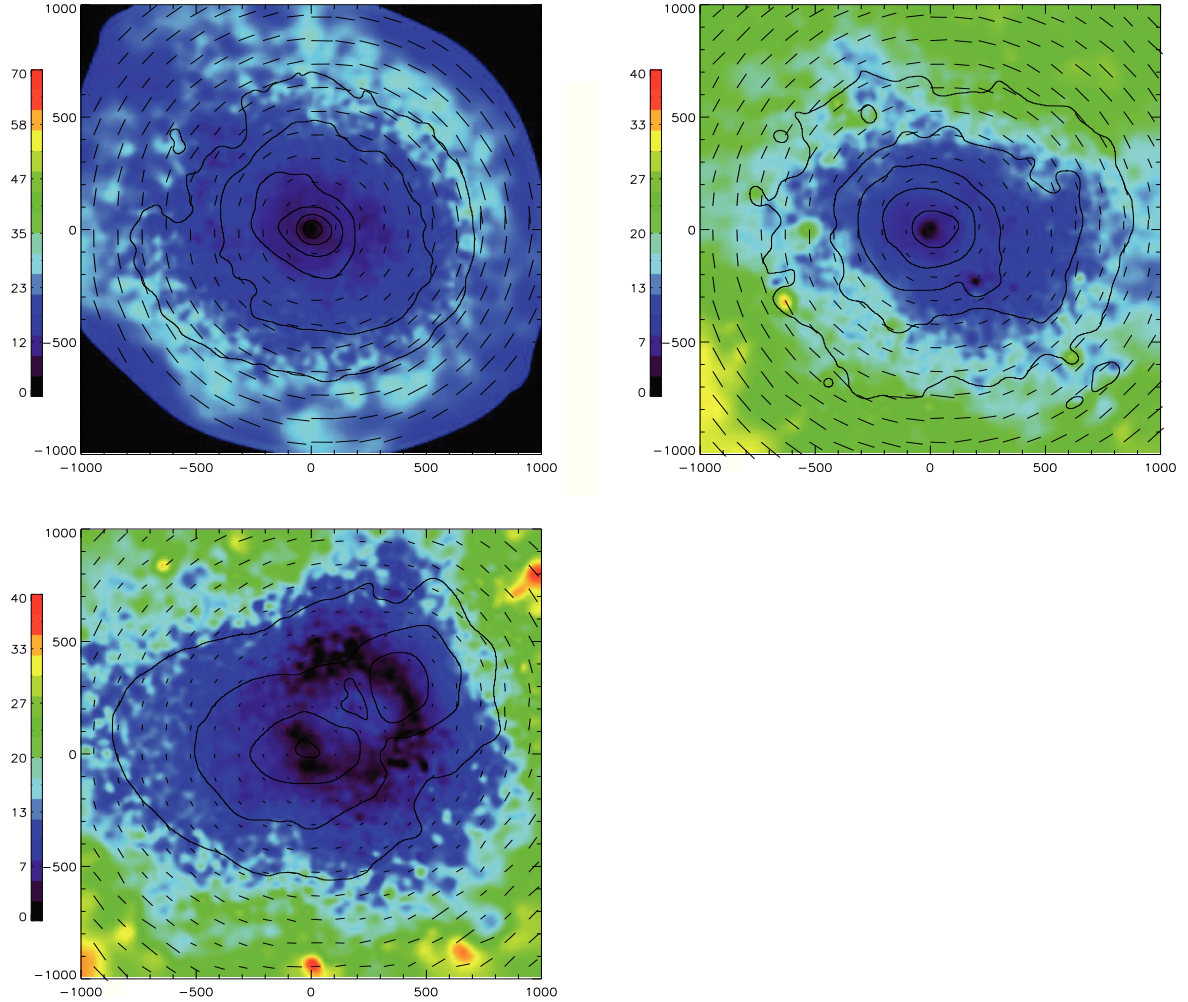
Figure 4.16: Polarization degree for simulated clusters g6212 (the top left panel), g8 (the top right panel) in the lines of Fe XXI at 1.0092 keV and Fe XXV at 6.7 keV, respectively, and for the g72 cluster (the bottom panel) in the 6.7 keV line. The polarization degree was evaluated as $P = \sqrt{Q^2 + U^2}/I$, the value of which is shown in colorbar in percent. I in a total intensity, i.e. intensity of scattered and direct emission. The colors in the images show polarization degree, the short dashed lines show the orientation of the electric vector. The contours of the X-ray surface brightness (factor of 4 steps) in the chosen line are superposed. The size of each picture is 2×2 Mpc. The gas is motionless ($f_{\rm v} = 0$, $M = 0$). The CXB radiation is included and the energy resolution is 0.01 keV. Also the decrease of polarization degree due to the continuum and neighboring non-polarized lines is taken into account. According to Fig.4.15 the limiting factor for the 1.0092 keV line in g6212 cluster is 0.6, for the 6.7 keV line in g8 cluster is 0.85 and for the same line in the g72 cluster is 0.95.

Table 4.4: The main characteristics of HXMT, IXO, GEMS and hypothetical polarimeters

	HXMT	IXO	GEMS	Hypothetical polarimeter
Mirrors Effective Area @ 6.7 keV	280 cm^2	750 cm^2	600 cm^2	1000 cm^2
Field of View	$22' \times 22'$	$2.6' \times 2.6'$	$14'$	$20' \times 20'$
Angular Resolution	$1'$	$7''$	$1.8'$[HPD]	$1'$
Energy Resolution	$\Delta E/E = 0.2$	0.2	0.2	100 eV
Modulation Factor @ 6 keV μ	0.65	0.65	0.55	0.65
Detector QE @ 6 keV	0.03	0.02	0.1	0.5

Magnetism SMEX) [5] of the NASA SMEX program. This polarimeter will provide polarization measurements in the standard 2-10 keV band with energy resolution $\Delta E/E = 0.2$, a modulation factor μ =0.55 and an effective area of ∼60 cm^2 at 6 keV.

Another proposed instrument is EXP (Efficient X-ray Photoelectric Polarimeter) polarimeter on-board HXMT (Hard X-ray Modulation Telescope). This telescope has a large field of view (FoV) $22' \times 22'$, mirrors effective area ∼280 cm^2 at 6.7 keV and the detector quantum efficiency (QE) of about 3%. The energy resolution is $\Delta E/E = 0.2$ at 6.7 keV (Costa et al., 2007; Muleri et al., 2007).

Polarimeters have been also proposed as focal plane instruments[6] for the International X-ray observatory (IXO) (Weisskopf et al., 2008).

Most important characteristics of discussed polarimeters are summarized in Table 4.4. We also show in this table the characteristics of a hypothetical polarimeter, which would be suitable for the study of polarized emission lines in galaxy clusters. The key difference of this hypothetical polarimeter with the currently discussed GEM polarimeters is the energy resolution of 100 eV and larger efficiency.

Obviously only the brightest clusters have a chance of being detected with the current generation of X-ray polarimeters. Discussed below is the case of the Perseus cluster, which is the brightest cluster in the sky and as such is the most promising target. The degree of polarization in the 6.7 keV resonant line flux is shown in Fig.4.3. While the surface brightness declines with radius, the degree of polarization is instead steadily increasing with radius. It is possible therefore that the optimal signal-to-noise ratio (S/N) is achieved at some intermediate radius. The expected modulation pattern in a given pixel of the cluster image is proportional to

$$c + \mu p c \cos(2\phi + \phi_0), \tag{4.15}$$

where c is a number of counts in this pixel, μ is a modulation factor, p and ϕ_0 are the degree of polarization and the angle of the polarization plane with respect to the reference

---

[5]http://projects.iasf-roma.inaf.it/xraypol/Presentations/
090429/morning/JSwank_GEMS.pdf

[6]E.g. http://projects.iasf-roma.inaf.it/xraypol/Presentations/
090428/afternoon/roma_09_04_sandro_Brez.pdf

coordinate system. One can fit the observed modulation pattern with a function

$$x_1 + x_2 \cos(2\phi), \qquad (4.16)$$

where x_1 and x_2 are the free parameters. In the above expression we set ϕ_0 to zero, since the polarization plane is perpendicular to the radial direction (in the first approximation) and therefore the angle is known. We assume below that for any pixel of the cluster image the reference system is aligned with the radial direction. This way the Stokes Q and U parameters obtained in individual pixel can be averaged over any region of interest. The final S/N ratio, characterizing the significance of the polarization detection from the region is

$$\left(\frac{S}{N}\right)_0 = \frac{<x_2>}{\sigma_{<x_2>}} = \mu \frac{\sum\limits_i p_i c_i}{\sqrt{2 \sum\limits_i c_i}}, \qquad (4.17)$$

where the summation is over all pixels in the region. If an unpolarized flux of the continuum and neighbouring lines is contributing to the total flux seen by the detector (see §4.6) then the S/N ratio will scale as the square root of the line and total fluxes:

$$\frac{S}{N} = \left(\frac{S}{N}\right)_0 \sqrt{\frac{F_{\text{line}}}{F_{\text{tot}}}}, \qquad (4.18)$$

where $\left(\frac{S}{N}\right)_0$ is the S/N ratio for the pure line flux.

The S/N ratio for the 6.7 keV line in Perseus is shown in Fig.4.17. For this plot we assume that a hypothetical polarimeter with the characteristics given in Table 4.4 is observing the cluster for 1 Megasecond. In the bottom panel the S/N ratio was calculated for $1' \times 1'$ square regions located at a given distance from the center of the Perseus cluster. The solid line is calculated assuming that only 6.7 keV line photons are detected (i.e. $\left(\frac{S}{N}\right)_0$), while the dashed line shows the S/N ratio for an instrument with the energy resolution of 100 eV (and therefore the continuum and nearby lines decrease the degree of polarization). In the top panel of Fig.4.17 the S/N ratio is calculated for a set of annuli with inner and outer radii $R_1 = R$ and $R_2 = 1.5 \times R$ and plotted as a function of R. In our model of the Perseus cluster its surface brightness in the outer regions is described by a β model with $\beta = 0.5$. Thus for large radii the surface brightness declines as $1/R^2$. If the solid angle of the region scales as R^2 (as is the case for the annuli used in the top panel of Fig.4.17) these two factors cancel each other and the S/N ratio as a function of radius simply follows the variations in the degree of polarization with radius (see Fig.4.3). The solid line in the top panel of Fig.4.17 again corresponds to the line photons only, while the dashed line assumes 100 eV energy resolution. Setting the energy resolution to 1 keV (realistic number for a gas detector) would decrease the S/N ratio from ∼18 to ∼8 in an annulus near $30'$.

The above analysis suggests that for an instrument with a very small FoV (few arcminutes) the optimal S/N ratio will be achieved if a region at a distance of $4' - 5'$ from the center of the Perseus cluster is observed. For a large FoV (few tens of arcminutes) the optimal strategy is to point directly at the center of the cluster and to combine the signal from the cluster outskirts.
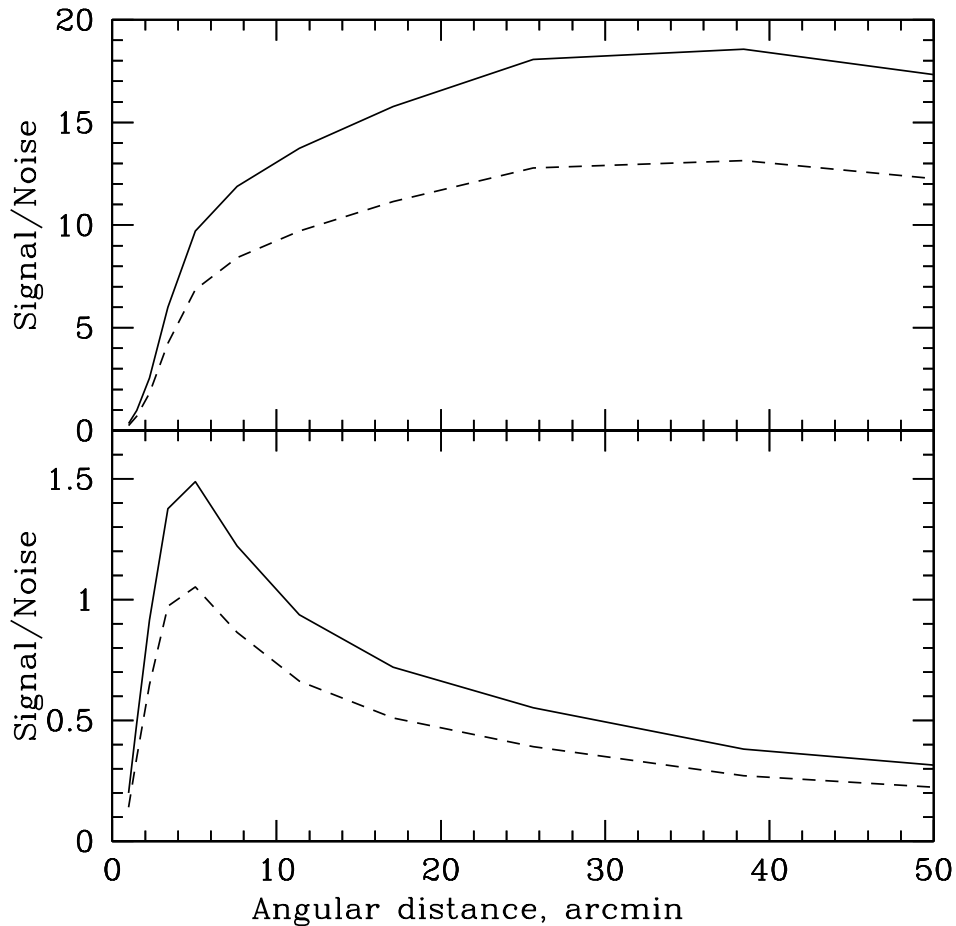
Figure 4.17: Significance of the 6.7 keV line polarization detection in Perseus cluster. For this plot we assume that a hypothetical polarimeter with characteristics listed in Table 4.4 is observing the cluster for 1 Megasecond. The solid line shows the detection significance if only line photons are detected, while the dashed line shows the S/N ratio for an instrument with the energy resolution of 100 eV (and therefore the continuum and nearby lines decrease the degree of polarization). **Top panel:** the S/N ratio is calculated using eq.(4.17) and eq.(4.18) for a set of annuli with inner and outer radii $R_1 = R$ and $R_2 = 1.5 \times R$ and plotted as a function of R. **Bottom panel:** the same as in the top panel, but for a $1' \times 1'$ square region.
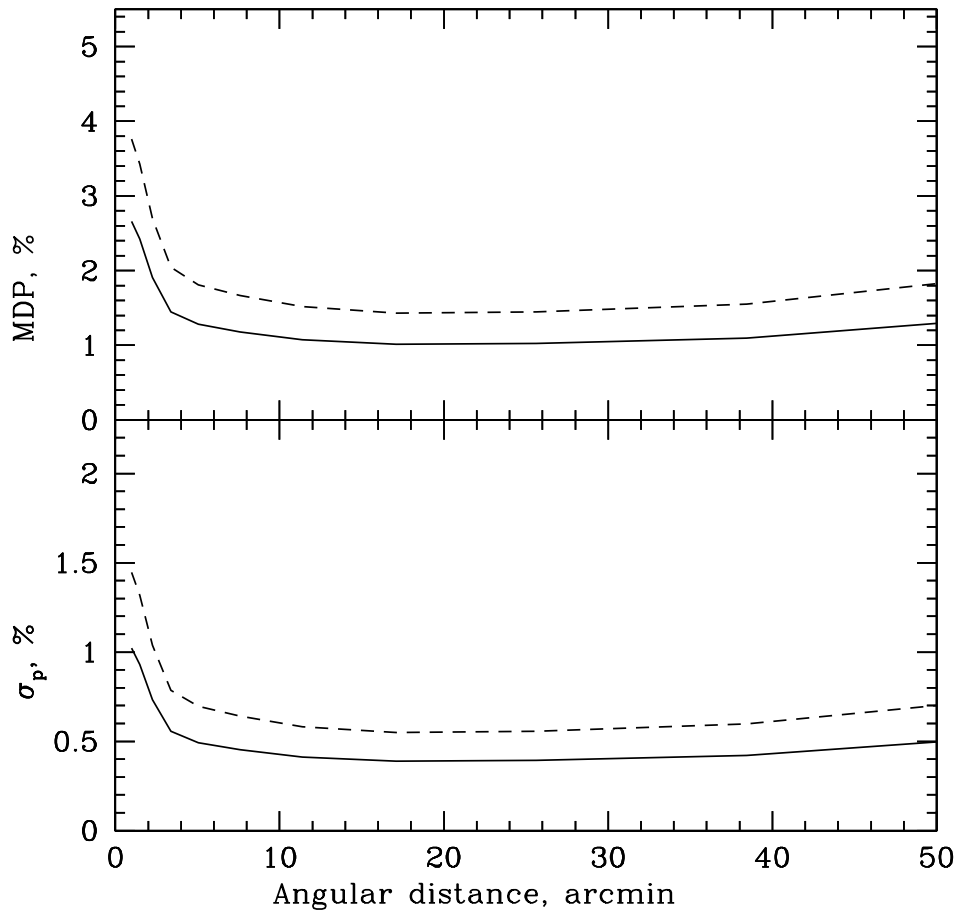
Figure 4.18: Top panel: MDP calculated using eq.4.19 in the Perseus cluster for a set of annuli with inner and outer radii $R_1 = R$ and $R_2 = 1.5 \times R$ as a function of R. The solid curve shows MDP when only flux from the line is included, the dashed curve shows the case when the unpolarized continuum is added. Characteristics of the hypothetical polarimeter were assumed (see Table 4.4)

The bottom panel: statistical uncertainty in P in the Perseus cluster. Notations are the same as in the top panel.

We can recast these results in a form of Minimum Detectable Polarization (MDP) in the line at the 90% confidence level ($S/N = 2.6$). From eq.4.18 we get

$$\mathrm{MDP_{line}} = \frac{2.6}{\mu} \sqrt{\frac{2}{\sum\limits_i c_i} \frac{F_\mathrm{tot}}{F_\mathrm{line}}} = \mathrm{MPD_0} \sqrt{\frac{F_\mathrm{tot}}{F_\mathrm{line}}}, \tag{4.19}$$

where $\mathrm{MPD_0}$ corresponds to the case when only line photons are detected. Resulting MDP is shown on the top panel of Fig.4.18. We see that outside the central $4'$ the MDP is $\sim 1.5\%$ for any annuli where the ratio of outer to inner radii is a factor of 1.5. Shown in the bottom panel of Fig.4.18 is the $1\,\sigma$ statistical error in the measured polarization signal in the line $\sigma_\mathrm{p} = \frac{\sqrt{2}}{\mu \sqrt{\sum\limits_i c_i}} \frac{F_\mathrm{tot}}{F_\mathrm{line}} = \sigma_{p,0} \sqrt{\frac{F_\mathrm{tot}}{F_\mathrm{line}}}$, where $\sigma_{p,0}$ corresponds to the case when only line photons are detected.

Assuming parameters of the hypothetical polarimeter listed in Table 4.4 we can explicitly estimate the expected polarization signal from the Perseus cluster. The FoV of the polarimeter is $20' \times 20'$ and from Fig. 4.17 we see that the maximal S/N ratio is expected for the largest annulus which still fits in the FoV, that is with $R \approx 10'$. From Fig. 4.3 we see that at this distance ($10'$ corresponds to ~ 200 kpc for the Perseus cluster) the degree of polarization in the 6.7 keV line flux is about 6%. For the annuli with $R = 10'$ the expected statistical error is 0.6% (Fig. 4.18; bottom panel, dashed line, assuming 100 eV energy resolution). Thus the expected polarization signal in the direction perpendicular to the center of the Perseus cluster is $6\% \pm 0.6\%$[7].

From Table 4.4 we see that two key requirements should be improved to detect polarization from galaxy clusters: detector quantum efficiency and energy resolution. One possibility to achieve good energy resolution is to use narrow-band dichroic filters[8] (Martindale et al., 2007; Bannister et al., 2006). In such instruments the polarization sensitivity arises from the difference in transmission of a family of materials which exhibit dichroism in narrow (~ 10 eV) energy bands close to atomic absorption edges, where the electron is excited into a bound, molecular orbital. The simplicity of such a device makes it an interesting option for future X-ray observatories as it decouples the polarization sensitivity from the intrinsic efficiency of the detector. Effective area is defined by mirrors of the telescope, energy resolution by a bolometer. Hence, the resulting polarimeter can achieve quantum efficiency close to $\sim 100\%$ and thus such filters may offer a simple and compact method of measuring X-ray polarization. The only problem is that narrow-band polarimeters operate only at a certain energy and we have to select the appropriate filter material and redshift of the cluster in order to study a certain line. For example, if a filter based on the K-edge of Mn at 6539 eV is feasible then it would be possible to study the polarization degree in the 6.7 keV line in nearby clusters at a redshift of $z \approx 0.024$.

---

[7]We emphasize again that this estimate refers to the polarization perpendicular to the direction towards the center of the cluster.

[8]http://projects.iasf-roma.inaf.it/xraypol/Presentations/
090427/Morning/XpolRoma_Fraser.pdf

A Bragg polarimeter could be another possibility. In the soft band (below 1 keV) there are strong resonant lines emitted by relatively cool gas of elliptical galaxies. For a plasma with temperature below 0.4-0.5 keV the lines of oxygen and nitrogen are extremely strong. However elliptical galaxies usually contain somewhat hotter gas ($T \geq 0.6$ keV). At these temperatures, the lines of Fe XVII and Fe XVIII, rather than N and O lines, become very strong. We performed calculations for a set of elliptical galaxies and found a polarization degree of $\sim 20\%$ in the line of Fe XVIII at 0.8 keV in the galaxy NGC1404. The degree of polarization increases rapidly with radius and reached a maximum at $r \sim 10$ kpc. If the Bragg angle can be changed (by tilting the scattering surface) to probe several lines in the 0.8-1 keV region then such instrument could be useful for studies of elliptical galaxies.

4.8   Acknowledgements

Bibliography

Anders E., Grevesse N., 1989, Geochim. Cosmochim. Acta, 53, 197

Asplund M., Grevesse N., Jacques Sauval A., 2006, NuPhA, 777, 1

Bannister N.P., et al., 2006, Exp. Astron., 21:1-12

Bellazzini R., et al., 2007, NIMPA, 579, 853

Cavaliere A., Fusco-Femiano R., 1976, A&A, 49, 137

Chandrasekhar S., 1950, Radiative Transfer, Oxford, Clarendon Press, 1950

Churazov E., Forman W., Jones C., Böhringer H., 2003, ApJ, 590, 225

Churazov E., Forman W., Jones C., Sunyaev R., Böhringer H., 2004, MNRAS, 347, 29

Churazov E., Forman W., Vikhlinin A., Tremaine S., Gerhard O., Jones C., 2008, MNRAS, 388, 1062

Churazov E., et al., 2007, A&A, 467, 529

Costa E., et al., 2007, UV, X-Ray, and Gamma-Ray Space Instrumentation for Astronomy XV, eds H.O.Siegmund, proc. of the SPIE, v. 6686, 66860Z

De Grandi S., Ettori S., Longhetti M., Molendi S., 2004, A&A, 419, 7

Dolag K., Vazza F., Brunetti G., Tormen G., 2005, MNRAS, 364, 753

Dolag K., Borgani S., Murante G., Springel V., 2008, arXiv, arXiv:0808.3401

Fabian A. C., 1994, ARA&A, 32, 277

Forman W., et al., 2005, ApJ, 635, 894

Forman W., et al., 2007, ApJ, 665, 1057

Forman W. R., et al., 2009, AAS, 41, 338

Gilfanov M. R., Sunyaev R. A., Churazov E. M., 1987, SvAL, 13, 3

Gruber D. E., Matteson J. L., Peterson L. E., Jung G. V., 1999, ApJ, 520, 124

Hamilton D. R., 1947, ApJ, 106, 457

Iapichino L., Niemeyer J. C., 2008, MNRAS, 388, 1089

Inogamov N. A., Sunyaev R. A., 2003, AstL, 29, 791

Jahoda K., Black K., Deines-Jones P., Hill J. E., Kallman T., Strohmayer T., Swank J. H., 2007, arXiv:astro-ph/0701090

Lodders K., 2003, M&PSA, 38, 5272

Markevitch M., Gonzalez A. H., Clowe D., Vikhlinin A., Forman W., Jones C., Murray S., Tucker W., 2004, ApJ, 606, 819

Martindale A., et al., 2007, UV, X-ray and Gamma-ray Space Instrumentation for Astronomy XV, eds Oswald H.W. Siegmund, proc. of the SPIE, 6686, 66860X

Mazzotta P., Mazzitelli G., Colafrancesco S., Vittorio N., 1998, yCat, 413, 30403

Mitsuda K., 2009, hrxs.conf, eds G. Branduardi-Raymont, A. Blustin, proc. of the international workshop held at the Mullard Space Science Laboratory of University College London, E28

Mitsuda K., Kelley R., McCammon D., Herder J., Ohashi T., 2008, Journal of Low Temperature Physics, v. 151, 703

Muleri F., et al., 2007, UV, X-Ray, and Gamma-Ray Space Instrumentation for Astronomy XV, eds H.O.Siegmund, proc. of the SPIE, v. 6686, 668610

Muleri F., et al., 2008, Space Telescopes and Instrumentation 2008: Ultraviolet to Gamma Ray, eds J.L.Turner,K.A.Flanagan, proc. of the SPIE, v. 7011, 70112A

Porquet D., Mewe R., Dubau J., Raassen A. J. J., Kaastra J. S., 2001, A&A, 376, 1113

Pozdniakov L. A., Sobol I. M., Sunyaev R. A., 1983, ASPRv, 2, 189

Pratt G. W., Böhringer H., Croston J. H., Arnaud M., Borgani S., Finoguenov A., Temple R. F., 2007, A&A, 461, 71

Sarazin C. L., 1996, UV and X-ray Spectroscopy of Astrophysical and Laboratory Plasmas : proc. of the Eleventh Colloquium on UV and X-ray, eds K. Yamashita and T. Watanabe, 9

Sazonov S. Y., Churazov E. M., Sunyaev R. A., 2002, MNRAS, 333, 191

Sazonov S. Y., Sunyaev R. A., 1999, MNRAS, 310, 765

Smith R. K., Brickhouse N. S., Liedahl D. A., Raymond J. C., 2001, ApJ, 556, L91

Soffitta P., et al., 2001, NIMPA, 469, 164

Soffitta P., et al., 2008, Space Telescopes and Instrumentation 2008: Ultraviolet to Gamma Ray, eds J.L.Turner, K.A.Flanagan, proc. of the SPIE, v. 7011, 701128

Springel V., Yoshida N., White S. D. M., 2001, NewA, 6, 79

Syunyaev R. A., 1982, SvAL, 8, 175

Sunyaev R. A., Norman M. L., Bryan G. L., 2003, AstL, 29, 783

Sunyaev R. A., Zeldovich I. B., 1980, MNRAS, 190, 413

Vazza F., Brunetti G., Kritsuk A., Wagner R., Gheller C., Norman M., 2009, A&A, 504, 33

Weisskopf M. C., et al., 2008, Space Telescopes and Instrumentation 2008: Ultraviolet to Gamma Ray, eds J.L.Turner K.A.Flanagan, proc. of the SPIE, 7011, 70111I

Werner N., Böhringer H., Kaastra J. S., de Plaa J., Simionescu A., Vink J., 2006, A&A, 459, 353

Werner N., Zhuravleva I., Churazov E., Simionescu A., Allen S. W., Forman W., Jones C., Kaastra J. S., 2009, MNRAS, 398, 23

Chapter 5

Constraints on the ICM velocity power spectrum from the X-ray lines width and shift

I.Zhuravleva, E.Churazov, A.Kravtsov, R.Sunyaev

Abstract. Future X-ray observations of galaxy clusters by high spectral resolution missions will provide spatially resolved measurements of the energy and width for the brightest emission lines in the intracluster medium (ICM) spectrum. In this paper we discuss various ways of using these high resolution data to constrain velocity power spectrum in galaxy clusters. We argue that variations of these quantities with the projected distance R in cool core clusters contain important information on the velocity field length scales (i.e. the size of energy-containing eddies) in the ICM. The effective length $l_{\rm eff}$ along the line of sight, which provides dominant contribution to the line flux, increases with R, allowing one to probe the amplitude of the velocity variations at different spatial scales. In particular, we show that the width of the line as a function of R is closely linked to the structure function of the 3D velocity field. Yet another easily obtainable proxy of the velocity field length scales is the ratio of the amplitude of the projected velocity field (line energy) variations to the dispersion of the velocity along the line of sight (line width). Finally the projected velocity field can be easily converted into 3D velocity field, especially for clusters like Coma with an extended flat core in the surface brightness. Under assumption of a homogeneous isotropic Gaussian 3D velocity field we derived simple expressions relating the power spectrum of the 3D velocity field (or structure function) and the observables. We illustrate the sensitivity of these proxies to changes in the characteristics of the power spectrum for a simple isothermal β-model of a cluster. The uncertainties in the observables, caused by stochastic nature of the velocity field, are estimated by making multiple realizations of the random Gaussian velocity field and evaluating the scatter in observables. If large scale motions are present in the ICM these uncertainties may dominate the statistical errors of line width and shift measurements.
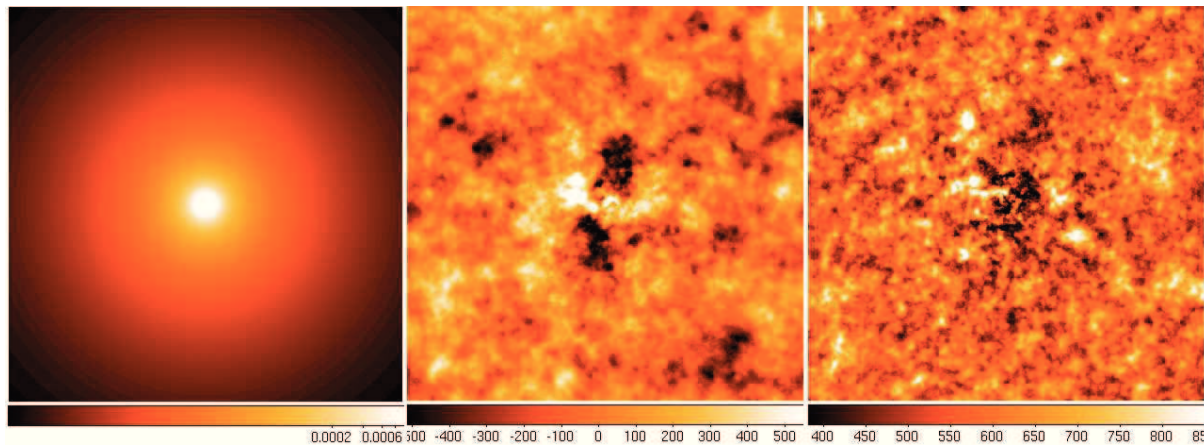
Figure 5.1: Maps of observables. Left: surface brightness in line (arbitrary units); middle : emissivity-weighted projected velocity field in km/s (centroid shift of the line); right: velocity dispersion in km/s (line broadening). Here we consider only the velocity component along the line of sight. We assume β-model of the emissivity with $\beta = 0.6$ and $r_c = 10$ kpc and a random, uniform and homogeneous Gaussian velocity field with cored power 3D power spectrum (eq. 5.37) with $k_m = 0.005$ kpc^{-1} and Kolmogorov slope $\alpha = -11/3$ (see Section 2). The size of each map is 1Mpc×1Mpc.

5.1 Introduction

Properties of gas motions in the hot intracluster medium (ICM) are still little known. It is believed that turbulent motions are driven when matter accretes onto the filaments or during shocks in the hot gas. Turbulence transfer kinetic energy injected on large scales $L \sim$ Mpc to small (unknown) dissipative scales l. These two scales are connected with a cascade of kinetic energy, which occurs over inertial range (Kolmogorov, 1941; Landau & Lifshitz, 1966).

Knowing the properties of gas motions in clusters, we would be able to address a number of important question, e.g., what is the bias in the cluster mass measurements based on hydrostatic equilibrium and whether the bias is due to the motions alone or due to the clumping in gas density (see, e.g., Rasia et al., 2006; Nagai, Vikhlinin, & Kravtsov, 2007; Jeltema et al., 2008; Lau, Kravtsov, & Nagai, 2009), what is the ICM turbulent heating rate in clusters (e.g. Churazov et al., 2008) and what is the role of gas motions in particle acceleration (see, e.g. Brunetti, 2006; Brunetti & Lazarian, 2011).

Properties of turbulence in galaxy clusters were studied by means of numerical simulations (e.g., Dolag et al., 2005; Cassano & Brunetti, 2005; Norman & Bryan, 1999; Iapichino et al., 2011; Vazza et al., 2011). However despite the good "global" agreement between all simulations, the results on turbulent motions are still controversial, mainly due to insufficient resolution of simulations and, in particular, low Reynolds number (effective $Re < 1000$ in cosmological simulations) and other numerical issues (see, e.g., Kitsionas et al., 2009; Dobler et al., 2003; Beresnyak & Lazarian, 2009).

Current generation of X-ray observatories cannot provide robust direct measurements of turbulence in the ICM. Only XMM RGS grating can provide weak upper limits on velocity amplitude in cool core clusters (Sanders, Fabian, & Smith, 2011). Indirect indications of the ICM turbulence come from measurements of the resonant scattering effect (e.g. Churazov et al., 2004; Werner et al., 2009), from measurements of pressure fluctuations (Schuecker et al., 2004) or surface brightness fluctuations (Churazov et al., 2011)

Future X-ray observatories, such as *Astro-H*[1] and *ATHENA*[2], with their high energy resolution will allow us to measure shifts and broadening of individual lines in spectra of galaxy clusters with high accuracy. Combination of direct measurements of velocity amplitudes with indirect measurements via resonant scattering will give us constraints on anisotropy of motions (Zhuravleva et al., 2011). X-ray polarimetric measurements can also provide information on gas motions perpendicular to the line of sight (Zhuravleva et al., 2010).

Here we discuss the possibility of getting information about the length scales of gas motions (e.g. the size of energy-containing eddies). We discuss various ways to constrain structure function and power spectrum of gas motions via measurement of the projected velocity (shift of the line centroid) and the velocity dispersion (broadening of the line) as a function of projected distance from the cluster center. These ideas are illustrated with a very simple model of a galaxy cluster. An application of our methods to simulated galaxy clusters will be considered in future work.

A similar problem of constraining the structure function of turbulence through the observed line width has been discussed in the context of Galactic inter stellar medium. In particular, it was shown that the width of molecular spectral lines increases with the size of a cloud (see, e.g., Myers et al., 1978; Heyer & Brunt, 2004; Heyer et al., 2009). This correlation was interpreted in terms of turbulent velocity spectrum (Larson, 1981). A way to constrain structure function of turbulence in the ISM by means of velocity centroids (mean velocity) was considered by Scalo (1984) (see also Esquivel & Lazarian, 2005; Esquivel et al., 2007).

The structure of the paper is as follows. In Section 2 we describe and justify models and assumptions we use in our analysis. In Section 3 we specify observables which can be potentially measured and their relation to the 3D velocity power spectrum. Section 4 shows the relation between observed velocity dispersion and the structure function of the velocity field. A way to constrain length scales (size of the energy containing eddies) of motions using observed projected velocity is presented in Section 5. Method to recover 3D velocity PS from 2D projected velocity field is discussed in Section 6. Discussions and conclusions are in Sections 7 and 8 respectively.

---

[1]http://astro-h.isas.jaxa.jp/
[2]http://sci.esa.int/ixo
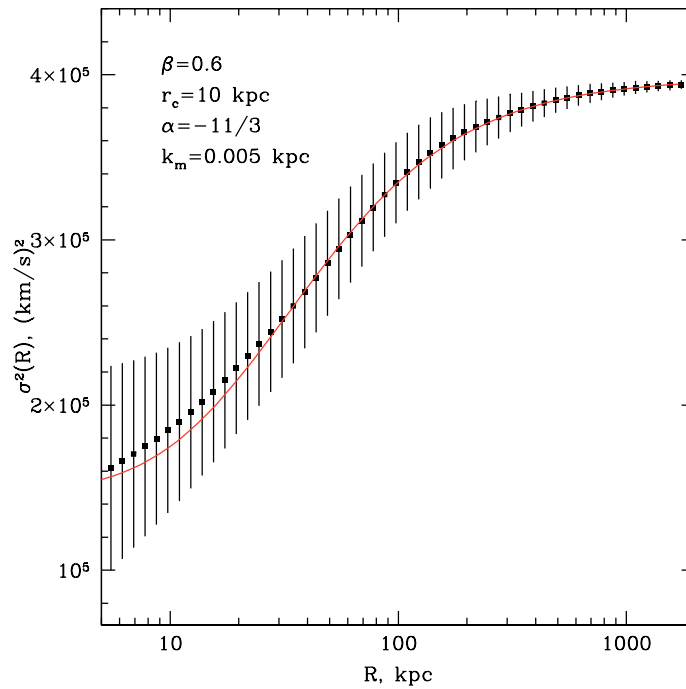
Figure 5.2: Expected dependence of the line-of-sight velocity dispersion (line width) on the projected distance R from the cluster center. The increase of the effective length along the line of sight with the projected distance R implies that larger and larger eddies contribute to the observed line broadening. We assume a β model of the density distribution in an isothermal galaxy cluster (eq. 5.1) and a cored 3D power law model of the velocity power spectrum with slope α and break at $k = k_m$ (eq. 5.2). Parameters are shown on the top left corner of the plot. Black dots with error bars: velocity dispersion with uncertainties in a single realization, obtained by averaging over 100 realizations (the left part of eq. 5.5), red curve: analytic expression of the velocity dispersion (the right hand side of eq. 5.5, see Appendix 5.10.2).
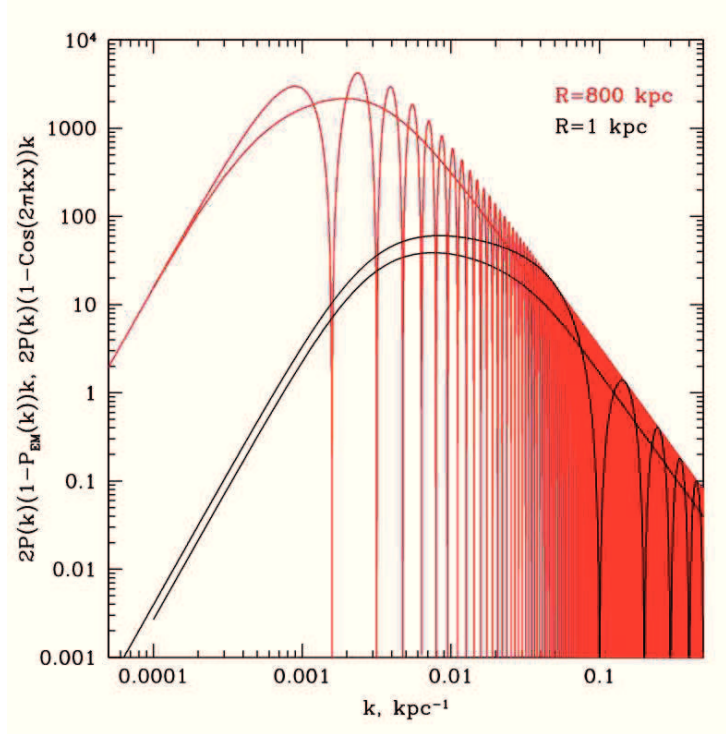
Figure 5.3: Integrand from eq. 5.8 multiplied by k (oscillating function) and integrand from eq. 5.9 multiplied by 2k (non-oscillating function) calculated for projected distance $R = 1$ kpc (black curves) and $R = 800$ kpc from the center (red curves). The scales $\left(l \propto \dfrac{1}{k}\right)$ where these functions have maxima provide dominant contribution to the line-of-sight velocity dispersion and structure function. The shift of the dominant scale to smaller k at large projected distances shows that different parts of the power spectra are probed with $\sigma^2(R)$ measured at different R. The shift of the dominant scale in the $SF(l_{\text{eff}}(R))$ traces the similar shift for $\sigma^2(R)$. This suggests that $\sigma^2(R)$ measurements can be used as a proxy for the structure function at a range of scales.

5.2   Basic assumptions and models

We consider a spherically symmetric galaxy cluster, which has a peaked X-ray emissivity profile. The electron number density is described by the β-model profile

$$n_e(r) = \frac{n_0}{\left[1 + \left(\dfrac{r}{r_c}\right)^2\right]^{\frac{3}{2}\beta}}, \tag{5.1}$$

where n_0 is the electron number density in the cluster center (normalization) and r_c is the core radius. The β-model provides a reasonably good description of observed surface brightness (Cavaliere & Fusco-Femiano, 1978) in the central regions of galaxy clusters. At large radii $\beta-$ model is not a good description of surface brightness (see e.g. Vikhlinin et al., 2006). However the simplicity of the model allows us to illustrate the method and make analytical calculations.

We have chosen $\beta = 0.6$ and $r_c = 10$ kpc for demonstration of our analysis. Parameter β usually varies $0.4 < \beta < 1$ for galaxy clusters (see, e.g., Chen et al., 2007), herewith a large fraction of clusters have $\beta \sim 0.6$. r_c can vary from few kpc to few hundreds kpc. In order to better illustrate the main idea of the method, we considered cool-core clusters with small core radius r_c (it is necessary to have a gradient of surface brightness down to the smallest possible projected distances, see Section 4 for details).

We describe the line-of-sight component of the 3D velocity field as a Gaussian isotropic and homogeneous random field. This assumption is a strong one, however the goal of our study is to gauge whether useful statistics could in principle be obtained. As the next step we will apply this method on clusters from cosmological simulations.

Power spectrum (PS) of velocity field is described by a cored power law model [3]

$$P_{3D}(k_{\mathrm{x}}, k_{\mathrm{y}}, k_{\mathrm{z}}) = \frac{B}{\left(1 + \dfrac{k_x^2 + k_y^2 + k_z^2}{k_{\mathrm{m}}^2}\right)^{\alpha/2}}, \tag{5.2}$$

where k_{m} is a break wavenumber (in our simple model k_{m} characterizes the injection scale), α is a slope of the PS at $k > k_{\mathrm{m}}$ (inertial range) and B is the PS normalization, which is defined so that the characteristic amplitude A of velocity fluctuations at $k = k_{\mathrm{ref}}$ is fixed, i.e.

$$B = \frac{A^2}{4\pi k_{\mathrm{ref}}^3 P_{3D}(k_{\mathrm{ref}})}. \tag{5.3}$$

The cored power law model of the PS is a convenient description of the PS for analytical calculations and at the same time resembles widely used broken power law model.

Now let us specify the choice of parameters α and k_m in the model of the velocity PS. Cluster mergers, motions of galaxies and AGN feedback lead to turbulent motions with

---

[3]Here and below we adopt the relation between a wavenumber k and a spatial scale x as $k = 1/x$ (without a factor 2π).

eddy sizes ranging from Mpc near the virial radius down to few tens of kpc near the cluster core (see, e.g., Sunyaev, Norman, & Bryan, 2003). For our analysis we vary injection scales from 20 kpc ($k_m = 0.05$ kpc^{-1}) to 2000 kpc ($k_m = 0.0005$ kpc^{-1}).

Parameter α - the slope of the PS - can be selected using standard arguments. If most of the kinetic energy is on large scales (injection scales), i.e. the characteristic velocity V decreases with k then the power spectrum $PS = V^2/k^3 \propto k^\alpha$ with $\alpha \leq -3$. At the same time the turnover time of large eddies should not be larger than the turnover time of small eddies, i.e $t = l/V = 1/(kV)$ is a decreasing function of the wavenumber k. Therefore, $V \propto k^\gamma$ with $\gamma \geq -1$ and $PS \propto V^2/k^3 \propto k^\alpha$ with $\alpha \geq -5$. So we expect the slope of the PS to be in the range $-5 \leq \alpha \leq -3$. We will use $\alpha = -11/3$ (slope of the Kolmogorov PS), $\alpha = -4$ and $\alpha = -4.5$.

5.3   Observables and 3D velocity power spectrum

Gas motions in relaxed galaxy clusters are predominantly subsonic, and to the first approximation the width and centroid shift of lines measured with X-ray observatories contain most essential information on the ICM velocity field (see, e.g., Inogamov & Sunyaev, 2003; Sunyaev, Norman, & Bryan, 2003). That is, we have information about:

(i) surface brightness in lines (Fig. 5.1, left panel), i.e. $I(x,y) \propto \int n_e^2(x,y,z)dz$ if one assumes isothermal galaxy cluster (effects of non-constant temperature and abundance of elements are discussed in Section 6),

(ii) emissivity-weighted projected velocity (Fig. 5.1, middle panel) $V_{2D}(x,y) = \dfrac{\int V(x,y,z)n_e^2(z)dz}{\int n_e^2(z)dz}$ (in practice measured projected velocity is averaged over some finite solid angle, see Section 5),

(iii) emissivity-weighted velocity dispersion (Fig. 5.1, right panel) $\sigma(x,y) = \sqrt{\langle V^2(x,y,z)\rangle_z - \langle V(x,y,z)\rangle_z^2} = \sqrt{\langle V^2(x,y,z)\rangle_z - V_{2D}^2(x,y)}$,
where n_e denotes the number electron density and V is a velocity component along the line of sight. Here $\langle\rangle_z$ denotes emissivity-weighted averaging along the line of sight, which we assume to be along z direction.

Relation between the PS of the 3D velocity field, the 2D projected velocity and the velocity dispersion for a line of sight with projected coordinates (x,y) are the following:

$$\langle|\hat{V}_{2D}(k_x, k_y, x, y)|^2\rangle = \int P_{3D}(k_x, k_y, k_z)P_{EM}(k_z, x, y)dk_z \qquad (5.4)$$

and

$$\langle\sigma^2(x,y)\rangle = \int P_{3D}(k_x, k_y, k_z)(1 - P_{EM}(k_z, x, y))dk_x dk_y dk_z, \qquad (5.5)$$

where $\langle\rangle$ is the ensemble averaging over a number of realizations, $\langle|\hat{V}_{2D}(k_x, k_y, x, y)|^2\rangle$ is an expectation value of the 2D PS of the observed projected velocity field $V(x,y)$, P_{3D} is the PS of the 3D velocity field and P_{EM} is the PS of normalized emissivity distribution along the line of sight. For more details see Appendixes 5.10.1 and 5.10.2.
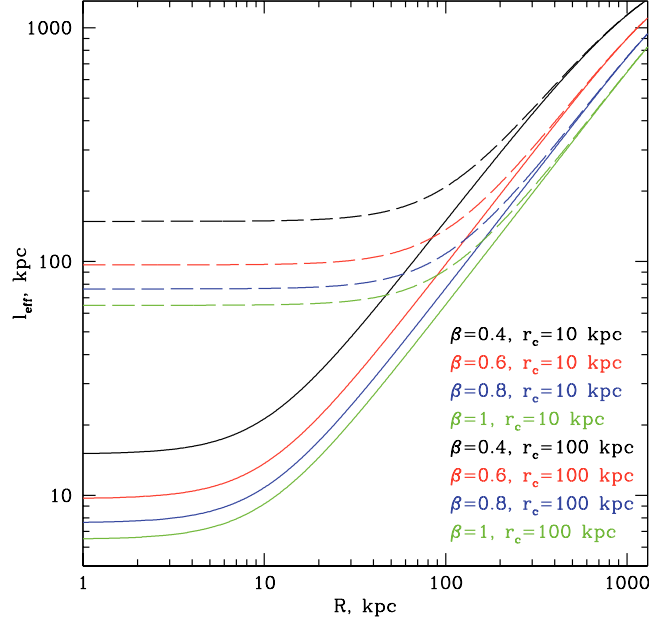
Figure 5.4: Dependence of the effective length along the line of sight $l_{\text{eff}}(R)$ (eq. 5.12) on the projected distance R for different $\beta-$models of galaxy clusters.

In Fig. 5.2 we illustrate the eq. 5.5 for a simple spherically symmetric β-model of galaxy cluster with core radius $r_c = 10$ kpc and $\beta = 0.6$. 3D velocity PS has a cored power law model (eq. 5.2), i.e. is flat on $k < k_m = 0.005$ kpc^{-1} and has a Kolmogorov slope $\alpha = -11/3$ on $k > k_m$. Observed velocity dispersion averaged over 100 realizations is shown with dots, the error bars show the expected uncertainty in one measurement. The right hand side of eq. 5.5 is shown in red. Minor difference between two curves at small R is due to finite resolution of simulations.

Once we construct the map of projected velocity $V_{2\text{D}}(x, y)$, one can also find RMS velocity of the 2D field at each distance r from the cluster center as

$$V_{\text{RMS}}(r) = \sqrt{\langle V_{2\text{D}}(x, y)^2 \rangle_r - \langle V_{2\text{D}}(x, y)_r \rangle^2}, \qquad (5.6)$$

where $\langle V_{2\text{D}}(x, y) \rangle_r$ denotes mean velocity in ring at distance r from the center. Below we use the observed velocity dispersion and RMS of the projected velocity field to constrain the power spectrum.

5.4 Structure function and observed velocity dispersion

Often a structure function of the velocity field is used instead of the power spectrum, which is defined as

$$SF(\Delta x) = \langle (V(x + \Delta x) - V(x))^2 \rangle, \tag{5.7}$$

where averaging is over a number of pairs of points in space separated by distance Δx. The line-of-sight velocity dispersion can be linked to the structure function. Indeed, since the emissivity peaks at the center of the cluster and declines with the radius, the largest contribution to the total flux and to the line-of-sight velocity dispersion at distance R from the center comes from the region, the size of which is $\propto R$.

The structure function and the observed velocity dispersion can be related to the PS (see Appendixes 5.10.3 and 5.10.4):

$$SF(x) = 2 \int_{-\infty}^{+\infty} P_{1D}(k_z)(1 - \cos 2\pi k_z x) dk_z \tag{5.8}$$

and

$$\langle \sigma^2(R) \rangle = \int_{-\infty}^{\infty} P_{1D}(k_z)(1 - P_{EM}(k_z)) dk_z, \tag{5.9}$$

where P_{1D} is an expectation value of the 1D velocity PS and P_{EM} is a PS of normalized emissivity along the line of sight. Fig. 5.3 shows the integrands in eq. 5.8 and eq. 5.9 multiplied by k and $2k$ respectively for the line of sight near the cluster center (black curves) and at a projected distance $R = 800$ kpc from the center (red curves). Extra factor of 2 for $\sigma^2(R)$ is introduced to compensate for the factor of 2 in front of the expression 5.8 for the structure function. It is more clear if one considers the limits of these equations at large x and R. When $x \to \infty$ then $\cos 2\pi k_z x$ oscillates with high frequency over relevant interval of k and mean value of $1 - \cos 2\pi k_z x$ is ~ 1. When $R \to \infty$ the emissivity distribution is very broad and P_{EM} is almost a δ-function. Therefore,

$$\lim_{x \to \infty} (SF(x)) = 2 \int_{-\infty}^{\infty} P_{1D}(k_z) dk_z \tag{5.10}$$

and

$$\lim_{R \to \infty} (\sigma^2(R)) = \int_{-\infty}^{\infty} P_{1D}(k_z) dk_z. \tag{5.11}$$

From Fig. 5.3 it is clear that the integrands in eq. 5.8 and eq. 5.9 are very similar, suggesting that observed $2\sigma^2(R)$ should correlate well with the structure function.
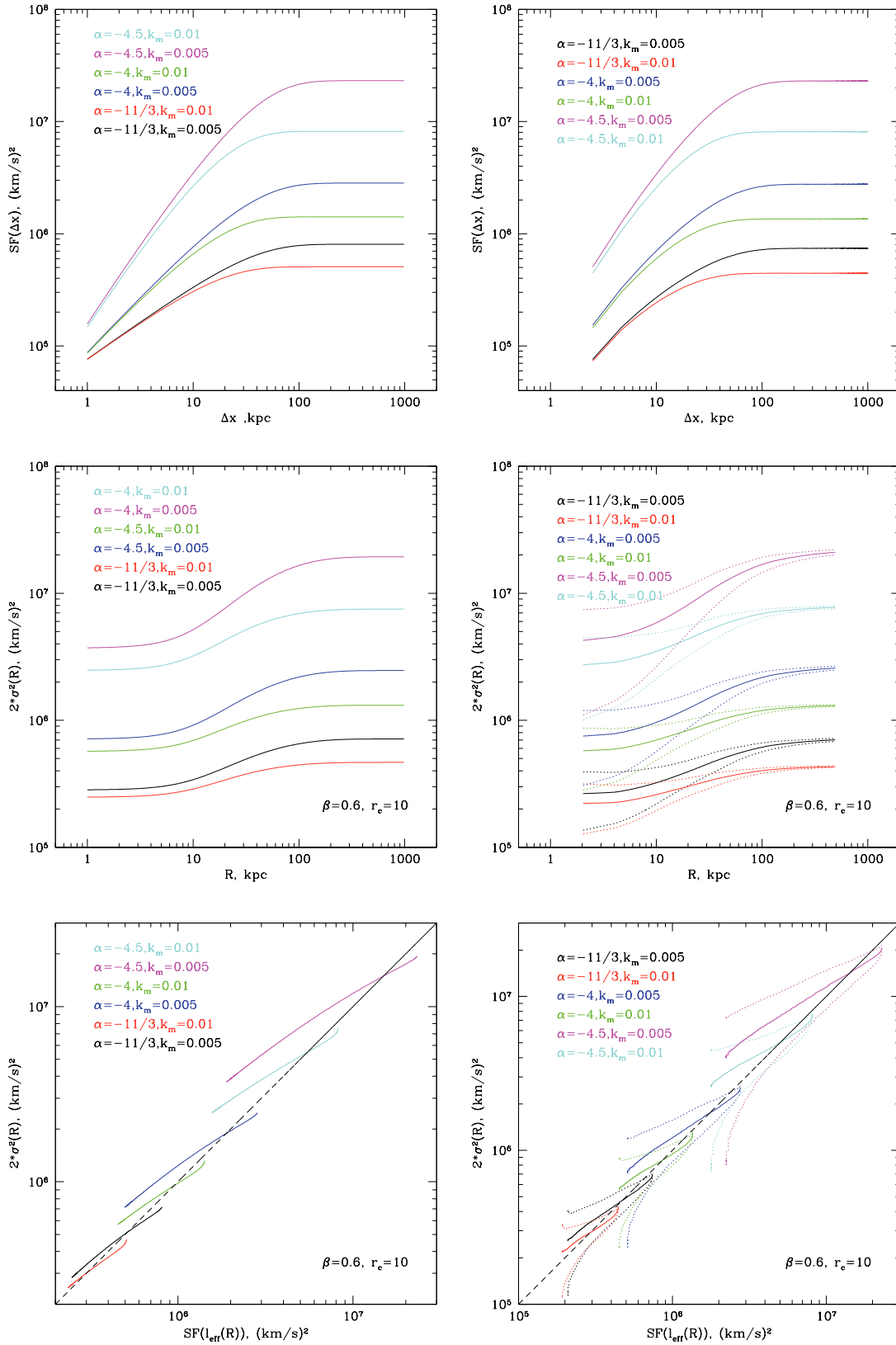
Figure 5.5: **Left column:** structure function (see analytical expression 5.41), line-of-sight velocity dispersion multiplied by factor 2 (eq. 5.42 and eq. 5.46) and their relation for different models of cored power law power spectrum (eq. 5.37). Parameters for power spectrum (slope and break frequency) are shown in the top left corner. Parameters of the $\beta-$ model are given in the bottom right corner.
Right column: the same as left column, but calculated by averaging over 100 statistical realizations of velocity field. The uncertainties in single measurement of the velocity dispersion are shown with dotted curves.
The choice of parameters is discussed in Section 5.2.

The structure function and the velocity dispersion (eq. 5.41 and 5.42 respectively) are plotted in Fig. 5.5 in left column. We fixed parameters of the $\beta-$model of the cluster and varied the slope α and break k_m of the power spectrum model (eq. 5.2). The relation of SF and $2\sigma^2$ is shown in the left bottom panel in Fig. 5.5. For a given R, $2\sigma^2(R)$ is used for $x-$axis, while the SF is plotted as a function of $l_{\text{eff}}(R)$, where l_{eff} is an effective length along the line of sight, which provides dominant contribution to the line flux. l_{eff} is found from the condition that

$$\frac{\int_0^{l_{\text{eff}}} n_e^2(\sqrt{R^2 + l^2})dl}{\int_0^\infty n_e^2(\sqrt{R^2 + l^2})dl} \approx 0.5. \tag{5.12}$$

Relation between l_{eff} and projected distance depends on the $\beta-$ model of galaxy cluster as shown in Fig. 5.4

We then made multiple statistical realizations of the PS for a simple $\beta-$model of galaxy cluster with $\beta = 0.6$ and $r_c = 10$ kpc to estimate the uncertainties. The size of the box is 1 Mpc^3 and resolution is 2 kpc. We assume that the 3D PS of the velocity field has a cored power law model (eq. 5.37) with slope α and break wavenumber (injection scale) at k_m. We made 100 realizations of a Gaussian field with random phases and Gaussian-distributed amplitudes in Fourier space. Taking inverse Fourier transform, we calculated one component of the 3D velocity field (component along the line of sight) in the cluster. Structure function and the line-of-sight velocity dispersion are evaluated using resulting velocity field. Right column in Fig. 5.5 shows velocity dispersion along the line of sight and structure function averaged over 100 realizations. The expected uncertainty in single measurement of the velocity dispersion is shown with dotted curves. One can see that the overall shape and normalization of SF and $2\sigma^2$ are the same as predicted from analytical expressions (left column in Fig. 5.3), however, there are minor differences (especially at small R) due to limited resolution of simulations. Relation between $2\sigma^2$ and SF is in a good agreement with expectation relation, however the uncertainty in measured velocity dispersion (due to stochastic nature of the velocity field) is significant (see Section 6).
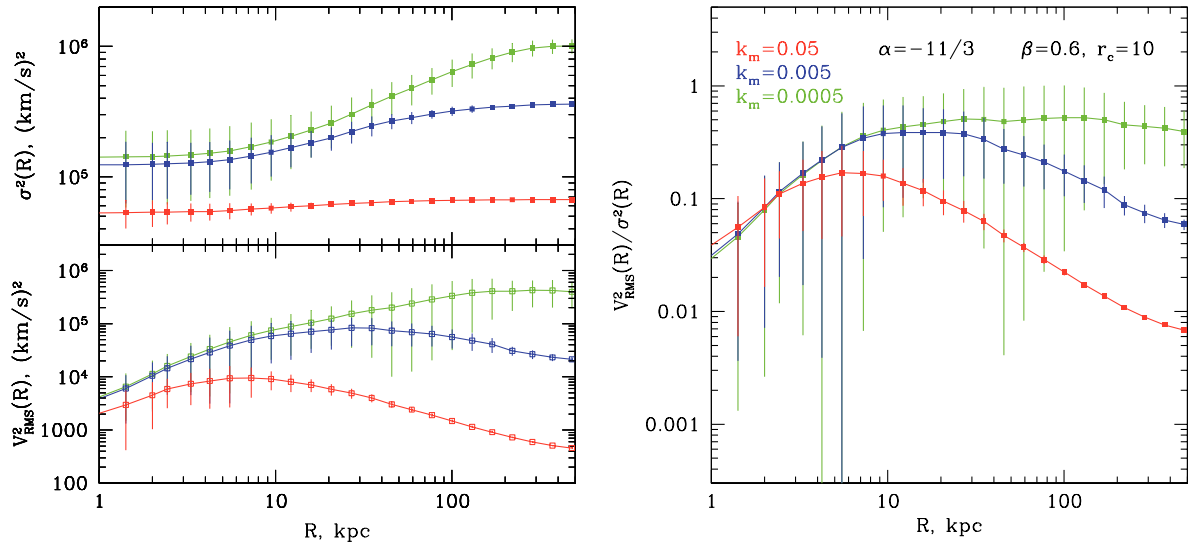
Figure 5.6:   Velocity dispersion and V_{RMS} as functions of distance from the cluster center with uncertainties due to stochastic nature of the velocity field (left panels) and their ratio from eq. 5.15 (right panel). $V_{\mathrm{RMS}}(R)$ and $\sigma(R)$ are averaged over a ring at distance R from the cluster center. Errors show the characteristic uncertainties in one measurement. The slope of assumed velocity PS is -11/3. Break wavenumber k_m of the PS is shown on the right panel. Color coding is the same in both panels.

5.5   Length scales of motions and observed RMS velocity of projected velocity field

Let us now consider RMS of the projected velocity field. During observations one gets spectra from a region, minimum size of which is set by angular resolution and/or the sensitivity of the instrument. RMS velocity at certain position (x,y) for random realizations of the velocity field is defined as (see Appendix 5.10.5)

$$\langle V_{\mathrm{RMS}}^2 \rangle = \int P_{\mathrm{3D}}(k_x, k_y, k_z) P_{\mathrm{EM}}(k_z)(1 - P_{\mathrm{SH}}(k_x, k_y)) d^3k, \tag{5.13}$$

where $P_{\mathrm{SH}}(k_x, k_y)$ is a PS of a mask, where the mask is defined as zero outside and unity inside the region, from which the spectrum is extracted (see Appendix 5.10.5 for details). Velocity dispersion (i.e. the line broadening) measured from the same region is

$$\langle \sigma^2 \rangle = \int P_{\mathrm{3D}}(k_x, k_y, k_z)(1 - P_{\mathrm{EM}}(k_z) P_{\mathrm{SH}}(k_x, k_y)) d^3k. \tag{5.14}$$

Therefore the ratio $\langle V_{\mathrm{RMS}}^2 \rangle / \langle \sigma^2 \rangle$ is

$$\frac{\langle V_{\mathrm{RMS}}^2 \rangle}{\langle \sigma^2 \rangle} = \frac{\int P_{\mathrm{3D}}(k_x, k_y, k_z) P_{\mathrm{EM}}(k_z)(1 - P_{\mathrm{SH}}(k_x, k_y)) d^3k}{\int P_{\mathrm{3D}}(k_x, k_y, k_z)(1 - P_{\mathrm{EM}}(k_z) P_{\mathrm{SH}}(k_x, k_y)) d^3k}, \tag{5.15}$$

which can be used as an additional proxy of the length scales of gas motions. This ratio is mostly sensitive to the break of the cored power law model of the PS k_m. Basically at a given line of sight, which is characterized by an effective length l_{eff} the small scale motions (i.e. $k > 1/l_{eff}$) are mostly contributing to line broadening, while larger scale motions predominantly contribute to the RMS of the projected velocity field.

Fig. 5.6 shows the ratio $\langle V_{\mathrm{RMS}}^2 \rangle / \langle \sigma^2 \rangle$ and its uncertainty calculated for different values of parameter k_m. V_{RMS} and σ are averaged over rings at distance R from the cluster center. Clearly, if k_m is large then all motions are on small scales and the ratio is small. The larger is the k_m, the more power is at large scales and the larger is the V_{RMS}. The larger is the injection scale, the stronger is the increase of the ratio with distance and the more prominent is the peak (see Fig. 5.6). Here we assume that the full map of projected velocity field is available. Clearly, the uncertainties will increase if the data are available for several lines of sight, rather than for the full map.

Looking at eq. 5.15 it is easy to predict behavior of the ratio on small and large projected distances R. Let us specify the shape of area, namely assume that we measure velocity in circles with radius R around the cluster center. When $R \to 0$ then the region is very small and $P_{\mathrm{SH}}(k_x, k_y) \to 1$ over broad range of wavenumbers $k < 1/R$ and the ratio $V_{\mathrm{RMS}}^2 / \sigma^2 \to 0$. At large R $P_{\mathrm{SH}}(k_x, k_y) \to 0$ and $P_{\mathrm{EM}}(k_z) \to 0$ (since $n_e^2(z)$ distribution along the line of sight on large R is broad), eq. 5.15 becomes

$$\frac{\langle V_{\mathrm{RMS}}^2 \rangle(R)}{\langle \sigma^2 \rangle(R)} = \frac{\int P_{\mathrm{3D}}(k_x, k_y, k_z) P_{\mathrm{EM}}(k_z) d^3k}{\int P_{\mathrm{3D}} d^3k} \tag{5.16}$$

and it is a decreasing function of R.

The sensitivity of ratio $V_{\mathrm{RMS}}^2/\sigma^2$ to the slope of the power spectrum is modest. There are only changes in normalization, but, the overall shape is the same.

5.6 Recovering 3D velocity power spectrum from 2D projected velocity field

Mapping of the projected velocity field $V_{2D}(x, y)$ provides the most direct way of estimating the 3D velocity field PS. The 2D and 3D PS are related according to eq.5.4, which we re-write as

$$P_{2D}(k) = \int P_{3D}(\sqrt{k^2 + k_z^2}) P_{\mathrm{EM}}(k_z, x, y) dk_z, \tag{5.17}$$

where $k = \sqrt{k_x^2 + k_y^2}$. This equation can be written as

$$P_{2D}(k) = \int\limits_0^{1/l_{\mathrm{eff}}} P_{3D}(\sqrt{k^2 + k_z^2}) P_{\mathrm{EM}}(k_z, x, y) dk_z +$$

$$+ \int\limits_{1/l_{\mathrm{eff}}}^{\infty} P_{3D}(\sqrt{k^2 + k_z^2}) P_{\mathrm{EM}}(k_z, x, y) dk_z \qquad . \tag{5.18}$$

Contribution of the second term to the integral is small since $P_{\mathrm{EM}}(k_z, x, y) \to 0$ on $k \gg 1/l_{\mathrm{eff}}$. In the limit of $k \gg 1/l_{eff}$ (at a given projected distance) the expression reduces to

$$P_{2D}(k) \approx P_{3D}(k) \int P_{\mathrm{EM}}(k_z, x, y) dk_z, \tag{5.19}$$

i.e. 2D PS is essentially equal to the 3D PS of the velocity field apart from the normalization constant $\int P_{\mathrm{EM}}(k_z, x, y) dk_z$, which is easily measured for a cluster. We show below that this simple relation (5.19) provides an excellent approximation for full expression (5.17) for a Coma-like clusters with flat surface brightness core. For peaked clusters (cool core) P_{3D}/P_{2D} depends on projected distance from the cluster center since l_{eff} changes significantly with distance.

It is convenient to use characteristic scale-dependent amplitudes of the velocity field variations, rather than the PS. The amplitude for 3D and 2D spectra are defined as

$$A_{3D}(k) = \sqrt{P_{3D}(k) 4\pi k^3} \tag{5.20}$$

$$A_{2D}(k) = \sqrt{P_{2D}(k) 2\pi k^2} \tag{5.21}$$

In these notations the relation 5.19 between PS transforms to

$$A_{2D}(k) = A_{3D}(k) \sqrt{\frac{1}{2} \frac{\int P_{\mathrm{EM}}(k_z, x, y) dk_z}{k}}. \tag{5.22}$$
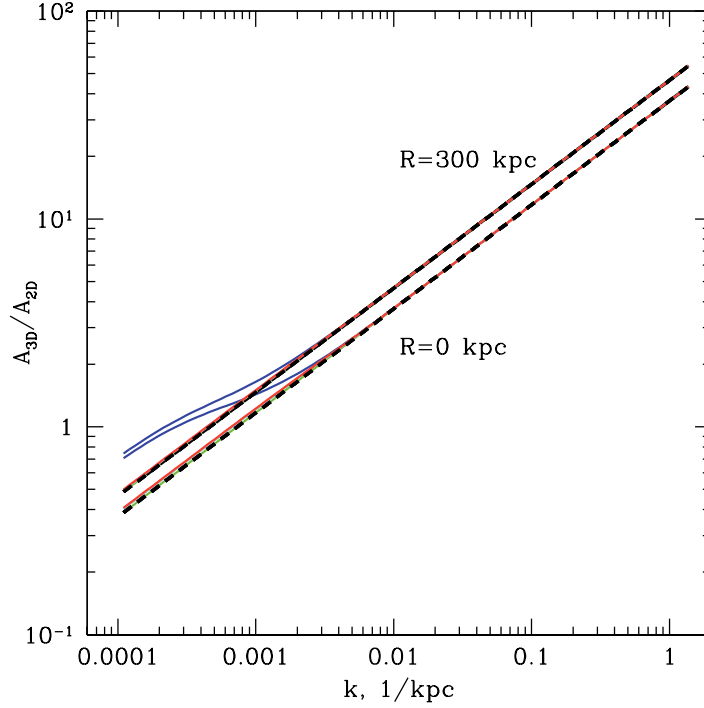
Figure 5.7:   Ratio of 3D and 2D amplitudes as a function of k (eq. 5.17) for a β-model cluster with $\beta = 0.6$ and $r_c = 245$ kpc (Coma-like cluster). A cored power law model is used for the 3D power spectrum, according to eq.(5.2). Two projected distances R were used: $R = 0$ and 300 kpc. Solid lines with different colors correspond to different break wavenumbers in the 3D power spectrum: $k_m = 3 \cdot 10^{-4}, 3 \cdot 10^{-3}, 3 \cdot 10^{-2}$ kpc^{-1} and different slopes of the spectrum $\alpha = 3.5$, 4.0, 4.5. For a given projected distance the curves, corresponding to different power spectra model, lay on top of each other, independently on the slope of the power spectrum, except for the case with very low break wavenumber $k_m = 3 \cdot 10^{-4}$ (blue curves). For comparison the thick dashed lines show the ratio, calculated using simplified equation (5.19). Clearly in the range of scales from Mpc and below the simple relation between 3D and 2D amplitudes is fully sufficient to convert the observed 2D power spectrum into the power spectrum of the 3D velocity field, unless the break of the power spectrum is at very large scales of few Mpc.

Integral $\int P_{\text{EM}}(k_z, x, y)dk_z$ can be estimated as $\dfrac{1}{l_{\text{eff}}}$, since the largest contribution is on $k < 1/l_{\text{eff}}$. Eq. 5.22 becomes

$$A_{2D}(k) = A_{3D}(k)\sqrt{\frac{1}{2}\frac{1}{l_{\text{eff}}k}} = A_{3D}(k)\sqrt{\frac{1}{2}\frac{1}{N_{\text{edd}}}}. \tag{5.23}$$

The essence of this relation is that the amplitude of the 3D velocity fluctuations is attenuated in the 2D projected velocity field by a factor of order $\sqrt{\dfrac{1}{N_{edd}}}$, where N_{edd} is the number of independent eddies which fit into effective length along the line of sight.

We illustrate the above relation for the case of the Coma cluster. The density distribution in the Coma can be characterized by a β-model with $\beta = 0.6$ and co-radius $r_c = 245$ kpc. In Fig. 5.7 we plot the ratio $A_{3D}(k)/A_{2D}(k)$ evaluated using equations (5.19) and (5.17) for a number of 3D PS models calculated at two projected distances from the Coma center. One can see that on spatial scales of less than 1 Mpc the equation (5.22) is fully sufficient. The variations of the relation for different projection distances (projected distances from 0 to 300 kpc were used) affect only the normalization of the relation and can easily be accounted for.

With ASTRO-H the 2D velocity field in the Coma can be mapped with the $\sim 1.7'$ resolution, which corresponds to ~ 46 kpc. Mapping 450×450 kpc central region of the Coma would require about 36 pointings. For practical reasons it may be more feasible to make a sparse map (e.g. two perpendicular stripes) to evaluated A_{2D} (e.g. computing correlation function or using a method described in Arévalo et al., 2011)

5.7 Discussion

Future X-ray missions, such as *Astro-H* and *ATHENA* will have energy resolution of order of few eV. Such resolution will be sufficient to measure accurately currently missing data on the line shift and broadening. In particular, *Astro-H* will have energy resolution ~ 5 eV, field-of-view $2.85'$ and angular resolution $1.7'$, which means that it will be possible to measure shift and broadening of lines as a function of projected distance from the center in nearby clusters. E.g. if one assumes that RMS velocity of gas motions in Perseus cluster is ~ 300 km/s, then $\sim 4 \cdot 10^5$ s is enough to measure profiles of mean velocity and velocity dispersion with a statistical uncertainty of ~ 30 km/s (90% confidence) in a stripe ± 200 kpc (7 independent pointing and 28 independent measurements in $1.4' \times 1.4'$ pixels) centered in the center of the cluster [4]. In order to measure velocity with the same accuracy at larger distances from the center , e.g. at 500 kpc and 1 Mpc, one would need $8 \cdot 10^5$ s and $4 \cdot 10^6$ s exposure respectively.

---

[4]The estimates were done using the current version of *Astro-H* response at http://astro-h.isas.jaxa.jp/researchers/sim/response.html

5.7.1 Limiting cases of small and large scale motions

Measuring characteristic amplitude of mean velocity (V_{RMS}) and velocity dispersion (σ) we can distinguish whether the turbulence is dominated by small or large scale motions. Clearly, the motions on scales much smaller than the effective length along the line of sight near the cluster center can only contribute to the line broadening. This sets the characteristic value of the lowest spatial scale which can be measured. The largest measurable scale is set by the maximum distance R_{max} from the cluster center where the line parameters can be accurately measured without prohibitively long exposure time. Thus the range of scales l, which can be probed with these measurements is $l_{\mathrm{eff}}(R = 0) < l < R_{\mathrm{max}}$. The crucial issue in measurements is "sample variance" of measured quantities caused by stochastic nature of turbulence. We can expect two limiting cases (see Fig. 5.6).
A: *Small scale motions*
In case of small scale motions $l \ll l_{\mathrm{eff}}(R = 0)$ (i.e. $k_m \gg l_{\mathrm{eff}}(R = 0)$ one expects $\sigma(R)$ to be independent of radius and $V_{\mathrm{RMS}}(R) \ll \sigma(R)$. $\sigma(R)$ is expected to have low sample variance and can be measured accurately even for a single line of sight, provided sufficient exposure time. Measurements of $V_{\mathrm{RMS}}(R)$ are strongly affected by sample variance and depend on the geometry of the measured map of the projected velocity dispersion $V(x, y)$. If $V(x, y)$ is measured only at two positions, then the uncertainty in $V_{\mathrm{RMS}}(R)$ is of the order of its value and the ratio $\sigma(R)/V_{\mathrm{RMS}}(R)$ gives only low limit on k_m. We note that in this limit of small scale motions the assumption of a uniform and homogeneous Gaussian field can be relaxed and measured values of line broadening σ simply reflect the total variance of the velocity along the given line of sight, while the possibility of determining the spatial scales of motions are limited. Variations of σ with radius will simply reflect the change of the characteristic velocity amplitude.
B: *Large scale motions*
In case if most of turbulent energy is associated with large scales (i.e. $k_m \ll l_{\mathrm{eff}}(R = 0)$, $\sigma(R)$ is expected to increase with R and $V_{\mathrm{RMS}}(R) \sim \sigma(R)$. In this case sample variance affects both $\sigma(R)$ and $V_{\mathrm{RMS}}(R)$. Mapping the whole area (as opposed to measurements at few positions) would help to reduce the sample variance. Knowing the shape of $\sigma(R)$ and estimates of k_m from $\sigma(R)/V_{\mathrm{RMS}}(R)$ we can constrain the slope of power spectrum.

5.7.2 Effect of thermal broadening and radial variations of the gas temperature and metallicity

Measuring velocity dispersion one should account for line broadening due to thermal motions of ions. Thermal broadening should be subtracted from measured width of line. The broadening of the line $\Delta E = \sqrt{2}\sigma$, where σ is measured Gaussian width of the line, is defined as

$$\Delta E = \frac{E_0}{c}\sqrt{2(\sigma_{therm}^2 + \sigma_{turb}^2)}, \tag{5.24}$$
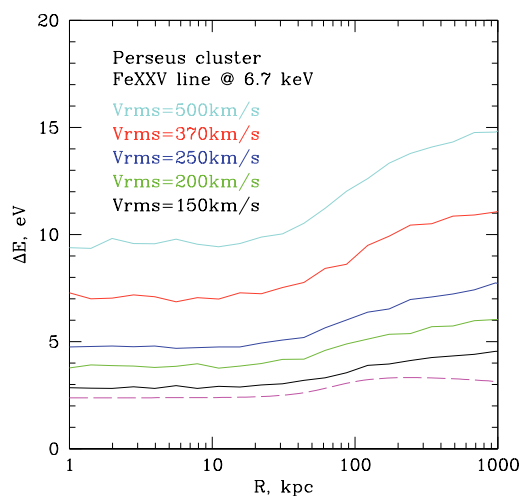
Figure 5.8: Width of the line of He-like iron line at 6.7 keV in Perseus cluster, assuming different 1D RMS velocities. Solid curves show broadening due to gas motions only, dashed curve shows the thermal broadening. Here we assumed the cored power law 3D power spectrum with $\alpha = -11/3$ and $k_m = 0.001$ kpc^{-1}.

where σ_{turb} is the width due to turbulent motions and $\sigma_{therm} = \sqrt{\dfrac{kT}{Am_p}}$ is the thermal broadening for ions with atomic weight A ($A = 56$ for iron). Because of large value of A the contribution of thermal broadening is very small even for modest amplitudes of turbulent velocities. As an example, we calculated the expected broadening of the He-like iron line at 6.7 keV for the Perseus cluster, assuming Kolmogorov-like PS of the velocity field with $k_m = 0.001$ kpc^{-1}. The model of the Perseus cluster was taken from Churazov et al. (2004) and modified at large distances according to Suzaku observations at the edge of the cluster (Simionescu et al., 2011), i.e. the electron number density is

$$N_e(r) = \frac{4.68 \cdot 10^{-2}}{\left[1 + \left(\frac{r}{56}\right)^2\right]^{1.8}} + \frac{4.86 \cdot 10^{-3}}{\left[1 + \left(\frac{r}{194}\right)^2\right]^{0.87}} \qquad (5.25)$$

and the temperature profile is

$$T(r) = 7\frac{1 + \left(\frac{r}{69}\right)^3}{2.3 + \left(\frac{r}{69}\right)^3} \times \left(1 + \frac{r}{5000}\right)^{-1}. \qquad (5.26)$$

Abundance of heavy elements is assumed to be constant 0.5 relative to Solar (Anders & Grevesse, 1989). Fig. 5.8 shows the calculated width of 6.7 keV line assuming various 1D RMS velocities. Thermal broadening is shown with the dashed magenta curve. One can see that
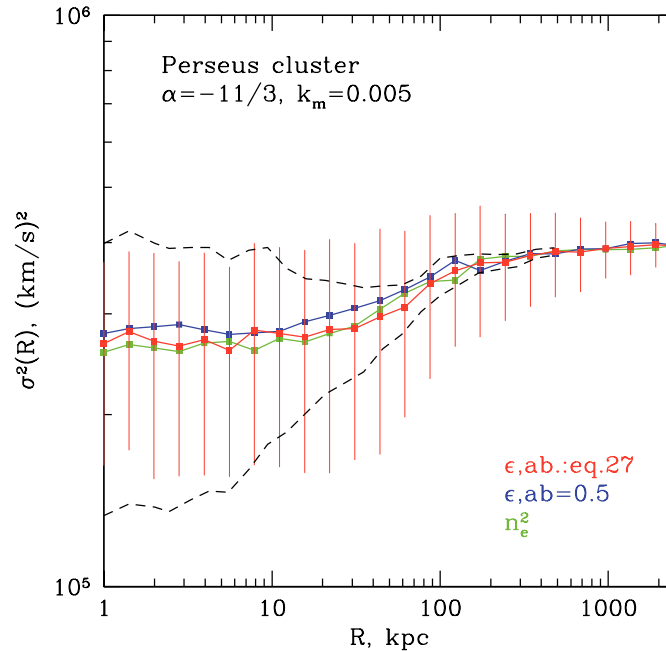
Figure 5.9: Velocity dispersion in the Perseus cluster as function of distance from the center for different emissivity and abundance profiles. Parameters of assumed velocity PS are shown in the top left corner. Green: simple approximation of emissivity $\approx n_e^2$; blue: emissivity at 6.7 keV line and flat abundance; red: emissivity at 6.7 keV line and peaked abundance abundance (eq. 5.27) in the center (see text for details). Black dashed curve shows expected uncertainty in measurements of velocity dispersion observed in a ring.

thermal broadening starts to dominate broadening due to motions only if $V_{RMS} < 150$ km/s. However, the lack of resonant scattering signatures in the spectrum of the Perseus cluster suggests that the expected velocity is higher than 400 km/s in the center of the Perseus cluster (Churazov et al., 2004). $Astro - H$ will have energy resolution of 7 eV at 6.7 keV, therefore broadening due to gas motions with $V_{\rm RMS} \propto 400$ km/s will be easy to observe (Fig. 5.8) in the Perseus cluster.

The analysis described in the previous sections was done assuming an isothermal β-model spherically symmetric cluster with emissivity simply $\propto n_e^2$. Clearly, real clusters are more complicated, even if we keep the assumption of spherical symmetry. First of all the gas temperature and metallicity often vary with radius. These variations will be reflected in the weighting function $n_e^2(\sqrt{R^2 + z^2})$, which relates 3D velocity field and observables. To verify how strongly these assumptions affect the results, we calculated velocity dispersion assuming detailed model of the Perseus cluster (see above). We assumed constant abundance profile and more realistic peaked abundance profile, taken from *Suzaku*

(Simionescu et al., 2011) and *Chandra/XMM* observations

$$Z(r) = 0.4 \frac{2.2 + \left(\frac{r}{80}\right)^2}{1 + \left(\frac{r}{80}\right)^2}. \tag{5.27}$$

We calculated the emissivity of the He-like iron line at 6.7 keV and used this emissivity as a weighting function for the calculation of the expected projected velocity and velocity dispersion. Fig. 5.9 shows the velocity dispersion along one line of sight calculated for the most simple model of emissivity and assuming more complicated models described above. One can see that mean value and uncertainties are very similar in all cases. Clearly that averaging velocity dispersion over a ring will decrease the uncertainty in one measurement (Fig. 5.9, black dashed curve).

5.8   Conclusions

Various methods of constraining the velocity power spectrum through the observed shift of line centroid and line broadening are discussed.

- Changes of the line broadening with projected distance reflects the increase of the spread in the velocities with distance, closely resembling the behavior of the structure function of the velocity field.

- Another useful quantity is the ratio of the characteristic amplitude of the projected velocity field to the line broadening. Since the projected velocity field mainly depends on large scale motions, while the line broadening is more sensitive to small scale motions, this ratio is a useful diagnostics of the shape of the 3D velocity field power spectrum.

- Projected 2D velocity field power spectrum can be easily converted into 3D power spectrum. This conversion is especially simple for cluster with an extended flat core in the surface brightness (like Coma cluster).

Analytical expressions are derived for a β-model clusters, assuming homogeneous isotropic Gaussian 3D velocity field. The importance of the sample variance, caused by the stochastic nature of the turbulence, for the observables is emphasized.

5.9   Acknowledgements

5.10 Appendix

5.10.1 3D velocity power spectrum and projected velocity field

Let us assume that the line-of-sight component of the 3D velocity field $V_{3D}(x, y, z)$ is described by a Gaussian (isotropic and homogeneous) random field. We assume that the centroid shift and the width of lines contain most essential information on the velocity field. Here and below we adopt the relation $k = 1/r$ without factor 2π (see Section 2 for details).

Projected 2D velocity along the line of sight (observed centroid shift of the emission line) in z direction is

$$V_{2D}(x, y) = \frac{\int V_{3D}(x, y, z) n_e^2(x, y, z) dz}{\int n_e^2(x, y, z) dz}, \tag{5.28}$$

where V_{3D} is z component of the 3D velocity field and n_e is the electron number density. Denoting normalized emissivity along the line of sight at a certain position with coordinates (x,y) as $\epsilon(z) = n_e^2(x, y, z)/\int n_e^2(x, y, z) dz$ the previous relation can be re-written as

$$V_{2D}(x, y) = \int V_{3D}(x, y, z)\epsilon(z) dz. \tag{5.29}$$

Applying the convolution theorem one can find the Fourier transform of $V_{3D}(x, y, z)\epsilon(z)$ as

$$\int \hat{V}_{3D}(k_x, k_y, k_{z_1})\hat{\epsilon}(k_z - k_{z_1}) dk_{z_1}, \tag{5.30}$$

where $\hat{V}_{3D}$ and $\hat{\epsilon}$ are Fourier transforms of the 3D velocity field and normalized emissivity respectively. The projection-slice theorem states that

$$\hat{f}_{2D}(k_x, k_y) = \hat{f}_{3D}(k_x, k_y, 0). \tag{5.31}$$

Accounting for 5.30 and 5.31 we can write the Fourier transform of 2D velocity field as

$$\hat{V}_{2D}(k_x, k_y) = \int \hat{V}_{3D}(k_x, k_y, k_{z_1})\hat{\epsilon}^*(k_{z_1}) dk_{z_1}, \tag{5.32}$$

where * denotes conjugation.

Averaging over a number of realization we find the power spectrum of the projected mean velocity

$$\langle |\hat{V}_{2D}(k_x, k_y)|^2 \rangle = \langle |\int \hat{V}_{3D}(k_x, k_y, k_{z_1})\hat{\epsilon}^*(k_{z_1}) dk_{z_1}|^2 \rangle. \tag{5.33}$$

The right part of the equation above can be re-written as

$$\int \langle \hat{V}_{3D}(k_x, k_y, k_{z_1})\hat{V}_{3D}^*(k_x, k_y, k_{z_2}) \rangle \hat{\epsilon}^*(k_{z_1})\hat{\epsilon}(k_{z_2}) dk_{z_1} dk_{z_2}.$$

Since phases are random, all cross terms after averaging over a number of realizations will give 0 if $k_{z_1} \neq k_{z_2}$. Therefore,

$$\langle |\hat{V}_{2D}(k_x, k_y)|^2 \rangle = \int |\hat{V}_{3D}(k_x, k_y, k_{z_1})|^2 |\hat{\epsilon}(k_{z_1})|^2 dk_{z_1}. \tag{5.34}$$

Denoting power spectra of the 3D velocity field and normalized emissivity as P_{3D} and P_{EM} respectively the final expression is

$$\langle |\hat{V}_{2D}(k_x, k_y)|^2 \rangle = \int P_{3D}(k_z, k_y, k_z) P_{EM}(k_z) dk_z. \tag{5.35}$$

5.10.2 3D velocity power spectrum and projected velocity dispersion

Projected mean velocity dispersion for the line of sight with coordinates (x,y) averaged over a number of realization is defined as

$$\langle \sigma^2(x, y) \rangle = \langle \int V_{3D}^2(x, y, z)\epsilon(z)dz \rangle - \langle \left(\int V_{3D}(x, y, z)\epsilon(z)dz \right)^2 \rangle.$$

It can be re-written as

$$\langle \sigma^2(x, y) \rangle = \int \langle V_{3D}^2(x, y, z) \rangle \epsilon(z)dz - \langle V_{2D}^2(x, y) \rangle.$$

Expanding V_{3D} and V_{2D} through the Fourier series, averaging over realizations and keeping non-zero cross terms will give

$$\langle \sigma^2(x, y) \rangle = \int |\hat{V}_{3D}(k_x, k_y, k_z)|^2 dk_x dk_y dk_z \int \epsilon(z)dz - \int |\hat{V}_{2D}(k_x, k_y)|^2 dk_x dk_y.$$

Since emissivity along the line of sight is normalized so that $\int \epsilon(z)dz = 1$ and accounting for eq.5.35 the final expression for projected velocity dispersion is

$$\langle \sigma^2(x, y) \rangle = \int P_{3D}(k_x, k_y, k_z)(1 - P_{EM}(k_z)) dk_x dk_y dk_z. \tag{5.36}$$

5.10.3 Relation between structure function and cored power law 3D power spectrum

Let assume 3D isotropic and homogeneous power spectrum (PS) of the velocity field is described as

$$P_{3D}(k_x, k_y, k_z) = \frac{B}{\left(1 + \dfrac{k_x^2 + k_y^2 + k_z^2}{k_m^2} \right)^{\alpha/2}}, \tag{5.37}$$

where k_{m} is a wavenumber where β model has a break (e.g. an injection scale in turbulence model), α is a slope of PS on $k > k_{\mathrm{m}}$ and B is PS normalization, which is defined so that the characteristic amplitude A of velocity fluctuations at k_{ref} is fixed, i.e.

$$B = \frac{A^2}{4\pi k_{\mathrm{ref}}^3 P_{\mathrm{3D}}(k_{\mathrm{ref}})}. \tag{5.38}$$

Integrating 5.37 over $dk_x dk_y = 2\pi k dk$, one can find 1D PS

$$P_{\mathrm{1D}}(k_{\mathrm{z}}) = \frac{2\pi B k_{\mathrm{m}}^2 \left(1 + \frac{k_{\mathrm{z}}^2}{k_{\mathrm{m}}^2}\right)^{-\alpha/2+1}}{\alpha - 2}. \tag{5.39}$$

Structure function (SF) is related to 1D PS by the transformation (Rytov et al., 1988)

$$SF(x) = 2 \int_{-\infty}^{+\infty} P_{\mathrm{1D}}(k_{\mathrm{z}})(1 - \cos 2\pi k_{\mathrm{z}} x) \mathrm{d}k_{\mathrm{z}}. \tag{5.40}$$

Substituting 5.39 to 5.40 and assuming $\alpha > 3$ yields

$$SF(x) = \frac{4 B k_{\mathrm{m}}^3 \left(\pi^{\frac{3}{2}} \Gamma(\xi) - 2\pi^{\frac{\alpha}{2}} k_{\mathrm{m}}^\xi x^\xi K_\alpha(\xi, 2\pi x k_{\mathrm{m}})\right)}{(\alpha - 2)\Gamma\left(\frac{\alpha}{2} - 1\right)}, \tag{5.41}$$

where $\xi = \frac{\alpha}{2} - \frac{3}{2}$ and K_α is a modified Bessel function of the second kind.

5.10.4 Relation between velocity dispersion along the line of sight and power spectrum

P_{1D} and P_{3D} are related as $P_{\mathrm{1D}}(k_{\mathrm{z}}) = \int P_{\mathrm{3D}}(k_x, k_y, k_{\mathrm{z}}) dk_x dk_y$, therefore eq. 5.36 can be re-written as

$$\langle \sigma^2(R) \rangle = \int_{-\infty}^{\infty} P_{\mathrm{1D}}(k_{\mathrm{z}})(1 - P_{\mathrm{EM}}(k_{\mathrm{z}})) \mathrm{d}k_{\mathrm{z}}, \tag{5.42}$$

where R is projected distance from the center.

If electron number density is described by β model with normalization n_0 and core radius R_{c}

$$n_{\mathrm{e}}(r) = \frac{n_0}{\left(1 + \dfrac{R^2 + z^2}{R_{\mathrm{c}}^2}\right)^{\frac{3}{2}\beta}} \tag{5.43}$$

then the emissivity is

$$\epsilon(r) = \frac{R_{\mathrm{c}}^{6\beta}}{(C + z^2)^{3\beta}}, \tag{5.44}$$

where $r^2 = R^2 + z^2$, $C = R_{\mathrm{c}}^2 + R^2$ and we assume normalization $n_0 = 1$. The Fourier transform of emissivity is

$$\hat{\epsilon}(k_{\mathrm{z}}) = \int_{-\infty}^{\infty} \frac{R_{\mathrm{c}}^{6\beta}}{(C + x^2)^{3\beta}} \cos(2\pi k_{\mathrm{z}} x) \mathrm{d}x, \tag{5.45}$$

where terms with $i\sin(2\pi k_z z)$ are zero since integrand is symmetrical. Dividing 5.45 by the total flux and assuming $\beta > 1/6$ one can find weight $W(k_z)$ as

$$W(k_z) = \frac{2C^{\frac{\zeta}{2}}k_z^{\zeta}\pi^{\zeta}K_\alpha(-\zeta, 2\sqrt{C}k_z\pi)}{\Gamma(\zeta)}, \tag{5.46}$$

where $\zeta = 3\beta - \frac{1}{2}$ and K_α is a modified Bessel function of the second kind.

5.10.5 Ratio of observed RMS velocity to observed velocity dispersion

Let us assume that spectrum is extracted from the region with the area $\int\limits_{shape} dxdy$. The RMS velocity from this spectrum averaged over a number of realizations is

$$\langle V_{\mathrm{RMS}}^2 \rangle = \left\langle \frac{\int\limits_{shape} V_{2D}^2(x,y)dxdy}{\int\limits_{shape} dxdy} \right\rangle - \left\langle \left(\frac{\int\limits_{shape} V_{2D}(x,y)dxdy}{\int\limits_{shape} dxdy} \right)^2 \right\rangle,$$

where $\langle\rangle$ denotes averaging over realizations. Accounting for eq. 5.29 we can re-write the first term in the above equation as

$$\left\langle \frac{\int\limits_{shape} \left(\int V_{3D}(x,y,z)\epsilon(z)dz \right)^2 dxdy}{\int\limits_{shape} dxdy} \right\rangle = \frac{1}{\int\limits_{shape} dxdy} \int\limits_{shape} \int \langle \hat{V}_{3D}(k_{x_1}, k_{y_1}, k_{z_1}) \rangle e^{i2\pi k_{x_1} x} e^{i2\pi k_{y_1} y} \times$$

$$\times F_{\mathrm{EM}}(k_{z_1}) \langle \hat{V}_{3D}(k_{x_2}, k_{y_2}, k_{z_2}) \rangle e^{i2\pi k_{x_2} x} e^{i2\pi k_{y_2} y} F_{\mathrm{EM}}(k_{z_2}) d^3k_1 d^3k_2 dxdy,$$

where F_{EM} is a Fourier transform of emissivity along the line of sight. Averaging over a number of realizations will leave non-zero terms only if $k_1 = k_2$. Therefore, the first term in eq. 5.47 is

$$\frac{\int\limits_{shape} \int P_{3D}(k_x, k_y, k_z)P_{\mathrm{EM}}(k_z)d^3k dxdy}{\int\limits_{shape} dxdy} = \int P_{3D}(k_x, k_y, k_z)P_{\mathrm{EM}}(k_z)dk_x dk_y dk_z.$$

The second term in eq. 5.47 can be written as

$$\left\langle \left(\frac{\int\limits_{shape} \int\limits_z V_{3D}(x,y,z)\epsilon(z)dxdydz}{\int\limits_{shape} dxdy} \right)^2 \right\rangle = \left\langle \left(\frac{\int\limits_{shape} \int \hat{V}_{3D}(k_x, k_y, k_z)e^{i2\pi xk_x}e^{i2\pi yk_y}F_{\mathrm{EM}}(k_z)d^3k dxdy}{\int\limits_{shape} dxdy} \right)^2 \right\rangle \tag{5.47}$$

Squaring and averaging over realizations yield

$$\frac{1}{\left(\int\limits_{shape} dxdy \right)^2} \int P_{3D}(k_x, k_y, k_z)P_{\mathrm{EM}}(k_z) \int\limits_{shape} e^{-i2\pi k_{x_1} x_1}e^{-i2\pi k_{y_1} y_1} \times$$

$$\times \int\limits_{shape} e^{i2\pi k_{x_2} x_2}e^{i2\pi k_{y_2} y_2} dx_1 dy_1 dx_2 dy_2 d^3k, \tag{5.48}$$

or

$$\frac{1}{\left(\int\limits_{shape} dxdy\right)^2} \int P_{3D}(k_x, k_y, k_z) P_{EM}(k_z) \int S(x_1, y_1) e^{-i2\pi k_{x_1} x_1} e^{-i2\pi k_{y_1} y_1} \times$$

$$\times \int S(x_2, y_2) e^{i2\pi k_{x_2} x_2} e^{i2\pi k_{y_2} y_2} dx_1 dy_1 dx_2 dy_2 d^3k, \tag{5.49}$$

where $S(x, y)$ is a mask, which is zero outside and unity inside the area, from which spectrum is extracted. Denoting power spectrum of $S(x, y)/(\int\limits_{shape} dxdy)^2$ as $P_{SH}(k_x, k_y)$, the second term in eq. 5.47 becomes

$$\int P_{3D}(k_x, k_y, k_z) P_{EM}(k_z) P_{SH}(k_x, k_y) dk_x dk_y dk_z. \tag{5.50}$$

Therefore, the final expression for the RMS of the projected velocity field is

$$\langle V_{RMS}^2 \rangle = \int P_{3D}(k_x, k_y, k_z) P_{EM}(k_z)(1 - P_{SH}(k_x, k_y)) d^3k. \tag{5.51}$$

And the ratio of V_{RMS}^2 and velocity dispersion along the line of sight is

$$\frac{\langle V_{RMS}^2 \rangle}{\langle \sigma^2 \rangle} = \frac{\int P_{3D}(k_x, k_y, k_z) P_{EM}(k_z)(1 - P_{SH}(k_x, k_y)) d^3k}{\int P_{3D}(k_x, k_y, k_z)(1 - P_{EM}(k_z)) d^3k}. \tag{5.52}$$

Bibliography

Arévalo P., Churazov E., Zhuravleva I., Hernández-Monteagudo C., Revnivtsev M., 2011, ApJ, submitted

Anders E., Grevesse N., 1989, GeCoA, 53, 197

Beresnyak A., Lazarian A., 2009, ApJ, 702, 1190

Brunetti G., 2006, AN, 327, 615

Brunetti G., Lazarian A., 2011, MNRAS, 412, 817

Cassano R., Brunetti G., 2005, MNRAS, 357, 1313

Cavaliere A., Fusco-Femiano R., 1978, A&A, 70, 677

Chen Y., Reiprich T. H., Böhringer H., Ikebe Y., Zhang Y.-Y., 2007, A&A, 466, 805

Churazov E., Forman W., Jones C., Sunyaev R., Böhringer H., 2004, MNRAS, 347, 29

Churazov E., Forman W., Vikhlinin A., Tremaine S., Gerhard O., Jones C., 2008, MNRAS, 388, 1062

Churazov E. et al., 2011, MNRAS, in prep.

Dobler W., Haugen N. E., Yousef T. A., Brandenburg A., 2003, PhRvE, 68, 026304

Dolag K., Vazza F., Brunetti G., Tormen G., 2005, MNRAS, 364, 753

Esquivel A., Lazarian A., 2005, ApJ, 631, 320

Esquivel A., Lazarian A., Horibe S., Cho J., Ossenkopf V., Stutzki J., 2007, MNRAS, 381, 1733

Heyer M. H., Brunt C. M., 2004, ApJ, 615, L45

Heyer M., Krawczyk C., Duval J., Jackson J. M., 2009, ApJ, 699, 1092

Iapichino L., Schmidt W., Niemeyer J. C., Merklein J., 2011, MNRAS, 483

Inogamov N. A., Sunyaev R. A., 2003, AstL, 29, 791

Jeltema T. E., Hallman E. J., Burns J. O., Motl P. M., 2008, ApJ, 681, 167

Kitsionas S., et al., 2009, A&A, 508, 541

Kolmogorov A., 1941, DoSSR, 30, 301

Landau L. D., Lifshitz E. M., 1966, hydr.book,

Larson R. B., 1981, MNRAS, 194, 809

Lau E. T., Kravtsov A. V., Nagai D., 2009, ApJ, 705, 1129

Myers P. C., Ho P. T. P., Schneps M. H., Chin G., Pankonin V., Winnberg A., 1978, ApJ, 220, 864

Nagai D., Vikhlinin A., Kravtsov A. V., 2007, ApJ, 655, 98

Norman M. L., Bryan G. L., 1999, LNP, 530, 106

Rasia E., et al., 2006, MNRAS, 369, 2013

Rytov S.M., Kravtsov Yu.A., Tatarskii V.I., 1988, Principles of statistical radiophysics, Vol.2. Springer-Verlag, Berlin.

Sanders J. S., Fabian A. C., Smith R. K., 2011, MNRAS, 410, 1797

Scalo J. M., 1984, ApJ, 277, 556

Schuecker P., Finoguenov A., Miniati F., Böhringer H., Briel U. G., 2004, A&A, 426, 387

Simionescu A., et al., 2011, Sci, 331, 1576

Sunyaev R. A., Norman M. L., Bryan G. L., 2003, AstL, 29, 783

Vazza F., Brunetti G., Gheller C., Brunino R., Brüggen M., 2011, A&A, 529, A17

Vikhlinin A., Kravtsov A., Forman W., Jones C., Markevitch M., Murray S. S., Van Speybroeck L., 2006, ApJ, 640, 691

Werner N., Zhuravleva I., Churazov E., Simionescu A., Allen S. W., Forman W., Jones C., Kaastra J. S., 2009, MNRAS, 398, 23

Zhuravleva I. V., Churazov E. M., Sazonov S. Y., Sunyaev R. A., Forman W., Dolag K., 2010, MNRAS, 403, 129

Zhuravleva I. V., Churazov E. M., Sazonov S. Y., Sunyaev R. A., Dolag K., 2011, AstL, 37, 141

Chapter 6

A Mexican Hat with holes: a method to calculate low resolution power spectra from data with gaps

Based on the paper submitted to Astrophys. Journal.
P. Arévalo, E. Churazov, I. Zhuravleva, C. Hernández-Monteagudo, M. Revnivtsev

Abstract. A simple method for calculating a low-resolution power spectrum from data with gaps is described. A Mexican Hat filter (or analogous band-pass filter) is used to single out fluctuations at a given spatial scale and the variance of the convolved image is calculated. The gaps in the image, defined by the mask, are corrected for by representing the Mexican Hat filter as a difference between two Gaussian filters with slightly different widths, convolving the image and mask with these filters and dividing the results before calculating the final filtered image. This method cleanly compensates for data gaps even if these have complicated shapes and cover a significant fraction of the data. The method was developed to deal with problematic 2D images, where irregular detector edges and masking of contaminating sources compromise the power spectrum estimates, but it can also be straightforwardly applied to 1D timing analysis or 3D data cubes from numerical simulations.

6.1   Introduction

The calculation of the Power spectrum through direct Fourier transform of 2D data in astrophysics is often hampered by two problems.

I.   Images may have irregular boundaries or parts of the image are missing. In many cases masks are applied to remove contaminating foreground sources, creating holes in the data that are hard to correct for in Fourier analysis. Such problems arise, for example, when Cosmic Microwave Background (CMB) angular fluctuations are analyzed and the whole area near the Galactic Plane has to be removed from the analysis (see e.g. Smoot et al., 1992; Barreiro et al., 2004; Sato et al., 2010; Jasche et al., 2010).

II.   Another problem often encountered when dealing with limited data sets is the presence of large scale structures, which are not fully covered by the image. The large scale power can leak into the observable Fourier frequency range, distorting the measured spectrum. This often occurs in 1D timing analysis when the noise process monitored has power on timescales longer than the total length of the time series (e.g. Scott et al., 2003), or in 3D data cubes of hydrodynamical simulations for example, when characterizing the turbulent velocity field in a sub-volume of a larger simulated volume (e.g. Dolag et al., 2006).

These problems are illustrated in the left panel of Fig.6.1, which shows the Fourier power density spectrum (PDS) calculated for a 2D image. As input an image with steep PDS ($\propto k^{-11/3}$) was used. The red points show the Fourier PDS for the whole image, blue points show the PDS calculated for a section one third of the linear size of the original image and green points show the case when about 25% of the data in the original image are missing and replaced with zero. Changes in the slope and normalization are readily visible for blue and green curves.

In this paper we propose a simple method to compute the power spectrum that avoids the issues described above. The method allows to compute low resolution power spectra (strictly speaking the convolution of the true power spectrum with a broad filter) even when a large fraction of the original data is missing. The method is analogous to the Δ-variance method of Stutzki et al. (1998) (see also Bensch et al. 2001 and Ossenkopf et al. (2008) but uses a different implementation of the filter, which simplifies the procedure while cleanly compensating for missing data. In the following section we will describe the method (Sec. 6.2) and demonstrate its ability to recover the original power spectrum from simulated 2D images in Sec. 6.3, including effects of irregular masks. This is illustrated in the right panel of Fig.6.1, where the filter is applied to the same set of data as in the left panel.

It is important to stress that the method proposed here measures the convolution of the power spectrum with a relatively broad filter in frequency, so it is not suitable to detect sharp features such as periodic oscillations. The method is best suited to cases where the underlying power spectrum is a smooth powerlaw or bending powerlaw with zero or negative slope, which is the case of many fluctuation patterns in astrophysics. Here we

apply the method to 2D projections of turbulent density fields similar to X-ray images of galaxy clusters, and 3D sections of such systems taken from numerical simulations. Among other possible applications one can also mention characterization of a 3D velocity field in numerical simulations and analysis of Faraday Rotation Measure maps over irregularly shaped regions. All of these cases are normally affected to varying degrees by gaps in the data, given mainly by time constraints on the observations in the first case, patching of different exposures and deletion of contaminating sources in the second case and limited computational volumes in the third case.

We demonstrate that for data sets of sufficiently large dynamic range (ratio of maximal to minimal wavenumbers) the method recovers the overall shape of the spectrum with only modest deviations from the true power spectrum (typically 10–30%) and is robust against plausible gaps patterns, even when these occupy large fraction of the data set.

In terms of uncertainties on the power estimation at a given frequency the method is analogous to the regular Fourier power spectrum (for the data set without gaps), provided that similar binning of the Fourier powers in made in the frequency space.

6.2 Method

We consider an isotropic random Gaussian field, so that it can be characterized by a power spectrum $P(k)$, where k is a scalar. Instead of calculating the "true" power spectrum $P(k)$, where k is the wave number, we propose to evaluate the amplitude of fluctuations for a broad interval of wave numbers $\Delta k \sim k$. We allow for gaps in the data and intend to produce a method capable of recovering the correct shape and normalization of the power spectrum, provided that $P(k)$ does not contain sharp features.

The method consists of few simple steps for any given spatial scale σ:

(i) the original image is convolved with two filters (e.g. Gaussian) having different smoothing lengths $\sigma_1 = \sigma/\sqrt{1+\epsilon}$ and $\sigma_2 = \sigma\sqrt{1+\epsilon}$.

(ii) convolved images are corrected for the data gaps (see §6.2.2).

(iii) the difference of two images is calculated. This difference image is dominated by fluctuations at scales $\sim \sigma$.

(iv) The variance of the resulting image is calculated and recast into an estimate of the power.

The variance values are collected as a function of length scale or, correspondingly, wave number $k_r \propto 1/\sigma$ to produce the power spectrum $\tilde{P}(k_r)$. The tilde is added to distinguish the result from the true power spectrum.

We first consider the case of data without gaps (§6.2.1, steps i,iii and iv) and then discuss the procedure of correcting for gaps (§6.2.2) using a Mexican Hat filter as an example.
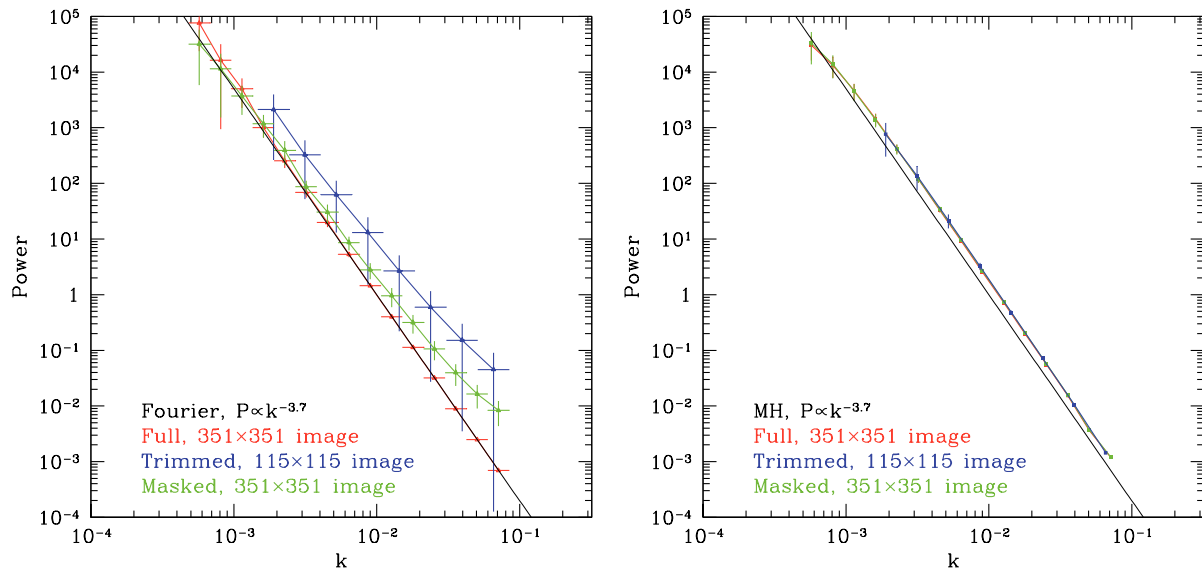
Figure 6.1: **Left:** Fourier power density spectrum (PDS) calculated for a 2D image. As input a 351×351 pixel image with steep PDS ($\propto k^{-11/3}$) was used (shown by the black line). The red points show the Fourier PDS for the whole image, blue points show the PDS calculated for a small section (115×115 pixel) of the original image and green points show the case when about 25% of the data in the original 351×351 pixel image are missing and replaced with zero. Clearly both the normalization and the shape of the PDS are modified when parts of the data are missing or significant power is present on spatial scales larger than the size of the image (case of image subsection). **Right:** Power estimated using the Mexican Hat filter, corrected for the gaps in the data. The same set of data is used as in the left panel. Clearly the result is insensitive to the presence of the data gaps. There is a weak bias in the normalization, which is discussed in the text and in the Appendix 6.6.2.
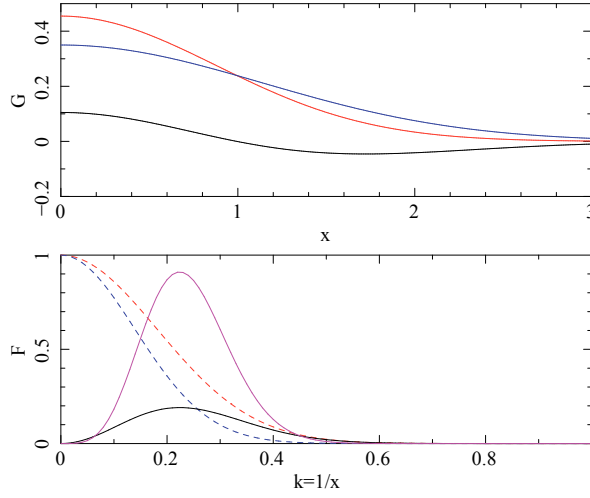
Figure 6.2: **Top panel:** 2 Gaussians of $\sigma \sim 1$ used for filtering (red, blue) and their difference (black). **Bottom panel:** Fourier transforms of the Gaussian functions shown above (red, blue), their difference (black) and the difference squared, amplified for clarity (magenta). The magenta curve is the filter effectively applied on the power spectrum of the image treated, therefore the variance of the filtered image is normalized by the area under this curve and the transmited power peaks at $k = 0.225/\sigma$.

6.2.1   Data without gaps

To isolate structures of a characteristic length-scale, we first smooth the image I with two Gaussian filters (for simplicity we consider 1D case):

$$G_\sigma(x) = \frac{1}{(2\pi\sigma^2)^{1/2}} e^{-\frac{x^2}{2\sigma^2}} \tag{6.1}$$

of slightly different widths $\sigma_1 = \sigma/\sqrt{1+\epsilon}$ and $\sigma_2 = \sigma\sqrt{1+\epsilon}$. The top panel in Fig. 6.2 shows an example in the shape of Gaussian filters, normalized to unity, together with their difference. After convolving the image with each of these filters, both resulting images I_1 and I_2 will retain structures larger than σ_2 and lose structures smaller than σ_1 so the difference image $I_1 - I_2$ will predominantly contain structures with the characteristic scales $\sim \sigma$.

For $\epsilon \to 0$ the resulting filter

$$F(x) = G_{\sigma_1}(x) - G_{\sigma_2}(x) \propto \frac{\partial G_\sigma(x)}{\partial \sigma} \propto \left[1 - \frac{x^2}{\sigma^2}\right] e^{-\frac{x^2}{2\sigma^2}}, \tag{6.2}$$

which is the familiar Mexican Hat filter. Obviously the shape of the filter does not depend on ϵ in the limit of $\epsilon \to 0$, but for numerical reasons it is advantageous to keep ϵ of order unity.

In terms of power, the convolution and difference procedure is equivalent to multiplying the power spectrum by the magenta curve in the bottom panel of Fig. 6.2. This panel
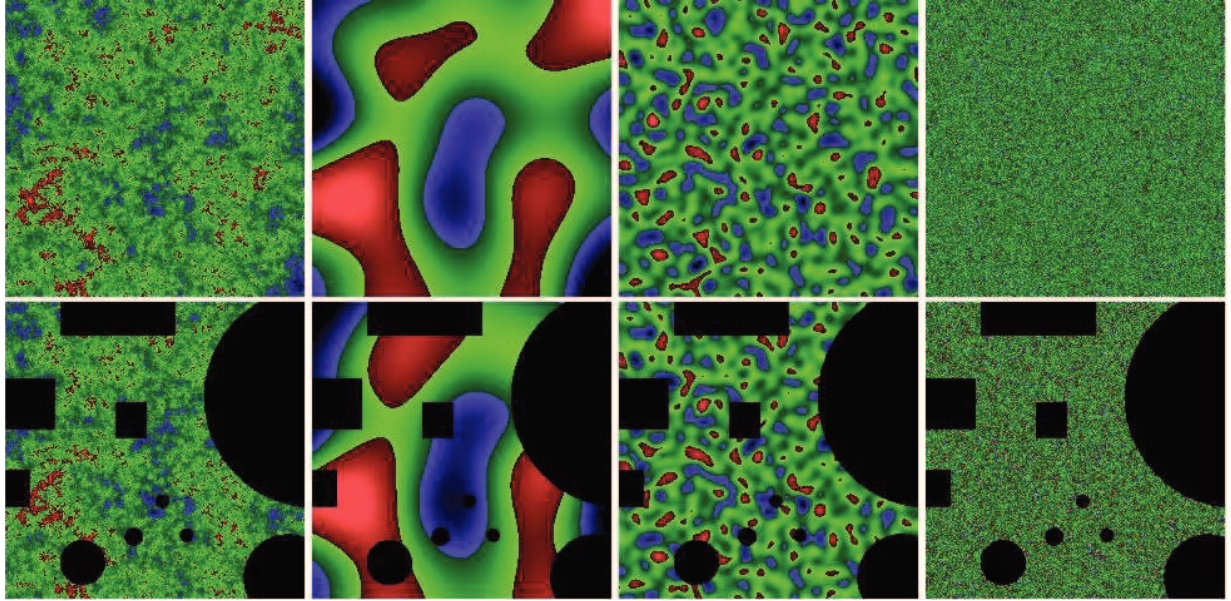
Figure 6.3: **Top row:** On the left - simulated image with power law shaped PDS, each subsequent panel shows the result of filtering the image at a different spatial scale k as described in the text, from left to right: $k^{-1} = 159$ arcsec, 21 arcsec and 6.2 arcsec, each image is 4 arcmin a side. **Bottom row:** On the right - original image, multiplied by the mask, i.e. $I \times M$. Each subsequent panel shows filtered images calculated from the same simulated masked image after application of eq.6.6 and multiplication by the original mask, i.e. $I_c(k_r) \times M$. No spurious structure is evident around the mask holes or edges. These parts of the filtered images where $M = 1$ are used to calculate the variance for a given k_r.

displays the Fourier transforms of the Gaussian filters shown above, which are of course also Gaussian and, given the filter normalization, their difference, plotted in the black dashed line, is always positive. The square of the difference, plotted in magenta, is therefore the filter effectively applied to the power spectrum of the image. As shown in Appendix 6.6.1, for Gaussian filters the peak of the magenta curve is at $k_r = 0.225/\sigma$ and its width is $\sim 1.155 k_r$, independent of ϵ, for small values of this quantity. The resulting filter is relatively broad and it cannot be made narrower by using smaller values of ϵ. This has the limitation that sharp features in the power spectrum will be smeared out, so our aim is to recover the broad band shape and normalization of the power spectrum but not narrow features. Gaussian filters were chosen for computational convenience, since the 2D convolution in this case can be easily separated into 1D convolutions in x and y coordinates.

Thus the difference between two convolved images, which we denote as $I(k_r)$ is

$$I(k_r) = I_1 - I_2 \equiv G_{\sigma_1} * I - G_{\sigma_2} * I \equiv F * I, \tag{6.3}$$

can be used to calculate the variance at scales $\sim 1/k_r$ and evaluate $\tilde{P}(k_r)$ using a simple relation for the normalisation (see Appendix 6.6.1).

6.2.2 Data with gaps

We now consider the image with gaps and introduce a mask M such that

$$M = \begin{cases} 1 & \text{where } I \text{ is defined} \\ 0 & \text{where } I \text{ is undefined} \end{cases} \tag{6.4}$$

Here "undefined" refers not only to gaps, but also to areas outside the image boundaries. Essentially for an n-dimensional image we treat the whole n-dimensional space outside the image boundaries as a data gap. The image I is also set to zero in the gaps and outside image boundaries. Thus, one can write $I = M \times I_0$, where I_0 is the true image without gaps, defined over the whole n-dimensional space.

Direct application of the filter F described by eq.6.2 to the image I with gaps will produce many spurious structures, which are difficult to correct for. However one can use the fact that the $I(k_r)$ image can be represented as the difference of two smoothed images. Consider, for instance, $I_1 = G_{\sigma_1} * I$. Convolving the image with gaps with a Gaussian will still produce spurious features, but their amplitude can be drastically reduced by dividing I_1 by the mask M, convolved with the same Gaussian, to produce a corrected image $I_{1,c}$:

$$I_{1,c} = \frac{I_1}{M_1} = \frac{G_{\sigma_1} * (M \times I_0)}{G_{\sigma_1} * M}. \tag{6.5}$$

Note, that we make the convolution in the infinite n-dimensional space without assumption of the image periodicity outside the image boundaries. Intuitively the effect of the division by the convolved mask is clear – the amplitude of $I_1 = G_{\sigma_1} * I = G_{\sigma_1} * (M \times I_0)$ is going to be lower close to the gaps or close to image boundaries. The convolved mask $M_1 = G_{\sigma_1} * M$ largely shares these properties and the ratio $\frac{I_1}{M_1}$ will lack an obvious trend of the amplitude decrease near the gaps. The same argument applies to $I_{2,c} = \frac{I_2}{M_2}$. Finally

$$I_c(k_r) = (I_{1,c} - I_{2,c}) \times M = \left(\frac{G_{\sigma_1} * I}{G_{\sigma_1} * M} - \frac{G_{\sigma_2} * I}{G_{\sigma_2} * M} \right) \times M. \tag{6.6}$$

The final step of the variance calculation is done only for the part of the corrected image $I_c(k_r)$ where the mask $M = 1$ (see Appendix 6.6.1). In summary, the biases introduced by the shape of the image boundaries and holes in the mask are corrected for by subjecting the mask to the same smoothing procedure and then dividing the smoothed image by the smoothed mask. Therefore, the flux lost by smearing the image out of the mask boundaries is compensated by an equal loss of mask area around the edges. When approaching a gap, the convolved mask $G_{\sigma_1} * M$ decreases smoothly from a value of 1 before the gaps to 0 well into the gap if it is longer than the filter size, or to a value between 0 and 1 for shorter gaps, so that the filtered mask has a value greater or equal to 0.5 at the edge of the original gap. As $I_c(k_r)$ is finally multiplied by the original, non convolved mask M, points where the denominators in Eq. 6.6 vanish are automatically discarded.

Our approach is analogous to the Δ-variance method of Stutzki et al. (1998); Bensch et al. (2001) and Ossenkopf et al. (2008). In our implementation of the Mexican Hat filter the

role of the core and annulus filters (see Stutzki et al. 1998; Ossenkopf et al. 2008 for definitions) is played by two Gaussians with slightly different widths. Representing the Mexican Hat as a difference between two Gaussians simplifies the whole procedure when correcting for the missing data. Also, the convolution with a Gaussian can be done fast both in real multi-dimensional space, using factorization of the Gaussian in each dimension, or in the Fourier space.

6.3   Test on simulated images

We generated 2D Gaussian fluctuation fields to test the method's ability to reproduce the original power spectrum. We simulated the effect of irregular edge shapes and contaminating sources in the generated image by masking out regions with different shapes and size scales. Figure 6.3 shows a simulated image with an isotropic power law power spectrum of slope $\alpha = -2$. The top row in this figure shows the image decomposition into components of different spatial scales. The bottom row displays the same simulated image overlaid on an arbitrary mask and the decomposition performed on the *masked* image. The method is quite insensitive to the presence of the mask, as seen in Fig.6.3 the fluctuations on different spatial scales can be recovered in the masked image without introducing spurious structures around the edges.

Figure 6.4 shows the variance of the filtered images as a function of their characteristic filter scale k, for images of different power spectra. The simulated images had a size of 1024^2 pixels and a section of the central 300^2 pixels was used to calculate the power spectra. We checked for overall biases by generating many images with a given underlying power spectrum, randomizing phase and amplitude to generate simulations of a Gaussian noise process (Timmer & König, 1995). The $\tilde{P}(k_r)$ spectra were computed for the simulated images and the mean and rmsscatter of the realizations for each spatial scale are plotted in Fig. 6.4. As expected, the scatter of individual measurements increases towards low values of k (large spatial scales), but the mean of each set of 100 realizations lies very close to the power law fit.

The input power law slopes shown in Fig. 6.4 were -1 and -3 and the recovered slopes, obtained from fitting a power law to the $\tilde{P}(k_r)$ spectra are $-0.99^{+0.02}_{-0.01}$ and $-2.995^{+0.01}_{-0.01}$. The input nomalizations of 1 are also recovered $0.92^{+0.02}_{-0.02}$ and $1.01^{+0.01}_{-0.003}$. The $\tilde{P}(k_r)$ method biases the normalization of the power spectrum, and this bias is computable if the shape of the power spectrum is known. The case of Gaussian filters on power law type power spectra is described in Appendix 6.6.2. The observed small deviation of the normalization from the expected value is consitent with this analysis.

The negligible effect of masking out a fraction of the image, as shown in Fig. 6.3 can also be seen in Fig. 6.4. The red and blue markers represent the mean and rmsscatter of 100 realisations of masked images with the same slopes as above. Clearly the match between masked and unmasked power spectral shapes and normalization is almost perfect. The recovered value for the slopes and normalisations were identical to the unmasked case. Tests with different slopes gave equally good results.
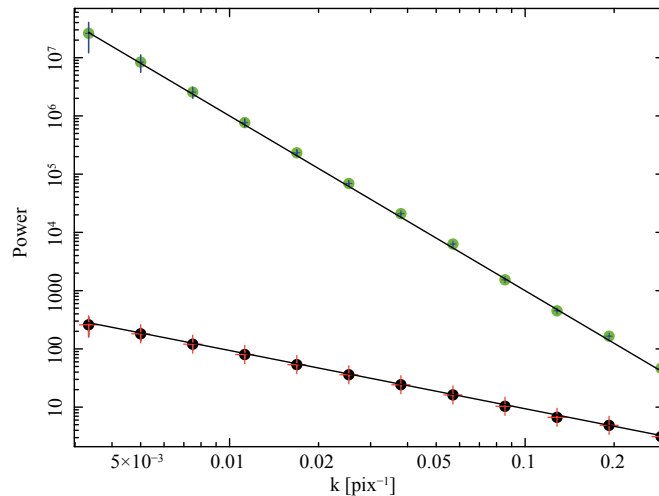
Figure 6.4: Power spectra of simulated images. Each set of filled circles corresponds to the mean of 100 realizations of simulated images with power law slopes -1 and -3, shown in black and green, respectively. The error bars represent the rmsscatter of these sets of realizations. Power law functions fitted to each set are shown in solid lines, the recovered slopes were -0.99, and -2.995. Red and blue markers represent the same calculation performed on sets of masked images. Clearly, the application of the mask does not distort the slope or normalisation of the recovered power spectra.

6.4   3D data cubes

When analyzing data of numerical simulations, e.g. a velocity field in hydrodynamic simulations, one often deals with cubes of data. In this section we extend the method on three dimensions and compare our power spectrum results with calculations using the conventional Fourier transform. As before we generate the Fourier amplitudes $F(i, j, k)$ as a Gaussian random field with a power law spectrum $Ak^{-\alpha}$:

$$F(i, j, k) = \sqrt{\frac{A}{2}k^{-\alpha}}\left(\zeta + i\eta\right), \tag{6.7}$$

where $k = \sqrt{i^2 + j^2 + k^2}/L$, and ζ and η are random variables with Normal distribution. We then apply an inverse Fourier transform to get the 3D data cube. In particular we consider a red noise process with the slope $\alpha = 11/3$, corresponding to the 3D Kolmogorov power spectrum, which is often assumed when dealing with the turbulent velocity field.

The power spectrum $\tilde{P}(k_r)$ is calculated analogously to the 2D case, by filtering the cube with 3-dimensional Gaussians. The analysis in Appendix 6.6.1 is directly applicable, for a value of $n = 3$ and as before we assume isotropy in the random field, so we are only interested in the power spectrum as a function of spatial scale.

The first question we address is whether the shape of the red noise is recovered if the noise extends below the lowest wave numbers set by the size of the cube. To this end we calculate the power spectrum for the full simulated cube and also for smaller

"trimmed" cubes, which are cut from the original larger cube. The mean of 100 power spectra evaluated through the variance (see §6.2) for the full cube and trimmed sections, of 1/2 and 1/4 of the original size on a side, are shown on the bottom panel of Fig. 6.5 with blue, red and green curves respectively. Power spectra calculated through the conventional Fourier transform are shown on the top panel of Fig. 6.5. In both panels the input power law power spectrum is shown by the dashed black line. Since trimmed cubes are not periodic anymore the power spectrum recovered through Fourier transform is strongly distorted, by leakage of power from very low frequencies. However, we see good agreement between the input and recovered power spectra, which are calculated through the variance method. There are minor discrepancies only on the smallest and highest wave numbers.

Both discrepancies are caused by the fact that the value of the variance is a convolution of the true PDS with the filter in frequency space. As a result at low k the power leaks out if the full simulated cube is used, since eq. 6.7 effectively assumes that there is zero power at frequencies lower then $1/L$. This effect goes away if the subsection of the original cube is used (see also 2D case in Fig. 6.1).

The statistical uncertainties for all three cases are shown on Fig. 6.6 with gray shadows. The mean of 100 cube realizations and their trimmed sections is shown by the red lines on each panel, while the rmsscatter is represented by the gray area. The relative errors of the PDS increase at low k for the trimmed cube. The origin of this increase is clear - trimming (windowing) in real space is equivalent to the convolution in the Fourier space. This causes the very low wave-number perturbations (lower than the $1/L_{\mathrm{trimmed}}$) in the original cube to leak into the k range covered by the trimmed cube. Thus Fourier modes in the trimmed cube are not longer independent and the relation between the PDS and the error (corresponding to χ_n^2 distribution, where n is the number of independent modes) deviates towards larger relative errors because the effective number of independent modes decreases. This effect is important for steep PDS and is absent for a flat spectrum (white noise).

We now proceed by considering the impact of data gaps on the recovered power spectra. We consider 3D masks covering different fractions of the cube volume. Sample slices of these masks are shown in Fig. 6.7. To generate masks with irregular boundaries we first generate an additional data cube with the power spectrum slope -3 and made an inverse Fourier transform to get a real value array $a(x, y, z)$. We then introduce a characteristic cutoff value a_{cut} and set the mask to 0 or 1 where the values are smaller or larger than a_{cut}, respectively. Setting different values of a_{cut} produces masks with different fractions of zeros (i.e. gaps). 2D slices of the mask M for different values of a_{cut} are shown in Fig. 6.7. The fraction of missing data varies from 50% in the left image to 85% in the right image. The resulting masks are applied to the original data cube with the Kolmogorov power spectrum.

Power spectra calculated for the data with gaps are shown on Fig. 6.8. Power spectra calculated with the variance method and through the conventional Fourier transform (setting values to zero in the data gaps) are shown in the bottom and top panels, respectively. Blue curves show the power spectrum for data without gaps, while red, green and magenta curves show power spectra calculated for the data with gaps (see Fig. 6.7: left, middle
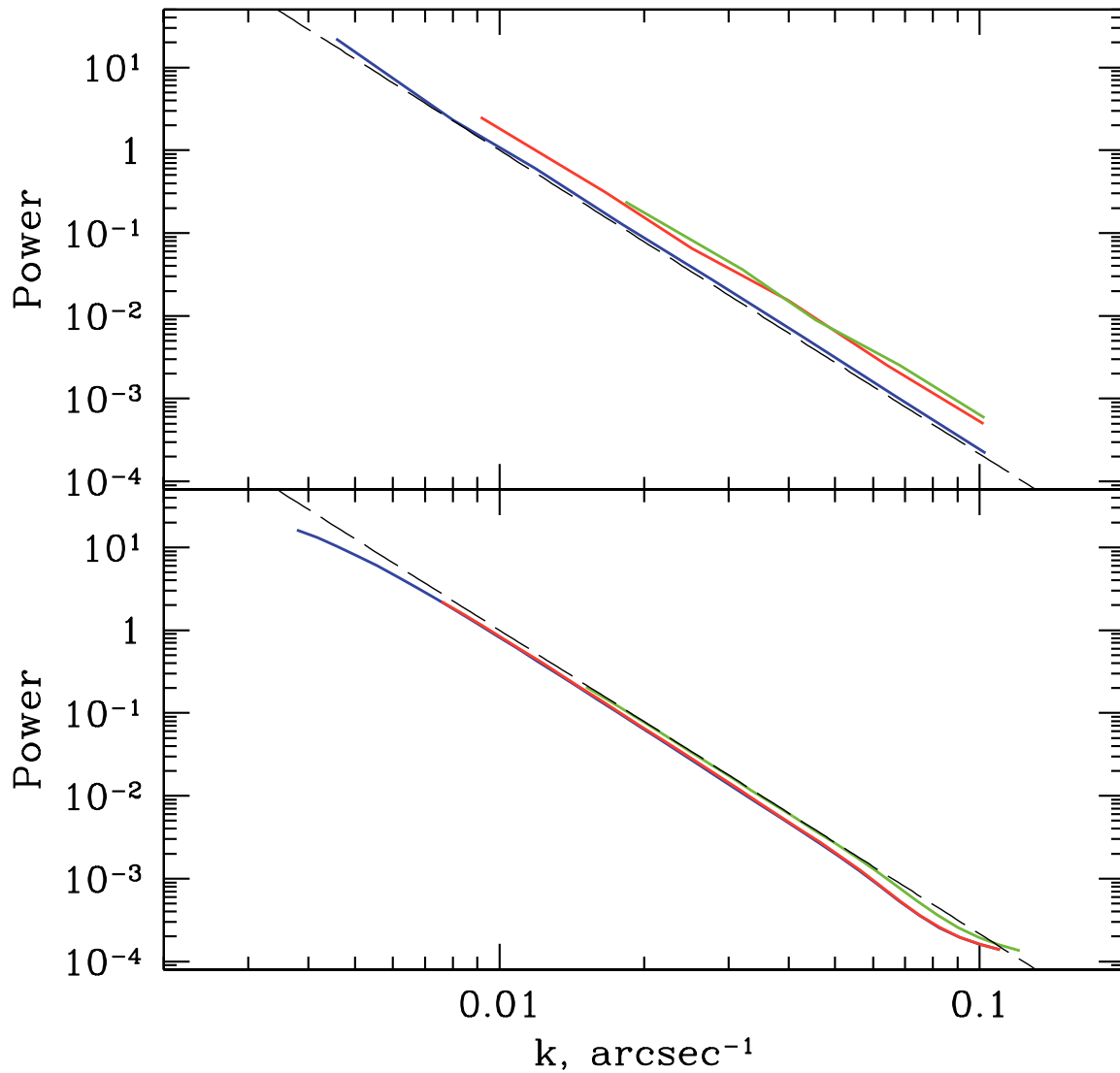
Figure 6.5: The mean of 100 power spectra of simulated cubes calculated through the variance (bottom panel) and the Fourier transform (the top panel). The input power spectrum is a power law with slope -11/3 (dashed black curve). Power spectra recovered through the procedure outlined in section 6.2 for the full cube and trimmed cubes 1/2 and 1/4 of the original side size are shown with blue, red and green curves respectively.
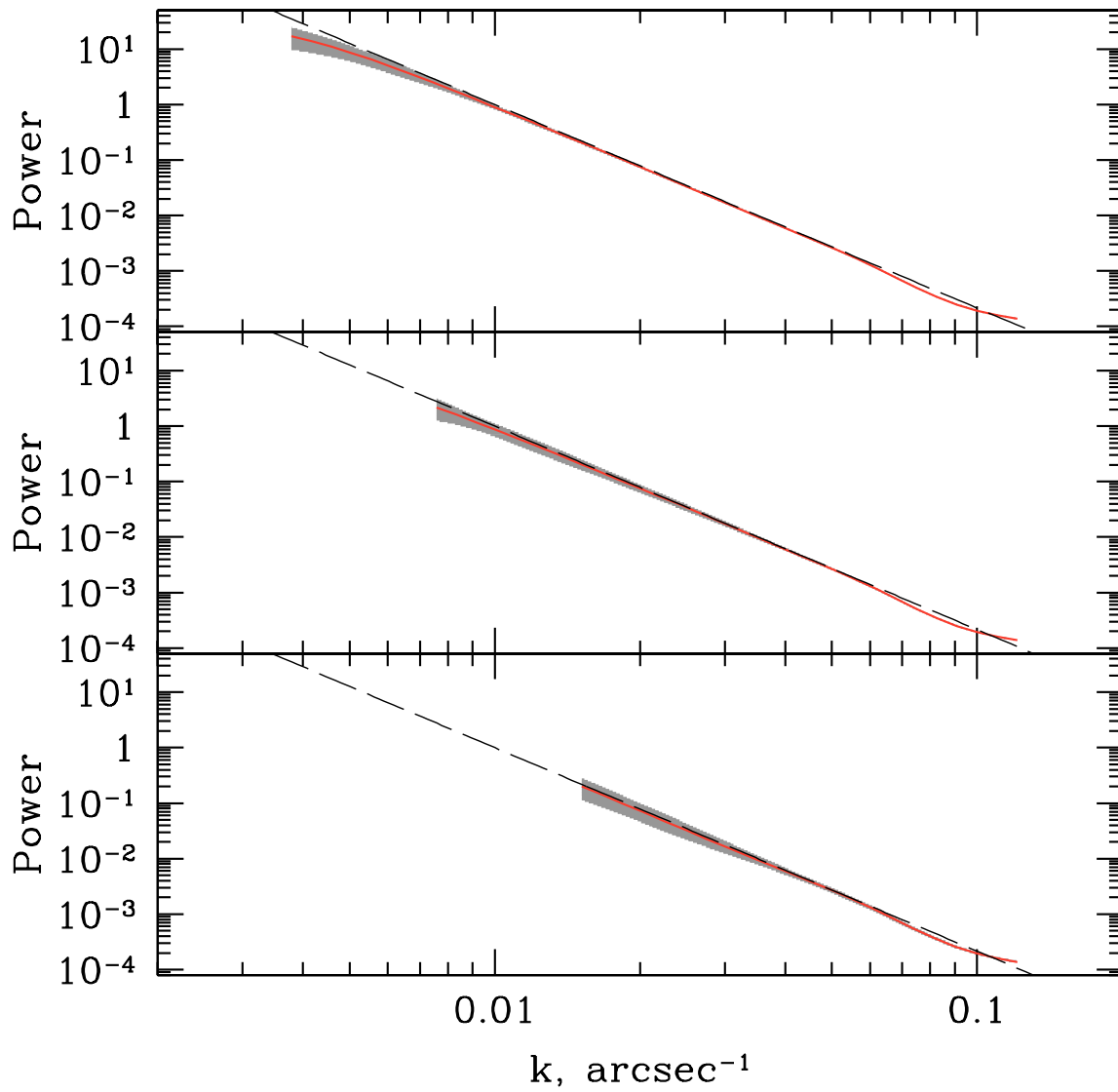
Figure 6.6: The same power spectra as on the bottom panel of Fig. 6.5, gray shadows show the range of statistical uncertainties.
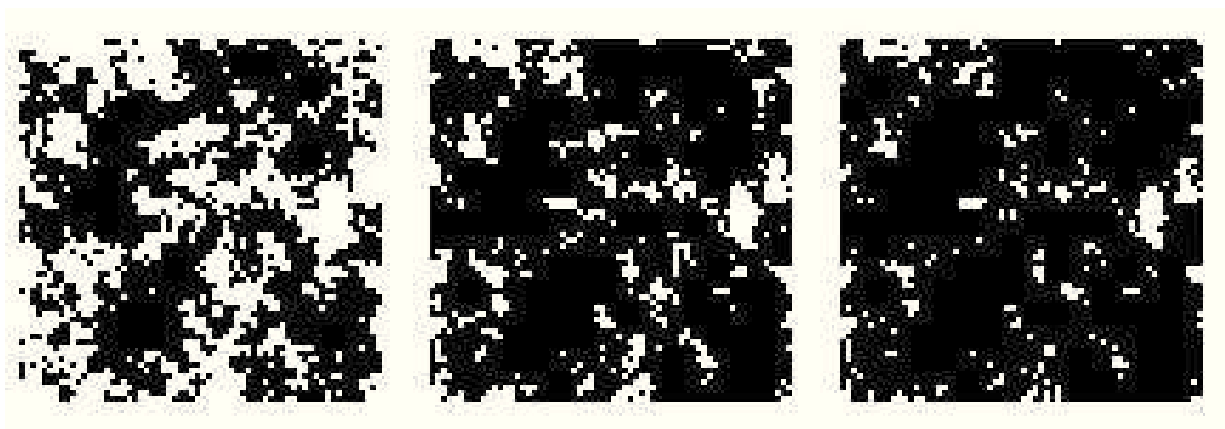
Figure 6.7: Slices of the masks considered in our calculation. Data gaps are shown in black. The fraction of discarded data is 50%, 75% and 85% for left middle and right panels, respectively.

and right panels). The direct Fourier method should not be used on these type of data as the gaps strongly affect the resulting power spectra. If there are only few small gaps then additional frequencies appear and the recovered spectrum is higher on large k. Clearly, the increase of the gaps fraction leads to the leakage of power causing the flattening of the spectrum and the decrease of its normalization. At the same time the power spectra calculated through the variance are perfectly recovered, with only minor changes on small and large wave numbers even in case when 85% of the data are in gaps.

6.5 Conclusion

A simple method for estimating a low resolution power spectrum from data with gaps is described. Essentially the variance associated with a given scale is calculated by convolving the image with a Mexican Hat filter (or similar band-pass filter). Gaps in the data, described by the mask M are corrected for by representing the Mexican Hat filter as a difference between two Gaussian filters, convolving the image and mask with these filters and dividing results before calculation of the final Mexican Hat-filtered image. The variance of the filtered image is then calculated and the power spectrum is evaluated by repeating the procedure for different filter scales. The calculated power spectrum is smeared out by the width of the filter, so sharp features are lost, but the broadband spectral shape and normalization are recovered well.

The strength of the method is in its ability to deal with gaps in the data. By dividing the filtered images by their correspondingly filtered masks and maintaining the calculation in the space domain, the method cleanly compensates for data gaps even if these have complicated shapes and cover significant part of the data set. We use simulations to show that the power spectrum recovered from complete data sets and from their masked versions are consistent and no additional biases are introduced by the masks. The method uses
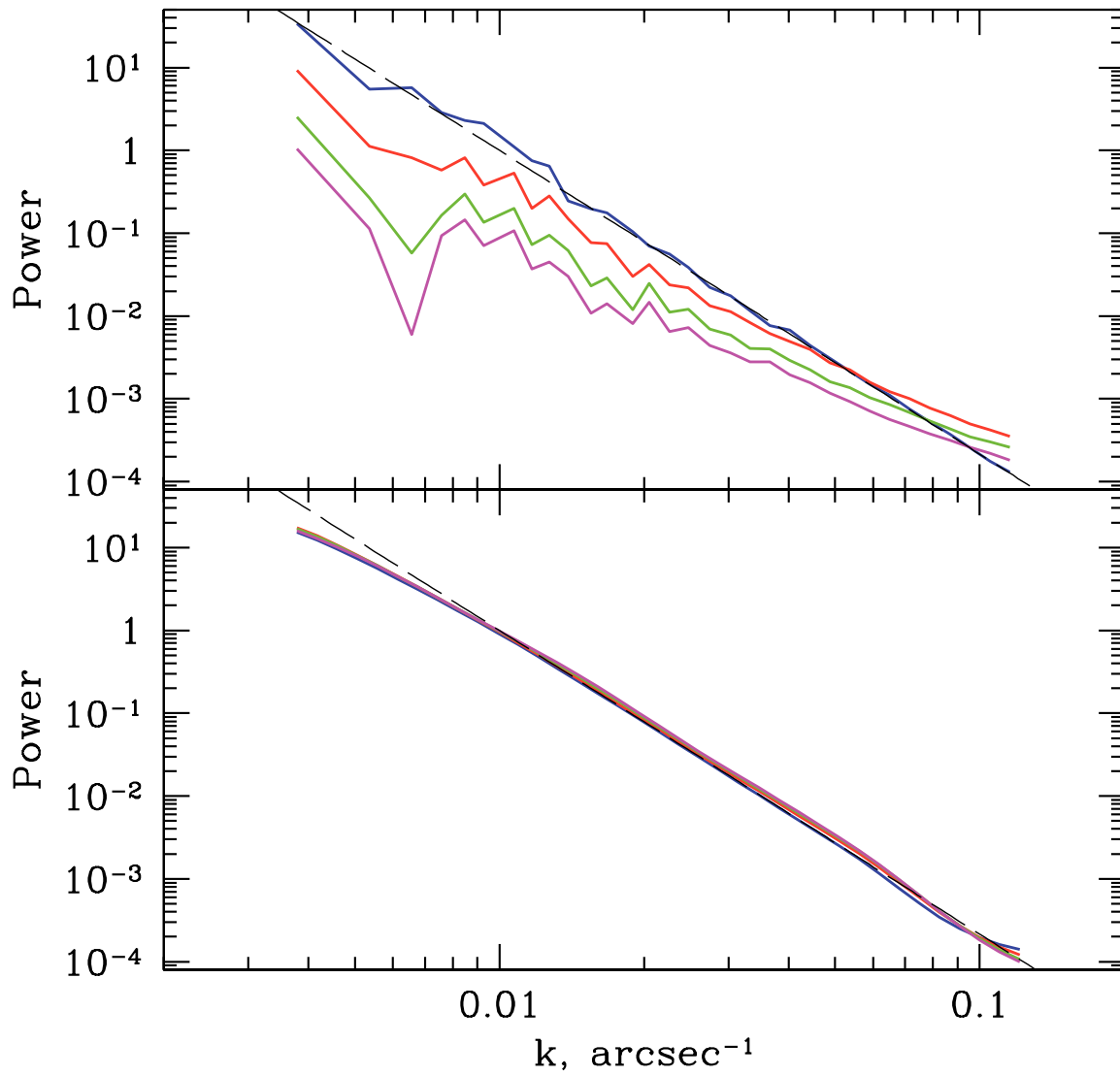
Figure 6.8: Power spectra of the data with gaps calculated through the variance (bottom panel) and the Fourier transform (the top panel). Blue: data without gaps; red, green and magenta: data with gaps (left, middle and right panels on Fig. 6.7 respectively). The black dashed curves show the input power spectrum.

Gaussian filters for computational simplicity as different dimensions of a multidimensional Gaussian are easily separable. The method can be applied straightforwardly to 1D timing analysis, 2D imaging as, for example, in the analysis of the Cosmic Microwave Background (CMB) angular fluctuations, and higher dimensional data cubes from numerical simulations.

6.6   Appendix

6.6.1   Cartesian coordinates

Consider a n-dimensional 'image' $I(x)$, where x is n-dimensional vector, and corresponding mask $M(x)$ with values of either 0 or 1. $M(x) = 0$ means that this particular region of the image does not contain useful information and should be ignored when calculating the power. We first consider Cartesian coordinates. Our goal is to estimate typical amplitude of the power spectrum for a given spatial scale a or, equivalently, given wave number k_r. Here and below we adopt the relation $k_r = 1/a$ without a factor 2π. The image is assumed to be an isotropic Gaussian random field so we will only compute the power as a function of the scalar k_r.

We start by defining a Gaussian filter in spatial domain, which will be convolved with the image:

$$G_\sigma(x) = \frac{1}{(2\pi\sigma^2)^{n/2}} e^{-\frac{x^2}{2\sigma^2}}. \tag{6.8}$$

Assuming first that the mask is equal to 1 everywhere we can combine two Gaussians to create a filter which selects fluctuations with a given scale (see Fig.6.2):

$$F_{k_r}(x) = G_{\sigma 1}(x) - G_{\sigma 2}(x), \tag{6.9}$$

where $\sigma 1 = \sigma/\sqrt{1+\epsilon}$, $\sigma 2 = \sigma\sqrt{1+\epsilon}$ and $\epsilon < 1$. The shape of the filter is identical to the Mexican Hat in the limit of small ϵ. In Fourier space the corresponding filter is:

$$\hat{F}_{k_r}(k) = e^{-2\pi^2 k \sigma_1^2} - e^{-2\pi^2 k \sigma_2^2}. \tag{6.10}$$

Making a Taylor expansion for ϵ we obtain

$$\hat{F}_{k_r}(k) \approx \epsilon 4\pi^2 k^2 \sigma^2 e^{-2\pi^2 k^2 \sigma^2}. \tag{6.11}$$

The peak of the filter is at $k = \frac{1}{\sqrt{2\pi^2}} \frac{1}{\sigma}$ (see Fig.6.2). It is therefore natural to relate the characteristic scale k_r corresponding to this particular filter width σ by:

$$\sigma = \frac{1}{\sqrt{2\pi^2}} \frac{1}{k_r} \approx \frac{0.225079}{k_r}. \tag{6.12}$$

Thus the final expression for the filter in Fourier domain is:

$$\hat{F}_{k_r}(k) \approx 2\epsilon \left(\frac{k}{k_r}\right)^2 e^{-\left(\frac{k}{k_r}\right)^2}. \tag{6.13}$$

Convolving the image $I(x)$ with the filter $F_{k_r}(x)$ described by eq. 6.9 and integrating the square of the convolved image is equivalent to integrating the product of the power spectrum $P(k)$ and the square of the Fourier transform of the filter, $\hat{F}_{k_r}(k)$. Below, V_{k_r} is the variance of the filtered image (F*I) since the mean of this filtered image is zero.

$$V_{k_r} = \int (F * I)^2 d^n x =$$
$$\int P(k)|\hat{F}_{k_r}(k)|^2 d^n k. \tag{6.14}$$

Notice that in eq.6.13 the filter drops to zero for k larger and smaller than k_r so that the function $P(k)$ can be approximated by $\tilde{P}(k_r)$ and taken out of the integral:

$$V_{k_r} \approx 4\epsilon^2 P(k_r) \int \left(\frac{k}{k_r}\right)^4 e^{-2\left(\frac{k}{k_r}\right)^2} d^n k =$$
$$\epsilon^2 P(k_r) n \left(\frac{n}{2} + 1\right) 2^{-\frac{n}{2}-1} \pi^{\frac{n}{2}} k_r^n \tag{6.15}$$

The last approximation breaks down for very steep power spectra, of positive or negative slope, where its product with the filter does not drop rapidly to zero for values of k different to k_r.

The quantity V_{k_r} is calculated from the image by following the filter and difference method described and expression 6.15 relates this quantity to the power $P(k)$ through a scale-dependent normalization. Therefore, the power $\tilde{P}(k_r)$ can be evaluated.

In practice the mask is not unity everywhere. In this case the above calculation is done by convolving the image and mask with the two Gaussian filters, dividing the convolved images; subtracting results and applying the original mask to the result:

$$S_{k_r}(x) = \left(\frac{G_\sigma * I}{G_\sigma * M} - \frac{G_{\sigma'} * I}{G_{\sigma'} * M}\right) M \tag{6.16}$$

The square of $S_{k_r}(x)$ is then integrated. The regions where the image is not defined ($S_{k_r}(x) = 0$), which do not contribute to the variance, are simply compensated for by counting all pixels where $M(x) = 0$ and making appropriate scaling:

$$V_{k_r,obs} = \frac{N}{N_{(M=1)}} \times \int S_{k_r}^2(x) d^n x, \tag{6.17}$$

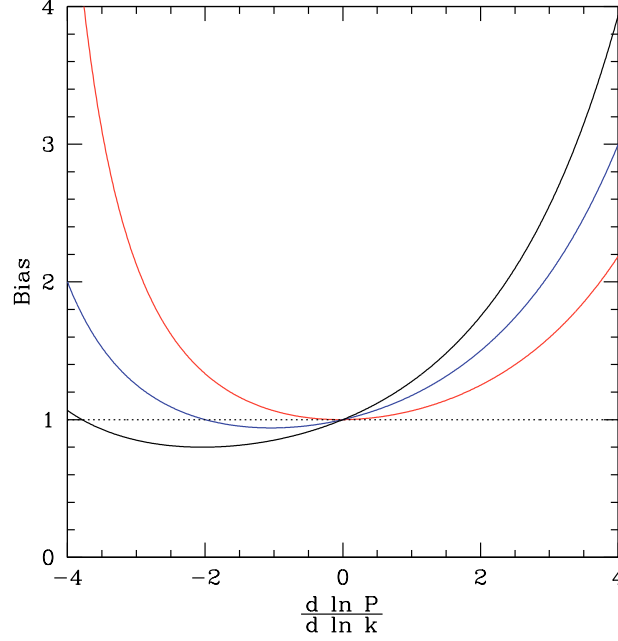where $N = \int d^n x$ and $N_{(M=1)} = \int M(x) d^n x$.

Figure 6.9: Bias $\frac{\tilde{P}}{P}$ in the normalization of the recovered spectrum for a pure power law spectra as a function of slope $\frac{d \ln P}{d \ln k}$ for different dimensions of the problem (red - 1D, blue - 2D, black - 3D).

Comparing eq.6.17 and 6.15 we get the final estimate of the power density spectrum $\tilde{P}_{k_r}$ for a given wave number k_r:

$$\tilde{P}_{k_r} = \frac{V_{k_r,obs}}{\epsilon^2 n \left(\frac{n}{2}+1\right) 2^{-\frac{n}{2}-1} \pi^{\frac{n}{2}} k_r^n} = \frac{V_{k_r,obs}}{\epsilon^2 \Upsilon(n) k_r^n}, \tag{6.18}$$

where

$$\Upsilon(n) = n \left(\frac{n}{2}+1\right) 2^{-\frac{n}{2}-1} \pi^{\frac{n}{2}}, \tag{6.19}$$

and $\Upsilon(n) = \frac{3}{4}\sqrt{\frac{\pi}{2}}, \pi, \frac{15\pi^{3/2}}{8\sqrt{2}}$ for $n = 1, 2, 3$.

The evaluation of the power density spectrum thus reduces to eq.6.18 for a set of values of k_r.

6.6.2 Normalization bias for a power law spectrum

For a pure power law spectrum $P(k) \propto k^{-\alpha}$ the expression 6.14 can be easily evaluated and exact relation between $\tilde{P}_{k_r}$ and $\tilde{P}(k_r)$ can be written. The shape of the spectrum is of

course recovered correctly, while the normalization may differ slightly, caused by moving $P(k)$ outside the integral in eq.6.15:

$$\frac{\tilde{P}}{P} = 2^{\alpha/2}\frac{\Gamma(\frac{n}{2} + 2 - \frac{\alpha}{2})}{\Gamma(\frac{n}{2} + 2)}. \tag{6.20}$$

Corresponding bias $\frac{\tilde{P}}{P}$ is shown in Fig.6.9. One can see that for the most relevant problems (2D or 3D geometry, $\frac{d\ln P}{d\ln k}$ in the range [-3:0]) the bias is modest.

Bibliography

Barreiro R. B., Hobson M. P., Banday A. J., Lasenby A. N., Stolyarov V., Vielva P., Górski K. M., 2004, MNRAS, 351, 515

Bensch F., Stutzki J., Ossenkopf V., 2001, A& A, 366, 636

Dolag K., Meneghetti M., Moscardini L., Rasia E., Bonaldi A., 2006, MNRAS, 370, 656

Jasche J., Kitaura F. S., Li C., Enßlin T. A., 2010, MNRAS, 409, 355

Markowitz A., Edelson R., Vaughan S., Uttley P., George I. M., Griffiths R. E., Kaspi S., Lawrence A., McHardy I., Nandra K., Pounds K., Reeves J., Schurch N., Warwick R., 2003, ApJ, 593, 96

Ossenkopf V., Krips M., Stutzki J., 2008, A& A, 485, 917

Sato T., Huetsi G., Yamamoto K., 2010, ArXiv e-prints

Scott D. M., Finger M. H., Wilson C. A., 2003, MNRAS, 344, 412

Smoot G. F., Bennett C. L., Kogut A., Wright E. L., Aymon J., Boggess N. W., Cheng E. S., de Amici G., 1992, ApJL, 396, L1

Stutzki J., Bensch F., Heithausen A., Ossenkopf V., Zielinsky M., 1998, A& A, 336, 697

Timmer J., König M., 1995, A& A, 300, 707

Chapter 7

Conclusions

The work presented in this thesis deals with the radiative transfer in bright X-ray emission lines in the spectra of galaxy clusters. In particular the aim was to use indirect ways to study the properties of the hot gas velocity field via the resonant scattering (RS) effect, which allows us already to probe the turbulence in galaxy clusters and is a source of additional information on the gas motions in a combination with future direct measurements. I (i) used RS to find the characteristic velocities of motions; (ii) used RS to constrain anisotropy and spatial scales of motions; (iii) investigated polarization due to RS and used it to constrain transverse motions; (iv) related near future observables, line shift and line width, to the properties of the 3D velocity power spectrum.

RS in the brightest X-ray emission lines causes distortions in the surface brightness distribution, changes in the line spectral shapes, variations in the abundance of heavy elements and the polarization in lines. The magnitude of these effects not only depends on the density, temperature and ionization state of the gas, but is also sensitive to the characteristics of the gas velocity field since the optical depth in lines sensitively depends on the turbulent broadening of resonant lines, especially for heavy elements like iron. Since iron is the most abundant element, the resonant lines of ionized iron are especially strong and bright. In these lines the cross section of scattering is much larger than the cross section in continuum and the optical depth in lines can be of the order unity or even larger, therefore RS starts to be important. For instance, the optical depth of the He-like iron line at 6.7 keV in the brightest clusters in the sky A426 (Perseus) and Virgo is ~ 3 and ~ 1.4 respectively.

If one accurately measures the line ratios of (optically thick) resonant and (optically thin) non-resonant lines, the velocity amplitudes of gas motions can be found. This method to constrain turbulence was applied to elliptical galaxy NGC4636 (see Chapter 2). We obtained high resolution spectra of the elliptical galaxy NGC 4636 using the RGS on the XMM-Newton satellite. The Fe XVII line at 15.01 Å is suppressed only in the dense core and not in the surrounding regions, while the line of Fe XVII at 17.05 Å is optically thin and is not suppressed. I modeled the radial intensity profiles of the optically thick line, taking into account the effect of RS for different values of the characteristic turbulent velocity. Comparing the model to the data, it was found that the isotropic turbulent velocities on

spatial scales smaller than ≈ 1 kpc are less than 100 km/s and the turbulent pressure support in the galaxy core is smaller than 5 per cent of the thermal pressure at the 90 per cent confidence level (taking into account only statistical errors).

The relation between the RS effect and the velocity field can be used to test anisotropy and spatial scales of gas motions (see Chapter 3). Purely radial motions naturally emerge if the energy from the central AGN passes into the shock and sound waves that propagate through the ICM mainly in the radial direction away from the central source. In contrast, tangential motions can arise in stratified atmospheres, where internal waves carry the energy of vertical motions away from the considered region. I showed that (i) the RS is sensitive mainly to small-scale gas motions; (ii) it is particularly sensitive to radial motions; (iii) the anisotropy of small-scale motions can be estimated by considering the broadening of spectral lines and the RS in lines simultaneously. Using the model of the Perseus cluster and the He-like iron line at 6.7 keV, we illustrate the sensitivity of RS to the anisotropy of small scale motions. The same ratio of the line fluxes corresponds to greatly different characteristic velocity amplitudes, namely, in the central 10 kpc $V_{\mathrm{RMS}} = 500$ km/s for isotropic motions, $V_{\mathrm{RMS}} \approx 200$ km/s for radial motions , and $V_{\mathrm{RMS}} \approx 1700$ km/s for tangential motions. Such a difference is related, in particular, to a nonlinear dependence of the line flux ratio on the velocities of gas motions.

RS also provides a unique opportunity to put constraints on transverse gas motions in galaxy clusters by means of future measurements of X-ray polarizations in lines (see Chapter 4). The atomic structure of the ions defines the process of line scattering (absorption and re-emission of the photon) as a combination of two components: isotropic and Rayleigh scattering. The Rayleigh component leads to the polarization (as in the case of Thomson scattering) if there is a quadrupole moment in the initial radiation field. In galaxy clusters such a quadrupole moment arises naturally if (i) the scattering takes place far from the bright central core of the cluster and/or (ii) if there are gas motions. I showed that the expected degree of polarization is high: in the Perseus cluster it reaches ~ 7 per cent in the He-like iron line at 6.7 keV. In the Virgo cluster it is about several per cent in the most promising lines. Transverse gas motions can change the expected degree and direction of polarization, since along the direction of motions the cross section of scattering in the line decreases. Using the hydrodynamical 3D simulations of galaxy clusters I calculated the degree of X-ray line polarization taking into account gas motions. I showed that polarization degree in the He-like iron line reaches ~ 25 per cent within the distance of 500 kpc from the core, if the cluster gas is at rest. The inclusion of gas motions decreases the polarization down to ~ 10 per cent and causes rotation of the polarization plane.

The current generation of X-ray observatories can not provide robust direct and indirect measurements of turbulence in ICM. The next future X-ray observatories, such as *Astro-H* and *Athena* will have an energy resolution of the order of a few per cent and will allow us to distinguish individual lines in spectra of galaxy clusters and measure their shifts and widths. The combination of direct measurements of the velocity field with indirect measurements via RS will provide a lot of new information on anisotropy and spatial scales of motions, allowing us to study deeper the dynamical state of hot gas in clusters. Polarimetric observations of galaxy clusters are very challenging since they

need high requirements of all basic characteristics of the telescopes, such as angular and energy resolutions, the effective area and the size of the field of view. Currently, several polarimeters based on the photoelectric effect are actively discussed and developed, among them GEMS, HXMT, polarimeter discussed in the frame of the IXO project and Bragg polarimeters for soft band. The current characteristics of these polarimeters and telescopes will soon reach the level of the required characteristics.

The last question I addressed in the thesis is whether we can use future observables to constrain the properties of the full 3D velocity field (see Chapter 5). It was shown that three observables, such as (i) the emissivity profile of clusters, (ii) the shift of line centroid , and (iii) line broadening are linked to the full 3D velocity power spectrum and to the structure function. In particular, I showed that (i) the ratio of observed amplitude variations of mean velocity and velocity dispersion can be used to find the break wavenumber (injection scale) of the velocity power spectrum and constrain the spatial scales of motions; (ii) the observed velocity dispersion is linked to the turbulence structure function; and (iii) mapping of the projected 2D velocity field provides the most direct way of estimating the 3D velocity power spectrum. I derived analytical expressions relating 3D velocity field and the main observables and illustrated the above mentioned effects using a simple model of a galaxy cluster.

Acknowledgements

It brings me a great joy to thank all the people who were part of my academic and private life during and before my PhD years.

I would like to thank Rashid Sunyaev that I could be a member of his group at MPA, for very useful and motivating discussions we had and for his generous support.

I would like to express my gratitude to my PhD supervisor Eugene Churazov for showing me the joy and fun of scientific world, for giving me interesting and challenging problems, for many insightful advices and for patience in answering my questions and discussing ideas which come to my mind.

I thank my collaborators, Klaus Dolag, Bill Forman, Andrey Kravtsov, Sergey Sazonov and Norbert Werner for their suggestions, critics and numerous discussions. It was a real pleasure for me to work with them.

I am grateful to all members of Sobolev Astronomical Institute in Saint-Petersburg State University for giving me broad knowledge of astrophysical basement and pointing me towards scientific direction. In particular, I thank my former supervisor Prof. Dmitry Nagirner for involving me to research and supporting me in finding PhD position.

Thanks to all my friends in Munich and Russia for support, pleasant distractions and a lot of fun.

Special thanks to Stefano for being close during all my PhD time.

I thank my family simply for being there for me and taking my dreams and ideas seriously.

Curriculum Vitae

Irina Zhuravleva
Max Planck Institute for Astrophysics
Karl-Schwarzschild-Str. 1
85741 Garching,Germany

Born: April 27,1986 in Pestovo, Russia
Citizenship: Russian
E-mail: izhur@mpa-garching.mpg.de
Telephone: +49 89 30000 2245

Education

International Max Planck Research School	Munich, Germany
PhD student at Max Planck Institute for Astrophysics	2008-2011
Dissertation: Radiative transfer in hot gas of galaxy clusters: constraints on ICM turbulence	
Advisors: Dr. Eugene Churazov, Prof. Dr. Rashid Sunyaev	
Saint-Petersburg State University	Saint-Petersburg,Russia
Faculty of Mathematics and Mechanics	2003-2008
Graduated in Theoretical Astrophysics	
Thesis: Polarization of radiation in X-ray lines in galaxy clusters	
Advisor: Prof. Dr. D.I. Nagirner	
Lyceum 384	Saint-Petersburg, Russia
Math profound learning	1993-2003

Additional research experience

Kavli Institute for Theoretical Physics	Santa Barbara, USA
Workshop "Galaxy Clusters: The Crossroads of Astrophysics and Cosmology", one month	2011
Space Research Institute (IKI)	Moscow, Russia
Summer internship, one month	2007
Special Astrophysical Observatory	Nizhnij Arkhyz, Russia
Summer internship, one month	2006
Observatory of Saint-Petersburg State University	Saint-Petersburg, Russia
Summer internship, one month	2006

Attended Conferences and Workshops

Structure in Clusters and Groups of Galaxies	Boston, USA
in the Chandra Era	2011
Contributed talk	
Galaxy Clusters: the Crossroads	Santa Barbara, USA
of Astrophysics and Cosmology	2011
Contributed talk	
High Energy Astrophysics Today and Tomorrow	Moscow, Russia
Contributed talk	2010
Non-thermal phenomena in colliding galaxy clusters	Nice, France
Contributed talk	2010
Galaxy Clusters: Observations, Physics and Cosmology	Garching, Germany
Poster presentation, member of LOC	2010
High-resolution X-ray Spectroscopy	Utrecht, The Netherlands
Poster presentation	2010
High Energy Astrophysics Today and Tomorrow	Moscow, Russia
Poster presentation	2009
The coming of age of X-ray polarimetry	Rome, Italy
Poster presentation	2009
High Energy Astrophysics Today and Tomorrow	Moscow, Russia
Poster presentation	2008
School on spectroscopy	Nizhnij Arkhiz, Russia
	2006
High Energy Astrophysics Today and Tomorrow	Moscow, Russia
Poster presentation	2006
School: Physics of Galaxies	Nizhnij Arkhiz, Russia
	2006

Languages: Russian native, **English** fluent,
German learning

List of publications

Constraints on the ICM velocity power spectrum from the X-ray lines width and shift
I.Zhuravleva, E. Churazov, A, Kravtsov, R. Sunyaev, 2011, MNRAS, submitted.

A Mexican Hat with holes: a method to calculate low resolution power spectra from data with gaps
P. Arévalo, E. Churazov, **I. Zhuravleva**, C. Hernández-Monteagudo, M. Revnivtsev, 2011, ApJ, submitted

Resonant scattering in galaxy clusters for anisotropic gas motions on various spatial scales.
I. Zhuravleva, E. Churazov, S. Sazonov, R. Sunyaev, K. Dolag, 2011, AstL, 37, 141.

Gas Turbulent Motions in Galaxy Clusters
I. Zhuravleva, 2011, proceedings of the conference "Non-thermal phenomena in colliding galaxy clusters"

Resonant Scattering of X-ray Emission Lines in the Hot Intergalactic Medium
E. Churazov, **I. Zhuravleva**, S. Sazonov, R. Sunyaev, 2010, SSRv, 157, 193

Steepening mass profiles, dark matter and environment of X-ray bright elliptical galaxies
P. Das, O. Gerhard, E. Churazov, **I. Zhuravleva**, 2010, MNRAS, 409, 1362

Polarization of X-ray lines from galaxy clusters and elliptical galaxies - a way to measure the tangential component of gas velocity
I. Zhuravleva, E. Churazov, S. Sazonov, R. Sunyaev, W. Forman, K. Dolag, 2010, MNRAS, 403, 129

Constraints on turbulent pressure in the X-ray haloes of giant elliptical galaxies from resonant scattering
N. Werner, **I. Zhuravleva**, E. Churazov, A. Simionescu, S. Allen, W. Forman, C. Jones, J. Kaastra, 2009, MNRAS, 398, 23

The Sunyaev-Zel'dovich effect in elliptical galaxies
B.V. Komberg, D.I. Nagirner, **I. Zhuravleva**, 2008, ARep, 52, 707